Simulation and modelling of turbulent reactive flows and heat transfer

Ronan Vicquelin

UNIVERSITÉ DE ROUEN NORMANDIE

MANUSCRIT

En vue de l'obtention de

L'HABILITATION À DIRIGER DES RECHERCHES

délivrée par : *l'Université de Rouen Normandie*

Présentée par

Ronan Vicquelin

Simulation et modélisation des écoulements turbulents réactifs et des transferts thermiques

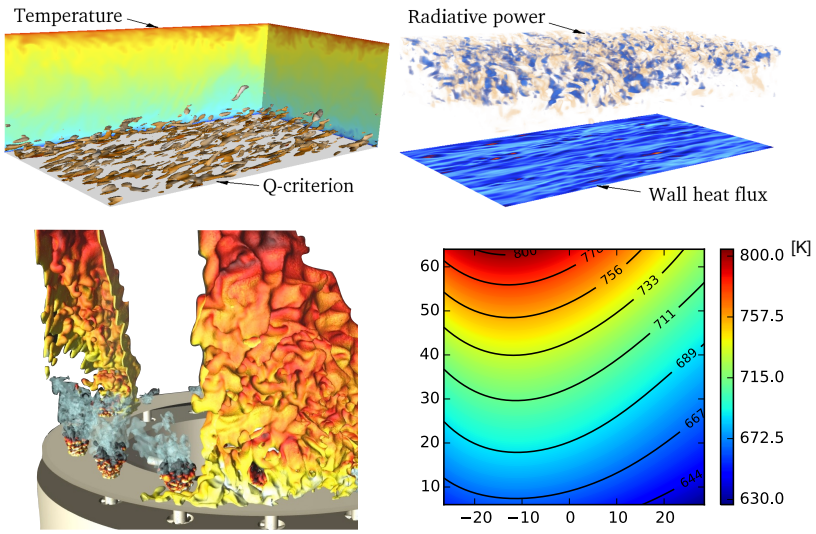

JURY

Françoise Baillot	Professeur - Université de Rouen	Membre du jury
Sébastien Candel	Professeur - CentraleSupélec	Membre du jury
Mouna El Hafi	Professeur - Ecole des Mines d'Albi	Rapporteur
Olivier Gicquel	Professeur - CentraleSupélec	Membre du jury
Christian Hasse	Professeur - Technische Universität Darmstadt	Rapporteur
Thierry Poinsot	Directeur de Recherche - CNRS - IMFT	Rapporteur
Jean Taine	Professeur - CentraleSupélec	Membre du jury
Luc Vervisch	Professeur - INSA Rouen	Membre du jury

MANUSCRIPT

Habilitation à Diriger des Recherches

presented by

Ronan Vicquelin

Position: Maître de Conférences in CentraleSupélec

Laboratoire d'Energétique Moléculaire et Macroscopique, Combustion (EM2C) du CNRS (UPR 288)

Numerical simulation and modelling of turbulent reactive flows and heat transfer

Manuscript version submitted in preparation for the defense scheduled on December 7, 2018

Committee composition:

Françoise	**Baillot**	Jury member
Sébastien	**Candel**	Jury member
Mouna	**El Hafi**	Referee
Olivier	**Gicquel**	Jury member
Christian	**Hasse**	Referee
Thierry	**Poinsot**	Referee
Jean	**Taine**	Jury member
Luc	**Vervisch**	Jury member

Remerciements

Je voudrais tout d'abord remercier Luc Vervisch qui a accepté d'être mon directeur de recherche pour cette HDR et pour son appui à ma candidature à l'obtention de l'Habilitation à Diriger des Recherches auprès des instances de l'Université de Rouen. Je tiens ensuite à remercier Mouna El Hafi, Christian Hasse et Thierry Poinsot qui m'ont fait l'honneur d'accepter d'examiner ce manuscrit comme rapporteur. Un grand merci également à Françoise Baillot pour sa participation au jury.

Le travail accompli est en grande partie grâce à un ensemble d'étudiants remarquables que j'ai eu la chance de co-encadrer et avec qui j'ai eu un grand plaisir à travailler. J'ai ainsi une pensée toute particulière pour Yufang Zhang, Chaï Koren, Maxime Philip, Nicolas Dumont, Théa Lancien, Pedro Rodrigues, Lorella Palluotto, Jan Mateu Armengol et Arthur Degenève. Merci à eux. Je sais que les nouveaux arrivés dans l'équipe (Kévin, Matteo, Karl, Stefano, Guilhem et Luc) se montreront à la hauteur d'un tel héritage ! ;-)

Je tiens à remercier le laboratoire EM2C et tout son personnel pour d'abord l'ambiance régnant au laboratoire propice à la camaraderie, aux échanges et à un cadre de travail exceptionnel. J'aimerais souligner ici le support proactif et efficace des pôles administratif avec Noï, Nathalie, Brigitte, et informatique avec Sébastien, Matthieu et maintenant Jean-Michel. Les différentes directions successives du laboratoire (Nasser Darabiha, Estelle Iacona, Olivier Gicquel et Sébastien Ducruix) ont eu et ont toujours à cœur de soutenir les jeunes chercheurs et je leur en suis reconnaissant. J'ai une pensée également pour les discussions fructueuses avec mes collègues que ce soit dans l'axe combustion ou dans les autres. Ne pouvant lister tout le monde, je souhaite souligner ici ma considération pour Nasser Darabiha, Denis Veynante, Thierry Schuller et Marc Massot. Ouvrir la porte de leur bureau est la promesse de discussions passionnées et stimulantes, et des meilleurs conseils. Je pense aussi à mes jeunes collègues (Matthieu, Thomas, Adam, Benedetta et Aymeric) avec qui j'ai démarré mon métier d'enseignant-chercheur. Je remercie particulièrement mes anciens collègues de bureau, Thomas Schmitt et Adam Larat, pour leur franche bonne humeur (si si, même Thomas le râleur!) et nos échanges toujours très enthousiastes.

Je souhaite témoigner de mon affection pour trois personnes qui m'ont accompagné dans mes activités de recherche : Sébastien Candel, Jean Taine et Olivier Gicquel. C'est sur l'invitation de Sébastien que j'ai participé à l'étude numérique de l'allumage sur la chambre MICCA. Avec son appui, cette activité s'est grandement enrichie. Sur ce sujet comme sur d'autres, ses conseils sont des plus pertinents et toujours fournis promptement malgré sa charge de travail incroyable. C'est avec Jean et Olivier que j'ai été initié au monde merveilleux des transferts radiatifs lors de la thèse de Yufang. La rigueur et l'esprit prolifique de Jean m'ont impressionné. Je me rappellerai toujours nos points de thèse animés pour essayer de suivre Jean.

Je veux exprimer mon immense reconnaissance à Olivier Gicquel pour le rôle qu'il a eu dans

ma vie (ce n'est pas rien !). Olivier m'apporte son soutien depuis ma thèse qui a commencé en 2006. Derrière sa bonne camaraderie et son esprit boute-en-train, on trouve un homme exigeant et qui déplace des montagnes pour ses collaborateurs. J'en ai été personnellement témoin et l'ai constaté auprès de ses autres étudiants, ses collègues et son laboratoire lorsqu'il en était le directeur. Il met maintenant son énergie au service de la direction de la recherche, tout en suivant d'un œil nos activités de recherche communes. J'apprécie le chercheur, l'homme et l'ami en Olivier, et même si nous nous voyons moins souvent pour encadrer au quotidien les étudiants, je sais que cette distance témoigne de la confiance qu'il me porte et en suis honoré.

Je ne saurai découpler mon métier de mon enseignement à l'école CentraleSupélec où j'ai un grand plaisir à côtoyer les élèves. Je tiens à remercier Franck Richecoeur et Thierry Schuller qui m'ont accordé, en tant que directeur de département, leur confiance pour plusieurs cours, et plus récemment Franck pour m'inviter à l'encadrement de l'option MAE. Je dois aussi souligner, de nouveau, le rôle de Sébastien Candel pour m'avoir associé à l'équipe d'enseignants en Mécanique des Fluides et que je remercie. La clarté et la dévotion de Sébastien à ses cours a été pour moi, comme à d'autres, un modèle. Ce cours a été poursuivi par Thierry et Franck avec les mêmes ambitions et c'est maintenant un privilège de poursuivre dans leurs pas.

Je voudrais enfin remercier mes parents et Juliette pour leur soutien inconditionnel. Bravo à Robin et Liam pour leur patience pendant que leur père rédigeait ce manuscrit.

Preface

This manuscript has been prepared for my application to the degree of Habilitation à Diriger des Recherches from Université Rouen Normandie. The document is organized with three parts and eight chapters.

The first part contains a Curriculum Vitae followed by a summary of my teaching and research activities. Since my appointment as assistant professor in CentraleSupélec in 2011, I have had the opportunity to participate to different funded projects and to the supervision of several Ph.D. students, whose list is detailed in Chapter 2. Part I ends with a list of publications and conferences.

The second part details my research activities along three axes. My activities on modelling and simulations of turbulent reactive flows initiated during my thesis are given in Chapter 4. Since 2011, two additional research themes have been developed: the first one on ignition in gas turbines (Chapter 5) and a second one on heat transfer and multiphysics simulation (Chapter 6).

After synthesizing the different contributions, the third part of the manuscript describes a new set of scientific objectives and my future projects planned at EM2C laboratory along with ongoing activities to achieve them.

Contents

Part I

Scientific animation and production

Chapter 1

Curriculum Vitae

1.1 General information

Ronan Vicquelin
Maître de Conférences / Assistant Professor
CentraleSupélec

Research interests

Turbulent reacting flows with a focus on numerical simulation and modelling. Turbulent combustion modelling. Reduction methods for chemistry: Tabulated chemistry, flamelet models. Large eddy simulations. Direct numerical simulations. Reacting compressible flows. Reacting two-phase flows. Ignition in gas turbines. Coupled multi-physics simulations. High Performance computing. Conjugate Heat transfer. Radiative energy transfer. Wall-bounded flows. Uncertainty quantification.

Contact information

Adress ..... Laboratoire EM2C, CNRS UPR 288
8-10 rue Joliot Curie
91192 Gif-sur-Yvette cedex, France
Phone number ..... +33 (0)1 75 31 60 90
Email ..... Ronan.Vicquelin@centralesupelec.fr
Homepage ..... em2c.centralesupelec.fr/Ronan_Vicquelin

ORCID 0000-0002-2055-5244
IdHAL ..... ronan-vicquelin (CV HAL)
ResearcherId M-7563-2018
Google Scholar ..... here

Other information

Date of birth ..... May 23, 1984
Nationality ..... French
Family situation ..... Married, two children

Current position

Laboratoire de rattachement	Laboratoire EM2C, CNRS UPR 288
Etablissement	CentraleSupélec 8-10 rue Joliot Curie 91192 Gif-sur-Yvette cedex, France
Grade	Maître de Conférences
Nomination	Septembre 2011
Titularisation	Septembre 2012
Echelon	05

Education

2010	Ph.D. in Energetics, Ecole Centrale Paris.
2006	M.Sc. in Mechanical Engineering and Aerospace, Ecole Centrale Paris.
2006	Diplôme d'Ingénieur, Ecole Centrale Paris.

Past experiences

2010-2011	Post-doctoral Fellow, Center For Turbulence Research, Stanford University, USA.
2006-2010	Engineer, GDF Suez, Centre de Recherche et d'Innovation Gaz et Energies Nouvelles, France.

Awards

2013	APS-DFD Milton van Dyke Award.

Other Professional Affiliations and Activities

◦ Member of the French section of the Combustion Institute
◦ Member of the French society of Heat transfer
◦ Referee for international journals: Combustion and Flame; Flow, Turbulence and Combustion; International Journal of Heat and Mass Transfer; International Journal of Thermal Sciences; Proceedings of the ASME Turbo Expo; Journal of Computational Physics; Proceedings of the Combustion Institute
◦ Referee for funding agencies: ANR, EU PRACE projects

2018-present	Supervisor of CentraleSupélec's Mésocentre (High Performance Computing center)
2016	Organizer of the uncertainty quantification workshop for the French section of the Combustion Institute
2015	Member of the organizing committee of the International Conference on Numerical Combustion (300 people)
2013-2014	Elected member of Ecole Centrale Paris' Conseil d'Administration
2013-present	Member of the executive board of CentraleSupélec's Mésocentre (High Performance Computing center)

1.2 Research activities

My research activities encompass numerical simulations, analysis and modelling of turbulent reactive flows and heat transfer. The considered approaches to describe turbulence are direct numerical simulations (DNS) and large-eddy simulations (LES). These studies can be gathered into three themes. The first one follows my initial expertise in modelling of turbulent reacting flows obtained during my Ph.D. thesis. The second theme was initiated in 2012 and focuses in the study of gas turbine ignition. Finally, since my arrival as an assistant professor in EM2C laboratory, I have had the opportunity to develop studies on heat transfer and multiphysics simulations, which is a third research theme.

Several illustrative highlights of the main achievements are also given in this section.

1.2.1 modelling and simulation of turbulent reacting flows

Despite the continuous growth in computational resources, numerical simulations of turbulent flames must rely on models to describe phenomena such as turbulence and kinetics whose detailed description would yield a prohibitive cost. During my research, we have mostly relied on tabulated chemistry methods also known as flamelet models to describe turbulent combustion. Besides, additional models are to be considered in more complex flows: two-phase reactive flows, sooted flames, ... The objectives in this research theme are then:

1. Development and implementation of models for turbulent reacting flows.
2. Simulation and validation of the numerical modelling setup.
3. Analysis of simulation results.

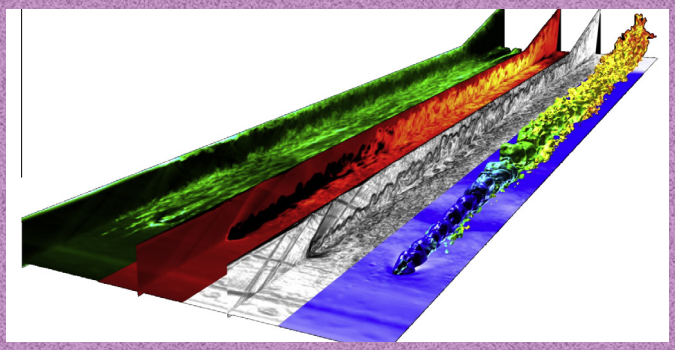

Highlight #1
Combination of an equilibrium wall-model and a flamelet-based model for large-eddy simulation of a scramjet combustor [A12].

Figure 1.1: Instantaneous snapshot from LES of the HyShot II scramjet. From the left, the slices show contours of streamwise velocity, temperature, simulated Schlieren and pressure

1.2.2 Ignition in annular combustors

This research theme extends the previous one to a specific and critical application of great interest that is ignition in aeronautical gas turbines. The last phase of ignition in an annular combustor equipped with multiple burners is here considered. It is called the *light-round* and exhibits a flame that propagates from one injector to the next inside the combustion chamber. When I began this activity in 2012 upon the kind invitation of Sébastien Candel, light-round studies were extremely scarce in the literature. This activity could not have been envisioned without the EM2C unique annular combustion chamber MICCA which has been extensively

studied by Daniel Durox, Sébastien Candel and their students and collaborators. The study of burner-to-burner flame propagation has recently increased significantly in the literature with the appearance of more and more multi-burner combustors in different research groups.

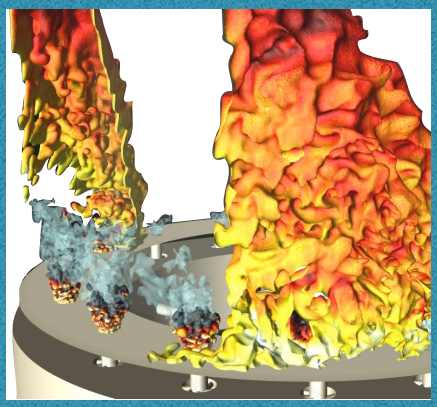

Highlight #2
First validation of light-round simulation in an annular combustion chamber. Such a study has been carried out in premixed gaseous conditions [T3] and with the injection of liquid fuel [T5].

Figure 1.2: Simulation of the ignition of the MICCA combustion chamber. The flame is identified by an iso-surface of reaction progress variable colored by axial velocity.

So far, successful events under atmospheric conditions with gaseous or liquid fuel injection have been studied in MICCA. In terms of simulations, the objectives are to

1. Carry out massively parallel large-eddy simulation of light-round (6 000 to 10 000 cpu cores for a mesh of 300 million elements).
2. Assess the accuracy of computational results and the impact of the chosen numerical models.
3. Analyse results to understand the physical mechanisms that drives the flame propagation.

1.2.3 Heat transfer and multiphysics simulations

Multiphysics simulations are here meant as the coupling of different modes of heat transfer with the presence of a turbulent flow which can be reactive or not. Such coupling phenomena significantly complexify the numerical simulations. Indeed, describing the different physical nature of the considered phenomena requires to use several separate solvers and to couple them with each other: a DNS/LES solver for turbulent flows, a heat-conduction solver for conjugate heat transfer in solid parts of the domain, and finally a solver dedicated to thermal radiation. This activity is rooted in the expertise of two research groups in the EM2C laboratory: one in combustion and one in heat transfer, thermal radiation in particular. My contributions is this area started with the opportunity to co-supervise the Ph.D. thesis of Yufang Zhang with Olivier Gicquel and Jean Taine on coupled radiative effects in turbulent boundary layers. Since then, I have pursued this research theme with Olivier Gicquel to additionally account for conjugate heat transfer (CHT) in order to predict wall temperature fields.

In my different works dealing with radiation, a Monte Carlo (MC) method combined with accurate narrow-band gas radiative properties is used. While expansive, the unusual combination of this approach with LES is a promising candidate for accurate prediction of radiative transfer in turbulent flows.

The combination of DNS/LES with CHT and a MC solver (separately or all together) has yielded several topics in this research theme:

Highlight #3
Impact of thermal radiation in turbulent boundary layers [T1]. This study was carried out by coupling direct numerical simulations and a reciprocal Monte Carlo method.

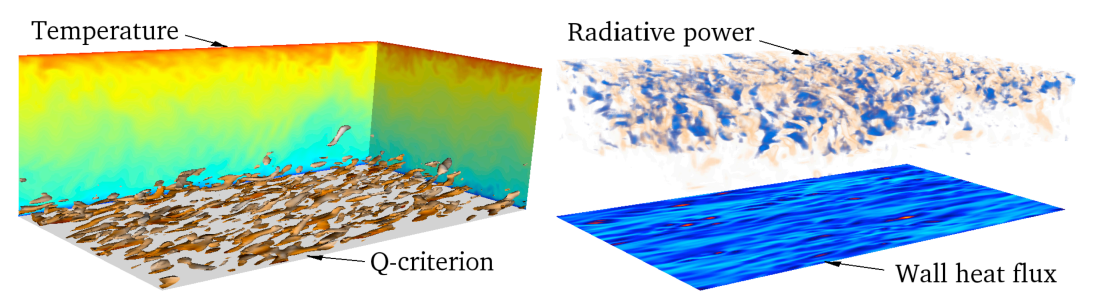

Figure 1.3 : Different fields of the coupled DNS results.

1. Characterization of heat transfer coupled effects on reactive and non-reactive flows turbulent flows.
2. Development and improvement of numerical methods: Monte Carlo solver for radiation, coupling algorithms.
3. Validation and analysis of coupled simulation results.
4. Dedicated applications: thermal radiation in sooted flames, heat transfer associated to oxy-combustion.

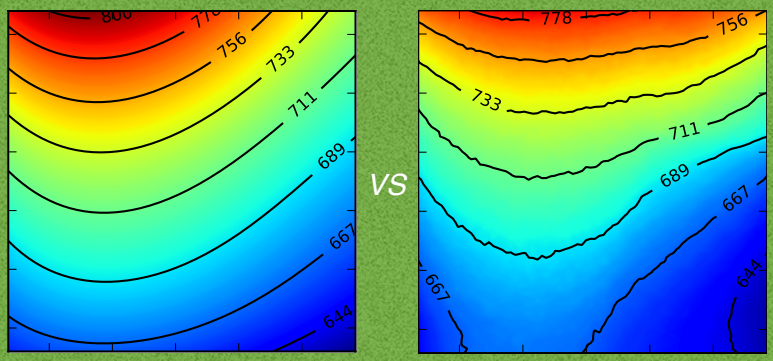

Highlight #4
Unprecedented accuracy of large-eddy simulation coupled to radiative transfer from burnt gases and wall heat conduction in a combustion chamber [A5]. The results analysis reveals the specific role of radiation in the studied configuration.

Figure 1.4: 2D field of wall temperature in Kelvin units. Left: experimental data obtained by LIP. Right: the field predicted by the coupled simulation

1.2.4 Bibliometric synthesis

Since 2011, these different studies have been carried out with the students I have had the chance to supervise. The list of these people is given in Sec. 2.1. Most of their work was supported by dedicated funded research projects whose list is given in Sec. 2.2. Other students benefited from individual fellowships or contracts. The list of publications and conferences which came out of the different research themes is given in Chap. 3. A bibliometric synthesis of these publications is provided in Tab. 1.1.

Table 1.1: Bibliometric synthesis

Source on August 2018	Number of references	Number of citations	Most cited reference	h-index
Web of Sciences	28	229	94 times	8
Scopus	25	278	110 times	8
Google Scholar	49	480	163 times	11

1.3 Teaching activities

Table 1.2 sums up the teaching hours realised since I start as an assistant professor in 2011. Several categories of activities are distinguished:

Courses: lectures, practice sessions.

Project supervision:

- projets enjeux (CentraleSupélec 1st-year students),
- projets TIME (CentraleSupélec 1st-year students),
- projets innovation (CentraleSupélec 2nd-year students),
- projets de synthèse (CentraleSupélec 3rd-year students and Master students).

Responsibilities:

- Aerospace track in 3rd-year option Mechanical and Aerospace Engineering,
- Coordination of course activities,
- Follow-up on students in academic international exchange,
- Follow-up on students in their last-year internship.

Option Mécanique Aéronautique et Espace - *since 2016 - 30 students* - I have been invited in 2016 by Franck Richecoeur to take the responsability of the Aerospace track which is part of the last year specializing option in Mechanical and Aerospace Engineering (*option MAE*) in Centrale Paris engineer cursus. This specialization gathers ∼30 students and was initially created by Sébastien Candel whose supervision was then handled by Olivier Gicquel before Franck Richecoeur took over. I have participated in the management and evolution of the *option MAE* composed of a core curriculum based on complex systems and scientific

Table 1.2: Synthesis of teacging activities since september 2011 (heures équivalent TD)

	Course	Projects	Responsibilities	Total
2011-2012	107 h	18h	76 h	201 h
2012-2013	125 h	53h	78 h	256 h
2013-2014	174 h	62 h	62 h	298 h
2014-2015	174 h	19h	52 h	245 h
2015-2016	182 h	16 h	50 h	248 h
2016-2017	204 h	5 h	62 h	271 h
2017-2018	170 h	0 h	40 h	210 h

specializations related to fluid mechanics (compressible flows, aerodynamic, flight mechanics, combustion, turbofans, ...). A little less than a dozen of industrial partners are involved in the *option MAE*. In particular, engineers approximatively participate to one half of the courses. Throughout the year, we visit industrial sites from our partners (Fig. 1.5).

Figure 1.5: Visit of the Centre Spatial Guyanais (Kourou, France) in 2018.

Sciences des Transferts - *since 2018 - 4×100 students* - This is a new course given in the new curriculum CentraleSupélec to 1st-year students in september 2018. This course introduces concepts of heat and mass transfer and fluid mechanics along with practical engineering problem solving. I share the course responsibility with Hervé Duval.

Fluid Mechanics - *since 2011 - 60 students* - This course was initially under the responsibility of Sébastien Candel, then of Thierry Schuller and now of Franck Richecoeur. Students from CentraleSupélec can choose this course during their 1st- or 2nd-year. I initially participated in the practice sessions, then taught the English version of the full course. I am now in charge of the 2nd-year occurrence of the course.

Numerical Methods in Engineering - *since 2013 - 30 students* - I am in charge of this course taught in English to CentraleSupélec 2nd-year students. Theory on numerical resolution

of ODEs and PDEs is illustrated by solving practical problems of heat and mass transfer and fluid mechanics.

Numerical Methods in Fluid dynamics - *since 2018 - 30 students* - I am in charge of this course given to CentraleSupélec 3rd-year students where fluid mechanics problems are solved with finite difference methods: turbulent diffusion of a scalar in a homogeneous isotropic turbulence, calculation of head loss in a square duct, effects of pressure gradient on a spatially evolving laminar boundary layer, resolution of Navier-Stokes equations to simulate a counterflow-stabilised flame.

Digital Signal Processing - *since 2012 - 30 students* - I took over Sebastien Candel's responsibility for this course given to CentraleSupélec 3rd-year students who are introduced to different notions: discrete signals and systems, Discrete Fourier transform, sampling and reconstruction, spectral analysis and power spectral density, digital filtering.

Turbulence - *since 2012 - 50 students* - I am in charge of this course given to CentraleSupélec 3rd-year students. Contents: fundamental mechanisms, Kolmogorov cascade, RANS/LES/DNS, RANS equations, closure models, turbulent wall-bounded flows, spectral analysis and large-eddy simulations.

Radiative Heat Transfer in Combustion - *since 2017, 20 students* - Lecturer (3h), VUB Master degree, Brussels, Belgium.

Applied Fluid Mechanics - *2016-2017 - 40 students* - Teaching assistant with CentraleSupélec 3rd-year students.

Heat Transfer Methodology - *2011-2013 - 5×5 students* - Teaching assistant of one group of CentraleSupélec 3rd-year students.

Computational Fluid Dynamics -*2011-2012* - Teaching assistant with EPF 3rd-year students under the supervision of Benoit Fiorina.

Chapter 2

Supervision and animation

2.1 Supervision of Master, Ph.D. and Post-doctoral fellows

Since I started my position as an assistant professor, I have been participating to the supervision of several Ph.D. theses. Table 2.1 lists the corresponding students along with their type of funding, their subject, their supervisors and my rate of participation in the supervision. (*: scheduled date of Ph.D. defense).

Table 2.1: List of supervised Ph.D. students

Period Participation (%)	**Student**, funding *Subject* Supervisors and scientific production
03/2018 - 03/2021*	**Karl Töpperwien** [T12]. European project Marie-Curie ANNULIGHT. *Etude de la dynamique transitoire de flamme dans les foyers annulaires multi-injecteurs*
100%	Supervisors: R. Vicquelin.
04/2018 - 04/2021*	**Matteo Gelain** [T11]. CIFRE Safran. *Simulations des transferts thermiques dans un échangeur de chaleur aéronautique : approches DES et WMLES*
20%	Supervisors: R. Vicquelin, M. Errera, O. Gicquel, Safran Aircarft Engines.
11/2017 - 11/2020*	**Kévin Torres** [T10]. European project SOPRANO. *Transferts radiatifs dans les flammes suitées turbulentes*
50%	Supervisors: R. Vicquelin, O. Gicquel.
01/2017 - 01/2020*	**Arthur Degenève** [T9]. CIFRE Air Liquide. *Etude expérimental et numérique de la stabilisation d'oxyflammes pressurisées swirlées et diluées en vapeur d'eau*
50%	Supervisors: R. Vicquelin, T. Schuller. Production: [A1, D1, D2, E1, E2]
10/2015 - 04/2019*	**Lorella Palluotto** [T8]. European project Marie-Curie Clean-Gas. *Simulations multiphysiques des transferts radiatifs en oxycombustion*
50%	Supervisors: R. Vicquelin, O. Gicquel. Production: [D3, D10, E8]

Table 2.1: (continued)

Period Participation (%)	**Student**, funding *Subject* Supervisors and scientific production
06/2015 - 04/2019*	**Jan Mateu Armengol** [T7]. Bourse Brésil.
	Simulations numériques directes des intéractions rayonnement-turbulence
30%	Supervisors: R. Vicquelin, O. Gicquel, R. dos Santos.
	Production: [D6]
11/2014 - 06/2018	**Pedro Rodrigues** [T6]. Chaire ANR OxyTec.
	Modélisation multiphysique de flammes turbulentes suitées avec la prise en compte des transferts radiatifs et des transferts de chaleur pariétaux
30%	Supervisors: R. Vicquelin, B. Franzelli, O. Gicquel, N. Darabiha.
	Production: [A5, A9, D3, D4, D5, D10, E10]
11/2014 - 10/2018*	**Théa Lancien** [T5]. ANR TIMBER.
	Etude numérique de l'allumage diphasique de foyers annulaires multi-brûleurs
100%	Supervisors: R. Vicquelin.
	Production: [A3, A8, D9, D11, E5]
11/2013 - 12/2018*	**Nicolas Dumont** [T4]. Bourse MESR.
	Quantification d'incertitudes des mécanismes chimiques dans les simulations aux grandes échelles
50%	Supervisors: R. Vicquelin, O. Gicquel.
	Production: [D3, D10, D11, D12, E13, E14]
11/2012 - 04/2016	**Maxime Philip** [T3]. Bourse IDEX.
	Dynamique de l'allumage circulaire dans les foyers annulaires multi-injecteurs
50%	Supervisors: R. Vicquelin, T. Schmitt, S. Candel.
	Production: [A12, A13, A14, D13, E9, E18, E21, E22]
11/2012 - 04/2016	**Chaï Koren** [T2]. CIFRE Air Liquide.
	Modélisation des transferts de chaleur couplś pour la simulation multiphysique des chambres de combustion
50%	Supervisors: R. Vicquelin, O. Gicquel.
	Production: [A2, A7, D3, D7, D8, D10, E16]
10/2010 - 09/2013	**Yufang Zhang** [T1]. CSC Felllowship.
	Coupled convective heat transfer and radiative energy transfer in turbulent boundary layers
50%	Supervisors: R. Vicquelin, O. Gicquel, J. Taine.
	Production: [A6, A10, A15, A16, A17, D15, D16, E23, E24]

I have also supervised one Master student during an internship and one postdoctoral position. They are listed in Tab. 2.2.

Table 2.2: Other supervision activities

Period Participation (%)	**Fellow**, funding *Subject*	Nature
06/2018 - 07/2019	**Stefano Puggelli**. ANR TIMBER. *Large-eddy simulation of light-round with a dynamic formulation of the flame subgrid wrinkling factor*	Postdoctoral Fellow
100%	Supervisors: R. Vicquelin.	
05/2012 - 10/2012	**Chaï Koren**. Ecole Centrale Paris. *Etude du couplage numérique de deux codes de résolution numérique et de l'influence de la différence des échelles temporelles à l'aide du phénomène de conduction de la chaleur*	Master Internship
100%	Supervisors: R. Vicquelin.	

Since 2012, my publications rely on my supervised students whose scientific production is also highlighted in Tab. 2.1. I am grateful to their hard-work and their dedication to their thesis. While most of them also contribute in parallel to the research theme on *modelling of turbulent reacting flows*, their theses have been focused on the other two themes and an emerging one that is *Uncertainty quantification* that will be detailed in Chap. 8:

- Ignition in annular combustors:

  M. Philip, T. Lancien, K. Töpperwien, S. Puggellli

- Heat transfer and multiphysics simulation:

  Y. F. Zhang, C. Koren, P. Rodrigues, L. Palluotto, J.M. Armengol, A. Degenève, K. Torres, M. Gelain

- Uncertainty quantification:

  N. Dumont

2.2 Funded research projects

Since 2012, I have participated, elaborated and supervised several national and international projects whose list is given in Tab. 2.3. The funding for EM2C activities is given in the right column.

Table 2.3: List of funded research projects

Period	**Project**, project coordinator, (Total budget) *Description* ◦ Funding agency ◦ Partners ◦ Role	Funding
2017-2021	**ANNULIGHT**, coordinated by J. Dawson (NTNU), 3 970 k€ *Combustion dynamics in annular combustors.* ◦ Funding agency: European Union Marie Skłodowska-Curie ◦ Partners: NTNU (Norway), CERFACS (France), CNRS (France), TUM (Germany), TUB (Germany), U. Cambridge (UK), ETH (Switzerland), SAFRAN, Ansaldo ◦ Role: Work package leader; Supervision of Ph.D. student on numerical simulations of ignition, extinction and instabilities in annular combustors.	>450 k€
2018-2019	**MRIC**, coordinated by R. Vicquelin, 68 k€ *Development of reduced models for combustion uncertainties.* ◦ Funding agency: LABEX LASIPS ◦ Partners: EM2C (CNRS) and LIMSI (CNRS) ◦ Role: Coordination; Supervision of postdoctoral fellow on uncertainty quantification in reactive LES.	>50 k€
2017-2018	**CRITICal**, coordinated by R. Vicquelin *Massively-parallel simulations to characterize two-phase ignition in combustors* ◦ Funding agency: European Union PRACE project ◦ Partners: CERFACS and EM2C (CNRS) ◦ Role: Coordination; LES of two-phase flow ignition in annular combustors.	33 million CPU hours
2016-2010	**SOPRANO**, coordinated by SAFRAN, 6 800 k€ *Deliver more accurate experimental and numerical methodologies for predicting the soot emissions in academic or semi-technical combustion systems.* ◦ Funding agency: European Union H2020 project ◦ Partners: ONERA, General Electric, ROLLS- ROYCE PLC, MTU, UNIFI, RRD, KIT, CNRS, TURBOMECA SA, DLR, INSA Rouen, SAFRAN, GE AVIO, SAFRAN SA, FEL, CERFACS, Imperial College ◦ Role: Supervision of Ph.D. student on toot radiation in multi-physics LES.	> 300 k€

Table 2.3: (continued)

Period	**Project**, project coordinator, Total budget *Description* ◦ Funding agency ◦ Partners ◦ Role	Funding
2015-2019	**CleanGas**, coordinated by Politecnico di Milano, 3 800 k€ *Develop new experimental and numerical tools for improving natural gas combustion in innovative burners.* ◦ Funding agency: European Union Marie Skłodowska-Curie ◦ Partners: Politecnico di Milano (Italy), CentraleSupélec (France), Technische Universität Darmstadt (Germany), Université Libre de Bruxelles (Belgium) ◦ Role: Supervision of Ph.D. student on enhancement of thermal radiation solver and its coupling with multiphysics LES.	>800 k€
2014-2019	**TIMBER**, coordinated by R. Vicquelin, 484 k€. *Combined experimental and numerical study of two-phase ignition in multi-burner combustors.* ◦ Funding agency: ANR ◦ Partners: CERFACS, CORIA (CNRS) and EM2C (CNRS) ◦ Role: Coordination; Supervision of Ph.D. student on numerical simulations of ignition in annular combustors.	> 200 k€
2013-2017	**NEXTFLAME**, coordinated by M. Boileau/M. Massot (EM2C), 420 k€ *Experimental and numerical study of laminar two-phase flames.* ◦ Funding agency: ANR ◦ Partners: Partners: CERFACS, EM2C (CNRS) ◦ Role: Enhancement of 1D code AGATH to simulate two-phase flames.	> 200 k€
2012-2020	**OXYTEC**, coordinated by T. Schuller (EM2C, now IMFT), 2 300 k€ *Experimental and numerical study of high-pressure oxy-combustion.* ◦ Funding agency: Air Liquide, CentraleSupélec, CNRS, ANR ◦ Partners: CentraleSupélec ◦ Role: Supervision of Ph.D. students on multiphysics simulation of heat transfer with LES.	> 2 000 k€
2012-2013	**SIMAC**, coordinated by M. Boileau (EM2C) *Simulation of ignition mechanisms in annular multi-injector combustors and comparison with experiments* ◦ Funding agency: European Union PRACE project ◦ Partners: CERFACS and EM2C (CNRS) ◦ Role: LES of ignition in annular combustors.	15 million CPU hours

Chapter 3

List of publications and conferences

3.1 Publications in international peer-reviewed journals

[A1] A. Degenève, R. Vicquelin, C. Mirat, B. Labegorre, P. Jourdaine, J. Caudal, and T. Schuller. "Scaling relations for the length of coaxial oxy-flames with and without swirl". In: *Proceedings of the Combustion Institute, accepted* (2018).

[A2] C. Koren, R. Vicquelin, and O. Gicquel. "Multiphysics simulation combining large-eddy simulation, wall heat conduction and radiative energy transfer to predict wall temperature induced by a confined premixed swirling flame". In: *Flow Turbulence and Combustion* 101.1 (2018), pp. 77–102.

[A3] T. Lancien, K. Prieur, D. Durox, S. Candel, and R. Vicquelin. "Leading point behavior during the ignition of an annular combustor with liquid n-heptane injectors". In: *Proceedings of the Combustion Institute, accepted* (2018).

[A4] P. Rodrigues, O. Gicquel, N. Darabiha, K. P. Geigle, and R. Vicquelin. "Assessment of external heat transfer modeling of a laboratory-scale combustor: effects of pressure-housing environment and semi-transparent viewing windows". In: *Journal of Engineering for Gas Turbines and Power* accpeted (2018).

[A5] P. Rodrigues, B. Franzelli, R. Vicquelin, O. Gicquel, and N. Darabiha. "Coupling an LES approach and a soot sectional model for the study of sooting turbulent non-premixed flames". In: *Combustion and Flame* 190 (2018), pp. 477–499.

[A6] Y. F. Zhang, R. Vicquelin, O. Gicquel, and J. Taine. "Practical indicators for assessing the magnitudes of wall radiative flux and of coupling effects between radiation and other heat transfer modes on the temperature law-of-the wall in turbulent gaseous boundary layers". In: *International Journal of Heat and Mass Transfer* 120 (2018), pp. 76–85.

[A7] C. Koren, R. Vicquelin, and O. Gicquel. "Self-adaptive coupling frequency for unsteady coupled conjugate heat transfer simulations". In: *International Journal of Thermal Sciences* 118 (2017), pp. 340–354.

[A8] T. Lancien, K. Prieur, D. Durox, S. Candel, and R. Vicquelin. "Large Eddy Simulation of Light-Round in an Annular Combustor With Liquid Spray Injection and Compari-

son With Experiments". In: *Journal of Engineering for Gas Turbines and Power* 140.2 (2017), p. 021504.

[A9] P. Rodrigues, B. Franzelli, R. Vicquelin, O. Gicquel, and N. Darabiha. "Unsteady dynamics of PAH and soot particles in laminar counterflow diffusion flames". In: *Proceedings of the Combustion Institute* 36.1 (2017), pp. 927–934.

[A10] Y. F. Zhang and R. Vicquelin. "Controlling bulk Reynolds number and bulk temperature in channel flow simulations". In: *Journal of Computational Physics* 305 (2016), pp. 208–216.

[A11] J. Larsson, S. Laurence, I. Bermejo-Moreno, J. Bodart, S. Karl, and R. Vicquelin. "Incipient thermal choking and stable shock-train formation in the heat-release region of a scramjet combustor. Part II: Large eddy simulations". In: *Combustion and Flame* 162.4 (2015), pp. 907–920.

[A12] M. Philip, M. Boileau, R. Vicquelin, E. Riber, T. Schmitt, B. Cuenot, D. Durox, and S. Candel. "Large Eddy Simulations of the ignition sequence of an annular multiple-injector combustor". In: *Proceedings of the Combustion Institute* 35.3 (2015), pp. 3159–3166.

[A13] M. Philip, M. Boileau, R. Vicquelin, T. Schmitt, D. Durox, J.-F.-F. Bourgouin, and S. Candel. "Ignition sequence of an annular multi-injector combustor". In: *Physics of Fluids* 26.9 (2014).

[A14] M. Philip, M. Boileau, R. Vicquelin, T. Schmitt, D. Durox, J.-F. Bourgouin, and S. Candel. "Simulation of the Ignition Process in an Annular Multiple-Injector Combustor and Comparison With Experiments". In: *Journal of Engineering for Gas Turbines and Power* 137.3 (2014), p. 031501.

[A15] R. Vicquelin, Y. F. Zhang, O. Gicquel, and J. Taine. "Effects of radiation in turbulent channel flow: analysis of coupled direct numerical simulations". In: *Journal of Fluid Mechanics* 753 (2014), pp. 360–401.

[A16] Y. F. Zhang, R. Vicquelin, O. Gicquel, and J. Taine. "A wall model for LES accounting for radiation effects". In: *International Journal of Heat and Mass Transfer* 67 (2013), pp. 712–723.

[A17] Y. F. Zhang, R. Vicquelin, O. Gicquel, and J. Taine. "Physical study of radiation effects on the boundary layer structure in a turbulent channel flow". In: *International Journal of Heat and Mass Transfer* 61 (2013), pp. 654–666.

[A18] P. Auzillon, B. Fiorina, R. Vicquelin, N. Darabiha, O. Gicquel, and D. Veynante. "Modeling chemical flame structure and combustion dynamics in LES". In: *Proceedings of the Combustion Institute* 33.Part 1 (2011), 1331–1338.

[A19] R. Vicquelin, B. Fiorina, S. Payet, N. Darabiha, and O. Gicquel. "Coupling tabulated chemistry with compressible CFD solvers". In: *Proceedings of the Combustion Institute* 33.Part 1 (2011), 1481–1488.

[A20] B. Fiorina, R. Vicquelin, P. Auzillon, N. Darabiha, O. Gicquel, and D. Veynante. "A filtered tabulated chemistry model for LES of premixed combustion". In: *Combustion and Flame* 157.3 (2010), pp. 465–475.

[A21] R. Vicquelin, B. Fiorina, N. Darabiha, O. Gicquel, and D. Veynante. "Coupling tabulated chemistry with Large Eddy Simulation of turbulent reactive flows". In: *Comptes Rendus Mecanique* 337.6-7 (2009), pp. 329–339.

3.2 Ph.D. Thesis

[B1] R. Vicquelin. "Tabulation de la cinétique chimique pour la modélisation et la simulation de la combustion turbulente". PhD thesis. Ecole Centrale de Paris, 2010.

3.3 Book chapters

[C1] B. Cuenot, R. Vicquelin, E. Riber, V. Moureau, G. Lartigue, A. Figuer, Y. Méry, J. Lamouroux, S. Richard, L. Gicquel, T. Schmitt, and S. Candel. "Advanced Simulation of Combustion in Aeronautical Burners". In: *Aerospace Lab Journal* (2016).

[C2] I. Bermejo-Moreno, J. Larsson, J. Bodart, and R. Vicquelin. "Wall-modeled large eddy simulations of the HIFiRE-2 scramjet". In: *Annual Research Briefs, Center for Turbulence Research, Stanford University*. 2013, pp. 3–19.

[C3] J. Larsson, I. Bermejo-Moreno, J. Bodart, and R. Vicquelin. "Predicting the operability limit of the HyShot II scramjet using LES". In: *Annual Research Briefs, Center for Turbulence Research, Stanford University*. 2012, pp. 241–251.

[C4] I. Bermejo-Moreno, J. Larsson, L. Campo, J. Bodart, R. Vicquelin, D. Helmer, and J. Eaton. "Wall-modeled large eddy simulation of shock/turbulent boundary-layer interaction in a duct". In: *Annual Research Briefs, Center for Turbulence Research, Stanford University*. 2011, pp. 49–62.

[C5] J. Larsson, R. Vicquelin, and I. Bermejo-Moreno. "Large eddy simulations of the HyShot II scramjet". In: *Annual Research Briefs, Center for Turbulence Research, Stanford University*. 2011, pp. 63–74.

[C6] R. Vicquelin, B. Fiorina, N. Darabiha, D. Veynante, V. Moureau, and L. Vervisch. "Coupling Tabulated Chemistry with Large Eddy Simulation of Turbulent Reactive Flows". In: *Proceedings of the Summer Program 2008* (2008).

3.4 Papers published in international refereed conference proceedings

[D1] A. Degenève, P. Jourdaine, C. Mirat, J. Caudal, R. Vicquelin, and T. Schuller. *Analysis of wall temperature and heat flux distributions in a swirled combustor powered by a methane air and a CO2-diluted oxyflame*. 2nd International Workshop on oxy-fuel combustion, Bochum, Germany, February 14-15, 2018. 2018.

[D2] A. Degenève, P. Jourdaine, C. Mirat, J. Caudal, R. Vicquelin, and T. Schuller. *Effects Of A Diverging Cup On Swirl Number, Flow Pattern And Topology Of Premixed Flames*. Proceedings of the ASME Turbo Expo. 2018.

[D3] L. Palluotto, N. Dumont, P. Rodrigues, C. Koren, R. Vicquelin, and O. Gicquel. *Comparison Of Monte Carlo Methods Efficiency To Solve Radiative Energy Transfer In High Fidelity Unsteady 3D Simulations*. Eurotherm Seminar 110 - Computational Thermal Radiation in Participating Media - VI, April 11-13, 2018, Cascais, Portugal. 2018.

[D4] P. Rodrigues, O. Gicquel, N. Darabiha, K. P. Geigle, and R. Vicquelin. "Assessment of external heat transfer modeling of a laboratory-scale combustor inside a pressure-casing environment". In: *Proceedings of ASME Turbo Expo* (2018).

[D5] P. Rodrigues, O. Gicquel, B. Franzelli, N. Darabiha, and R. Vicquelin. "Coupled Monte-Carlo simulation of a Turbulent Sooting Diffusion Jet Flame". In: *Eurotherm Seminar 110 - Computational Thermal Radiation in Participating Media - VI, April 11-13, 2018, Cascais, Portugal* (2018).

[D6] J. M. Armengol, R. Vicquelin, C. A., R. Santos, and O. Gicquel. *Turbulence-Radiation Interactions in a Spatially Developing Heated Jet*. 24th ABCM International Congress of Mechanical Engineering, December 3-8, 2017, Curitiba, PR, Brazil. 2017.

[D7] C. Koren, R. Vicquelin, and O. Gicquel. *An acceleration method for numerical studies of conjugate heat transfer with a self-adaptive coupling time step method: application to a wall-impinging flame*. ASME Turbo Expo, Charlotte, USA. 2017.

[D8] C. Koren, R. Vicquelin, and O. Gicquel. *High-fidelity multiphysics simulation of a confined premixed swirling flame combining large-eddy simulation, wall heat conduction and radiative energy transfer*. ASME Turbo Expo, Charlotte, USA. 2017.

[D9] T. Lancien, K. Prieur, D. Durox, S. Candel, and R. Vicquelin. *Large-eddy simulation of light-round in an annular combustor with liquid spray injection and comparison with experiments*. ASME Turbo Expo, Charlotte, USA. 2017.

[D10] L. Palluotto, N. Dumont, P. Rodrigues, C. Koren, R. Vicquelin, and O. Gicquel. *Comparison of monte carlo methods efficiency to solve radiative energy transfer in high fidelity unsteady 3d simulations*. ASME Turbo Expo, Charlotte, USA. 2017.

[D11] T. Lancien, N. Dumont, K. Prieur, D. Durox, S. Candel, O. Gicquel, and R. Vicquelin. "Uncertainty quantification of injected droplet size in mono-dispersed Eulerian simulations". In: *9th International Conference on Multiphase Flow, May 22nd-27th, Firenze, Italy*. 2016.

[D12] N. Dumont, R. Vicquelin, and O. Gicquel. *Comparison of different approaches to determine the effect of uncertainties in detailed chemistry on auto-ignition delay for air-hydrogen mixtures*. European Combustion Meeting, Budapest, Hungary. 2015.

[D13] M. Philip, M. Boileau, R. Vicquelin, T. Schmitt, D. Durox, J.-F. Bourgouin, and S. Candel. *Simulation of the ignition process in an annular multiple-injector combustor and comparison with experiments*. ASME Turbo Expo. 2014.

[D14] R. Vicquelin, O. Gicquel, and J. Taine. *Effect of radiation on enthalpy fluctuations and turbulent heat flux in turbulent boundary layers*. iTi Conference on Turbulence VI, September 21-24, 2014, Bertinoro, Italy. 2014.

[D15] Y. F. Zhang, R. Vicquelin, O. Gicquel, J. Taine, and Y. Huang. "Wall-modeled les with a new wall model accounting for radiation effects". In: *Proceedings of the 7th International Symposium on Radiative Transfer, RAD-13, Kusadasi, Turkey*. 2013.

[D16] Y. F. Zhang, R. Vicquelin, O. Gicquel, and J. Taine. "Direct numerical simulation of a turbulent channel flow coupled to radiative transfer". In: *International Congresses on Theoritical and Applied Mechanics (ICTAM), Beijing, China*. 2012.

[D17] D. Tudorache, P. Auzillon, L. Thobois, N. Darabiha, R. Vicquelin, O. Gicquel, and B. Fiorina. "Development of a chemical kinetics tabulation method for the prediction of Diesel engine pollutants". In: *23rd ICDERS, Irvine, USA*. 2011.

[D18] R. Vicquelin, B. Fiorina, and O. Gicquel. "A Turbulent Combustion Model for Jet Flames Issuing in a Vitiated Coflow". In: *23rd ICDERS, Irvine USA*. 2011.

[D19] P. Auzillon, R. Vicquelin, O. Gicquel, N. Darabiha, D. Veynante, and B. Fiorina. "A filtered tabulated chemistry model for large eddy simulation of reactive flows". In: *AIAA Paper* (2010).

[D20] O. Esnault, M. Boileau, R. Vicquelin, B. Fiorina, and O. Gicquel. "A method to accelerate LES explicit solvers using local time stepping". In: *AIAA Paper* (2010).

[D21] R. Vicquelin, B. Fiorina, O. Gicquel, G. Lartigue, and T. Poinsot. *Large Eddy Simulations of Mild Combustion*. 21th ICDERS, Poitiers, France. 2007.

3.5 Other conferences

[E1] A. Degenève, P. Jourdaine, J. Caudal, C. Mirat, R. Vicquelin, and T. Schuller. *An Experimental Study Of The Wall Temperature Of A Co2 Diluted Oxy-Flame And A Methane/Air Flame In A Technically Premixed Swirler*. IFRF 2018 Conference, 30-31 May 2018, Sheffield, UK. 2018.

[E2] A. Degenève, P. Jourdaine, C. Mirat, R. Vicquelin, J. Caudal, and T. Schuller. *Wall temperature and heat flux distributions in a swirled combustor powered by swirling methane air and CO2-diluted oxyflames*. Groupement Français de Combustion, Journée François Lacas, 19 Janvier 2018. 2018.

[E3] G. Vignat, D. Durox, K. Prieur, T. Lancien, R. Vicquelin, and S. Candel. *Tomographie à très haute cadence de flammes turbulentes swirlées au moyen du dioxyde d'étain*. Congrès Francophone de Techniques Laser, CFTL 2018. 2018.

[E4] C. Koren, R. Vicquelin, and O. Gicquel. "Simulation LES couplées permettant de prédire les températures dans les parois d'une chambre combustion". In: *Congrès Français de Thermique, Marseille, France* (2017).

[E5] T. Lancien, K. Prieur, D. Durox, S. Candel, and R. Vicquelin. *Large-eddy simulation of light-round in an annular combustor equipped with n-heptane spray injectors*. International Conference on Numerical Combustion, Orlando, USA. 2017.

[E6] T. Lancien, K. Prieur, D. Durox, S. Candel, and R. Vicquelin. "Light-round in an annular combustor with liquid n-heptane injectors: study of flame propagation under several operating conditions". In: *3ème colloque INCA* (2017).

[E7] L. Palluotto, N. Dumont, P. Rodrigues, C. Koren, R. Vicquelin, and O. Gicquel. "Comparaison de l'efficacité de méthodes Monte Carlo pour la résolution des transferts radiatifs dans des simulations haute-fidélité d'écoulements 3D instationnaires". In: *Congrès Français de Thermique, Marseille, France* (2017).

[E8] L. Palluotto, R. Vicquelin, P. Jourdaine, C. Mirat, T. Schuller, and O. Gicquel. *Towards Large Eddy Simulation of CO2 dilution in premixed swirling oxy-flames and assessment of radiation effects*. 16th International Conference on Numerical Combustion, Orlando, USA. 2017.

[E9] M. Philip, R. Vicquelin, T. Schmitt, and S. Candel. *Modeling of light-round in an annular combustor operating under perfectly premixed conditions*. International Conference on Numerical Combustion, Orlando, USA. 2017.

[E10] P. Rodrigues, R. Vicquelin, B. Franzelli, N. Darabiha, and O. Gicquel. "Impact of Radiation Modeling in Large Eddy Simulation of a Turbulent Sooting Diffusion Ethylene-Air Flame". In: *16th International Conference on Numerical Combustion, Orlando, Florida, USA* (2017).

[E11] P. Rodrigues, R. Vicquelin, B. Franzelli, N. Darabiha, and O. Gicquel. "Wall temperature and soot production prediction in a multi physics coupled simulation of a confined pressurized ethylene-air flame". In: *Colloque INCA, SafranTech* (2017).

[E12] P. Rodrigues, R. Vicquelin, B. Franzelli, O. Gicquel, and N. Darabiha. "Impact de la modélisation du rayonnement dans la simulation aux grandes échelles de flammes turbulentes suitées". In: *Congrès Français de Thermique, Marseille, France* (2017).

[E13] N. Dumont, R. Vicquelin, and O. Gicquel. *Modeling propagation of detailed chemical mechanism with tabulated chemistry*. Groupement Français de Combustion, Journée thématique : Incertitudes dans les écoulements réactifs. 2016.

[E14] N. Dumont, R. Vicquelin, and O. Gicquel. *Effect of uncertainties in detailed chemistry on combustion model parameters*. International Conference on Numerical Combustion, Avignon, France. 2015.

[E15] N. Dumont, R. Vicquelin, and O. Gicquel. *Vers la propagation d'incertitudes de cinétique chimique avec une méthode de chimie tabulé : Application aux calculs d'auto-allumage*. Groupement Français de Combustion, Journée François Lacas, 2015.

[E16] C. Koren, R. Vicquelin, and O. Gicquel. "Automatic determination of the coupling period in unsteady conjugate heat transfer. Application to large eddy simulation of flame-wall interaction". In: *15th International Conference on Numerical Combustion*. Avignon, France, 2015.

[E17] C. Koren, R. Vicquelin, and O. Gicquel. "Détermination automatique de la période de couplage entre un code de simulation aux grandes échelles et un code de conduction ther-

mique. Application à l'interaction flamme-paroi". In: *Congrès Français de Thermique, La Rochelle, France* (2015).

[E18] M. Philip, R. Vicquelin, M. Boileau, T. Schmitt, and S. Candel. *Detailed analysis of light-round in an annular multiple-injector combustor*. International Conference on Numerical Combustion, Avignon, France. 2015.

[E19] Y. Zhang, R. Vicquelin, O. Gicquel, and J. Taine. *Effets du rayonnement dans les couches limites turbulentes*. Journées SFT – ACCORT – GFC, Rayonnement Thermique et Couplages Rayonnement-Combustion, CETHIL, Lyon, 6-7 Février 2014. 2014.

[E20] J. Larsson, R. Vicquelin, J. Bodart, I. Bermejo-Moreno, and S. Laurence. *Quasi-dual-mode behavior in the combustor of the HyShot scramjet*. 66th Annual Meeting of the American Physical Society-Division of Fluid Dynamics, Pittsburgh, Pennsylvania, USA. 2013.

[E21] M. Philip, M. Boileau, T. Schmitt, R. Vicquelin, J.-F. Bourgouin, D. Durox, and S. Candel. *Large Eddy Simulation of ignition in an annular multi-injector combustor*. SIAM, 14th International Conference on Numerical Combustion, San Antonio, Texas, USA. 2013.

[E22] R. Vicquelin, M. Philip, M. Boileau, T. Schmitt, J.-F. Bourgouin, D. Durox, and S. Candel. *Large Eddy Simulation of ignition in an annular multi-injector combustor*. 66th Annual Meeting of the American Physical Society-Division of Fluid Dynamics, Pittsburgh, Pennsylvania, USA. 2013.

[E23] R. Vicquelin, Y. F. Zhang, O. Gicquel, and J. Taine. *Effects of radiation in turbulent boundary layers: Analysis of the mean temperature profile*. 66th Annual Meeting of the American Physical Society-Division of Fluid Dynamics, Pittsburgh, Pennsylvania, USA. 2013.

[E24] R. Vicquelin, Y. Zhang, O. Gicquel, and J. Taine. *A wall model for LES accounting for radiation effects*. 66th Annual Meeting of the American Physical Society-Division of Fluid Dynamics, Pittsburgh, Pennsylvania, USA. 2013.

[E25] J. Larsson, R. Vicquelin, I. Bermejo-Moreno, and J. Bodart. *LES of supersonic combustion in a realistic scramjet combustor*. 64th Annual Meeting of the American Physical Society-Division of Fluid Dynamics, Baltimore, Maryland, USA. 2011.

[E26] R. Vicquelin, J. Larsson, and J. Bodart. *Including compressibility effect in combustion modeling for LES of supersonic combustion*. 64th Annual Meeting of the American Physical Society-Division of Fluid Dynamics, Baltimore, Maryland, USA. 2011.

[E27] O. Esnault, R. Vicquelin, M. Boileau, B. Fiorina, and O. Gicquel. *Optimization of DNS/LES explicit solvers for combustor simulations using local time-stepping*. 4th European Combustion Meeting, Vienna, Austria. 2009.

[E28] R. Vicquelin, B. Fiorina, G. Lartigue, and O. Gicquel. *Large Eddy Simulation of a Methane-Air Turbulent Jet Flame in a Vitiated Co-Flow*. SIAM, 11th International Conference on Numerical Combustion, Monterey, USA. 2008.

3.6 Supervised Ph.D. theses

[T1] Y. F. Zhang. "Coupled convective heat transfer and radiative energy transfer in turbulent boundary layers". PhD thesis. Ecole Centrale de Paris, 2010-2013.

[T2] C. Koren. "Modélisation des transferts de chaleur couplés pour la simulation multi-physique des chambres de combustion". PhD thesis. Université Paris-Saclay, 2012-2016.

[T3] M. Philip. "Dynamique de l'allumage circulaire dans les foyers annulaires multi-injecteurs". PhD thesis. Université Paris-Saclay, 2012-2016.

[T4] N. Dumont. "Quantification d'incertitudes des mécanismes chimiques dans les simulations aux grandes échelles". PhD thesis. Université Paris-Saclay, 2013-...

[T5] T. Lancien. "Etude numérique de l'allumage diphasique de foyers annulaires multi-brûleurs". PhD thesis. Université Paris-Saclay, 2014-2018.

[T6] P. Rodrigues. "Modélisation multiphysique de flammes turbulentes suitées avec la prise en compte des transferts radiatifs et des transferts de chaleur pariétaux". PhD thesis. Université Paris-Saclay, 2014-2018.

[T7] J. M. Armengol. "Simulations numériques directes des intéractions rayonnement-turbulence". PhD thesis. Université Paris-Saclay, 2015-...

[T8] L. Palluotto. "Simulations multiphysiques des transferts radiatifs en oxycombustion". PhD thesis. Université Paris-Saclay, 2015-...

[T9] A. Degenève. "Etude expérimental et numérique de la stabilisation d'oxyflammes pressurisées swirlées et diluées en vapeur d'eau". PhD thesis. Université Paris-Saclay, 2017-...

[T10] K. Torres. "Transferts radiatifs dans les flammes suitées turbulentes". PhD thesis. Université Paris-Saclay, 2017-...

[T11] M. Gelain. "Simulations des transferts thermiques dans un échangeur de chaleur aéronautique : approches DES et WMLES". PhD thesis. Université Paris-Saclay, 2018-...

[T12] K. Töpperwien. "Etude de la dynamique transitoire de flamme dans les foyers annulaires multi-injecteurs". PhD thesis. Université Paris-Saclay, 2018-...

Part II

Research activities

Chapter 4

Modeling and simulation of turbulent reactive flows

While the increasing resources in computational power allow more and more realistic direct numerical simulations (DNS) of reactive flows, most configurations must rely on models to describe turbulent transfers, chemistry and turbulent combustion altogether. Additionally, multiphase flows comprising liquid fuel sprays or soot particles yield yet another level of complexity requiring further modelling efforts. This chapter presents my different works with my co-workers in developing and validating these models for turbulent reactive flows.

Among the different methods for chemistry reduction, my studies have mainly been focused in tabulated chemistry methods, also known as flamelet models. Section 4.1 briefly illustrates the limitation of Reynolds Average Navier-Stokes (RANS) simulations to show why the combustion community has quickly adopted a higher fidelity approach that is large eddy simulation (LES). The different flamelet models that we have either developed or implemented, and finally validated are presented in Sec. 4.2. A wide range of models has been considered: FPI, FPV, RFPV, compressible variant of FPV, unsteady igniting flamelets, FTACLES. The implementation of these models in the AVBP code which solves the compressible set of Navier-Stokes equations has required a dedicated study to do this in a physically consistent manner. This approach has later enabled the study of thermal choking in scramjets (**Highlight #1** in Fig. 1.1, Sec. 4.2.6) with the CharlesX code. Finally, several developments in multiphase flows are presented in Sec. 4.3.

Full list of **References**:

- Papers: [A1, A5, A9, A11, A18, A19, A20, A21]
- Book chapters: [C2, C3, C6]
- Theses: [B1] [T5, T6, T9]
- 14 conferences

4.1 Flamelet models and limitation of RANS simulations

4.1.1 Flamelet models

Reduced chemical models are used to replace detailed kinetic mechanisms where the number of species and reactions is too large to be accounted for in multidimensional computational fluid dynamics (CFD). Several approaches exist to build such reduced chemical models. A first approach consists in assembling a simpler kinetic mechanism by reducing the number of species and reactions [228, 226, 143, 238, 180]. Global mechanisms with a couple of reactions and fitted coefficients [239, 109, 70] yield the smallest mechanisms but loose connexion with detailed kinetic mechanisms and elementary reactions. The identification of Quasi Steady-State Approximation (QSSA) as manifolds in the state space of species mass fractions has led to a second family of approaches based on the mathematical identification of low-dimensional manifolds [144, 24, 198]. Finally, flamelet models [67, 229] is a third family which roots in combustion theory and the identification of key variables in different combustion regimes: the progress variable c in premixed combustion and the mixture fraction z in non-premixed combustion. To account for detailed kinetics, flamelet models describe turbulent flames as an ensemble of small laminar flame elements. These laminar flames can be computed with detailed kinetics before the turbulent flow computation and stored in a table as a function of the identified key parameters. That is why flamelet models can also be referred to as tabulation methods or techniques in a broader sense. The three mentioned categories of reduction method are not independent from each other and one can find many connexions between them. Flamelet models and global mechanisms have met a large success in their ability to scale up from academic to practical applications. However, global mechanisms do not account easily for detailed kinetics effects without specific tuning and cannot describe the intermediate species that are not included in the mechanism. For some time, this has favoured tabulated chemistry for a large set of problems. Recently, shortcomings of overly reduced mechanisms have been tackled by considering larger analytically reduced mechanisms [106, 62] in realistic systems. With a trade-off in computational efforts, such a promising approach can overcome the limitations of flamelet models. Nonetheless, when the combustion regime is well-identified and the flamelet assumption valid, tabulated chemistry methods yield the lowest computational cost in addition to being accurate.

Tabulation techniques can be based on several flame archetypes:

- **Flamelet Prolongation of ILDM** (FPI) or Flamelet-Generated Manifold (FGM) assembles one-dimensional laminar premixed flames in a database [77, 78, 230]. The main parameter is the progress variable. Mixture fraction is added by computing flamelets at different equivalence ratio. Fiorina et al. [65] also developed a non-adiabatic version including enthalpy as a new dimension of the database.

- **Homogeneous reactors**. Autoignition simulations follow a different path than premixed flamelets in the species mass fractions state space. That is why homogeneous reactors have been used to build chemical databases [55, 72, 40, 123] to describe configurations with such phenomena. The different input parameters can be c, z, the initial temperature, the pressure. In Perfectly Stirred Reactors (PSR) [64], a new parameter, the residence time, is added.

- **Steady non-premixed flamelets** can be computed and stored as function of mixture fraction [181]. This method has been extensively applied to diffusion flames. Each flamelet is generated for a given strain rate, a or a specified stoichiometric scalar dissipation rate χ_{st}.

- In order to tackle quenching and reignition phenomena, a **flamelet/progress variable approach** (FPV or FPVA) was used to tabulate diffusion flamelets from quenched to fully burning state [183, 100, 102]. Input parameters of the table are mixture fraction and a redefined progress variable.
- **Unsteady non-premixed flamelets** were chosen to include autoignition in stratified mixtures [251, 32, 103] or enthalpy variation [101].

As the flame exhibits more and more complex combustion modes, additional features are accounted in the flamelet generation such as separated fuel injection requiring multiple mixture fractions [94], partially premixed combustion with 2D z-c databases [167], heat losses with 2D z-Enthalpy tables [171], ... We note there the limitation of flamelet models: as one wishes to include more and more effects together, the size of the database exponentially increases.

Once the flame archetype is chosen and the database is built after parametrization by a selected set of variables, the CFD computation is carried out by only including transport equations for these variables (or directly related quantities) which are solved instead of the full set of species in the detailed mechanism whose information is stored in the database and is easily retrievable. For RANS or LES, a turbulent combustion model must be introduced. The tabulated quantities are now averaged (resp. filtered) quantities. These quantities are usually modelled by following a Presumed Conditional Moment (PCM) [231, 66, 73] where the joint PDF or FPF of the key parameters is modelled analytically. This procedure is illustrated in the next section.

4.1.2 RANS simulation of the H_2/N_2 Cabra flame

References: [B1]

The Cabra flame was designed to reproduce the stabilisation of turbulent jet flames in a vitiated coflow while promoting auto-ignition. Two fuel compositions were studied: hydrogen-nitrogen [26, 243, 83, 242] and methane-air [25, 83]. Both flames have been widely studied numerically with different models: transported PDF [150, 110, 80, 91], CMC [177, 165], flamelets [49, 155, 103, 164]. During my thesis an approach similar to Ihme and See [103] was used to describe autoignition in stratified mixtures from a set of unsteady 1D non-premixed flamelets.

Figure 4.1 shows the evolution of temperature in mixture fraction space for the hydrogen/nitrogen Cabra flame at a given scalar dissipation rate $\chi_{st} = 100$ s^{-1}. The unsteady flamelet equations are solved with the *FLAMEMASTER* code [185] with a detailed mechanism for hydrogen combustion [172]. Boundary conditions are given by the reference compositions [26] in fuel and coflow streams except for the 3%-uncertain coflow temperature which is set to 1052 K instead of the reported nominal value of 1045 K. Auto-ignition starts preferentially in a lean and hot temperature mixture. The stoichiometric mixture is $z_{st} = 0.475$ and the most-reactive mixture z_{MR} is 0.01 where z_{MR} is the mixture fraction for which the minimal ignition delay is found. Following the early ignition of lean mixtures, a combustion wave propagates in z-space until the steady solution is reached. Above a critical value $\chi_{st} = \chi_i$, auto-ignition does not occur because the flame strain rate is too high.

A flamelet library composed of unsteady self-igniting flamelets is computed for $0 < \chi_{st} < \chi_i$ in order to tabulate the chemistry. It captures all the physical phenomena mentioned above. Each flamelet solution is a function of mixture fraction, time and stoichiometric scalar dissipation rate. Any relevant variable can therefore be written as $\varphi(z, t, \chi_{st})$. The time variable is substituted by a reaction progress variable, c which varies between zero and unity for each flamelet solution.

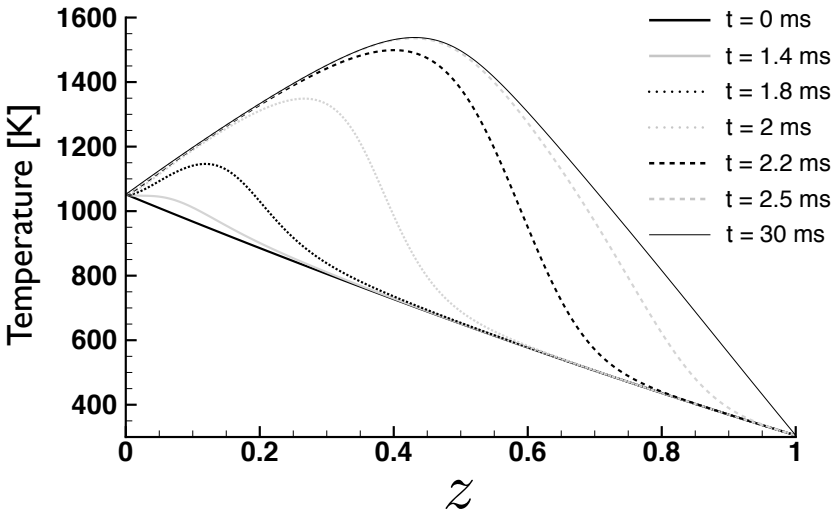

Figure 4.1: Time evolution of the temperature profile in mixture fraction space. The flamelet was generated with the stoichiometric scalar dissipation rate χ_{st} fixed to 100 s^{-1}.

It is defined as

$$c = \frac{Y_c(z,t,\chi_{st})}{Y_{c_b}(z,\chi_{st})} \text{ with } Y_c = Y_{H_2O} - Y_{H_2} + Y_{c_0}(z), \tag{4.1}$$

where Y_c is the non-normalised progress variable. $Y_{c_0}(z) = Y_{H_2}(z, t = 0)$ is added to the definition of Y_c in order to ensure that Y_c remains positive, and Y_{c_b} is the steady state burning solution, function of z and χ_{st}. Laminar flamelets quantities are then finally tabulated as $\varphi(z, c, \chi_{st})$.

For RANS simulations, Favre mean quantities $\tilde{\varphi}$ are modelled by assuming independency between z, c and χ_{st}:

$$\tilde{\varphi} = \int_0^{+\infty} \int_0^1 \int_0^1 \varphi(z^*, c^*, \chi^*_{st}) P(z^*) P(c^*) P(\chi^*_{st})\, dz^*\ dc^*\ d\chi^*_{st}. \tag{4.2}$$

The PDF $P(z^*)$ and $P(c^*)$ are modelled using β-PDF [66] parametrised by the mean and variance of the variables. A log-normal distribution is used to describe the scalar dissipation rate PDF, $P(\chi^*_{st})$ with a standard deviation set to 1.0 according to experimental measurements of [54] in turbulent flows. For the integration interval $[\chi_i, +\infty]$, unburnt solutions are considered. Averaged thermo-chemical quantities $\tilde{\phi}$ are computed and stored in a five entries look-up table: $\tilde{\varphi}(\tilde{z}, z_{var}, \overline{c}, c_{var}, \tilde{\chi}_{st})$. z_{var} and c_{var} are the mixture fraction and progress variable variances. The turbulent combustion model is completed by solving transport equations for $\tilde{z}$, z_{var}, $\widetilde{Y_c}$ and $\widetilde{Y_c^2}$. $\overline{c}$ and c_{var} are computed from $\widetilde{Y_c}$ and $\widetilde{Y_c^2}$ [66] and $\tilde{\chi}_{st}$ is related to the mean scalar dissipation rate computed in the RANS computation.

All RANS simulations are performed with the CFD code CFX [4] on a 2D axisymmetric mesh of 69 000 elements. A known shortcoming of the standard $k-\varepsilon$ model is its overestimation of the round jet spreading, known as the round jet anomaly. The error can be corrected by changing and specifying ad hoc coefficients in the k and ε balance equations [84].

Figures 4.2 and 4.3 show several radial profiles at different heights in the H_2/N_2 Cabra flame for a numerical configuration where the coflow temperature is fixed to 1052 K. Very good agreement is obtained for the mixing fields of mixture fraction and its root-mean-square (rms), the temperature and major species fields and the intermediate species OH.

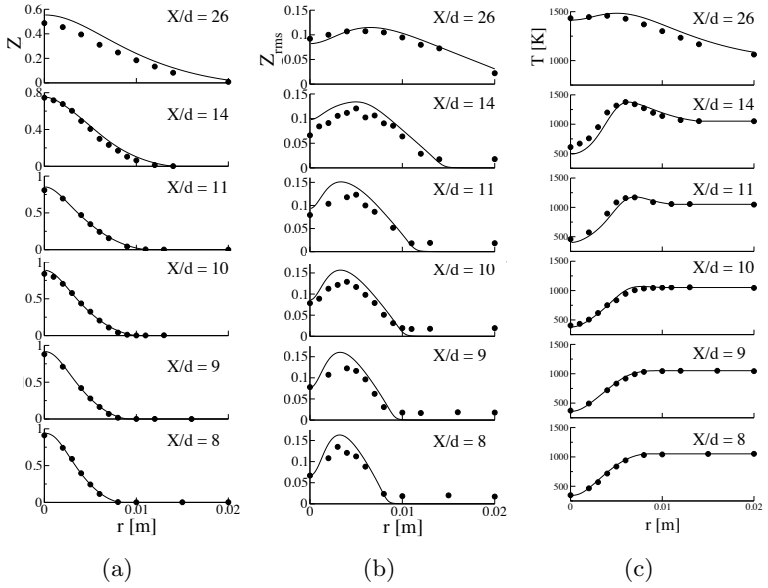

Figure 4.2: Radial profiles at six axial locations ($X/d = 8$, 9, 10, 11, 14 and 26) of Favre mean mixture fraction (a), its RMS (b) and Favre mean temperature (c) of the H_2/N_2 Cabra flame. Line: RANS simulation. Symbols: experimental data.

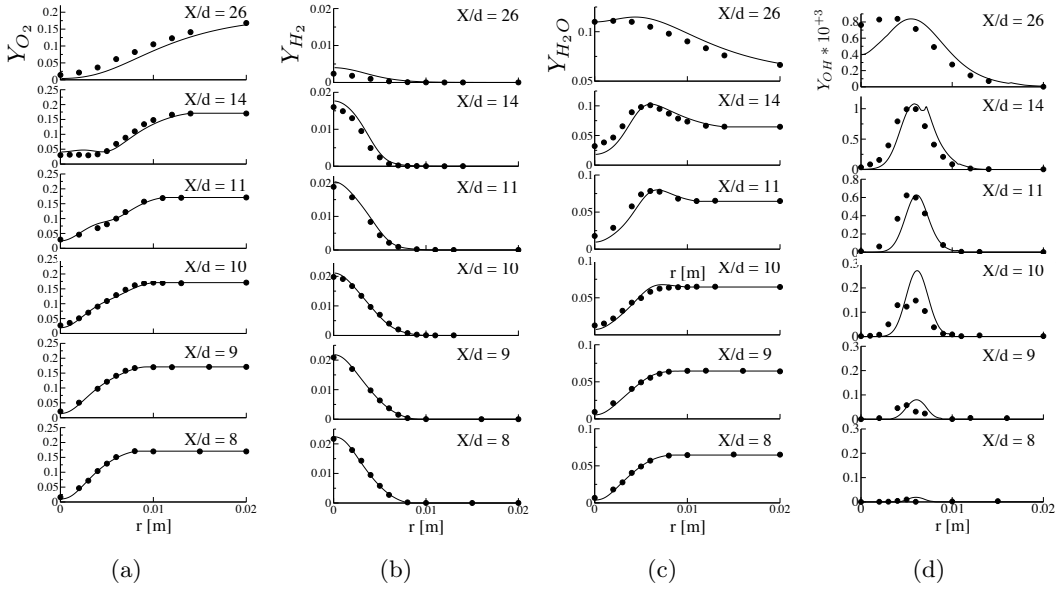

Figure 4.3: Profiles of Favre mean species mass fractions tabulated in the flamelet database (plain line) and measured (symbols). (a) Radial profiles of O_2. (b) Radial profiles of H_2. (c) Radial profiles of H_2O. (h) Radial profiles of OH.

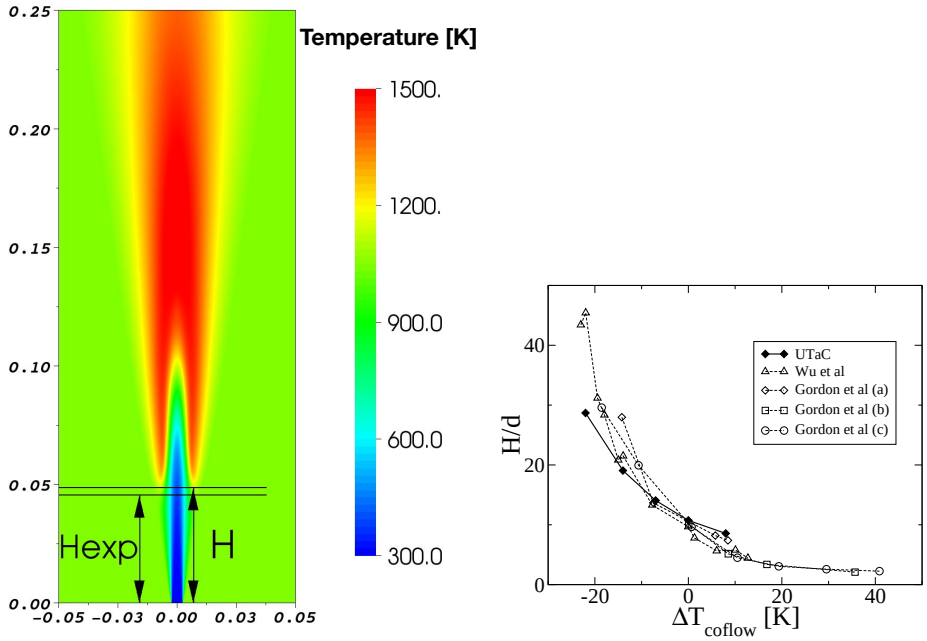

(a) (b)

Figure 4.4: Flame lift-off height H (a) and its sensitivity to the coflow temperature (b) given by the flamelet model and measurements [243, 83].

The predicted flame lift-off height is shown in Fig. 4.4 and highlights that the chosen coflow temperature yields a correct value. Note that the chosen value of 1052 K is within the experimental uncertainty of the nominal value. The sensitivity in the coflow temperature is finally studied by carrying out several RANS simulations. Results shown in Fig. 4.4(b) demonstrate the ability of the developed flamelet model to account for detailed kinetics effects such as the stabilisation of a jet flame through auto-ignition.

4.1.3 RANS and LES simulations of the CH_4/air Cabra flame

References: [B1]

The very same setup has been applied to the RANS simulation of the CH_4/air Cabra flame. A large-eddy simulation was also performed with the same flamelet model whose formulation was transposed to the LES context. In fact, the RANS approach yields a poor estimation of the lift-off height in this flame while the LES improves significantly the predicted value as seen in Fig. 4.5(a). Radial profiles of the LES results are represented in mixture fraction space in Fig. 4.5(b) and agree fairly with experimental model.

This shows that the derived flamelet model is still valid for the CH_4/air Cabra flame. Mismatch between RANS and LES results highlights a limitation of the former. In fact, in the methane/air configuration, the stoichiometric mixture is $z_{st} = 0.175$ and the most-reactive mixture z_{MR} is 0.0015, which is very small. The stabilisation height is then very sensitive to the predicted mixing field. This is where the RANS shortcoming issues from. The RANS approach is highly challenged to predict mean fields by modelling the full spectrum of turbulent scales. Standard models are known to break down in three-dimensional non-isotropic flows where no universal turbulence behaviour can be identified. Even in the simple case of a round jet, the standard k-ε

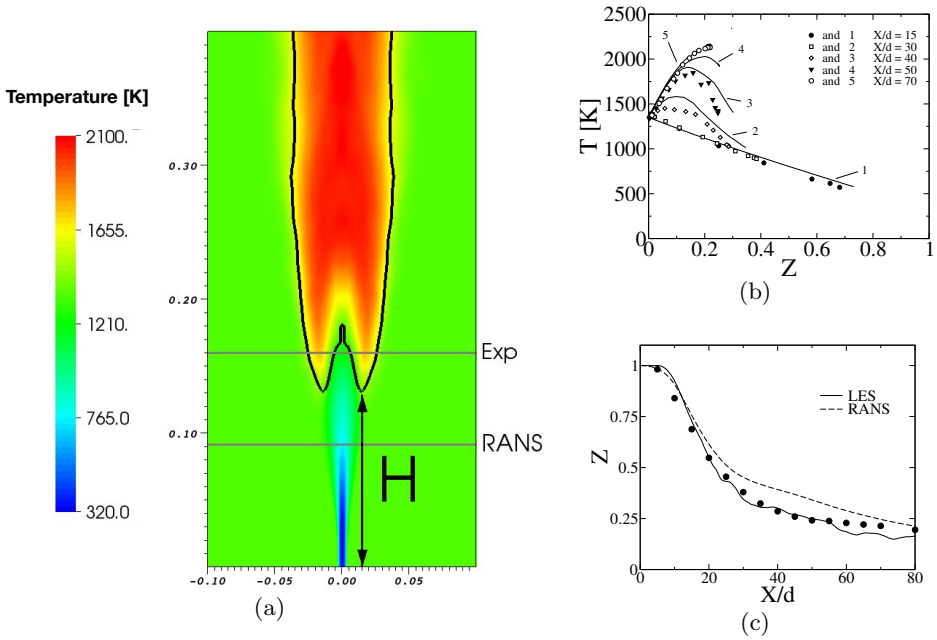

Figure 4.5: (a) Averaged LES field of temperature and comparison of predicted lift-off height H with experimental measurement and RANS result. (b) Radial profiles of mean temperature as a function of mean mixture fraction at different heights. Lines: LES results. Symbols: experimental data. (c) Comparison of RANS and LES predictions of mean mixture fraction on the centerline.

model fails to predict the correct mixing fields without any trick as outlined previously. On the other hand, in this case, by resolving energetic eddies, large-eddy simulation is able to predict a much better mixing (Fig. 4.5(c)). While errors can of course remain in LES due to imperfections in the subgrid-scale models, one can refine the mesh to lessen the impact of this errors. There is no equivalent in RANS.

This section illustrates why most works in turbulent combustion modelling nowadays rely on LES. The study of specific combustion dynamics such as combustion instabilities also endeavoured quickly on this path [186, 76] due to the necessary capture of unsteadiness provided by LES.

4.2 Tabulated chemistry methods in LES

4.2.1 Numerical codes

During my research activities, I have had the opportunity to work with and develop in several LES codes (Fig. 4.6): AVBP [160, 6] developed by CERFACS and IFPEN, YALES2 [158, 246] developed by Vincent Moureau and Ghislain Lartigue in CORIA and CharlesX [120, 15, 16] developed at CTR, Stanford University.

I would like here to acknowledge the initiative of the French combustion community to share the AVBP and YALES2 codes though the GIS SUCESS. I warmly thank the developers in CORIA and CERFACS that spend time to improve the solvers with new functionalities, make them

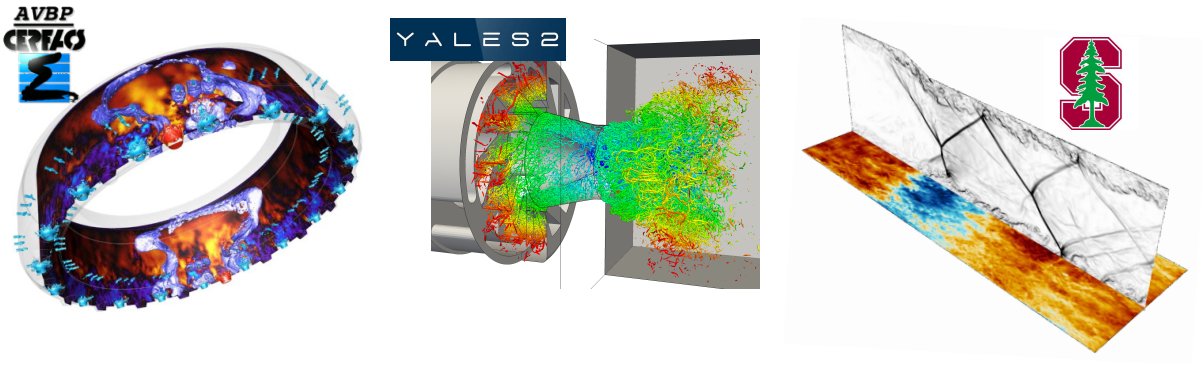

Figure 4.6: Different LES solvers used in my works: AVBP (Image from [18]), YALES2 (Image from [158]), CharlesX (Image from [16]).

more efficient for the entire community, and incorporate with patience our own contributions in their solver.

4.2.2 Tabulated chemistry in compressible CFD codes

References: [A11, A19], [B1]

YALES2 is a low Mach-number flow solver which then computes the velocity field from a predictor-corrector method and a Poisson equation for the pressure field. On the other hand, AVBP and CharlesX solve the full set of compressible Naviers-Stokes equations. In this framework, an adaptation of the implementation of flamelet models in compressible solvers is necessary. Indeed, during the flamelet database generation, perturbations due to compressibility effects are not considered. The derived method was called TTC which stands for *Tabulated Thermochemistry for Compressible flows*.

As imposing the tabulated temperature is simply not consistent physically in a compressible solver, a first adaptation is the necessary liberty of the temperature field to move away from the tabulated value for a fixed pressure. In order to inverse the relation between the transported energy e and the temperature, a first order truncated Taylor expansion of e around $T = T^{tab}$ is used:

$$T = T^{tab}(\psi_1, ..., \psi_n) + \frac{e - e^{tab}(\psi_1, ..., \psi_n)}{C_v^{tab}(\psi_1, ..., \psi_n)}. \tag{4.3}$$

A second adaptation deals with the characteristic boundary conditions [188] typically used in compressible solvers. Initially derived for multi-species mixture, they must now rely on the table parameters ψ_l. Transformation matrices between characteristic, primitive and conservative variables are then modified, and new terms appear:

$$\vartheta_{\psi_l} = \sum_{k=1}^{N} \left(\frac{RT}{W_k} - \beta e_k \right) \frac{\partial Y_k}{\partial \psi_l}. \tag{4.4}$$

However, these new terms are also sensitive to compressible effects and cannot be directly

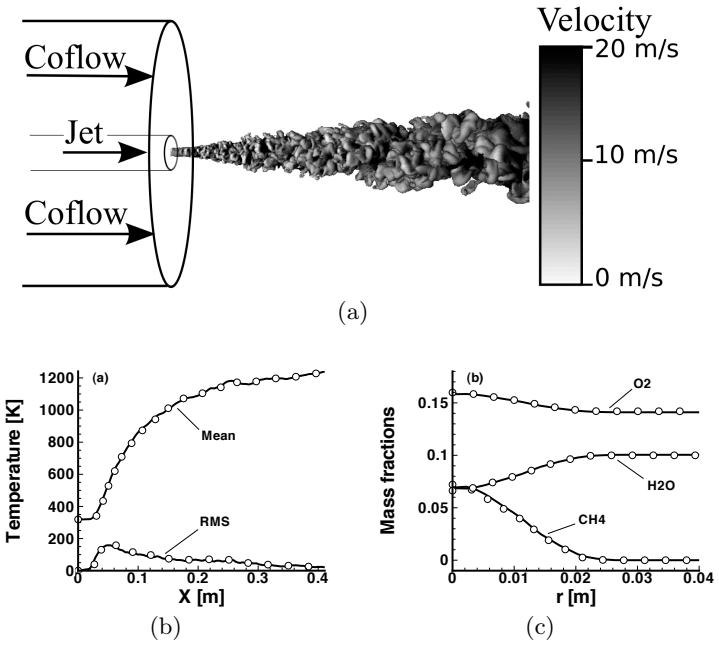

Figure 4.7: (a) Mixture fraction isosurface $z = 0.1$ coloured by longitudinal velocity. (b) Longitudinal mean and root-mean-square (rms) temperature profile. (c) Radial profiles of mean species mass fractions extracted at the axial distance $X = 30d$. Symbols: multi-species formulation. Line: tabulated chemistry formulation.

tabulated. As done for temperature, they are computed as

$$\vartheta_{\psi_l} = \vartheta^{tab}_{\psi_l}(\psi_1, ..., \psi_n) + \sigma^{tab}_{\psi_l}(\psi_1, ..., \psi_n)(T - T^{tab}) \tag{4.5}$$

$$\text{with} \qquad \sigma^{tab}_{\psi_l} = \sum_{k=1}^{N}(R/W_k - \beta C_{vk})\frac{\partial Y_k}{\partial \psi_l}. \tag{4.6}$$

The derived TTC method was validated by comparing with multispecies solutions in the AVBP code in several cases: traveling of acoustic waves, different types of characteristic boundaries, a non-reactive turbulent jet, a 1D premixed flame. In all cases, the tabulated chemistry yielded identical results to the reference case. Figure 4.7 shows the comparison of LES results for both multi-species and flamelet formulations in the non-reactive Cabra flame configuration. The tabulated model is based on the frozen mixing between the cold fuel jet and the hot coflow.

The derived method has enabled the use of flamelet models in compressible solvers and it was used in all the following results with the codes AVBP and CharlesX. It has been extended to real gases by Petit et al. [182] and too strongly compressible flows [A11, 203]. In the latter case, the validity of the first-order approximation in Eq. 4.3 is extended by considering an expansion in the polytropic coefficient γ instead. Furthermore, with larger compressible effects that can strongly deviate the pressure and temperature from the tabulated values, one must consider this impact on the reaction progress variable source term and other quantities such as the dynamic viscosity and thermal conductivity. Augmenting the table dimensions being too cumbersome, Saghafian et al. [203] have instead used power-law extrapolation from the reference flamelet table computed at a reference pressure.

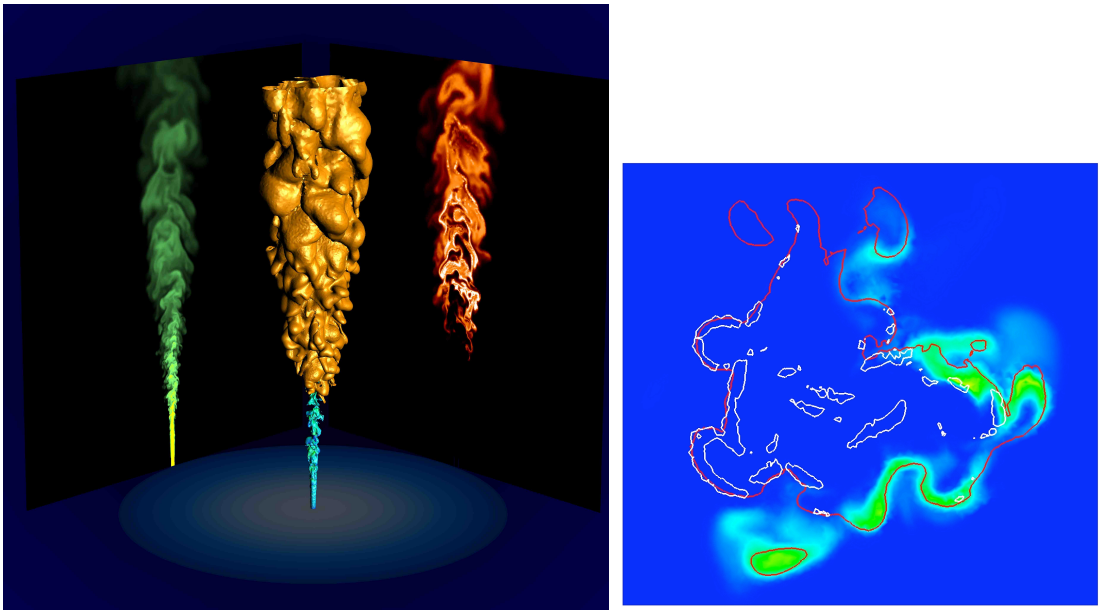

(a) (b)

Figure 4.8: (a) Three-dimensional view of an instantaneous LES solution of the CH_4/air Cabra flame: isosurfaces of temperature (1600 K) and mixture fraction ($\tilde{z} = 0.5$); planar slices coloured by mixture fraction (left) and OH mass fraction (right). (b) Plane at X/d = 25 coloured by the source term $\widetilde{\dot{\omega}_{Y_c}}$. White line: iso-line $\tilde{\chi} = 25$ s^{-1}. Red line: iso-line $\tilde{z} = 0.1$.

4.2.3 LES results of the Cabra flame

References: [B1]

The TTC method was used for the large-eddy simulation of the CH_4/air Cabra flame whose results were shown in Sec. 4.1.3. In this section, the richness of the reactive flow features captured by LES is outlined. The resolved flame shown in Fig. 4.8(a) exhibits a fluctuating lift-off height.

The transition from fresh gases to burnt gases along the flame height is studied by considering planes at different heights. For each plane, temperature colour map and scatter plot in mixture fraction space are drawn in Fig. 4.9. In the LES computation, combustion takes place as follows:

(a) The fuel jet mixes with the hot vitiated coflow without noticeable reaction. The scatter plot of temperature is identical to the frozen mixing line.
(b) Ignition starts in lean hot mixtures where departure from the pure mixing line is observed in the scatter plot. In lean mixtures, fresh, burnt and intermediate states are met for the same axis distance.
(c) Ignition spreads to richer mixtures. During the same time, dilution into the coflow goes on and the maximum mixture fraction that is encountered decreases.
(d) Lean mixtures are fully burnt while the others in the vicinity of the jet axis are still burning.
(e) Rich pockets reach the final burning state.
(f) Finally, all points form the steady flamelet solution, indicating a diffusion flame downstream the flame stabilisation zone as expected.

Consequently, combustion in LES takes place in the same way as the chosen unsteady flamelets to build the database. RANS simulation also follows the same pattern but LES allows for

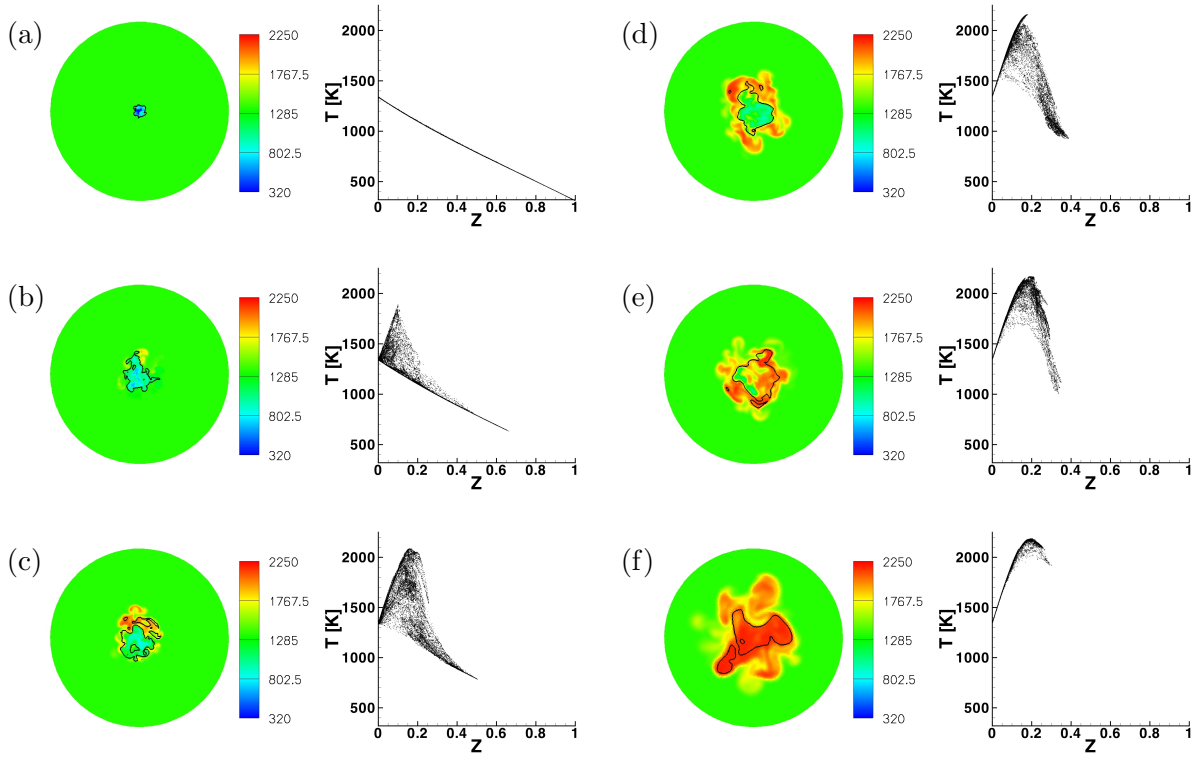

Figure 4.9: Instantaneous temperature colour maps and scatter plots in mixture fraction space at heights: (a) X/d = 10 ; (b) X/d = 25 ; (c) X/d = 30 ; (d) X/d = 35 ; (e) X/d = 40 ; (f) X/d = 60. Black line: iso-line $\tilde{z} = z_{st} = 0.175$.

describing much more complex effects. Indeed, auto-ignition being an unsteady phenomenon, it should be tackled efficiently by LES. In Fig. 4.9(b) for example, scatter plot shows that different burning states are encountered for a same mixture. This point is investigated more closely in Fig. 4.8(b) where the source term $\widetilde{\dot{\omega}_{Y_c}}$ is represented. Iso-lines of mixture fraction and mean scalar dissipation rates are also drawn. It appears that combustion does not occur in the left half-part of the figure. It explains the presence of burning and non-burning states in the scatterplot for the same mixture. The scalar dissipation rate contour tends to indicate that combustion in identical mixtures is or has been prevented by high strain rates. Consequently, fluctuations of ignition induced by unsteady scalar dissipation rates can be captured in LES. In a RANS context where the mean stationary solution is computed, modelling such dynamic effects is tremendously challenging.

4.2.4 Application of the RFPV model to a sooted jet diffusion flame

References: [A5], [T6]

During the thesis of Pedro Rodrigues, a sooted jet flame was computed to validate an LES soot sectional model presented in Sec. 4.3.3. Before modelling soot emission, one must describe the turbulent reactive flow in the gaseous phase. This was done with a non-adiabatic FPV model whose results for the gaseous phase are here presented. The configuration chosen for the simulation is the turbulent non-premixed pure ethylene/air diffusion flame which has been extensively characterised experimentally at Sandia [249].

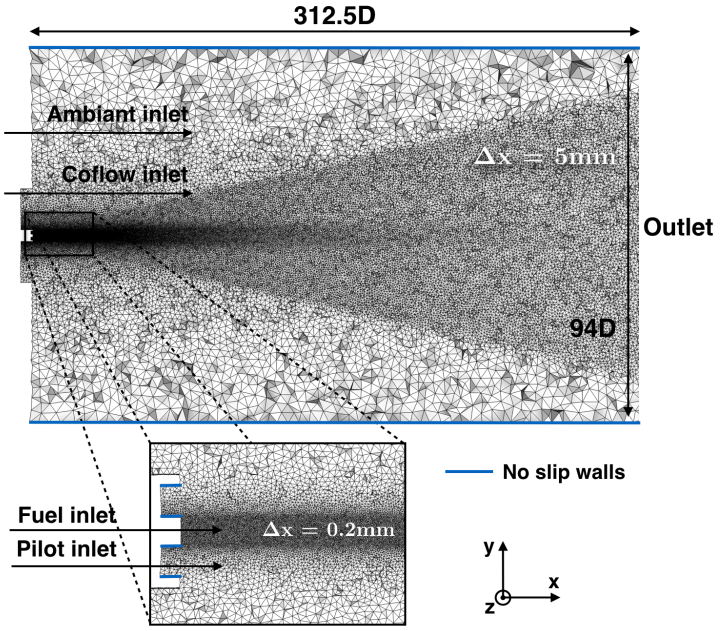

Figure 4.10: Longitudinal cut of the cylindrical computational domain.

Numerical setup Good prediction of LES is not straightforward and one must pay attention in particular to the numerical scheme, the mesh resolution and boundary conditions. As no data were available for the incoming turbulent flow in the fuel jet, a refined LES of a fully developed pipe flow for the configuration Reynolds number was computed in a periodic pipe. The computed profiles of mean velocities and Reynolds stresses are then imposed at the turbulent inlet of the full computational domain shown in Fig. 4.10. The adequacy of the mesh resolution was then verified in a non-reactive case by comparing the results to classical turbulent round jet laws for two different numerical schemes available in AVBP: the classical 2$^{\text{nd}}$-order Lax-Wendroff (LW) and the 3$^{\text{rd}}$-order Two-step Taylor Galerkin Type C (TTGC) [39] numerical schemes. From Fig. 4.11, we see that the classical results for round jet are reproduced correctly with the TTGC numerical scheme which is then selected in the following.

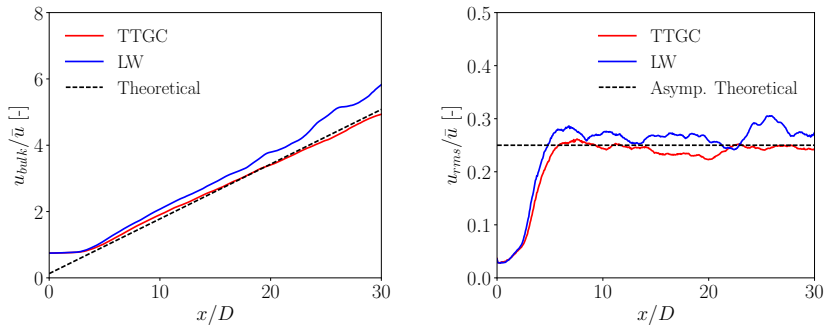

(a) (b)

Figure 4.11: Auto-similar evolutions of mean axial velocity decay (plotted as $U_{bulk}/\overline{u}$) and axial velocity rms compared with theoretical results [190].

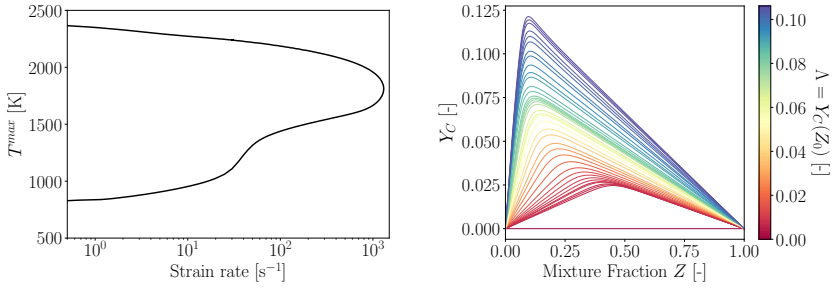

(a) (b)

Figure 4.12: (a) S-curve: Evolution of the maximal temperature T^{max} with the flamelet strain rate. The extinction limit ϵ^{ext} is found to be equal to $\epsilon^{\text{ext}} = 1308\text{s}^{-1}$, which is consistent with Sarnacki et al. [205]. (b) Evolution of Y_c with z for each flamelet.

Flamelet model For the studied flame which is stabilised at the fuel injector thanks to a pilot flame, the FPV flamelet model [183] is used. For the generation of the flamelet database, strain-imposed counterflow non-premixed flames are computed with the REGATH package [68] with the KM2 kinetic scheme [237]. The continuation technique based on the curvilinear abscissa parametrised by the temperature and the strain rate [117, 169] is used in order to generate the stable and unstable branches of the flamelet database (Fig. 4.12(a)).

The computed 1D flame fields are functions of mixture fraction and strain rate. In the FPV approach, these fields are uniquely mapped as functions of z and a parameter $\Lambda = Y_c(z_{st})$ where Y_c is the non-normalised reaction progress variable defined here as

$$Y_C = \frac{Y_{H_2O}/W_{H_2O} + Y_{CO_2}/W_{CO_2} + Y_{CO}/W_{CO} - 3Y_{CH_4}/W_{CH_4}}{1/W_{H2O} + 1/W_{CO_2} + 1/W_{CO} + 3/W_{CH_4}}, \tag{4.7}$$

which yields a proper unique mapping for each flamelet (see Fig.4.12(b)).

In order to take into account heat losses and therefore to generate a non-adiabatic flamelet progress variable table, the RFPV procedure initially proposed by Ihme and Pitsch [101] has been used. For each flamelet of the FPV dataset, unsteady flames are computed by adding a radiative source term and starting from the steady adiabatic flamelet solution without radiation source term. During the unsteady calculation, intermediate unsteady flamelets are stored as a part of the RFPV flamelet dataset. Each one of these unsteady flamelets are parametrised through a parameter $\Phi = H(z_{st})$ corresponding to the value of enthalpy at the stoichiometric mixture fraction. The final table built from laminar 1D flames is parameterised by z, Λ and Φ which are independent from each other by design. After turbulent closure of the different marginal FDF and a ultimate remapping of the database, the final lookup table is discretised with $100 \times 20 \times 100 \times 20$ grid points in the filtered $\tilde{z}$ dimension, the subfilter segregation factor S_z, the normalised filtered reaction progress variables $\bar{c}$ and the normalised filtered enthalpy $\overline{H}$, respectively.

Results The numerical results obtained for the chosen numerical setup combined through the TTC method with the built RFPV table have been compared to the available experimental data. Concerning the gaseous phase, Fig. 4.13 (top) shows a comparison of radial mean and root mean square (RMS) temperature profiles with experiments at $x/D = 134$ [116]. In Fig. 4.13 (bottom), results for mean and RMS of X_{O_2}/X_{N_2} ratio are presented for the same height. Good

prediction of the mixture and temperature is obtained. Small overestimation of temperature at the centerline is observed and peaks of radial temperature and X_{O_2}/X_{N_2} ratio RMS are slightly underestimated. Several aspects can affect the quality of these results: the predicted turbulent mixing, the turbulent combustion model and also the radiation modelling (here, optically thin assumption) which is important because of its coupling with temperature. Moreover, it should be reminded that this set of experimental data [116] comes from measurements at a different place than [249]. In fact, the altitude in [116] corresponds to a pressure about 15% lower than the one used in our numerical setup (1 atm).

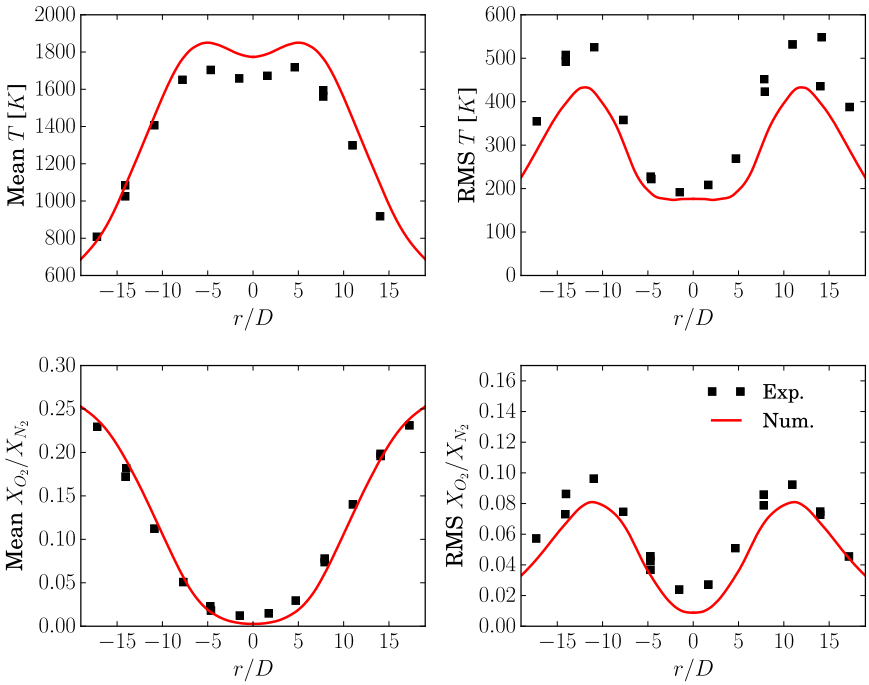

Figure 4.13: Comparison of mean and RMS temperature (top) and X_{O_2}/X_{N_2} (bottom) radial profiles between numerical (line) and experimental results (symbols) at $x/D = 134$. Experimental data is from [116].

In addition, Fig. 4.14 shows a comparison of mean OH radial profiles at different heights above the burner between predictions and measurements [104]. The experimental data being non-quantitative, experimental and numerical results are here normalised by their respective maximum values for each height above the burner. The obtained agreement confirms a good prediction of the position of the flame front and of the mean flame brush, necessary to correctly locate soot oxidation phenomena.

The overall agreement of available gaseous fields is satisfactory and good predictions of the gaseous phase are essential for the prediction of the source terms of the solid phase evolution. Results in terms of soot productions are presented later in Sec. 4.3.3. Regarding the gaseous phase predictions, the results are very satisfactory given that only three scalar transport equations (the filtered mixture fraction, its subgrid-scale variance, the reaction progress variable) have been added to the Naviers-Stokes equations to achieve this quality.

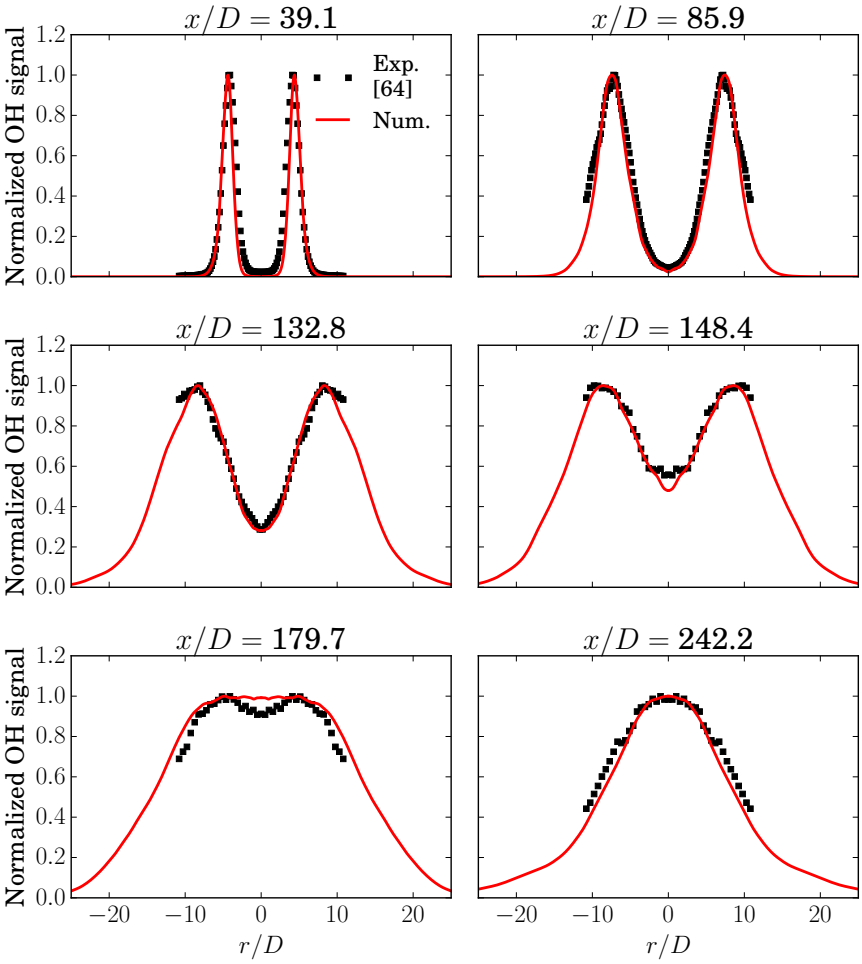

Figure 4.14: Normalised mean OH radial profiles at different heights above the burner: numerical results (line) are compared to experiments (symbols). Experimental data is from [104].

4.2.5 Filtered tabulated chemistry for LES (FTACLES)

References: [A18, A20, A21], [B1], [C6]

Most tabulated chemistry methods initially derived in RANS have been directly transposed in LES following a Presumed Conditional Moment (PCM) approach [231] were RANS statistical moments are replaced by filtered and subgrid-scale (sgs) moments while keeping the same distribution such as the β distribution. During my thesis, we have outlined the limitation of such an approach specifically for premixed combustion and have proposed another formalism based on filtered flamelets.

Need for a new class of models As computational resources keep increasing, the LES meshes get more and more refined, the corresponding filter size Δ decreases and the part of resolved flame wrinkling increases in the simulation. This is illustrated in Fig. 4.15(a) which positions a PRECCINSTA burner simulation from 2009 in the Pitsch LES regime diagram for turbulent premixed combustion [184]. The ratio Δ/δ_l is expressed as a function of the Karlovitz number Ka in logarithmic scale. For Ka < 1, combustion takes place in the corrugated flame

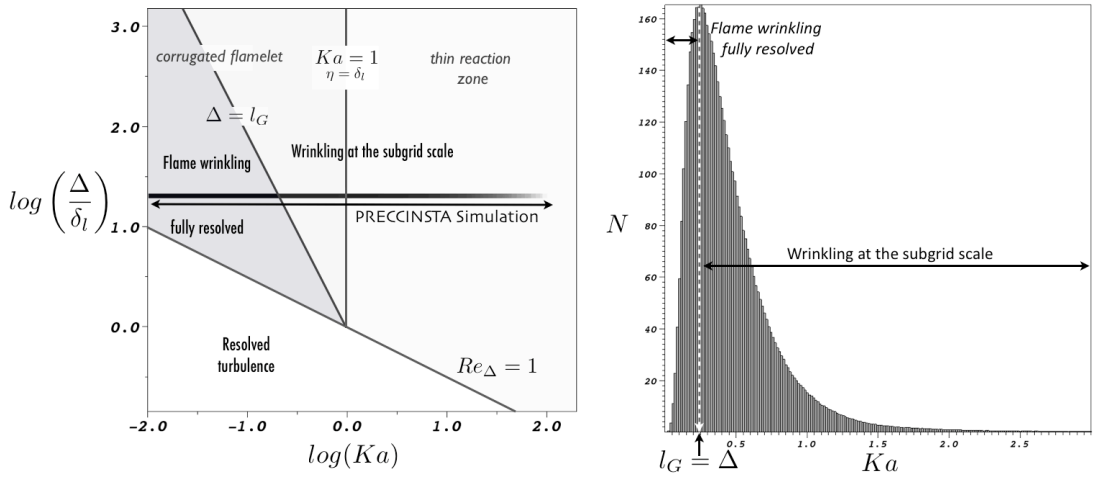

(a) (b)

Figure 4.15: (a) LES regime diagram for turbulent premixed combustion. The thick solid black line represent the range covered by the Preccinsta flame simulation.(b) Node distribution versus the Karlovitz number. Only nodes located into the filtered flame front have been considered, *i.e.* for $0.01 < \tilde{c} < 0.99$.

regime while the thin reaction zone regime is observed when Ka > 1. The smallest size of the flame wrinkling is given by the Gibson length l_G defined as [181]

$$\frac{\Delta}{l_G} = \frac{v'_\Delta}{S_l^0}. \tag{4.8}$$

The line corresponding to $\Delta = l_G$ is represented by a line of slope -2 in the LES diagram (Fig. 4.15(a)). In the corrugated flame regime, when the filter width becomes smaller than the Gibson length, the subgrid velocity fluctuation v'_Δ is smaller than the laminar flame speed S_l^0. In such cases, the flame wrinkling is fully resolved at the LES filter scale. At the opposite, on the right side of the line $l_G = \Delta$, subgrid scale wrinkling exists and will impact the filtered flame front propagation speed S_Δ. The node distribution versus the Karlovitz number is plotted in Fig. 4.15(b). First, it can be observed that most of the points are located in the corrugated flame regime (Ka < 1). The chemical flame structure remains therefore laminar, validating a flamelet approach. Secondly, for a substantial area of the flame surface (about 30 %), the Gibson length l_G is larger than the filter width and consequently the flame wrinkling is fully resolved at these nodes. With the increase of computational power since 2009, as meshes are getting finer, this proportion has increased substantially, even allowing a quasi-DNS treatment for the same setup with state-of-the-art simulations [159]. This preliminary study demonstrates the crucial need for modern turbulent combustion model to ensure a proper propagation of the filtered flame front when the flame wrinkling becomes fully resolved.

Inadequacy of the β FDF Figure 4.16 demonstrates that a β-PDF (or FDF in a LES context) does not fulfil this requirement. The original 1D flame front and filtered fields are shown in Fig. 4.16(a). These fields parametrise the β-distribution at each node to compute the filtered reaction rate of the reaction progress variable. The estimated burning flame speed S_Δ from the obtained filtered reaction rate is finally computed from the spatial integral of the

quantity:

$$\rho_0 S_\Delta = \int_{-\infty}^{+\infty} \overline{\rho}\widetilde{\dot{\omega}}_c(x)dx. \tag{4.9}$$

Figure 4.16(b) shows that S_Δ rapidly departs from the laminar burning speed S_l with a β-FDF contrary to the exact filtered reaction rate for which the ratio S_Δ/S_l remains unity as expected when there is no subgrid flame wrinkling. The intrinsic real FDF associated to the used Gaussian filter is compared to the β-distribution in Fig. 4.16(c), showing that, although the β-distribution has the correct qualitative behaviour, it differs quantitatively from the exact FDF.

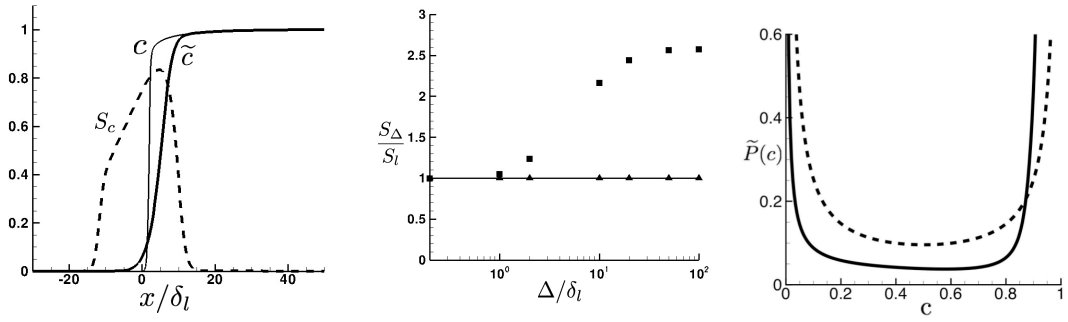

(a) (b) (c)

Figure 4.16: *A priori* test of the β-PDF formalism in laminar regime. (a) Progress variable c (solid line) and filtered progress variable $\widetilde{c}$ (bold line) profiles as a function of the spatial coordinate x. Dashed line is the subfilter progress variable segregation factor S_c. (b): *A priori* computations of the filtered progress variable propagation speed for different values of filter size. The filtered progress variable reaction rate is modelled by a β-PDF (squares) or by a Gaussian filter (triangles). (c): Exact probability density function (PDF) of the progress variable (solid line) compared with the presumed β-PDF (dashed line) at $\widetilde{c} = 0.5$.

FTACLES formulation This *a priori* analysis invites to use directly the filtered 1D flame solutions as a new tabulation method dedicated to LES. Nonetheless, to be fully consistent with the filtered equations, additional terms must be tabulated. The closed filtered transport equation for the progress variable $\tilde{c}$ is given by

$$\frac{\partial \overline{\rho}\widetilde{c}}{\partial t} + \nabla \cdot (\overline{\rho}\widetilde{\mathbf{u}}\widetilde{c}) = \nabla \cdot (\alpha_c[\widetilde{c}, \Delta]\, \overline{\rho} D\, \nabla \widetilde{c}) + \Sigma_c[\widetilde{c}, \Delta], \tag{4.10}$$

where $\alpha_c[\widetilde{c}, \Delta]$ accounts for the filtered molecular diffusion term and $\Sigma_c[\widetilde{c}, \Delta] = \overline{\rho}\widetilde{\dot{\omega}}_c + \Omega_c$ is the sum of the filtered reaction rate and the tabulated unresolved convection term that writes in a 1D filtered premixed flame as $\Omega_c = -\rho_0 S_l \frac{\partial}{\partial x}(\overline{c} - \widetilde{c})$. A posteriori validations have shown that the closed equation is able to predict the correct burning flame speed and filtered profiles for several filter values Δ/δ_l as long as at least 5-6 points are present in the filtered flame thickness. Finally, going back to the general case, a subfilter wrinkling factor Ξ must be accounted for. This gives the final expression of the FTACLES model:

$$\frac{\partial \overline{\rho}\widetilde{c}}{\partial t} + \nabla \cdot (\overline{\rho}\widetilde{\mathbf{u}}\widetilde{c}) = \Xi \nabla \cdot (\alpha_c[\widetilde{c}, \Delta]\, \overline{\rho} D\, \nabla \widetilde{c}) + \Xi \Sigma_c[\widetilde{c}, \Delta]. \tag{4.11}$$

(h]

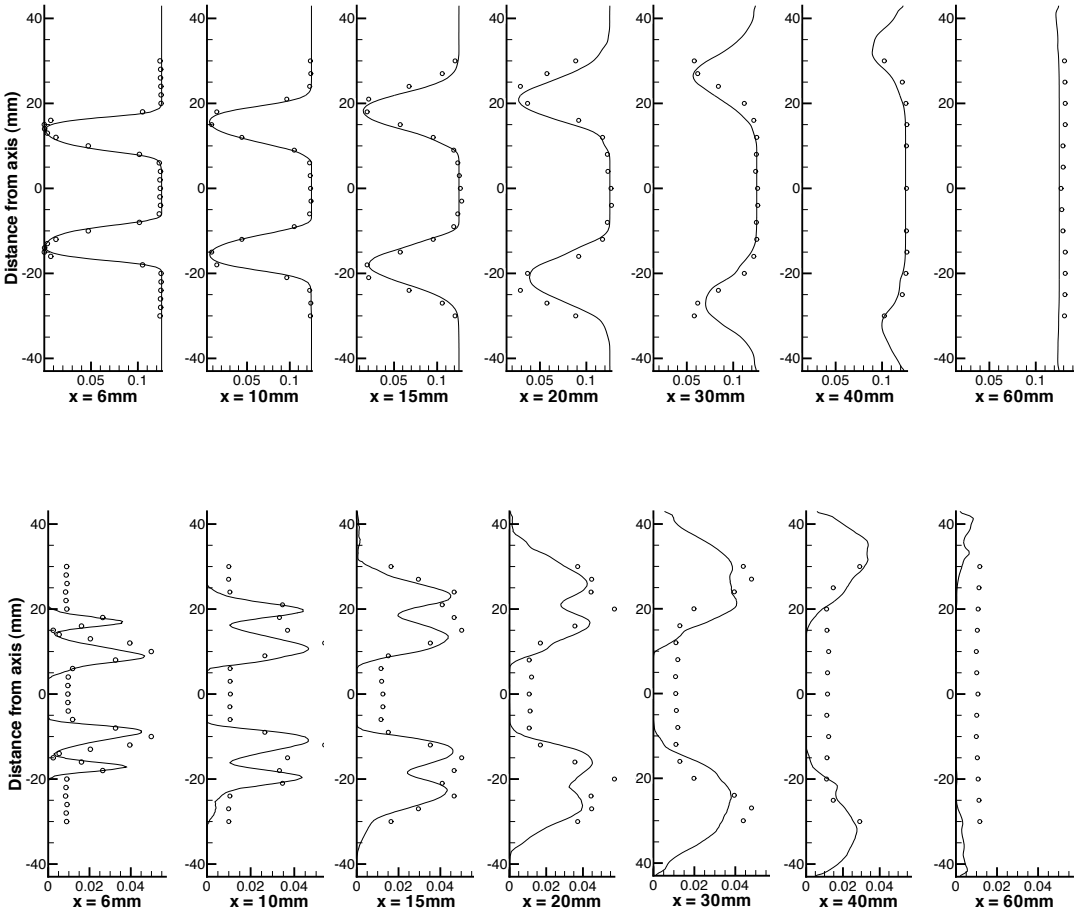

Figure 4.17: Predictions of mean (top) and rms (bottom) of CO_2 mass fraction in the PRECCINSTA burner. Symbols: measurements. Lines: simulation with F-TACLES.

Application to a swirled premixed flame The FTACLES model was applied to the premixed PRECCINSTA burner (case with equivalence ratio $\phi = 0.83$) with an algebraic model for the subgrid-scale flame wrinkling factor Ξ [38]. Details on the numerical setup are in [A20]. Predictions of CO2 mass fraction fields are seen in Fig. 4.17. A very good agreement is observed between experimental and numerical profiles, which demonstrates that the correct flame angle and mean flame thickness are reproduced by the model.

Further developments The FTACLES studies have been quite prolific since. Further investigations of the fully premixed formulation have been carried out [159, 154]. It has been extended to stratified premixed flames [5], heat losses effects [152] and combined with a dynamic model for the subfilter flame wrinkling [206]. Finally, a non-premixed variant has also been studied [45].

The FTACLES model has also been compared by Auzillon et al. [A18] to the popular Thickened Flame for LES (TFLES) model [23, 38]. In the thickened flame concept, the profiles are artificially thickened by doping the molecular diffusion to capture the flame front on the LES mesh

while modifying the reaction rate to consistently yield the correct laminar burning velocity. The flame dynamics of 2D Bunsen flames excited by acoustic perturbations was compared for both models (Fig. 4.18). The differences of flame response and the better behaviour of FTACLES were explained due to the different thermal flame thicknesses of both models. Indeed, for the same flame reaction thickness determined by the numerical requirement of the reaction rate integration, the TFLES model which is a spatial rescaling of the laminar flame yields a larger thermal thickness while the filtered thermal thickness of the FTACLES model remains close to the filtered reaction thickness.

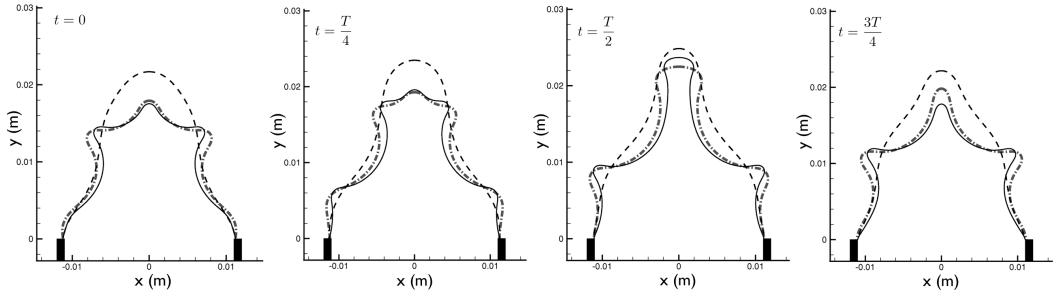

Figure 4.18: Isoline $\tilde{c} = 0.5$ during a cycle. Plain line: DNS. — filtered DNSf with $\Delta = 7.9\delta_r^0$. Dotted-dashed line: F-TACLES with $\Delta = 7.9\delta_r^0$. Dashed line: TFLES with the thickening factor $F = 5.7$.

4.2.6 Flamelet model in a scramjet

References: [A11], [C2, C3]

The reactive flow in the HyShot II scramjet combustor is studied using large eddy simulations. The computations are made feasible by two important modelling ingredients: an equilibrium wall-model and a flamelet-based combustion model. The first objective of the study is to assess the accuracy of this modelling approach through a validation study. The second objective is to study the flow for increased fuel/air equivalence ratios (ERs) until the unstart of the combustor due to thermal choking, *i.e.* when the heat release makes the flow entirely subsonic which, for a scramjet, is detrimental in terms of performance.

Numerical setup The geometry of the HyShot II vehicle can be seen in Fig. 4.19. With the use of the wall-model, the grid resolution is determined solely by the boundary layer thickness (i.e., not by the viscous length scale). The grids are mainly structured, with O-grids in and around the fuel injector. Three different grids are used to estimate the degree of grid sensitivity in the results, with total cell-counts of 100M (fine), 43M (medium), and 14M (coarse).

Flamelet-based models with a presumed PDF have been rather widely used in the area of subsonic combustion, but have been used much less for supersonic combustion. Sabelnikov et al. [201] studied the flamelet-concept for supersonic flows and how the large kinetic energies involved may change the flamelet solutions. Berglund and Fureby [14] used a flamelet/progress-variable approach in their LES of the flow around a wedge-shaped injector. Other studies have relied on other combustion modelling approaches. For example, the LES studies of the HyShot II scramjet by Fureby, Chapuis and co-workers [71, 33] solved transport equations for the species at the macro-level using a partially stirred reactor model to close the chemical source terms. Similarly, the LES of Edwards *et al.* [53] solved macro-level transport equations, but without

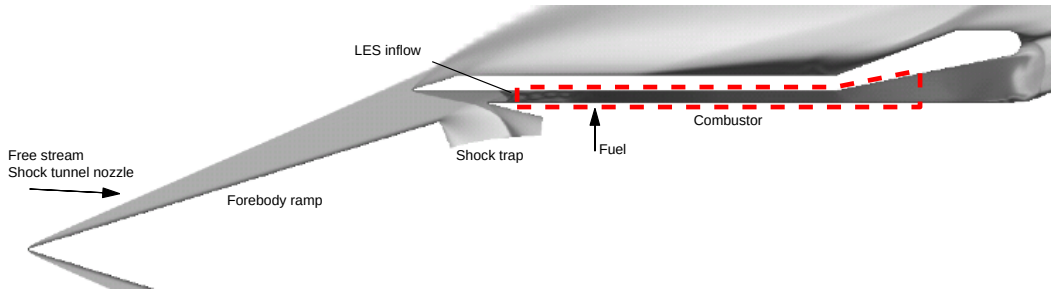

Figure 4.19: A slice through the HyShot II vehicle. The free stream (or flow from the shock tunnel nozzle) approaches at a slight angle-of-attack of 3.6°. The flow passes through the strong bow shock and the shock from the upper combustor wall; this shock is then swallowed by a shock-trap, leading to a relatively weak shock system in the isolator. The LES is performed in a domain covering the combustor and parts of the isolator and nozzle, respectively (shown with the dashed line). The inflow conditions to the LES domain are computed through an auxiliary 2D RANS computation, covering the full domain shown in the figure.

any special closure for the source term. The chief difficulty in applying a flamelet model to supersonic combustion is twofold: i) the high-speed flow and associated turbulent intensity is often believed to invalidate the flamelet assumption; ii) the hydrodynamically induced variations in pressure and enthalpy (due to, e.g., shock waves, wall-cooling, etc) are not easily handled in tabulated techniques. Regarding the former point, the estimated Damköhler number of order $\mathcal{O}(100)$ suggests that a flamelet approach is suitable. As for the second difficulty, we use an extension similar to Pecnik et al. [179] of the steady flamelet/progress-variable model of Pierce and Moin [183] to supersonic flows which is described hereafter.

Flamelets are solved and tabulated at a single reference pressure of $p_{\text{tab}} = 1.5$ bar, and at fixed temperatures at the fuel (pure hydrogen) and oxidizer boundaries ($T_{\text{tab},Z=1} = 210$ K and $T_{\text{tab},Z=0} = 1500$ K, respectively). These conditions are representative of the conditions in the HyShot II combustor. The H_2-air mechanism (9 species, 20 reactions) by Hong *et al.* [98] is used. Sample results of the pre-computed flamelets are shown in Fig. 4.20. The fully quenched (mixing only) stoichiometric temperature is 1160 K. At such high temperatures, there is no hysteresis and thus no S-curve, as shown in the figure.

As thermodynamic conditions (pressure, energy, density, temperature) can deviate strongly from the reference conditions used in the flamelet computations, the classical TTC inversion of energy-temperature relationship is replaced by a more robust method [203]:

$$\widetilde{T} = \widetilde{T}_{\text{tab}} + \frac{\gamma_{\text{tab}} - 1}{\gamma'_{\text{tab}}} \left(\exp\left\{ \frac{\gamma'_{\text{tab}} \left(\widetilde{e} - \widetilde{e}_{\text{tab}} \right)}{R_{\text{tab}}} \right\} - 1 \right) ,$$

where $\gamma'_{\text{tab}} = \left(\frac{\partial \gamma}{\partial T} \right)_{\text{tab}}$. The viscosity and thermal conductivity are computed using one-parameter power-law expansions around the tabulated conditions as $\sim (\widetilde{T}/\widetilde{T}_{\text{tab}})^a$, where the exponent a is computed for each quantity by perturbation around the flamelet solution and stored in the table.

Finally, the strong compressible effects on kinetics are accounted for by modifying the progress variable reaction rate. Saghafian [202] used a DNS database of a temporally evolving mixing layer for an *a priori* assessment, and found that the source term $\rho\dot{\omega}_{\widetilde{C}}$ (in kg.m^{-3}.s^{-1}) scales quadratically with pressure to a very good approximation. Inspired by these studies, the source

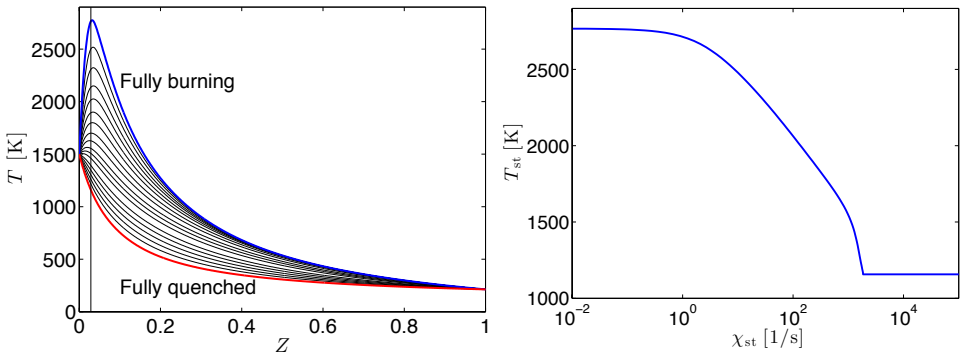

Figure 4.20: Flamelets used to model the H_2-air chemistry, computed at a reference pressure of 1.5 bar. Left: Temperature as a function of the mixture fraction Z, with stoichiometric mixture marked by the vertical line. The flamelets in the limits of zero and infinite stretch are shown in thick lines, with approximately every fifth intermediate flamelet shown in thin lines. Right: Stoichiometric temperature as a function of the flame stretch χ_{st}. Note the absence of an S-shape, which is due to the high oxidizer temperature.

term is modelled in this work as

$$\rho\dot{\omega}_{\widetilde{C}} = \left(\frac{\overline{p}}{p_{\text{tab}}}\right)\left(\frac{\overline{\rho}}{\overline{\rho}_{\text{tab}}}\right)\overline{\rho}_{\text{tab}}\dot{\omega}_{\widetilde{C},\text{tab}}\,. \tag{4.12}$$

The derived compressible-variant of the FPV model has been implemented in the code CharlesX used in this study. Further details on the code can be found in the article [A11].

Validation A subset of 9 experimental runs with reacting flow near the nominal operating condition are available from the campaign by Hannemann *et al.* [93, 92]; these have nominal equivalence ratios (ERs) from 0.27 to 0.35 due to run-to-run variations. The run with the highest ER (run #810) is chosen for the validation study, since this can be expected to be the most challenging (more heat release, stronger fuel jet, etc). The fuel stagnation pressure $p_{0,\text{fuel}}$ is 5.73 bar for run #810. A visualization of the simulated flow was shown in Fig. 1.1.

The comparison between the experimental pressure measurements and the LES results is shown in Fig. 4.21 for the lower and upper walls in the combustor. The rise in static pressure in the combustor is due to the heat release in the supersonic flow. We first note that the LES results for the mean pressure on the three grids are relatively close to each other, indicating that the results are close to (but not quite) grid-converged for this quantity.

The computed mean pressure profiles fall along the upper bound of the experimental data for the same reported ER=0.35. The experiment has about 8% uncertainty in the estimated ER [132], and thus the cases at reported ERs of 0.34 and 0.33 (lower by 3% and 6%, respectively) actually fall within the margin-of-error in terms of the ER. Since these ERs are nominally lower, the corresponding results should be seen as an approximate lower bound on the measurements. In the absence of cases with nominally higher ERs, it is reasonable to presume a similar margin-of-error towards larger values. With this, the computed pressure profiles all fall well within the experimental uncertainty.

The main focus of this study is on investigating the changes in the flow when the fuel/air equivalence ratio (ER) is increased. The incoming air flow is held constant at the average shock

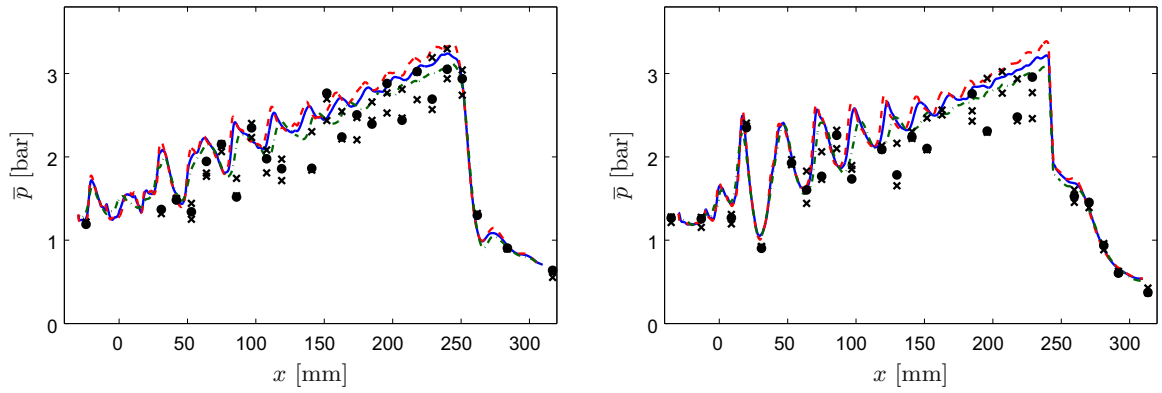

Figure 4.21: Mean wall pressure in HyShot II from LES (lines) for run #810 with ER=0.35. Compared with experiments [93, 92] for the same run #810 (circles) as well as runs #804 and #809 (ERs=0.34 and 0.33; both marked with crosses) to show the run-to-run variation. LES on fine mesh (100M cells, dashed), medium mesh (43M cells, solid) and coarse mesh (14M cells, dash-dotted). Left: Lower wall. Right: Upper wall.

tunnel conditions for the remainder of the study; thus the ER is directly controlled by the total pressure in the fuel feed $p_{0,\text{fuel}}$. For ER $\lesssim 0.38$, increasing the ER does not lead to any qualitative changes in the flow, only to a slightly larger pressure-rise within the combustor and a larger thrust. Increasing the ER beyond about 0.38, however, results in a qualitative change in the flow with the development of a stronger shock towards the end of the combustor. This shock travels then upstream, becoming the leading shock in a shock-train, and finds a seemingly stable position in the combustor. This shock-train is similar to the shock-trains that form in the isolator of scramjets in dual-mode operation, but differs in that here it forms in the combustor, concurrent with the mixing and heat release. For this reason, and to distinguish it from more common isolator shock-trains, we refer to it as a "combustor shock-train".

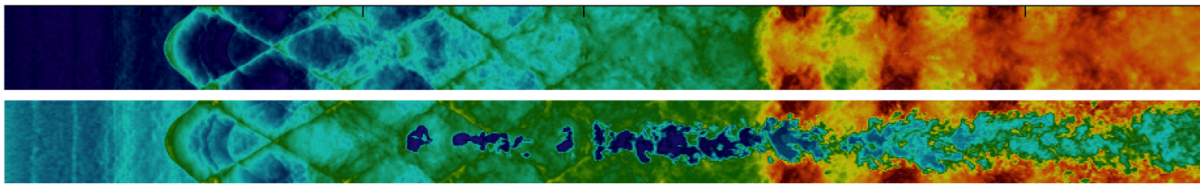

Figure 4.22: Contours in a horizontal plane at $y = 7$ mm (i.e., 2.8 mm from the upper wall), from $x = -30$ mm to $x = 242$ mm (the combustor exit), for ER=0.414. coloured from low (blue) to high (red) values. Top: pressure (0.6 to 6.0 bar). Bottom: density (0.1 to 1.1 kg/m^3).

The flow is partially visualised in Fig. 4.22. The combustor shock-train begins with the sharp rise in pressure and density towards the end of the combustor. Note the co-existence (or co-location) of the combustor shock-train and the fuel jet. The term "leading shock" is used to denote the beginning of this combustor shock-train. The location of the leading shock is denoted by x_s, and is defined as the point where the cross-sectionally averaged Mach number $\widehat{M}$ first decreases below 1.1.

Comparisons are made with a series of shock-tunnel experiments, described more fully in the companion paper [134]. The final location of the combustor shock-train $x_{s,\text{final}}$ is shown in Fig. 4.23 and compared to the results from the experiments [133, 134]. For both the LES and the experiments, the uncertainty due to variations in position over the finite time extent is

estimated and shown in the figure. The agreement is rather remarkable for ER $\lesssim 0.45$, but with differences for larger ERs. In fact, the earlier experiments of Laurence *et al.* [132] indicated that the combustor shock-train may be stable for even larger ERs (up to ∼0.7) than those considered here, at least within the limitation of the short test time.

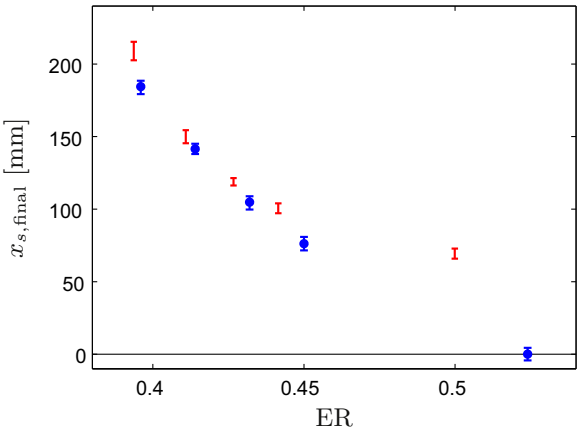

Figure 4.23: Final leading shock location $x_{s,\mathrm{final}}$ for different ERs. Comparison of results from LES (blue, with circles) with those from the experiment (red: [134]). Note that the $x_{s,\mathrm{final}}$ values are given in LES coordinates, i.e., relative to the fuel injector.

Analysis The basic effect of increasing the equivalence ratio (ER) is shown in Fig. 4.24. which shows quantities averaged in time and over the combustor cross-section (or across the upper and lower walls in the case of surface quantities). Note that simple cross-sectional averages are used, without any stream-thrust weighting or similar. The cross-sectionally averaged Mach number is close to 1 in the combustor shock-train. The cross-section 2D mean field remains however inhomogeneous with about 40-60% of the cross-section occupied by subsonic flow for those cases. For ER=0.414, the shock-train is not strong enough to drive the average flow to subsonic conditions, though for ER=0.450 $\widehat{M}$ becomes principally subsonic a short distance downstream of the leading shock. Increasing the ER to 0.524 pushes the combustor shock-train up to the fuel injector, where it merges with the fuel jet bow shock. This case produces up to 70% subsonic flow, yet it appears to be stable.

In the plot of the averaged source term, $\widehat{\dot{\omega}}_{\mathrm{H_2O}}$, (upper right) we see that the presence of the shock-train substantially increases H_2O production (and by proxy, the rate of heat release) in the region immediately downstream of the leading shock. This is consistent with the intensified OH* intensity seen associated with the shock-train in the experimental chemiluminescence images of Laurence *et al.* [134]. The average $\widehat{\dot{\omega}}_{\mathrm{H_2O}}$ tails off significantly downstream.

In the lower left plot we see that the shock-train causes the wall friction $\widehat{\tau_w}$ to decrease by approximately 10% in comparison to the ER=0.377 case. Much more significant, however, is the enhanced heat loss at the combustor walls $\widehat{q_w}$ (lower right), which can increase by 50% or more. Both these effects - decreased friction and increased heat loss - will tend to drive the combustor flow away from choking conditions.

Further analysis, notably the interconnection between the stoichiometric and sonic isosurfaces, can be found in the paper [A11]. The studied scramjet demonstrates how detailed LES combined with a cleverly designed flamelet model can describe fairly accurately such a complex flow. In

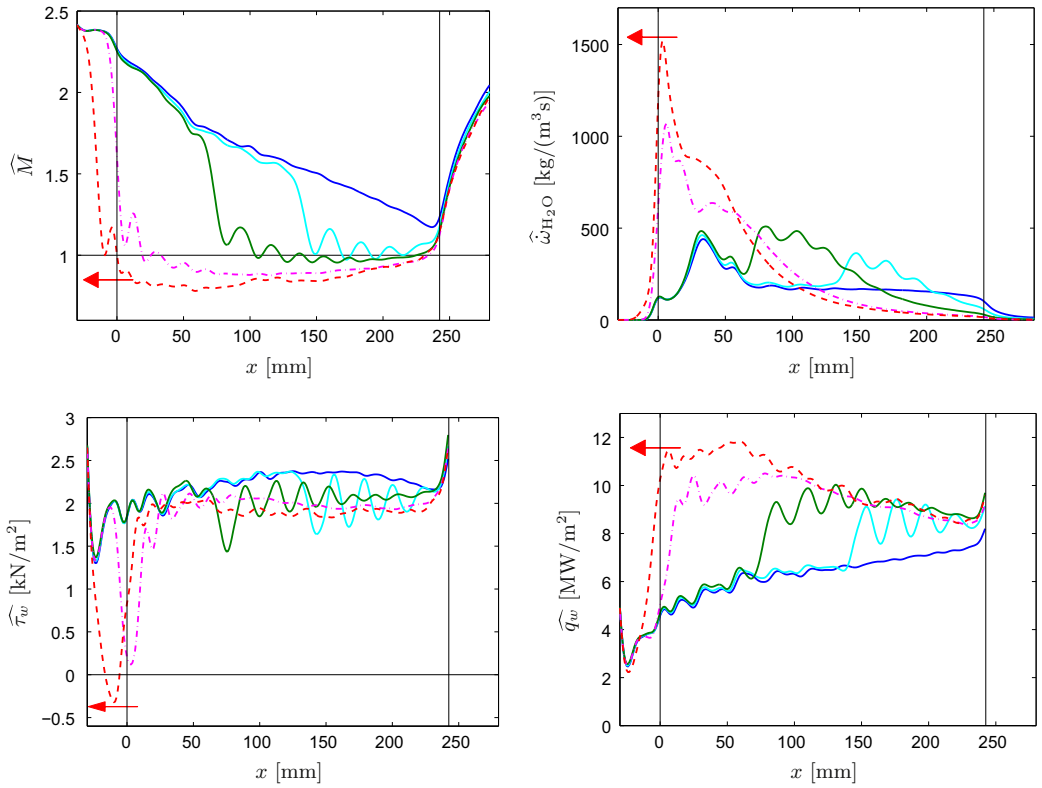

Figure 4.24: Time- and cross-sectionally averaged results during steady state at different ERs. In every plot, the different cases are, in order, ER=0.377 (nominal, fully started flow; blue solid line), ER=0.414 (with combustor shock-train starting at $x_s \approx 140$ mm; light blue solid), ER=0.450 (combustor shock-train starting at $x_s \approx 75$ mm; green solid), ER=0.524 (combustor shock-train merged with the fuel injector bow shock; pink dash-dotted), and ER=0.597 (combustor shock-train starting upstream of the injector, and moving upstream as indicated by the arrow; red dashed). Note that the ER=0.597 case does not reach steady state, and the simulation was halted due to the combustor shock-train reaching the LES inflow.

other types of flames, additional physical phenomena must be included and the number of submodels quickly increases. This is the topic of the next section.

4.3 Additional models in complex reactive flows

4.3.1 Droplet injection model in two-phase flows

References: [D11], [T5]

Simulations with liquid spray injection give rise to several modelling issues. A first one is the problem of describing the spray atomisation process which yields to a mist of small droplets. Reactive large-eddy simulations cannot afford to simulate this phenomenon. Therefore, the generated disperse liquid phase is instead injected directly in the simulations. One must then provide the parameters of the droplet injection model: profiles of droplet size, velocity, temperature and density. This can be done by modelling the primary and secondary atomisation. Another approach was followed during the thesis of Théa Lancien: the injection model param-

eters are optimised by reducing the error with downstream experimental measurement. This is based on the construction of a surrogate model assembled from multiple LES that are carefully selected.

Selection of the droplet diameter Without loss of generality in the principle of the optimisation method, the disperse liquid phase is described here with a monodisperse Eulerian description where moments of the droplet number density function (NDF) are transported [204, 207]. By fixing the shape of the injected profiles of droplet density and velocity, the remaining unknown in this monodisperse description is the injected droplet diameter d_l^{inj}. Selecting a representative single diameter of a polydisperse spray is a difficult task. A common approach is to retain the Sauter mean diameter $D_{32} = (\sum_N d^3)/(\sum_N d^2)$, which is 20 μm is the studied configuration SICCA-Spray [191]. Instead, an optimum value of the injected droplet diameter that best represents the evolution of the spray is deduced here by computing a surface response on mono-disperse Eulerian simulations thanks to uncertainty quantification (UQ) methodology. This analysis is carried out on an unconfined single injector configuration where liquid-phase experimental data are available 7.5-mm downstream the combustor inlet plane.

Table 4.1: Values of the evaluations of the injected diameter for each quadrature level.

	Quadrature level			
	1	2	3	4
Injected droplet diameter d_l^{inj} $[\mu m]$	0.5	0.5	0.5	0.5
	-	-	-	0.83
	-	-	1.81	1.81
	-	-	-	3.41
	-	5.55	5.55	5.55
	-	-	-	8.17
	-	-	11.15	11.15
	-	-	-	14.38
	17.75	17.75	17.75	17.75
	-	-	-	21.12
	-	-	24.35	24.35
	-	-	-	27.33
	-	29.95	29.95	29.95
	-	-	-	32.09
	-	-	33.69	33.69
	-	-	-	34.67
	35.0	35.0	35.0	35.0

The surface response is built with Polynomial Chaos Expansions (PCE) [244, 197]. PCE allows for approaching uncertain fields that depend on both deterministic and uncertain parameters. A given field u can then be written as $u(x, \omega)$ where x represents the deterministic parameters and ω the uncertain ones. In the present study the injected diameter d_l^{inj} is considered to be the unique uncertain parameter. Through PCE, one is able to estimate any given field with the polynomial decomposition:

$$u(x_j, d_l^{inj}) \approx \sum_{k=0}^{N} a_k(x_j) P_k(d_l^{inj}). \tag{4.13}$$

For any given point x_j, knowing the value of the coefficients $a_k(x_j)$, $u(x_j, d_l^{inj})$ becomes a continuous function of the uncertain parameter d_l^{inj}, whose study is then straightforward. Using non-intrusive methods, the computation of the coefficients $a_k(x_j)$, which are defined by integrals, is carried out with nested quadrature rules: $M = 2^l + 1$ evaluations of $u(x_j, d_l^{inj})$ are required for the l-quadrature level. In the context of LES, several simulations, corresponding to different values of d_l^{inj} are then performed. The retained Clenshaw-Curtis nested quadrature rule enables to limit the number of evaluations for several quadrature levels [121], which is a great benefit given the computational cost of carrying out several large-eddy simulations. The considered injected diameter distribution is considered uniform between 0.5 μm and 35 μm. Due to the cost of each simulation, the maximum quadrature level was limited to 4 for this study. The corresponding values for the evaluations of d_l^{inj} obtained according to the Clenshaw-Curtis quadrature rule are summarised in Table 4.1. For the highest quadrature level that was considered, 17 simulations were performed. Each simulation was started from the same converged air flow field, the two-phase flow was converged for 15 ms and averaged over 30 ms. A preliminary study not shown here confirmed the quality of the mesh and LES setup to accurately predict the gaseous flow.

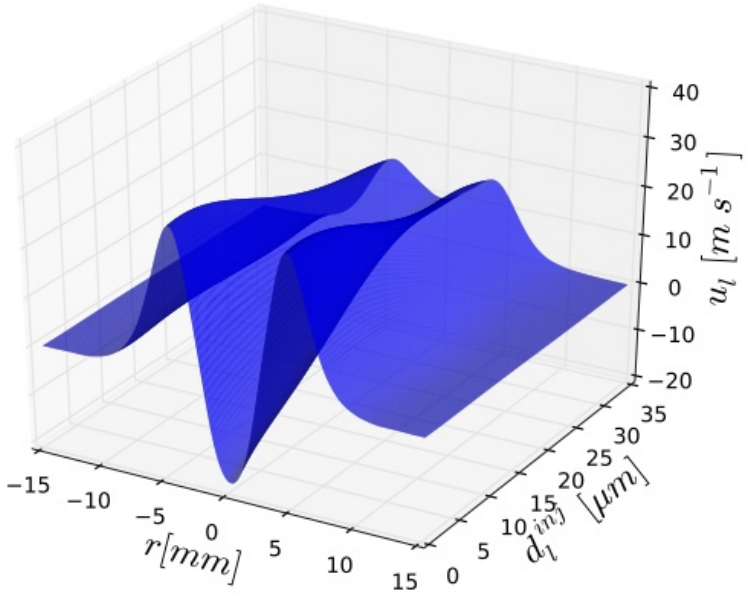

Figure 4.25: Response surface for the liquid-phase axial velocity at $x = 7.5$ mm.

Each field can then be estimated by the polynomial approximation for any value of the injected diameter, even ones that were not simulated. In other words, at a given point in space and for a given physical field, the polynomial reconstruction yields an estimation of this field according to the injection diameter. This provides a way to determine an optimal diameter more efficiently than by carrying out a parametric study with a finite set of values. An example of response surface is given in Fig. 4.25 for the liquid velocity at $x = 7.5$ mm. Each radial profile of the axial liquid velocity can now be obtained for any value of the injected diameter and becomes a 3D surface. The figure shows that when smaller droplets are injected, the central recirculation zone present is the gaseous flow is more intense in the liquid phase field and the velocity profiles are closer to the gaseous one as expected for small Stokes number droplets. On the other side of the plot, when the droplets are bigger, they have a more ballistic behaviour, leading to the disappearance of the central recirculation zone and less intense velocity peaks.

The optimization criterion was based on the prediction of the correct two-phase flame burning velocity at the flame stabilisation height. The reference field is estimated from experimental data on the polydisperse spray and the expression by Ballal and Lefebvre [8] for the two-phase flame burning velocity. This value is compared to the burning velocity of the equivalent monodisperse spray at the same height. The found optimal diameter is 15.3 μm which yields a 16% error on the flame speed. This value is between the mean diameter $D_{10} = 10$ μm, which in fact minimises the error with the liquid velocity measurements, and the Sauter mean diameter which controls the evaporation rate.

Reactive flow simulations The choice of the injected diameter is compared to other diameters in Figs. 4.26 and 4.27 in reactive simulations of the confined spray flames. The TFLES model is used with a 2-step-chemistry for n-heptane (see Sec. 5.3.2 for details). The simulation with the Sauter mean diameter ($d_l^{inj} = D_{32}$) yields the poorer results while the D_{opt} and D_{10} cases exhibit similar results. The study shows that selecting naively the Sauter mean diameter would have yielded incorrect results.

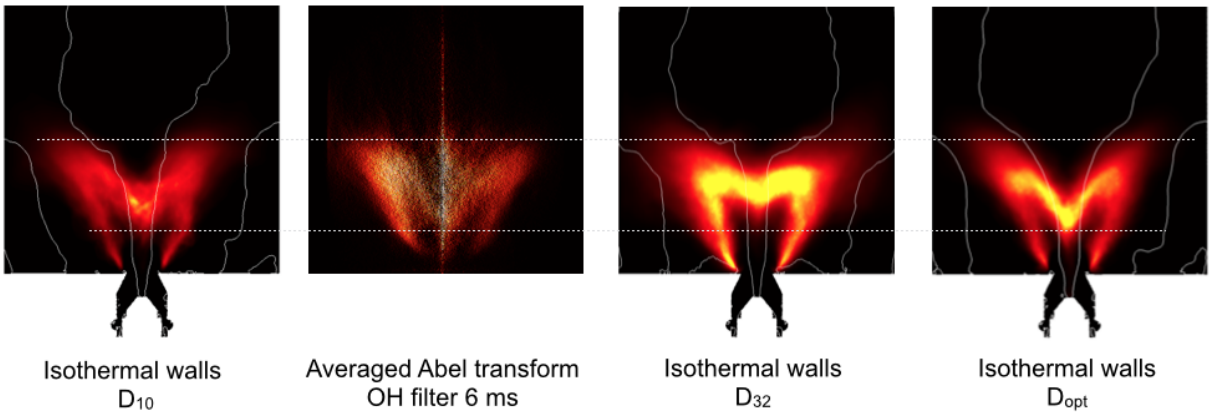

Figure 4.26: Average flame shapes for several values of the injected diameter, for $d_{inj} = D_{10} = 8$ μm (left), $d_{inj} = D_{32} = 20$ μm (center right), and $d_{inj} = D_{opt} = 15.3$ μm (right), compared to the experimental averaged Abel transform (center left). The white lines are iso-lines of the gaseous axial velocity at $u = 0$ m.s^{-1}.

The derived methodology can also be applied in a multiparameter and polydisperse context. It allows for replacing the heuristic manual tuning by a sound optimization problem to match downstream measurements. Indeed, the liquid fuel injector is often hidden upstream in the combustors where no optical apparatus can access it. The sparse grid cubature methods enabled by PCE surface response will prove to be very efficient in such multiparameter problems.

4.3.2 Limitation of flamelet models to predict PAHs and soot particles emission

References: [A9], [T6]

Chemical species such as Polycyclic Aromatic Hydrocarbons (PAHs) and soot particles that are characterised by large chemical time scales are known not to remain in flamelet manifolds as soon as they are solicited by an external perturbation such as occurring permanently in turbulent flows. The unsteady dynamics of sooted flames has been studied in pulsating counterflow flames

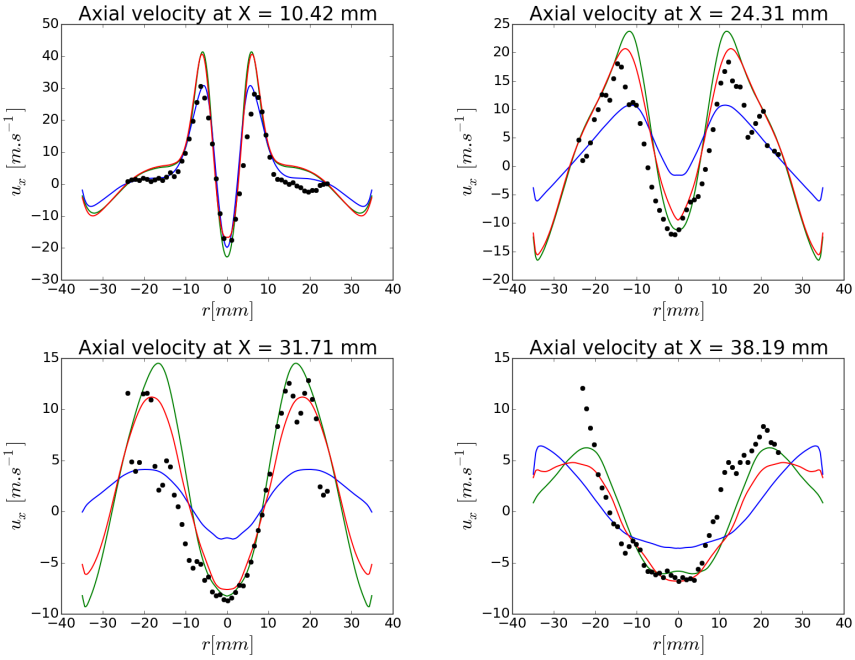

Figure 4.27: Mean axial velocity profiles for the gas phase at different heights for different values of the injected diameter. –: $d_l^{inj} = D_{opt}$; –: $d_l^{inj} = D_{32}$; –: $d_l^{inj} = D_{10}$; •: Experimental data.

with the code REGATH [68]. The gaseous chemistry is described with the KM2 mechanism [237] and the soot size distribution is computed through a sectional model.

Figure 4.28 (left) presents the unsteady response of the soot maximum volume fraction and pyrene ($A4$) maximum mass fraction (the smallest considered soot precursor) to the unsteady imposed strain rate during two oscillating cycles. Quantities have been normalised with their respective steady values at the lowest and highest strain rates for three frequencies. The higher the frequency, the more $f_V^{\max}$ and $Y_{A4}^{\max}$ fluctuations are dumped and phase-lagged. Looking at the results in the a-space (Fig. 4.28, right) enables a clear comparison with the quasi-steady solution (grey line). A quasi-steady response is observed at low frequency ($f = 0.1$Hz), while for higher frequencies, solutions step aside from the steady results. Similar behaviour is observed for the temporal evolution of the particle size distribution (PSD).

These computations have enabled to derive a model of the dynamic response of PAHs and individual soot section. Figure 4.29 presents these responses in terms of gain and phase lag of maximum temperature, $Y_{A2}^{\max}$, $Y_{A4}^{\max}$, maximum soot mass fraction of two sections (sections 12 and 16) and $f_V^{\max}$. The response of precursors and soot is more phase-lagged and damped than temperature. Moreover, phase-lag and damping increases with their size (not shown for all precursors). Big particles are the main contributions to soot volume fraction, so that f_V response is mainly governed by the last soot sections. A good agreement is obtained between the numerical results (lines) and the analytical model (symbols). Discrepancies are mainly observed at high frequencies but the hierarchical behaviour between temperature, soot precursors and soot sections is well predicted.

The nature of PAHs and soot response outlines the inaccuracy of a flamelet assumption for these chemical species characterised by a slower chemistry than the main flame oxidation. Hence, it was recognised that mass fractions of PAHs must be solved in separated transport equations with

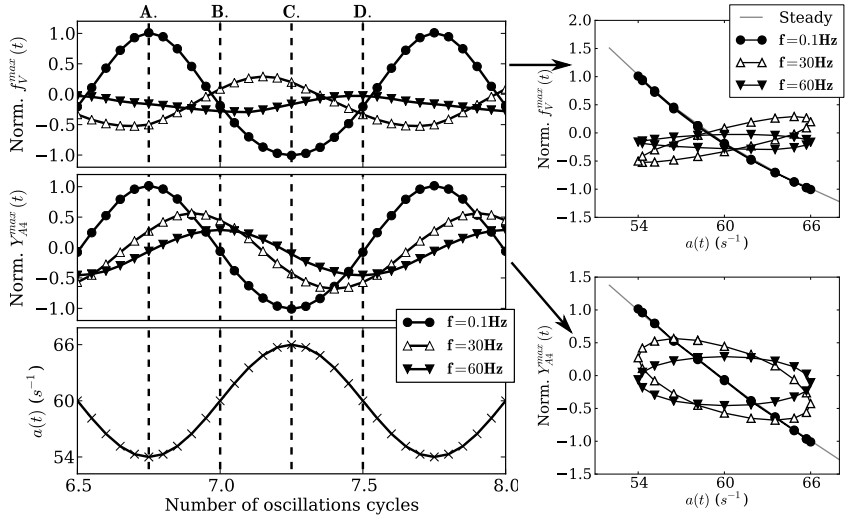

Figure 4.28: Normalised response of soot maximum volume fraction ($f_V^{\max}$), pyrene maximum mass fraction ($Y_{A4}^{\max}$) to the unsteady imposed strain rate $a(t)$.

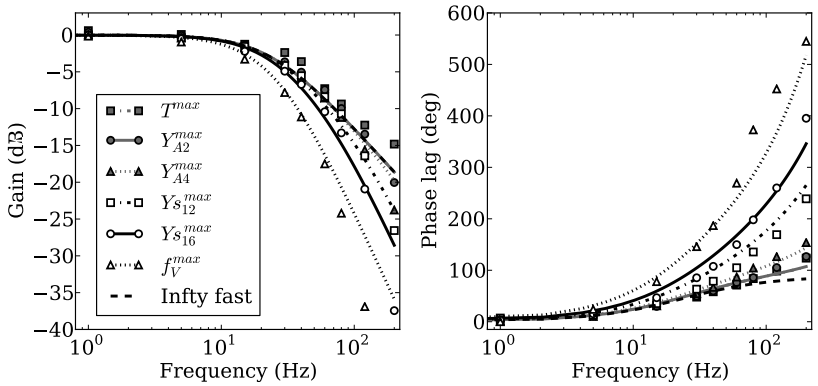

Figure 4.29: Comparison between the derived analytical model predictions (lines) and numerical results (symbols) of amplitude gain and phase lag for maximum temperature, naphthalene ($A2$) and pyrene ($A4$) maximum mass fractions, maximum mass fractions of the 12^{th}, the 16^{th} soot sections and maximum soot volume fraction. Analytical results for $T^{\max}$ and $Y_{A2}^{\max}$ are superposed.

specific models to let them interact with gaseous species stored in the flamelet table [162, 245]. Similarly, soot particle fields cannot be interpolated in the table and must be solved separately.

4.3.3 Large-eddy simulation of a jet sooted flame with a sectional approach

References: [A5], [T6]

This study follows Sec. 4.2.4 where results for the gaseous phase in the Sandia ethylene/air diffusion flame were presented. The original RFPV model is here augmented with a lumped PAH equation [162] and an original addition of a sectional model in a LES context to predict soot emission. This work was done during the thesis of Pedro Rodrigues with the main supervision of Benedetta Franzelli and Nasser Darabiha on soot modelling. The main results are here

synthesised.

25 sections are transported to describe the particles size distribution describing particles with volumes comprised between 0.7 nm^3 and 5×10^9 nm^3. Figure 4.30 shows instantaneous fields of soot volume fraction f_V and of particles number density N_{part} (from the left). An iso-contour of mixture fraction at value Z_0 localising the flame front is also shown with a solid line. It can be noticed that soot particles are always located on the rich side of the flame ($Z > Z_0$) close to the jet axis. Figure 4.30 also presents the instantaneous total soot volume fraction source terms: nucleation $\dot{Q}_{\text{nu}}$, condensation $\dot{Q}_{\text{cond}}$, surface growth $\dot{Q}_{\text{sg}}$ and oxidation $\dot{Q}_{\text{ox}}$ and coagulation source terms. This illustrates the richness of the phenomena to describe in sooted flames. Analysis of the different field can be found in the article [A5]. Surface reactivity of soot particles has been identified as the most important contributions to the total soot mass production and destruction, which is in contrast with other computations in the literature.

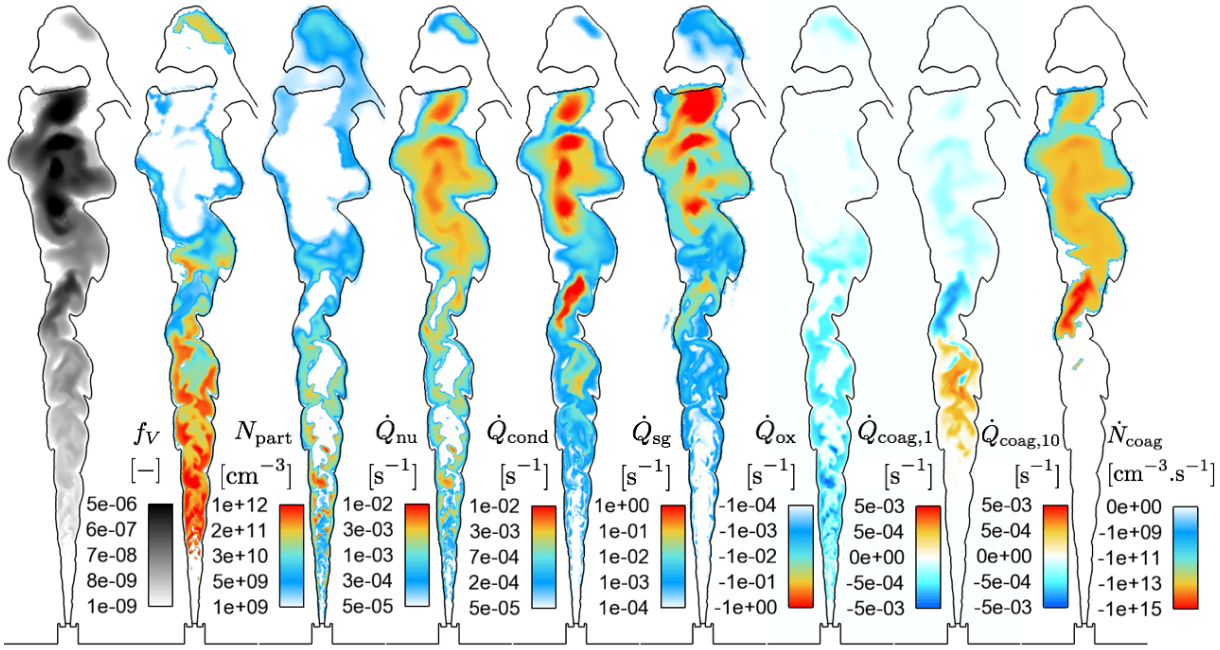

Figure 4.30: From left to right: typical instantaneous fields of soot volume fraction, particles number density, nucleation, condensation, surface growth and oxidation volume source terms for all the sections, volume coagulation source term for the first and tenth section and number coagulation source term for all the sections. The iso-contour of mixture fraction at Z_0 (indicating the flame front) is shown in solid line.

In order to validate the proposed approach for sooting turbulent flames, it is firstly possible to quantify the resolved temporal soot intermittency. This quantity is defined experimentally at each point as the probability of finding an instantaneous value of f_V lower than 0.03 ppm. Figure 4.31(a) shows a comparison of numerically-resolved soot intermittency and experimental probe-resolved soot intermittency along the flame centerline as a function of the axial position. It can be seen that the model reproduces well this quantity even if numerical results seem slightly translated upstream. Axial mean soot volume fraction profile is compared with experiments in Fig. 4.31(b). A reasonable agreement of soot production is obtained, but the peak soot volume fraction is overestimated by a factor two. Soot destruction is also predicted too early compared to experiments. However, when compared to other published results, the present prediction of soot volume fraction is quite satisfactory compared to state-of-the-art large eddy simulations of

soot production. The radial profiles of mean soot volume fraction show the same trend although the numerical profiles are persistently narrower. Finally, as observed experimentally, the relative root-mean-square is larger than 100% denoting strong fluctuations in the soot production. Comparisons of all numerical results have globally confirmed a good prediction of soot particles production dynamics.

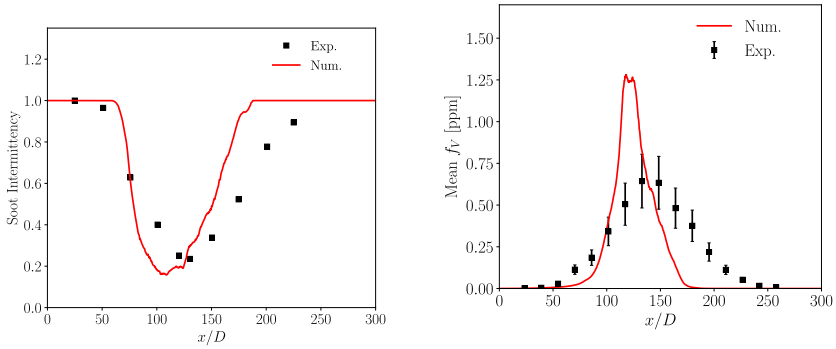

(a) (b)

Figure 4.31: Comparison of numerical (line) and experimental (symbols) soot intermittency (a) and mean soot volume fraction (b) axial profiles. Experimental data is from [208, 104].

Further analysis on the soot unsteady dynamics has been carried out. It revealed the intermittency between one-peak and two-peak PSD and the importance of history effects in the soot production mechanisms.

Chapter 5

Ignition in annular combustors

During the design of new aeroengines, the reliability of high-altitude relight must be certified. The use of new technologies to make the combustors less pollutant modifies the flame behaviour, making it more sensitive to unsteady phenomena such as ignition, blow-off and instabilities. The study of ignition in an aeroengine is then critical and of prime importance. The MICCA combustor developed in EM2C by Daniel Durox and Sébastien Candel allows for studying the ignition and the propagation of the flame in an annular combustion chamber equipped with multiple burners as in actual engines. The large-eddy simulation of light-round in the MICCA chamber with the FTACLES model achieved the first experimental and numerical cross-comparison of ignition in such configurations (**Highlight #2** in Fig. 1.2, Sec. 5.2.3). In order to get closer to realistic chambers, the study was extended with the injection of liquid sprays, which complexifies computations that are already challenging. The joint experimental and numerical analysis has outlined the shared characteristics and the differences of ignition with this new type of injection. All these simulations are massive and have required a large amount of cpu resources to carry out 3D unsteady computations on several hundreds of millions of elements. These resources were obtained thanks to the awarding of two PRACE European projects in addition to national GENCI projects. Finally, the numerical results give access to quantities that are not accessible experimentally and allow additional analysis to outline mechanisms that control the flame propagation.

Numerical results and their validation are presented in Sec. 5.2 for the premixed gaseous configuration and in Sec. 5.3 for liquid spray injectors. Further analysis of the numerical fields is presented in Sec. 5.4 before investigating different scenarios for the flame propagation mechanisms in Sec. 5.5.

Full list of **References**:

- Papers: [A3, A8, A12, A13, A14]
- Book chapters: [C1]
- Theses: [T3, T5]
- 8 conferences

5.1 Context

In realistic gas turbines, a successful ignition sequence, from the generation of a spark to the stabilisation of a steady-state flame around each injector, can be decomposed into several phases that may be studied separately or successively. Lefebvre and Ballal [138] identified three phases for the ignition of a combustor composed of several burners, that are described hereafter:

(1) **Kernel generation**: the ignition triggering device deposits certain amounts of energy in the cold flow which locally increases the temperature until a flame kernel is created that is able to propagate.
(2) **Kernel propagation**: the kernel, having met with favourable conditions for its expansion, propagates towards the first fuel injector until a flame stabilises in its vicinity.
(3) **Flame propagation from burner to burner**: in the case of multiple injector combustion chamber, as is found in most industrial gas turbines, the flame propagates on each side of the initial injector in order to ignite the rest of the chamber until a flame has stabilised around each injector. In annular combustors, this phase is called *light-round.*

It is well known that the physical mechanisms involved in phase (1) are quite complex because they involve an energy deposition through a spark and a subtle competition between convective, diffusive and reactive processes. Numerous works have studied the factors that determine the minimum ignition energy (MIE) [12, 31, 130], the flow conditions around the spark plug [11, 118, 60], the effects due to detailed kinetics [124, 125] or pressure [212]. Recently, a couple of numerical simulations [30, 42] have incorporated the simulation of the generated plasma to predict the complex initiation of combustion in this phase.

In phase (2), one of the key issues is to understand and predict the survival of the generated flame kernel in the turbulent flow field. Indeed, depending on the local stochastic flow conditions that are encountered by the kernel, it can either develop towards a turbulent flame or become extinguished, leading to a measurable probability of ignition. In the recent years, experimental studies have measured ignition probabilities in realistic burners with gaseous premixed [210, 29] and non-premixed [2] injection and more recently in the presence of liquid fuel [147, 141, 234, 149]. The recent advances in computing performance have allowed the use of LES for determining the failure or success of ignition in gaseous partially premixed or non-premixed configurations [131, 219]. Computing a full probability map numerically demands tremendous computational resources, since many ignition events must be simulated. This has been achieved in the recent work by Esclapez et al. [59], where a good agreement between the numerical and experimental probability maps has quantitatively validated the predictability of LES. Such simulations have also enabled a better physical understanding of the stochasticity of the ignition process to be achieved and a low-order predictive model that can be used repeatedly at the industrial design stage [61, 58] to be provided. In the last few years, an increasing number of studies have focused on the kernel creation in two-phase flows, using LES [112, 61, 41] or DNS [166] in an effort to study configurations as close as possible to industrial ones.

Much fewer studies have been dedicated to the study of phase (3) for a long time. This is due the numerical and experimental difficulty to study a full-scale multi-burner configuration and to the necessity to first secure success of phases (1) and (2) to ensure the full ignition of the engine. Nevertheless, the interest in the need to cope with burner to burner initiation has recently led to an increasing number of studies of ignition on multiple injector systems. Pioneering results of the first large-eddy simulation of the ignition of a helicopter combustion chamber reported by Boileau et al. [18] have shown the strong impact of burnt gases volumetric expansion on the flame propagation velocity but with no comparison with experiments. Flame propagation has

been studied experimentally in a linear array of injectors with varying inter-injector spacing with gaseous premixed injection by [9] and liquid n-heptane injection by [149]. Inter-injector distance was found to modify the pattern of flame motion giving rise to two propagation modes. This feature has been retrieved in LES by [9] and also observed in an annular combustor experiments [145, 146]. Nonetheless, such linear configurations do not account for specific phenomena arising in annular geometries. In 2013, two experimental studies have been reported on successful light-round sequences in idealised annular systems, with premixed propane-air injection [21] and methane-air injection [7]. Both studies highlight the influence of the mixture equivalence ratio and bulk velocity on the light-round duration. Later on, investigations have reported the effects of non-premixed injection [145], inter-injector spacing [145, 146], and liquid fuel injection [192, 193], bringing new insights into the ignition of realistic gas turbines.

The availability of these new experimental configurations for validation have led to new numerical studies. This chapter present original results obtained from the study of light-round in the EM2C MICCA combustor.

5.2 Simulations of light-round under perfectly premixed conditions

5.2.1 Presentation of the SICCA and MICCA combustors

References: [A14], [T3]

The experimental setup MICCA [21] shown in Fig. 5.1(a) comprises an annular chamber which is dimensionally similar to that of a helicopter combustor. A mixture of propane/air is carried through eight tubes to a plenum. The mixture is delivered by sixteen swirl injectors forming a periodic pattern in the chamber backplane and defining sixteen equal angular sectors ($\Delta\theta = 22.5°$) delineated in Fig. 5.1(b). The chamber is divided in two main parts, namely *H+* and *H-*. Each of these parts features seven sectors (numbered from *S1* to *S7* for *H+* and from *S-1* to *S-7* for *H-*), and share sectors *S0* and *S8*. Two concentric cylindrical tubes made of quartz form the chamber side walls. Burnt gases are exhausted to the atmosphere and evacuated through a heat exchanger by a hood. The present geometry of the combustion chamber slightly differs from that used in [21]. The quartz tubes are shorter (it was 400 mm in [21]) to reduce the computation time and the swirlers have a simpler design.

The companion configuration SICCA is shown in Fig. 5.2. It is a mono-burner configuration with an injector identical to those mounted in MICCA. This configuration allows more elaborated diagnostics to characterise a single flame setup.

Figure 5.3 presents light-round duration of premixed propane/air mixture in the MICCA combustor for the different operating conditions detailed in Tab. 5.1. The increase in bulk velocity is seen to accelerate the ignition of the burners. More importantly, a large impact of the thermal state of the combustor walls is observed. The *COLD* conditions corresponds to ignition experiments with the initial wall temperature being at the ambient cold temperature. In *PREHEATED* conditions, the combustor is ignited after being operated for a dozen of minutes which let the walls reach their thermalized steady-state temperature. The walls are then hot during these experimental events that correspond to fast relight conditions where the walls do not have time to cool down. In *COLD* conditions, the light-round is seen to last 160% longer than in *PREHEATED* conditions.

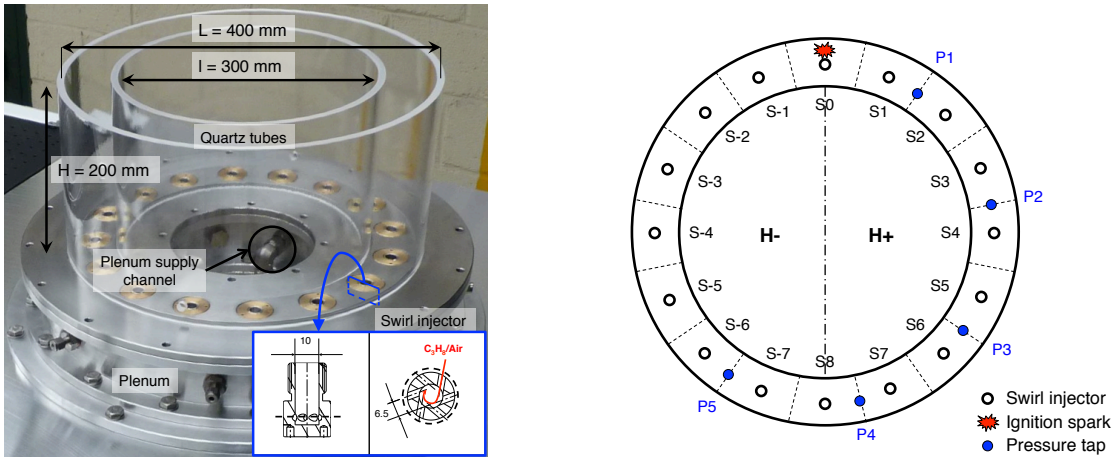

(a) (b)

Figure 5.1: (a) Direct view of the MICCA combustion chamber. The swirler geometry appears as an inset on the right side of this photograph. (b) Schematic top view of the MICCA combustor providing the position of the swirlers, pressure taps and spark plug.

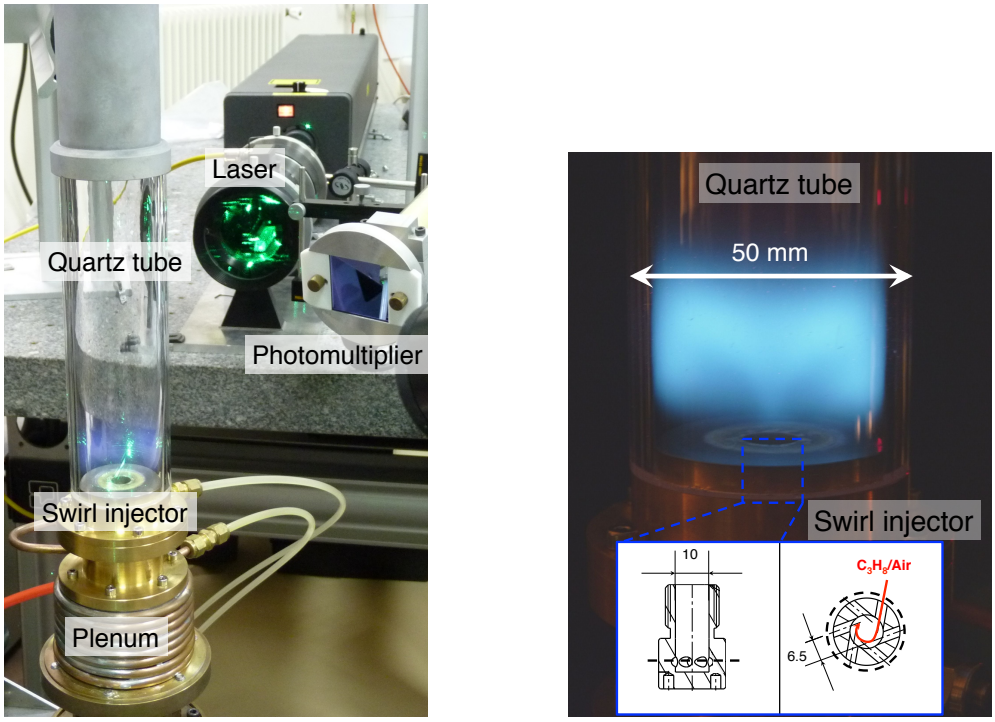

(a) (b)

Figure 5.2: (a) Photograph of the mono-injector with the LDV apparatus; (b) Photograph of the stabilised flame in SICCA.

To compare experimental and numerical results, it is primordial to achieve similar conditions. In this respect, one central issue is the numerical treatment of the boundary conditions. The impact of temperature on the ignition delay is significant as aforementioned. As a first approximation, the choice is made to neglect heat transfer at the walls in the numerical simulation and assume that the walls are adiabatic. In order to match as closely as possible this condition

Table 5.1: Physical parameters for the three operating conditions. The bulk velocity U_{bulk} is based on the inner cross-section area of the swirler injection tube.

Physical parameters	**#1**	**#2**	**#3**
Mass flow rate $\dot{m}_{air}$ [g.s^{-1}]	16.7	23.4	30.1
$\dot{m}_{C_3H_8}$ [g.s^{-1}]	0.81	1.13	1.45
Bulk velocity U_{bulk} [m.s^{-1}]	12.2	17.1	22.0
Thermal power $\mathcal{P}$ [kW]	37	52	67
Injection temperature T_{inj} [K]	298		
Ambient pressure p_{res} [Pa]	101325		
Equivalence ratio ϕ [-]	0.74		
Swirl numberS_N [-]	0.82		

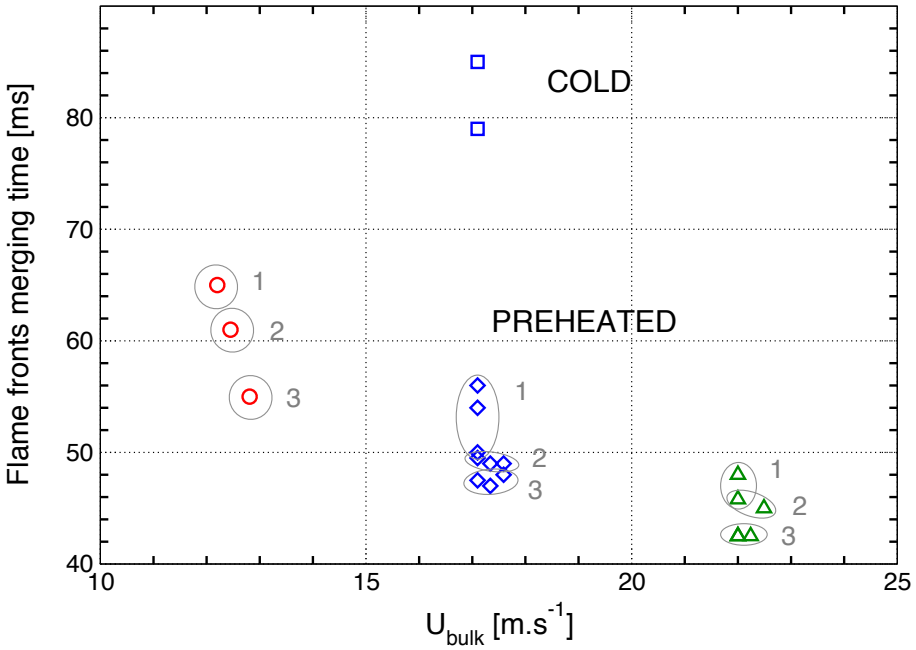

Figure 5.3: Light-round durations, also called merging time, defined as the time taken by both flame fronts issued from the spark plug ignition to travel the whole annular combustion chamber until they meet and merge at the last injector. The numbered ellipses denote the order in which the preheated acquisitions were carried out, showing an asymptotic value of the hot wall conditions.

experimentally, one must reduce the difference in temperature between the burnt gases and the walls. The ignition is then examined under relight *i.e.* *PREHEATED* conditions, when the walls are at a temperature corresponding to the steady-state stabilised flame regime. With such hot walls, heat losses are minimal. In practice, MICCA is first operated for approximately 10 min until the steady-state is reached. Fuel supply is then turned off and immediately turned on again. In practical conditions, ignition is initiated as soon as fuel begins to flow in the chamber. However, the transient ramping of the fuel mass flow rate to the nominal value is not well controlled, and this would complicate comparisons of ignition simulations since the light-round would then occur in an unknown fuel–air mixture. To allow a consistent comparison, the ignition in experiments is initiated once a permanent regime has been reached for the fresh gases mixture in the chamber. In practice, this requires a few seconds, a duration that exceeds the

residence time in the combustor, so that the burnt gases are fully evacuated from the chamber and replaced by the fresh mixture.

5.2.2 Numerical modelling and setup

References: [A12, A14], [T3]

Simulations rely on the AVBP flow solver with TTGC scheme introduced in part I. Sub-grid scale viscosity is provided by the Wall Adapting Local Eddy (WALE) model [168]. The correct mesh resolution in the injector and downstream in the combustion chamber is first verified in LES of the non-reactive flow in the single-injector configuration SICCA. Results are presented in Fig. 5.4 and were shown to vary marginally in a mesh convergence study.

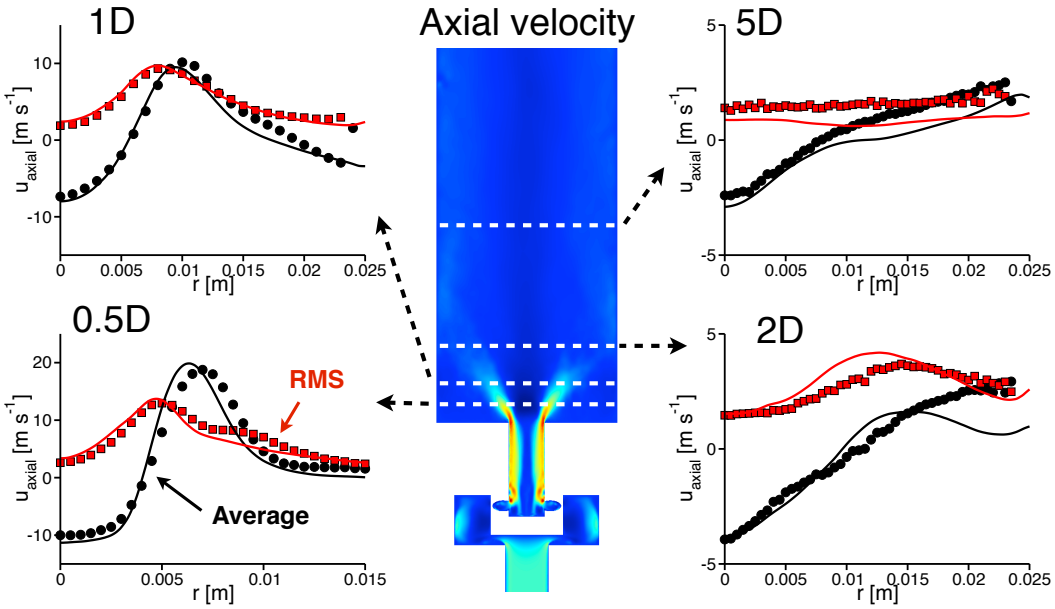

Figure 5.4: Longitudinal cut of the computed mean cold flow in SICCA (center). The curves (left and right) show mean (black) and rms (red) axial velocity profiles from different heights above the injector exit plane ($x = 0.5D$, $1D$, $2D$ et $5D$). Solid lines: numerical results. Symbols: experimental LDV data.

The premixed reactive flow in MICCA is described with the F-TACLES model. 1D premixed flames are computed with a chemical mechanism for propane/air flame [195] for the investigated perfectly premixed conditions. The profiles are then filtered for different filter size to account for the grid non-uniformity, post-treated and assembled in a two-dimensional FTACLES table parametrised by $[\widetilde{c}, \Delta]$. The filtered flame resolution is dynamically controlled setting $\Delta = n_x \Delta_x$ where Δ_x is the cubic root of the local cell volume and $n_x = 5$ is the minimum resolution requirement to properly capture the flame propagation on the grid. Only one scalar transport equation for the progress variable is necessary to describe the turbulent premixed flame. The FTACLES model was implemented in the compressible solver AVBP using the TTC approach. It is combined with a wrinkling function which describes effects of subgrid scale turbulence [34].

The computational domain (Fig. 5.5) exactly corresponds to the MICCA setup, it includes the plenum, swirlers and chamber walls. No slip and adiabatic walls have been chosen for the combustor. The entire mesh has been constructed by replicating seven times a double-sector

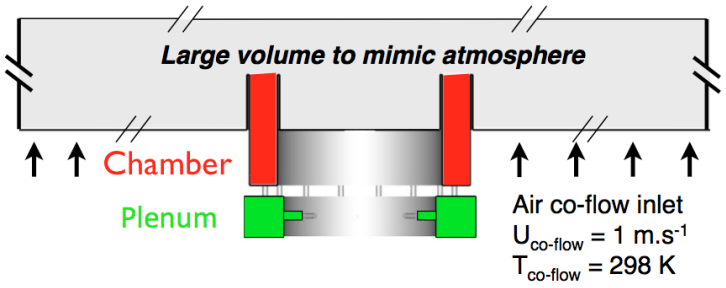

Figure 5.5: Axial slice of the computational domain (in red: the combustion chamber; in green: the plenum). The black arrow symbolises the air co-flow.

grid (Fig. 5.6). The regions of high velocity gradients, turbulence and/or combustion are adequately refined as verified by the separate LES on SICCA. To capture the light-round in the whole annulus, the cell size growth factor has been limited to 2, so that the largest cell at the exit of the chamber is 1 mm. Finally, the number of tetrahedra in the domain is 310 million (corresponding to 55 million nodes). Cases #2 and #3 (see Table 5.1) have been simulated.

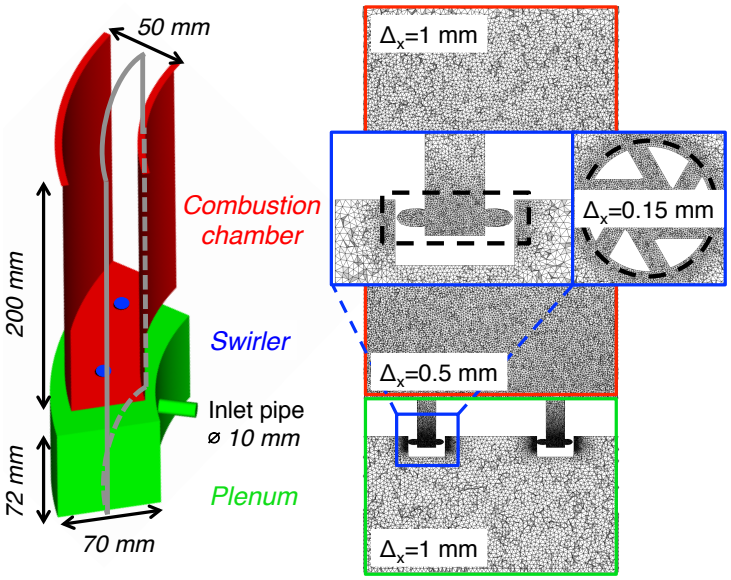

Figure 5.6: A double-sector domain and matching cylindrical mesh slice. Δ_x corresponds to the size of the cell.

The simulation is started on a double-sector geometry, featuring two injectors, by injecting the mixture of propane and air. This is not ignited but serves to establish the turbulent flow delivered by the swirlers. After convergence the result is replicated on the whole domain and the full-scale simulation is continued a little longer to cancel any flow correlation between the sectors. A 3-mm-wide spherical kernel of hot gases is then placed at the exact location of the spark to mimic a successful ignition in phase (1). This initial hot region is rapidly carved up by the flow at the outlet of the swirlers producing an initial flame kernel igniting the first injector. The flame is then conveyed to the neighbouring swirlers and the light-round is in progress.

5.2.3 Simulation results

References: [A13, A14], [C1], [T3]

Results for case #2 are mainly discussed below as results for case #3 are similar.

Flame topology In order to evaluate the simulation fidelity, the computational results are first compared to the experimental images captured from the CMOS camera. The mutual initial time for both experiment and computation was fitted based on a match of their respective ignition of the sector S1 (see Fig. 5.1(b)) which is the burner located after the one where the spark plug is placed. A comparison of various instants of the light-round process in case #2 is carried out in Figs. 5.7 and 5.8. The experimental images show light intensity emitted by the flame during the process of ignition, and represented in false colours on a yellow to red scale to improve visualization. Regarding the numerical snapshots, an iso-surface of the progress variable highlights the flame front, coloured by axial velocity levels. The flow originating from the swirlers are exhibited by an iso-surface of the velocity field.

It appears clearly from the direct comparison carried out in Fig. 5.7 and Fig. 5.8 that the simulation suitably retrieves many of the features observed experimentally. One observes a great similarity between the flame shapes at the largest scales found in the experimental and numerical data. The initial propagation in the form of an arch observed during the first instants of ignition is well obtained. This is followed by two turbulent fronts progressing in clockwise and counter-clockwise directions. The foot of each of these fronts is seen to be ahead of the top during the whole process in both experiment and calculation. The F-TACLES model retrieves a relatively high level of flame surface wrinkling at the smallest resolved scales.

Figure 5.9 compares the time evolution of the normalised values of the numerical integrated heat release and the experimental integrated light intensity. Both signals present fives phases which have been identified in the light-round process:

- (I) During the first instants, the energy provided for ignition generates a small flame kernel, which is rapidly distorted by the flow coming out of the swirl injector. Since the chamber is initially filled with fresh gases, this kernel produces a sudden initial expansion, and as a result the heat release grows sharply,
- (II) The flame brush takes the form of an arch which expands outwards (image (a) in Fig. 5.7) within the height of the combustor, and starts igniting the surrounding injectors. In that phase, the integrated heat release grows nearly linearly until the arch reaches the exit of the chamber,
- (III) The process of light-round progresses with burner-to-burner ignition by the two formed flame fronts at a fairly constant rate between 20 and 50 ms when the two fronts merge (around 50 ms, see image (b) in Fig. 5.8),
- (IV) The remaining fresh gases are burnt, decreasing the heat release, and hot gases are evacuated,
- (V) Finally, the steady state is reached (image (c) in Fig. 5.8) at the nominal power corresponding to the selected injection conditions (52 kW in the present case).

Although the numerical and experimental signals are defined differently, flame light intensity is often considered as a fair indicator of local heat release especially in lean premixed combustion. In that respect, normalised profiles in Fig. 5.9 show a close agreement during phases I, II and

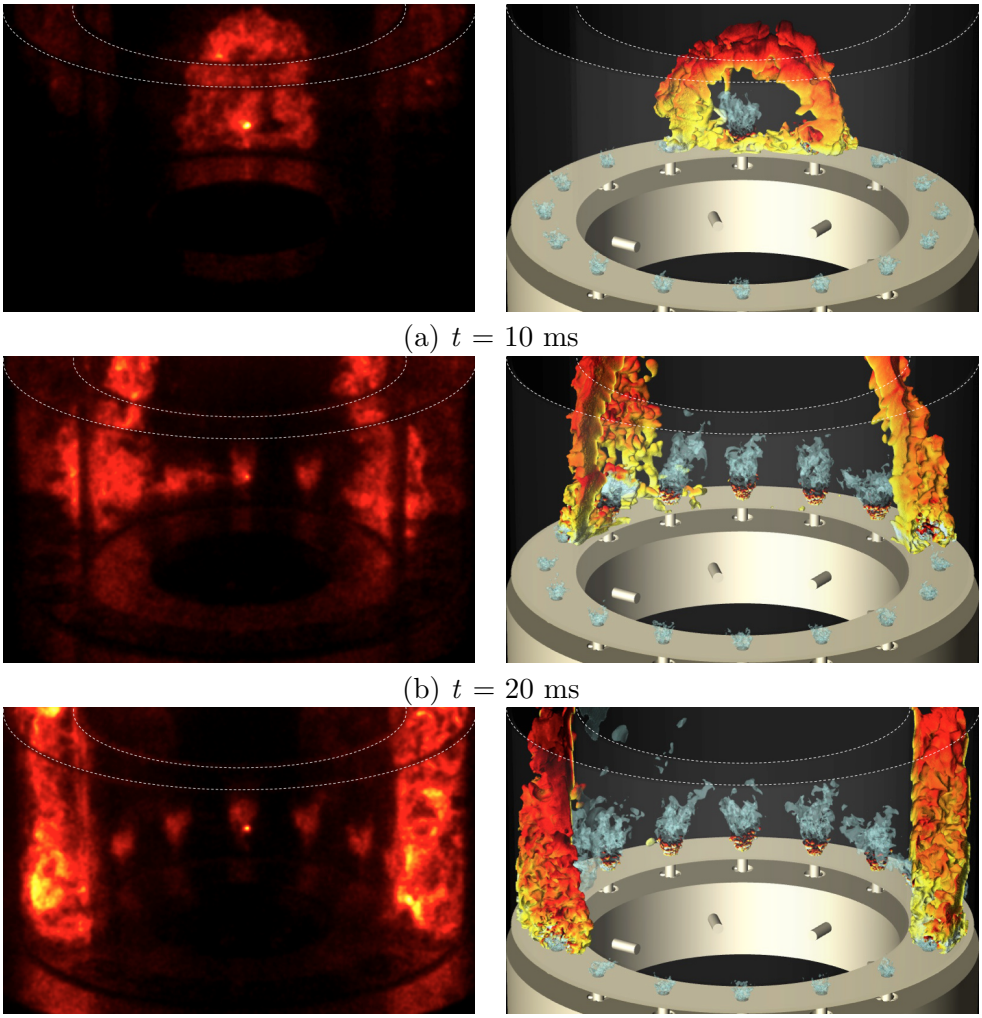

(a) t = 10 ms

(b) t = 20 ms

(c) t = 30 ms

Figure 5.7: Three instants in the ignition sequence, respectively corresponding to t =10 (a), 20 (b) and 30 ms (c) for the operating point #2. Left: experimental visualization in false colours. Right: computation results for the same physical time. The flame front is outlined by an iso-surface of the progress variable c = 0.9, and coloured by the axial velocity (light yellow: -30 m.s^{-1}; black: +15 m.s^{-1}). Blue iso-surfaces correspond to the velocity field U = 25 m.s^{-1}.

III. The light grey area corresponds to the plume of flame outside the chamber (see inset in Fig. 5.9) which is not accounting for in the simulation. The difference between the numerical and the experimental steady state levels can be explained by the light radiated by the flames located in the back, which have a reduced contribution because they are fainted by the quartz tubes and present a smaller apparent surface due to perspective.

Light-round duration and burning velocity Figure 5.10 shows the flame fronts merging time (i.e., the time when the two flame fronts meet) measured for the three experimental conditions mentioned in Table 5.1, as well as the merging time deduced from the simulations in case #2 and case #3. In case #2, a dispersion of 10% is observed, but the major part of the points is around a value of 50 ms. The LES merging time calculated by assuming that the chamber walls are adiabatic closely matches the time taken by the flame to cross the whole annular space

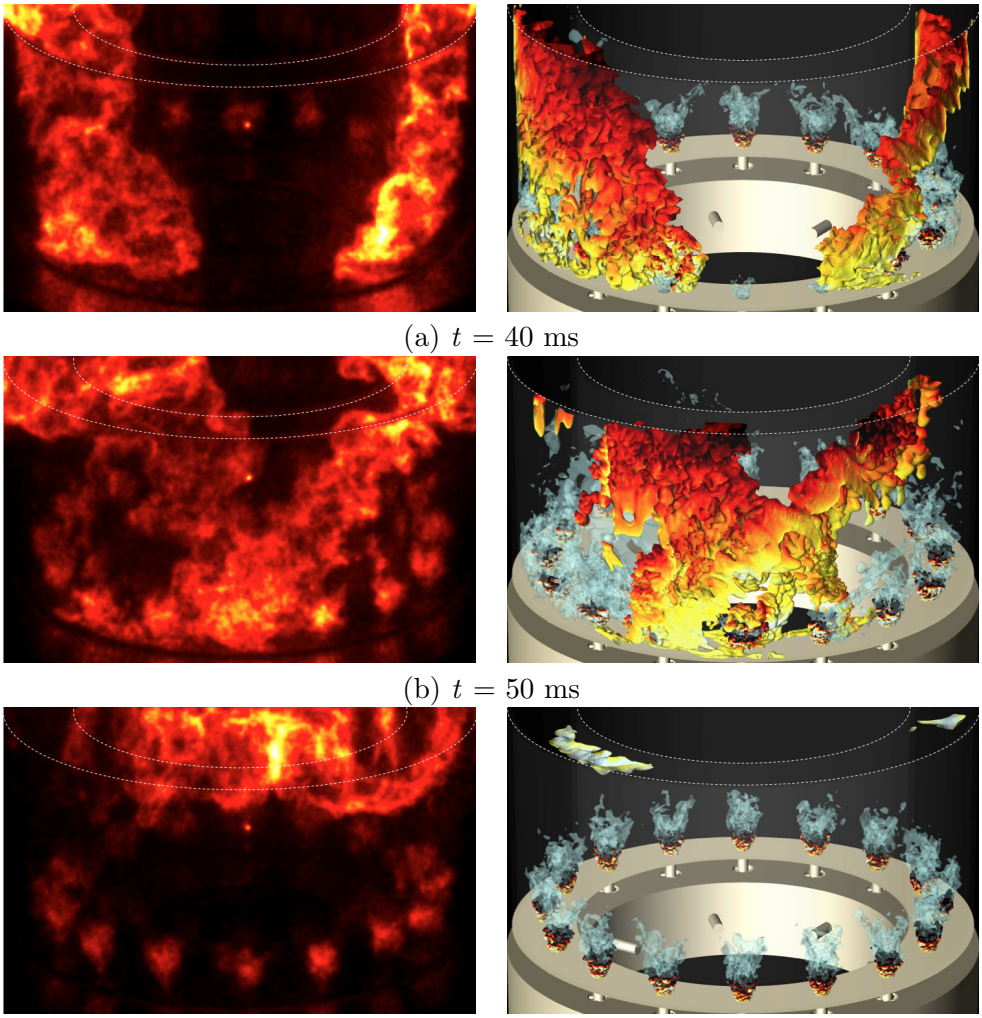

(a) $t = 40$ ms

(b) $t = 50$ ms

(c) $t = 65$ ms

Figure 5.8: Three instants of an ignition sequence, respectively 40 ms (a), 50 ms (b) and 65 ms (c). Same legend as in Fig. 5.7.

obtained under *PREHEATED* conditions for both investigated cases (#2 and #3).

To get a more precise quantification of the transit time of the flame front when it passes by the flow established by the swirl injectors, a sector ignition time is defined as the instant when the sector-averaged heat release reaches its maximum. In the experiment, the transit times are estimated from the CMOS camera snapshots. A comparison between LES and experiment is given in Fig. 5.11. One finds that in both half chambers the transit time is a quasi linear function of the azimuthal angle, corresponding to an absolute propagation velocity of 12 m.s^{-1}. This value is well retrieved in both the experiment and the simulation.

5.2.4 Comparison with TFLES results

References: [A12], [C1], [T3]

The FTACLES computation of the light-round process was compared to another simulation carried out with a 2-step-chemistry-TFLES approach. Both simulations and the experimental

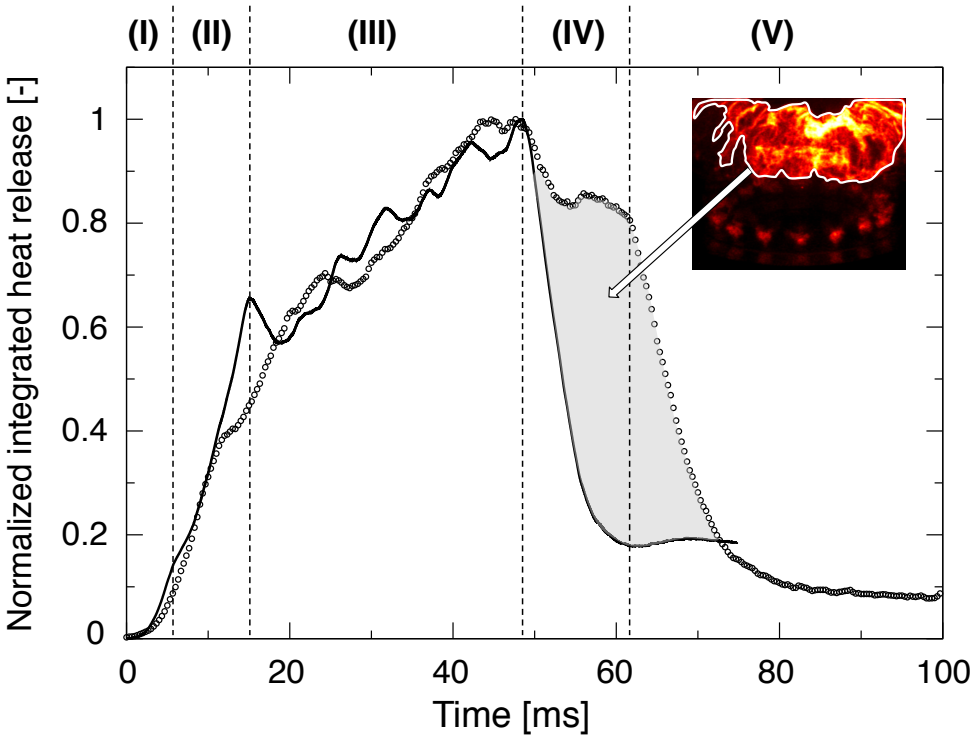

Figure 5.9: Time evolution of the numerical integrated heat release (solid line) and the experimental integrated light intensity (symbols) normalised by their respective maximum. The light grey area corresponds to reacting material outside the chamber, producing additional light intensity in the experiment. This is illustrated in the subfigure appearing as an inset.

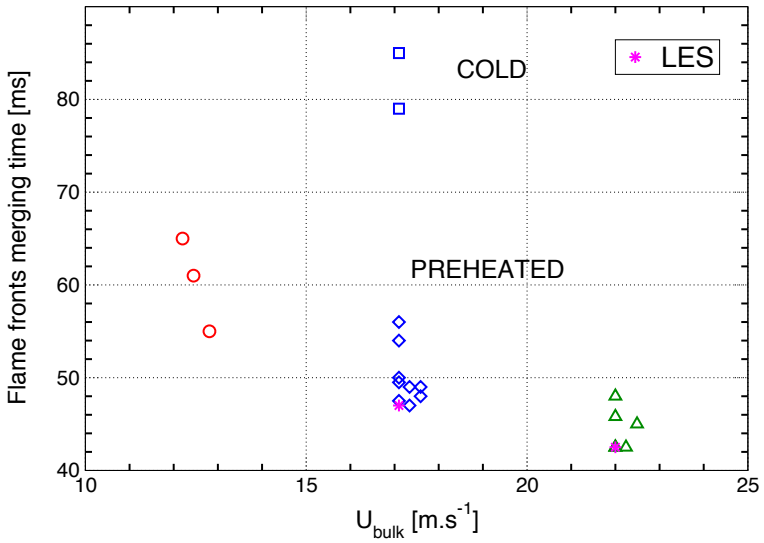

Figure 5.10: Flame fronts merging time as a function of the bulk velocity U_{bulk}. Red (case #1), blue (case #2) and green (case #3) symbols represent experimental data at three various conditions. The magenta stars stand for the time obtained from the LES calculations (case #2 and case #3).

observations are shown in Fig. 5.12 and exhibit remarkable similarities. The flame obtained by TFLES is slightly faster, different instants are then considered to highlight the similar topology

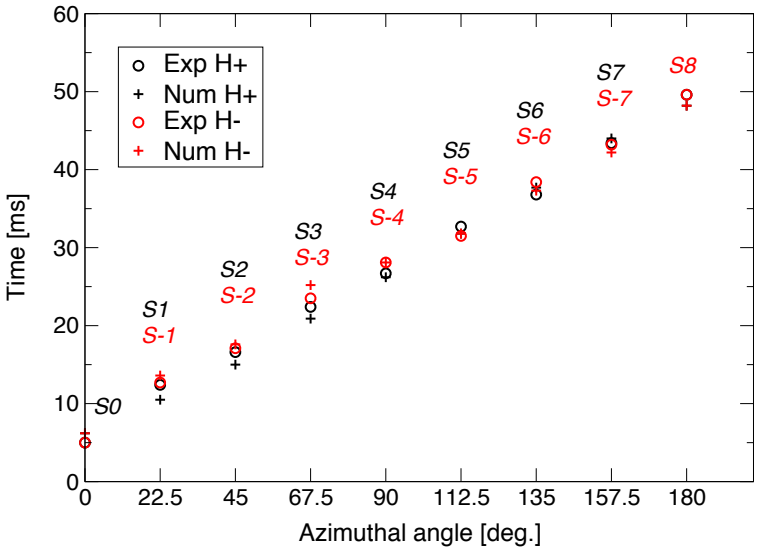

Figure 5.11: Transit time of the flame fronts as a function of azimuthal angle. Circle and plus symbols represent experimental and numerical times, respectively; black and red colours stand for H+ and H-, respectively (see Fig. 5.1(b) for designation of the sectors).

of the flames during their ignition sequence. Indeed, the flame shapes at the largest scales are well reproduced by the two combustion models, and the five phases can be clearly recognised in the process of ignition: Phase (I) The deposit of energy produces a little flame kernel in the first instants that expands rapidly in the fresh propane/air mixture; Phase (II) The flame front propagates to the surrounding burners in the form of an arch. The arch opens up as soon as it reaches the exit of the chamber; Phase (III) A two-front propagation takes over, leading to a burner-to-burner propagation; Phase (IV) The two flame fronts join and merge on the injector opposite the ignition sector; Phase (V) The burnt gases evacuate the chamber and the steady state is reached. For each phase, the shape of the flame front is in very good agreement: the wrinkled ball in phase (I), the arch shape in phase (II), the large oblique front in phase (III) and the front merging starting at the chamber bottom in phase (V) are all very similar for F-TACLES, TFLES and the experiment.

The TFLES computation also showed very good agreement in terms of total heat release. The sector ignition times highlights that the TFLES case features a flame that propagates a little slower than the FTACLES case. This could be the result of the different modelling choices or more simply an inherent variability in the predicted light-round duration. Finally, the resolved flame front calculated by F-TACLES appears more wrinkled than for TFLES. This could be due to the different nature of both models and their different response to turbulent perturbations as the preliminary study by Auzillon et al. [A18] suggests.

To conclude, such simulations of the third phase of the ignition process in a gas turbine have provided a unique comparison with experimental data in a full annular combustion chamber with premixed gaseous injection. The next section presents the extension of this work to liquid fuel injection.

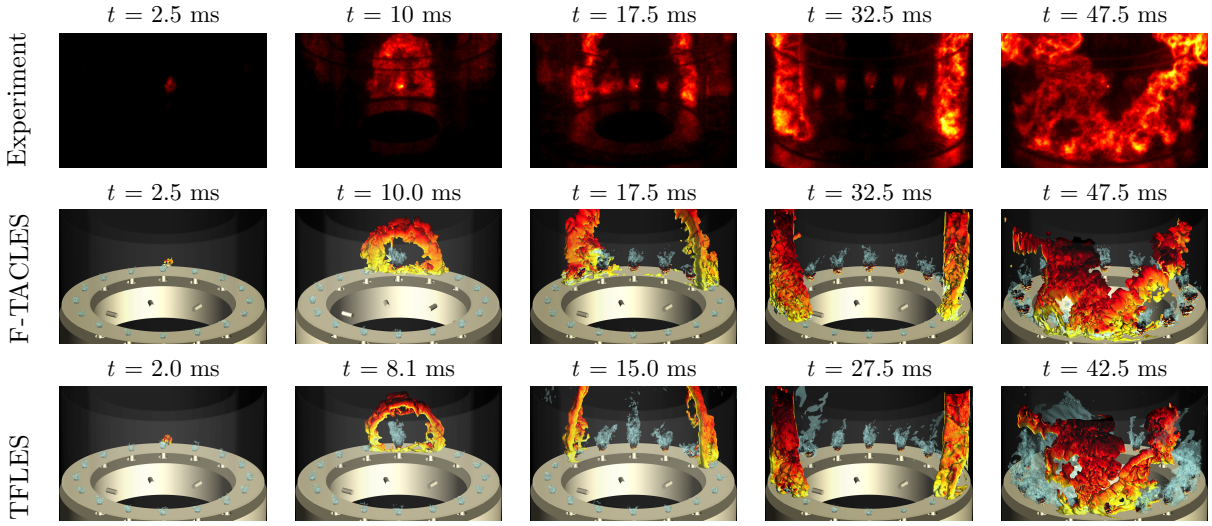

Figure 5.12: Five instants in an ignition sequence of the MICCA chamber. Top: Experimental images showing light intensity emitted by the flame during the light-round process, and represented in false colours to improve visualization. Middle and bottom: Respectively F-TACLES and TFLES simulations. Flame fronts are represented by an isosurface of progress variable c=0.9 for F-TACLES corresponding to an isosurface of temperature T= 1781 K for TFLES.

5.3 Simulations of light-round with liquid fuel injection

5.3.1 Presentation of the MICCA-spray combustor

The MICCA-Spray set-up (Fig. 5.13) is a modified MICCA combustor to study the impact of liquid sprays on the flame in the annular combustion chamber [192]. It is composed of sixteen swirled injectors placed in the backplane of an annular chamber made of two cylindrical coaxial quartz walls. These injectors are fed with air and liquid n-heptane. The air is injected at ambient temperature into an annular plenum by eight identical channels and then into the chamber through the sixteen injectors. The fuel is fed to sixteen simplex atomisers placed after the swirlers (see the sketch in Fig. 5.13) and positioned with a 6 mm recess with respect to the chamber backplane. The measured swirl number is 0.68.

As in purely gaseous conditions, a companion mono-injector setup SICCA-Spray allows for characterising the two-phase reactive flow for an individual flame. Section 4.3.1 previously presented several elements of the simulation of this setup.

Prieur et al. [192] studied the light-round in MICCA-Spray and reported several light-round durations for several types of fuel (see Fig. 5.14). As in gaseous conditions, a large sensitivity was noticed in respect to the thermal state of the wall combustors.

In the present study, n-heptane cases with three operating points are considered, for three different global equivalent ratios, $\Phi = 0.8$, $\Phi = 0.89$ and $\Phi = 1.0$, which are summarised in Table 5.2. In Sec. 4.3.1, the study carried out on the single burner SICCA-Spray has enabled to select an optimal value for the injected diameter for the case $\Phi = 0.89$. In order to keep these conclusions as relevant as possible for the other two cases, the choice was made to vary the equivalence ratio for a constant combustor power $\mathcal{P} = 79.3$ kW. The liquid fuel flowrate is therefore kept identical while the air flowrate is modified. The assumption is made that in that way, the droplet size distribution does not vary significantly between the operating points, so

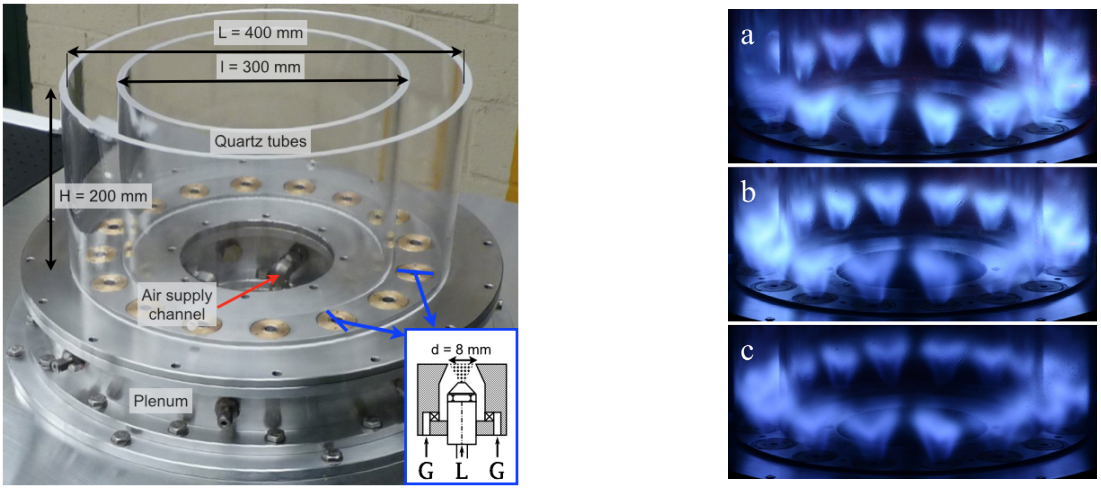

Figure 5.13: Left: Direct view of the MICCA-Spray combustion chamber; the sketch at the bottom right represents a cut of the swirler unit showing the gaseous (G arrows) and liquid (L arrow) injection. Right: Photograph of the annular chamber with different types of injection: (a) premixed propane and air, (b) n-heptane spray and air, (c) dodecane spray and air. Extracted from [192].

that the same value of the injected diameter can be used in all three simulations.

5.3.2 Numerical modelling and setup

References: [A8], [T5]

Simulations are carried out with the AVBP code with the TTGC scheme for both gaseous and liquid phases. The liquid phase is modelled using an Eulerian mono-disperse approach. The evaporation of the uniform temperature droplets is described by the Abramzon-Sirignano (AS) model [1]. Later, two variations of the AS evaporation model will be distinguished, the *simplified* version, which was originally used for the first $\Phi = 0.89$ simulation and the *complex* version, used for a second simulation of case $\Phi = 0.89$ as well as for the $\Phi = 0.8$ and $\Phi = 1.0$ cases. The *simplified* and *complex* versions differ in their estimation of film dynamic viscosity and thermal

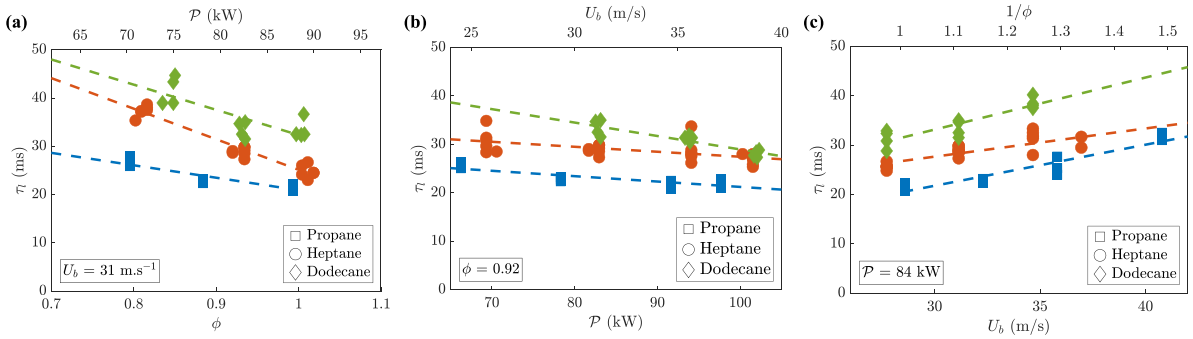

Figure 5.14: Light-round durations τ_l when: (a) the bulk velocity U_b, (b) the equivalence ratio Φ or (c) the power $\mathcal{P}$ is kept constant for multiple fuels: propane (gaseous), n-heptane (liquid spray) and dodecane (liquid spray). Linear fits in dashed lines give the general trend for the different fuels. Extracted from [192].

Table 5.2: Summary of the considered operating points with liquid n-heptane injection in MICCA-Spray.

Equivalence Ratio		0.8	0.89	1.0
Liq. fuel flowrate	$[g.s^{-1}]$	1.778	1.778	1.778
Air flowrate	$[g.s^{-1}]$	33.57	30.19	26.85

conductivity in the expression of the Abramzon-Sirignano evaporation model.

The n-heptane chemistry is described using the two-step mechanism described in [178, 209]. The large eddy simulation combustion model describing the unresolved small scale flame structures, the propagation of the flame and its interaction with turbulence relies here on the TFLES model. It is used in combination with the efficiency function derived in [34]. The only adaptation of the TFLES model, initially derived for gaseous premixed flames, to describe spray flames is the application of the thickening to the evaporation source terms, as recommended by [19]. This choice of combustion modelling will allow for investigating the adequacy of such a robust set-up before considering more advanced models in the future.

As done in fully gaseous conditions, ignition is triggered with the flow in its permanent regime. The steady-state flow is then first computed on the bisector-configuration, before being duplicated in the annular geometry. The full mesh for MICCA-Spray is composed of 290 million tetrahedra and 51 million nodes. Finally, *PREHEATED* relight conditions are approximated by adiabatic boundary conditions.

The computation of converged fields on the bisector configuration revealed a long transient time to stabilise the injected inhomogeneous mixture. Simulations were interrupted at approximatively 1 s of physical time when the mean gaseous equivalence ratio in the chamber reached 95% of its estimated final value. Instantaneous snapshots of these converged bi-sector solutions are displayed in Fig. 5.15 where slices at $r = 175$ mm are coloured by the liquid density $\alpha_l \rho_l$ and the local gaseous equivalence ratio Φ_{gas}. The liquid density fields show that for $\Phi = 0.8$ and $\Phi = 0.89$, the n-heptane is fully prevaporised before the chamber's exit and no liquid remains in the upper half of the chamber. Logically, the local gaseous equivalence ratio is higher for $\Phi = 0.89$ than for $\Phi = 0.8$. For case $\Phi = 1.0$ however, a saturated state is reached and some liquid remains everywhere in the chamber.

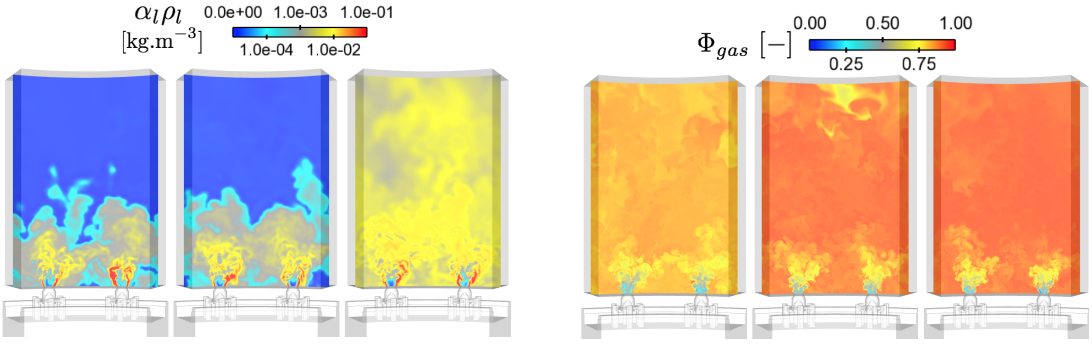

(a) (b)

Figure 5.15: Visualisation of the instantaneous liquid density $\alpha_l \rho_l$ (a) and local gaseous equivalence ratio Φ_{gas} (b) on a slice at $r = 175$ mm for cases $\Phi = 0.8$ (left one), $\Phi = 0.89$ (middle one) and $\Phi = 1.0$ (right one), on a solution at 95% of the estimated final state.

The mean velocity fields in Fig. 5.16 show that the identical orientation of swirler units makes the flow in the chamber not axi-symmetrical around their respective injector's axis, but rather inclined in the same tangential direction, indicating that a mean clockwise tangential flow is present in the annulus as suspected in [21].

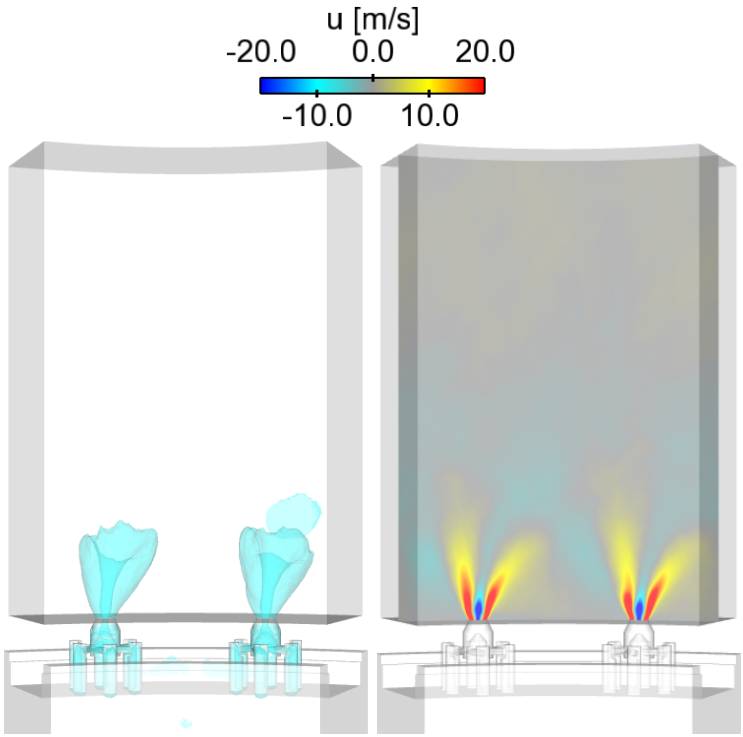

Figure 5.16: Fields extracted from a solution averaged over $\Delta t = 0.12$ s for case $\Phi = 0.89$. Left: iso-surface of the axial velocity $u = 5$ m.s^{-1}. Right: Slice at $r = 175$ mm coloured by the axial velocity u.

5.3.3 Simulation results

References: [A8], [T5]

Light-round durations The simulations of the light-round sequences were carried out over physical times of 50 to 60 ms, depending on the merging delay. The light-round durations give a first global metric of the quality of the numerical results. The experimental and numerical values for the light-round durations are shown in Fig. 5.17. The experimental data points are plotted as blue diamond symbols while the red dots stand for the three simulations. Very good results are achieved for cases $\Phi = 0.89$, for which the predicted duration falls in the experimental scatter of points, and $\Phi = 0.8$, where the duration is overestimated by 5%, which remains acceptable. However, the relative error of 30% in the $\Phi = 1.0$ simulation indicates that this calculation is less adequate. One explanation could be the presence of locally rich conditions at the leading point, which is discussed later. The light-round duration predicted for case $\Phi = 0.89$ with the *simplified* evaporation model is marked as a green square and exhibits a 10% error, indicating that the model that accounts for the local species composition in the evaporation law is indeed necessary to capture the flame propagation velocity.

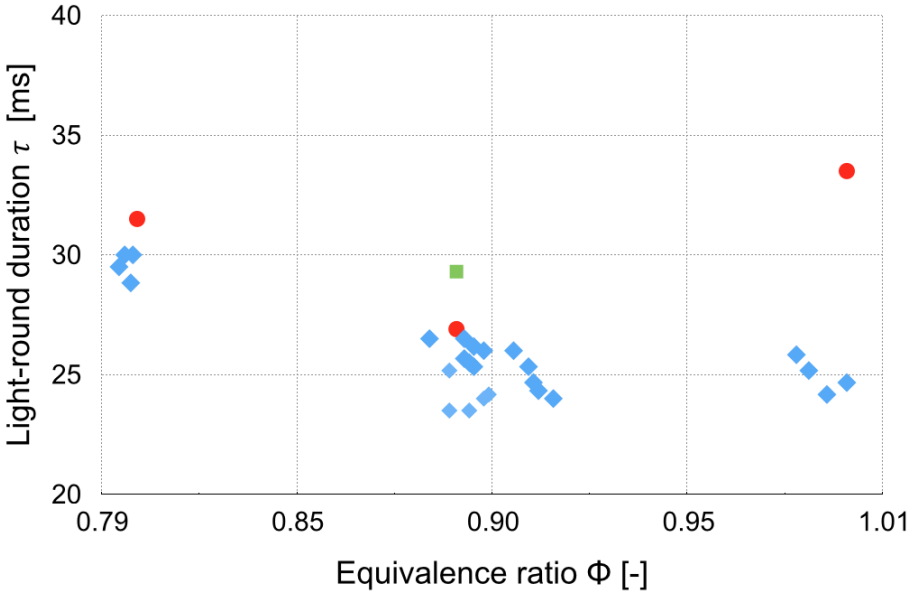

Figure 5.17: Light-round durations as a function of the global injected equivalence ratio. Diamond symbols stand for experimental results. The durations predicted by the simulations are represented by red circles. The green square indicates the light-round simulated before fixing the evaporation model.

Flame topology The experimental images of the propagating flame front are represented on a scale of colours from yellow to red for better clarity. To be able to draw comparisons, an iso-surface of the progress variable $c = 0.9$[†], defined as:

$$c = \frac{Y_{CO_2} + Y_{CO}}{Y^{eq}_{CO_2} + Y^{eq}_{CO}}, \tag{5.1}$$

is used in the numerical simulations to represent the flame front. This iso-surface is coloured by the axial gaseous velocity, from -10 m.s^{-1} in yellow to 25 m.s^{-1} in black. For better visualization, iso-surfaces of the axial gaseous velocity are added.

Figure 5.18 displays comparisons between the experimental and numerical evolutions of the flame fronts for the case $\Phi = 0.89$. Similarly to what was done for the global durations, experimental images and numerical visualisations are synchronised using the first burner ignition as reference. Figure 5.18 shows that the evolution of the flame in the simulation is in very good agreement with that of the experiment, up to the merging point. Similar agreement is seen for case $\Phi = 0.8$. However, in case $\Phi = 1.0$, presented in Fig. 5.19, as soon as the flame reaches the exit of the chamber and two separate fronts are formed, a steadily increasing delay appears between the experiment and the simulation, leading to the observed difference in the light-round duration.

Regardless of the propagation velocities, all snapshot series indicate that the simulation is able to reproduce the different stages of the ignition of MICCA-Spray. As in the previous gaseous studies, the five identified phases (I), (II), (III), (IV) and (V), can be identified in the experimental and numerical images. This agreement shows the ability of the simulation to predict the flame propagation behaviour during a successful ignition sequence.

[†]This value for the progress variable was chosen because it is close to the maximum value of the reaction rate in the Arrhenius law. The impact of the selected value fro the progress variable on the flame front shape and behaviour was investigated and showed no significant differences.

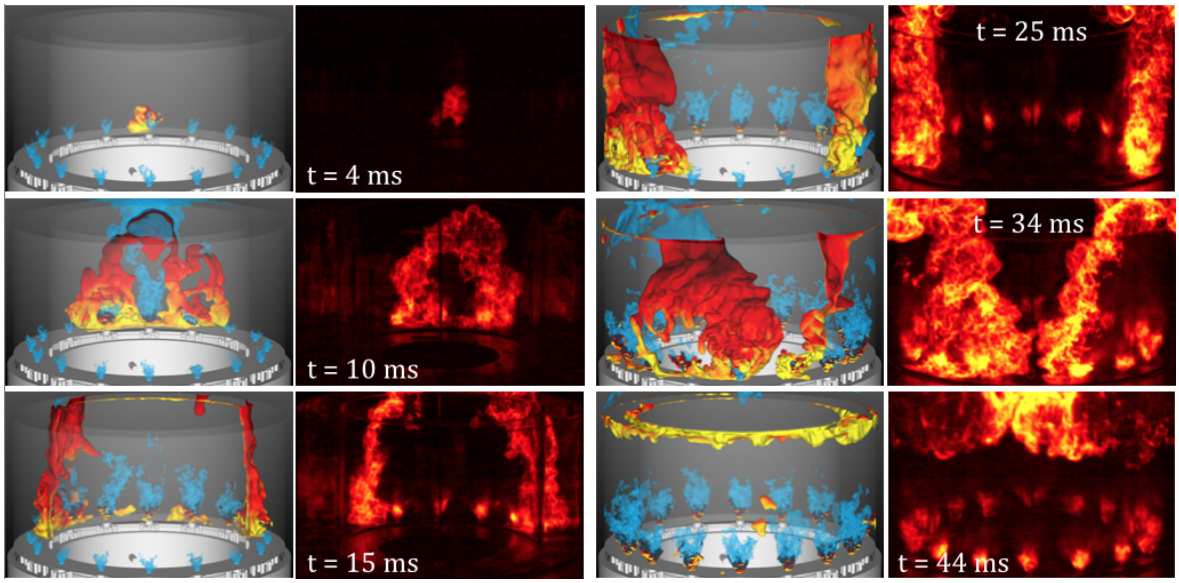

Figure 5.18: Comparison between experimental and numerical flame configurations at six instants during the light-round sequence for case $\Phi = 0.89$, $t = 4$ ms (top left), $t = 10$ ms (middle left), $t = 15$ ms (bottom left), $t = 25$ ms (top right), $t = 34$ ms (middle right) and $t = 44$ ms (bottom right).

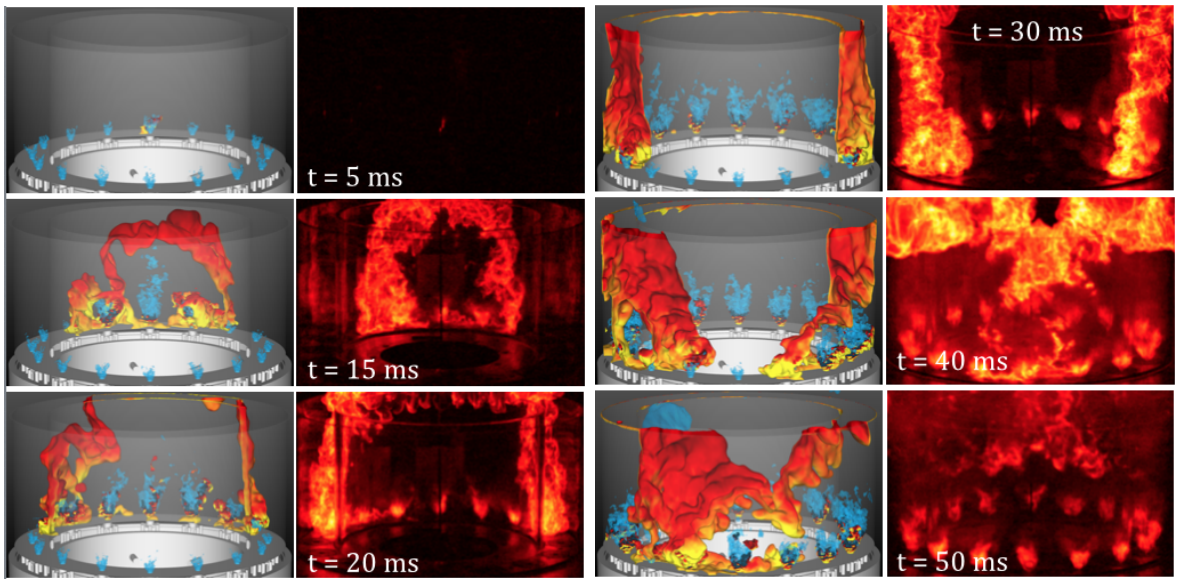

Figure 5.19: Comparison between experimental and numerical flame configurations at six instants during the light-round sequence for case $\Phi = 1.0$, $t = 5$ ms (top left), $t = 15$ ms (middle left), $t = 20$ ms (bottom left), $t = 30$ ms (top right), $t = 40$ ms (middle right) and $t = 50$ ms (bottom right).

Flame passage times Another assessment of the simulation consists in comparing durations between the ignition of two consecutive burners. As used previously, the maximum of heat release rate in a sector can also be used as an indicator of its ignition. An additional metric is here considered with the passage time of the flame leading-point. In the experiment, photo-multipliers (PM) placed in front of each injector on the H- side measure the evolution of the light intensity around them, and the maximum of the signal gives an estimation of the experimental ignition

times. For each operating point, two or three sets of measurements are plotted in Fig. 5.20 as symbols, each colour standing for one set of measurements, highlighting some variability in the experimental results. As was done for the global light-round duration, the numerical and experimental results are synchronised with respect to the ignition of the first sector (S_1 or S_{-1}), that sets the origin of times.

Figure 5.20 first show the consistency between the data extracted from the leading-point and from the sector-integrated heat release, which is a more global measure. Cases $\Phi = 0.8$ (Fig. 5.20 left) and $\Phi = 0.89$ (Fig. 5.20 center) show an excellent agreement between experiment and simulation. Both H+ and H- evolutions are close to that of the experimental sequences, indicating that the accuracy observed in the global light-round duration is linked to the ability of the simulation to capture the flame propagation velocity. On the H+ side of case $\Phi = 0.8$, the plot shows that the flame front slows down between sectors S_6 and S_7, indicating that the 5% difference observed in the light-round duration is due to a deceleration of one of the flame fronts towards the end of the sequence, when the two fronts collide head on and the flow is notably modified by the flame. Finally, the plot on the right in Fig. 5.20 allows for identifying the source of light-round duration error for the case $\Phi = 1.0$. The simulation systematically overestimates the ignition delay between sectors for both sides of the chamber, leading to a gradually increasing error in ignition time. Contrarily to the previous case, the error does not arise towards the end of the sequence, but is formed by an accumulation throughout the simulation, indicating that the propagation mechanisms are less well captured under these conditions.

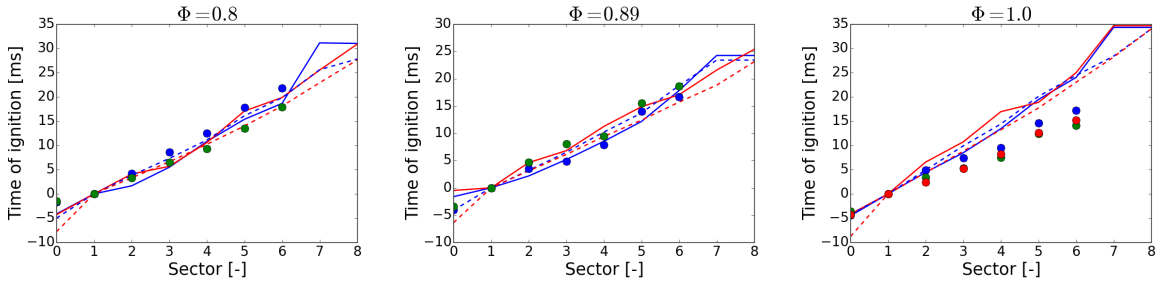

Figure 5.20: Comparison of sectors ignition times for cases $\Phi = 0.8$ (left), $\Phi = 0.89$ (center) and $\Phi = 1.0$ (right), in the simulation for H+: −: from sector-integrated heat release, −−: from the leading point position, for H-: −: from sector-integrated heat release, −−: from the leading point position, ●●: Experimental measurements on the H- side of the chamber, each colour stands for a different sequence. The origin of times is set for all sequences at the instant of ignition of sector S_1 (or S_{-1}).

The consistency between leading-point passage times and ignition delays determined by the more global sector-integrated heat release shows that the leading-point position can be used as an indicator of the flame progress in the chamber and that its evolution is strongly linked to the evolution of the amount of reaction in the chamber. This confirms that one possible scenario for the flame propagation involves the leading-point entraining the turbulent flame brush. Indeed, the average value of the leading point absolute tangential velocity during the fronts propagation in case $\Phi = 0.89$, approximately $v_\theta^{lp,mean} \approx 16$ m.s^{-1}, is consistent with the values obtained from by the PIV algorithms on the experimental images, as shown in Fig. 5.21. Propagation scenarios are detailed in Sec. 5.5.1. Before, additional features of the flow during light-round are outlined in the next section.

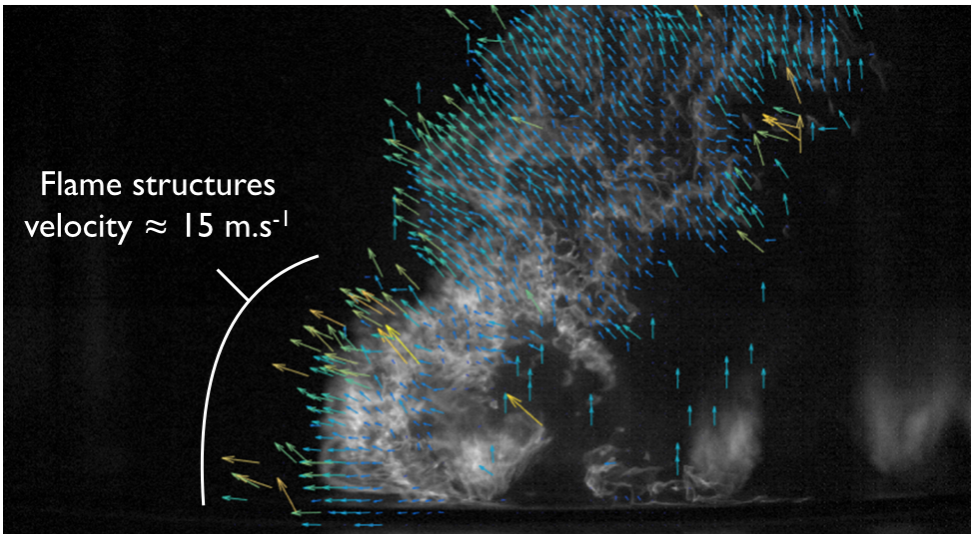

Figure 5.21: Instantaneous snapshot of the propagating flame in MICCA-Spray for a case with preheated walls at $\Phi = 0.89$. The camera is positioned behind sector S_4. The flame front propagates from right to left. Extracted from [193].

5.4 Analysis of light-round simulations

5.4.1 Flame surfaces in premixed case #2

References: [A12], [T3]

Different flame surface areas can be defined. The resolved flame surface in LES is defined as

$$A_{res}(t) = \int_{V_{cc}} |\nabla \widetilde{c}| \mathrm{d}V, \tag{5.2}$$

where $|\nabla \widetilde{c}|$ is the resolved flame surface density [232]. The subgrid-scale (sgs) and total flame surface areas are defined from the subfilter wrinkling factor Ξ_Δ:

$$A_{sgs}(t) = \int_{V_{cc}} (\Xi_\Delta - 1) \, |\nabla \widetilde{c}| \mathrm{d}V, \tag{5.3}$$

$$A_{tot}(t) = A_{res}(t) + A_{sgs}(t) = \int_{V_{cc}} \Xi_\Delta |\nabla \widetilde{c}| \mathrm{d}V = \int_{V_{cc}} \Sigma \mathrm{d}V, \tag{5.4}$$

where Σ is the total flame surface density [28, 232]. The different surface areas are plotted in Fig. 5.22(b).

The total surface has an evolution very similar to the one of integrated heat release (Fig. 5.9). This is expected as both quantities are usually assumed proportional [27, 232]. The similarity of the different flame surface profiles indicates that the subgrid-scale wrinkling factor must be somehow constant. This is verified by considering the resolved-surface average of Ξ_Δ defined as

$$\{\Xi_\Delta\}_{res} = \frac{\int_{V_{cc}} \Xi_\Delta |\nabla \widetilde{c}| \mathrm{d}V}{\int_{V_{cc}} |\nabla \widetilde{c}| \mathrm{d}V} = \frac{A_{tot}}{A_{res}}. \tag{5.5}$$

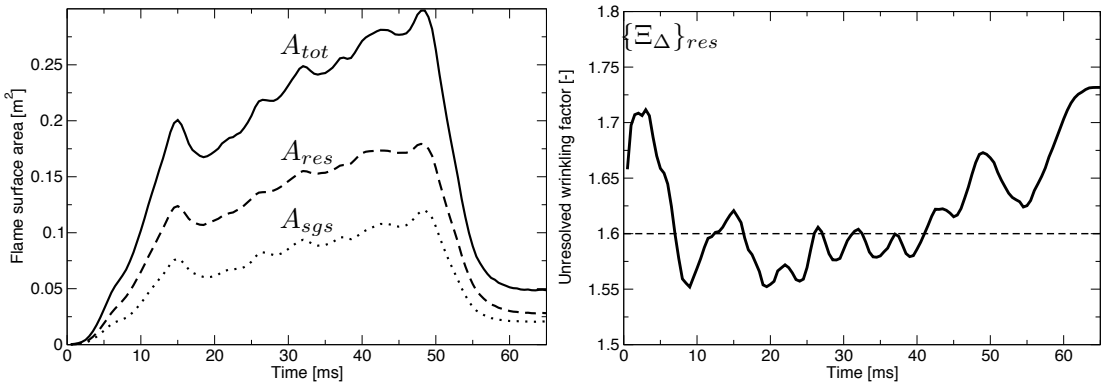

(a) (b)

Figure 5.22: (a) Temporal evolution of resolved (dashed line), subgrid-scale (dotted line) and total (plain line) flame surface areas. (b) Temporal evolution of the average subgrid-scale wrinkling factor $\{\Xi_\Delta\}$.

This quantity is shown in Fig. 5.22(b): it remains indeed constant around 1.6. This value indicates that 60% of the flame surface is predicted by the model for the subfilter wrinkling factor. The subgrid model has then a first-order impact on the LES results, highlighting its importance.

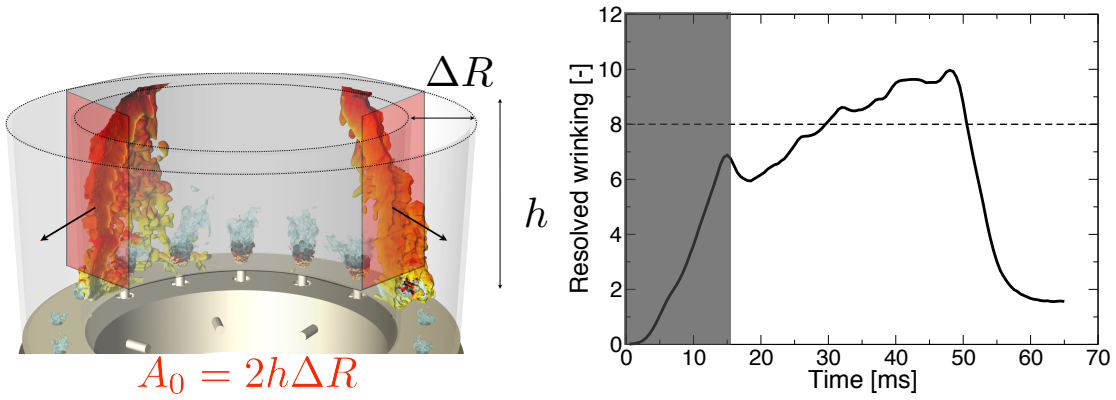

(a) (b)

Figure 5.23: (a) Definition of the reference surface A_0 ; (b) Temporal evolution of the resolved wrinkling factor Ξ_{res}. The grey area corresponds to phases (I) and (II) where the flame fronts cannot be assumed as two vertical planes.

The resolved flame wrinkling is estimated as the ratio

$$\Xi_{res} = \frac{A_{res}}{A_0}, \tag{5.6}$$

where A_0 is a reference surface taken as two vertical planes shown in Fig. 5.23(a) which schematically represent the mean flame fronts during phase (III) of the light-round. The evolution of Ξ_{res} shown in Fig. 5.23(b) is obviously similar to A_{res}. During phase (III) in the non-grey area of the plot, the resolved flame wrinkling factor takes ranges from 6 to 10. A global mean value is $\Xi_{res} = 8$, which outlines the level of resolved flame front in this detailed LES combined with the F-TACLES model.

The total flame wrinkling factor $\Xi_{tot} = \{\Xi_\Delta\}_{res}\,\Xi_{res}$ is approximatively $1.6 \times 8 \approx 13$. In case #2, the laminar burning velocity is $S_l^0 = 0.24$ m/s. The total turbulent consumption speed is then $S_c^T = \Xi_{tot} S_l^0 \approx 3.1$ m/s. This value is far from the reported flame propagation speed of 12 m/s. This shows that additional mechanisms are at play, notably the effect of the volumetric expansion of burnt gases detailed in the next section.

5.4.2 Flow induced by the volumetric expansion of burnt gases

References: [A8, A3], [T3, T5]

In order to observe the evolution of the flow field during the light-round, it is convenient to take cylindrical cuts of the chamber at a given radius r^{cut} and to unfold it as shown in Fig. 5.24 for better visualisation.

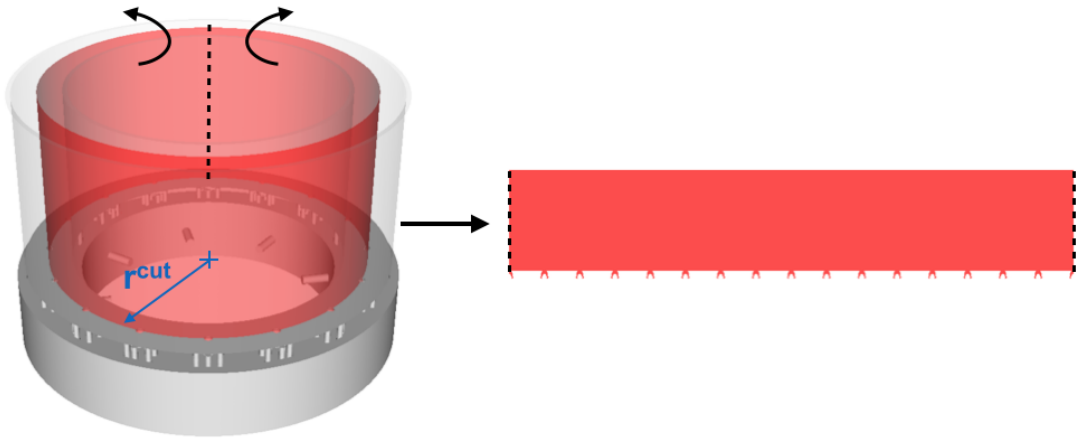

Figure 5.24: Schematic description of the unfolded surface for a given radius r^{cut}. The cylindrical cut is divided at sector S_0 and unfolded as shown.

The burnt gases volumetric expansion has a great impact on the axial velocity, which can be observed in Fig. 5.25 for the premixed case #2. The defined cylindrical developed cuts are coloured by the axial gaseous velocity. On the top image, at t = 0 ms, the cold flow axial velocity can be observed and typical multi-injector swirling flow features can be identified: a strong central recirculation zone (CRZ) is present above each injector, surrounded by two very intense positive velocity branches that correspond to the hollow cones generated by the swirlers; between two injectors, a negative velocity region is present, corresponding to the outer recirculation zone (ORZ); it is less intense but much wider and expands up to the middle of the chamber. Once the kernel starts to propagate, at t = 5 ms and then t = 15 ms, the axial velocity field is modified. The stabilisation of a flame around the injector in S0 generates burnt gases that are accelerated and push the arch-like front upwards. The fresh mixture above the arch is therefore propelled towards the outlet of the chamber, hence the positive values that appear. At first, the axial velocity in the rest of the chamber is not affected. During the two flame fronts propagation, at t = 15 ms or t = 30 ms, the flow is logically strongly accelerated above the ignited burners, but fresh gases are also entrained towards the outlet and the velocity field is globally positive everywhere in the chamber. Once the flame fronts have merged and all the fresh gases have been consumed, the velocity field relaxes towards its ignited steady-state. Due to combustion, the velocity peaks around each injector are much more intense than in the cold configuration. The CRZ is still present and the ORZ that had disappeared during the light-round sequence is back with a greater magnitude than before the ignition.

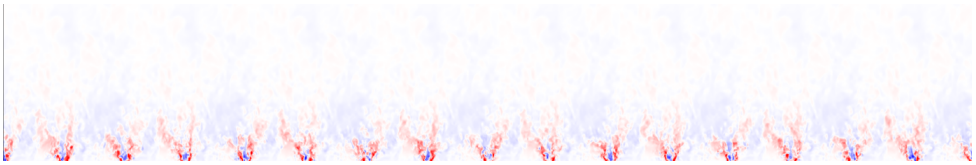

(a) $t = 0$ ms

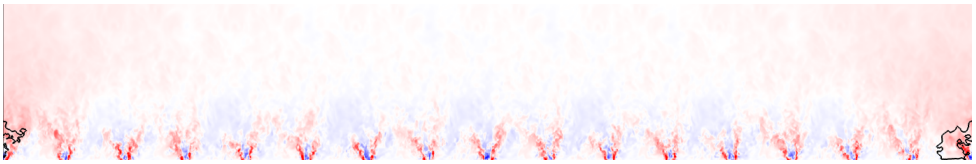

(b) $t = 5$ ms

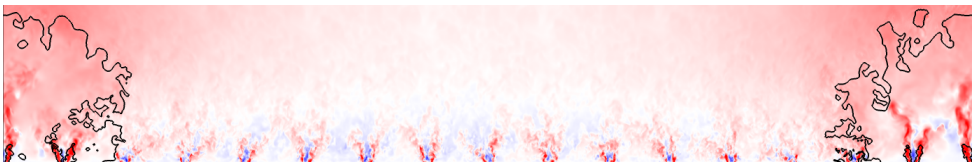

(c) $t = 15$ ms

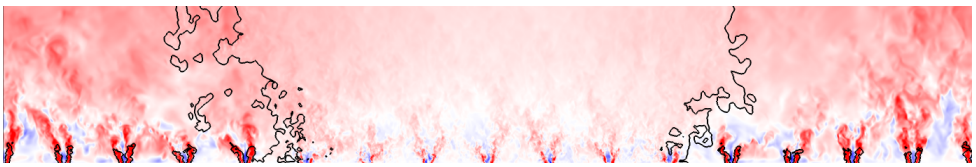

(d) $t = 30$ ms

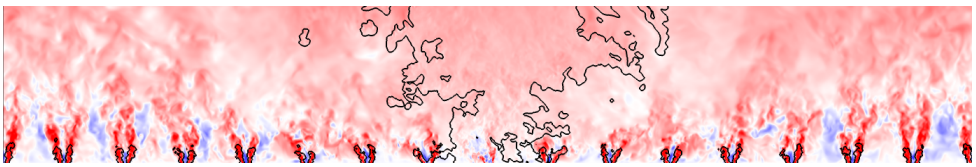

(e) $t = 45$ ms

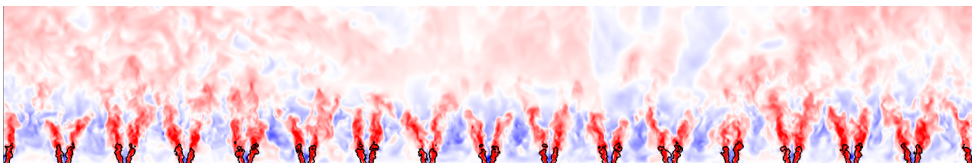

(f) $t = 60$ ms

Figure 5.25: Cylindrical cut of the MICCA chamber (premixed case #2) coloured by the axial velocity u_x (blue: -30 m.s^{-1} ; white: null ; red: +30 m.s^{-1}). The flame front is indicated by the black isoline of progress variable.

Figure 5.26 shows the developed cylindrical cut coloured by the azimutal velocity in the chamber for the premixed case #2. The azimuthal velocity is counted positive (red colour) from left to right.

At t = 0 ms, a sphere of burnt gases is inserted into a converged cold flow. The swirling motion generated by each injector is apparent and the tangential velocity in the chamber is mostly negative due to the global rotative flow that was evidenced on the bisector previously. At t =

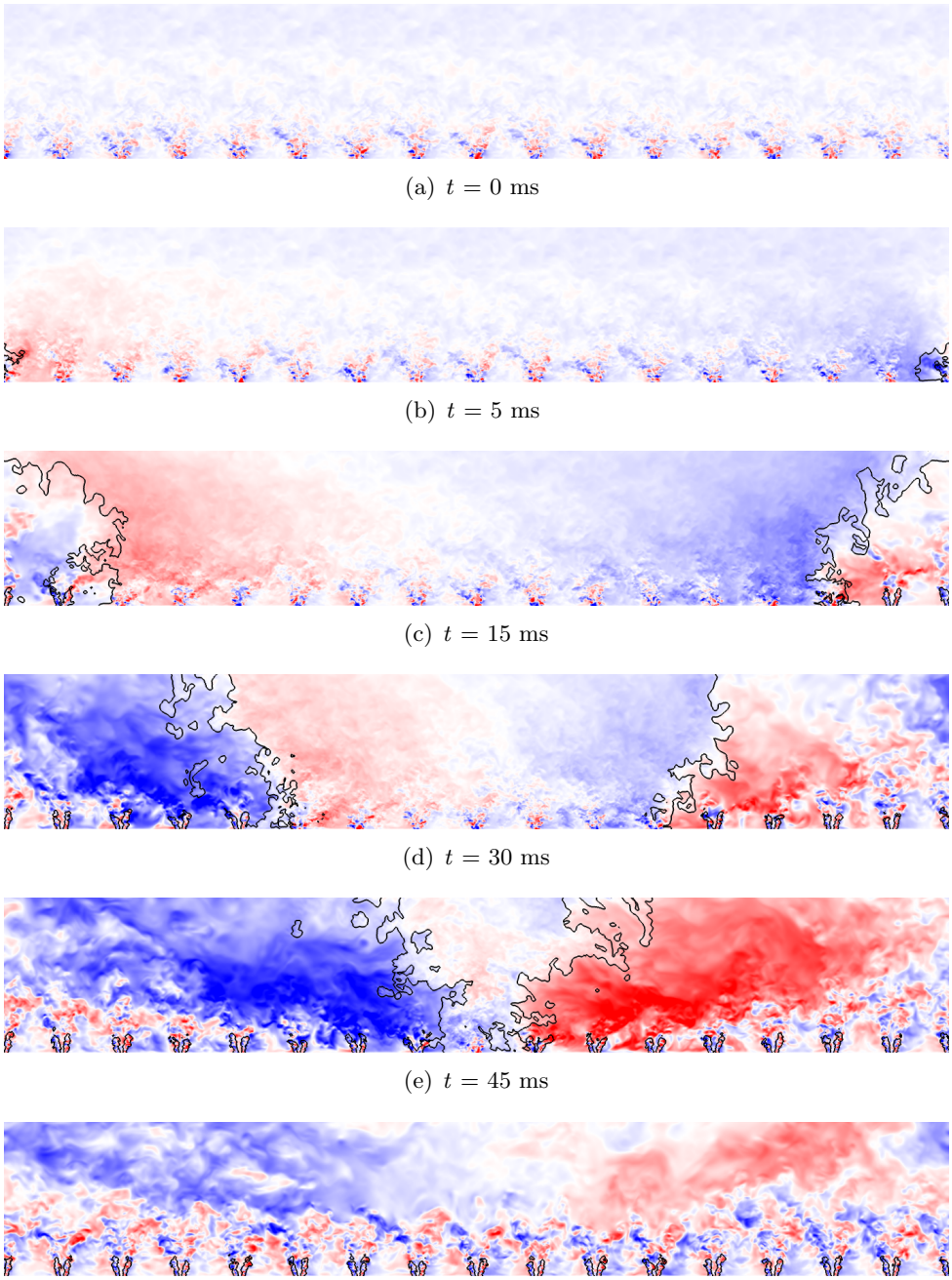

(a) $t = 0$ ms

(b) $t = 5$ ms

(c) $t = 15$ ms

(d) $t = 30$ ms

(e) $t = 45$ ms

(f) $t = 60$ ms

Figure 5.26: Cylindrical cut of the MICCA chamber (premixed case #2) coloured by the azimutal velocity u_θ (blue: -20 m.s^{-1} ; white: null ; red: +20 m.s^{-1}). The flame front is indicated by the black isoline of progress variable.

5 ms, the flame kernel has begun to propagate outwards in the form of an arch and already alters the azimuthal velocity distribution. The rapid expansion of the arch creates an additional tangential flow that impacts the first two injectors. This flow increases until the flame reaches the exhaust plane of the chamber at t = 15 ms and two separate fronts are formed. At this point, the generated azimuthal flow reaches a limit state and its intensity remains constant throughout all of phase (III). Finally, at t = 45 ms, the merging takes place, a flame has stabilised around

each injector and all the fresh gases in the chamber have been consumed. A steady state is later reached for the combustion and the tangential flow created by the light-round is gradually evacuated as seen at t = 60 ms until the velocity field becomes symmetric once again. This is estimated to require 10 to 20 additional milliseconds of physical time, which was not simulated due to computational cost. During the propagation of the flame fronts, the gases are accelerated upon crossing the flame, which leads to strong azimuthal velocities on the burnt gases side away from the flame. There is therefore a point close to the flame front where the tangential velocity goes to zero and changes sign (from positive to negative or the opposite, depending on the half-chamber H+ or H-). In fact, it can be seen that the zero-velocity region (not clear on the provided figure) is located behind the flame front, so that the whole region where there is combustion has a tangential gaseous velocity that goes in the direction of the flame propagation. The burnt gases volumetric expansion then plays a major role in the flame fronts absolute velocities by generating an azimuthal flow that entrains the whole fronts.

Figure 5.27: Field of azimutal velocity at $t = 30$ ms (see Fig. 5.26d). Arrows indicate the streamlines in the fresh gases (thick lines) and burnt gases (thin line).

The combination of the described features for the axial and azimutal flow yield the flow patterns shown in Fig 5.27. During phase (III), a counterflow configuration is formed in both the fresh gases and burnt gases with stagnation planes located at the sectors S0 and S8. Instantaneous velocity profiles (see Fig. 5.28) indeed exhibit linear profiles as function of spatial coordinates (better seen in fresh gases) as expected form the potential flow solution of counterflows. The slope of this profiles can even be well predicted by a macroscopic balance of mass in the time-varying volume of fresh gases.

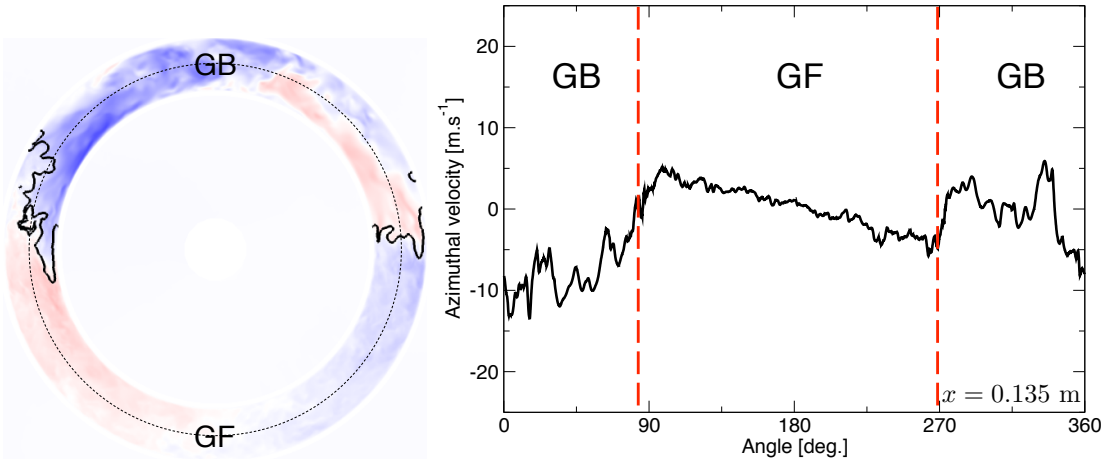

(a) (b)

Figure 5.28: Left: vertical cut coloured by azimutal velocity at $t = 30$ ms and $x = 0.135$ m. Right: profile of azimutal velocity (black plain line) on the center cylinder denoted by the dotted line in the left figure. The flame fronts are indicated by the vertical red dashed lines. GF (resp. GB) denotes the zone of fresh gases (resp. burnt gases).

5.4.3 Specificities of light-round in two-phase flows

References: [A8, A3], [T5]

Numerical studies of light-round with liquid fuel injection exhibit the same flow patterns as seen for the axial and azimutal velocities. Figs. 5.29 and 5.30 display fields of the liquid density $\alpha_l\rho_l$ for cases $\Phi = 0.89$ and $\Phi = 1.0$ at three different instants of the flame propagation on the $r^{cut} = 175$ mm unfolded cut. The difference in liquid mass repartition in the fresh gases depending on the case was already evidenced and commented on the bisector cold flow, but even in case $\Phi = 1.0$ where some liquid is present up the whole height of the chamber, it appears that it is completely evaporated in front of the flame front. Indeed, no liquid is present behind the first black line, the one that is on the fresh gases side, which stands for $\widetilde{c} = 0.1$, and where little reaction occurs. Inside the flame front, between the two iso-lines, all the liquid has evaporated and mixed with the air, thus indicating a premixed regime of the reaction zone which has been confirmed by a Takeno index analysis.

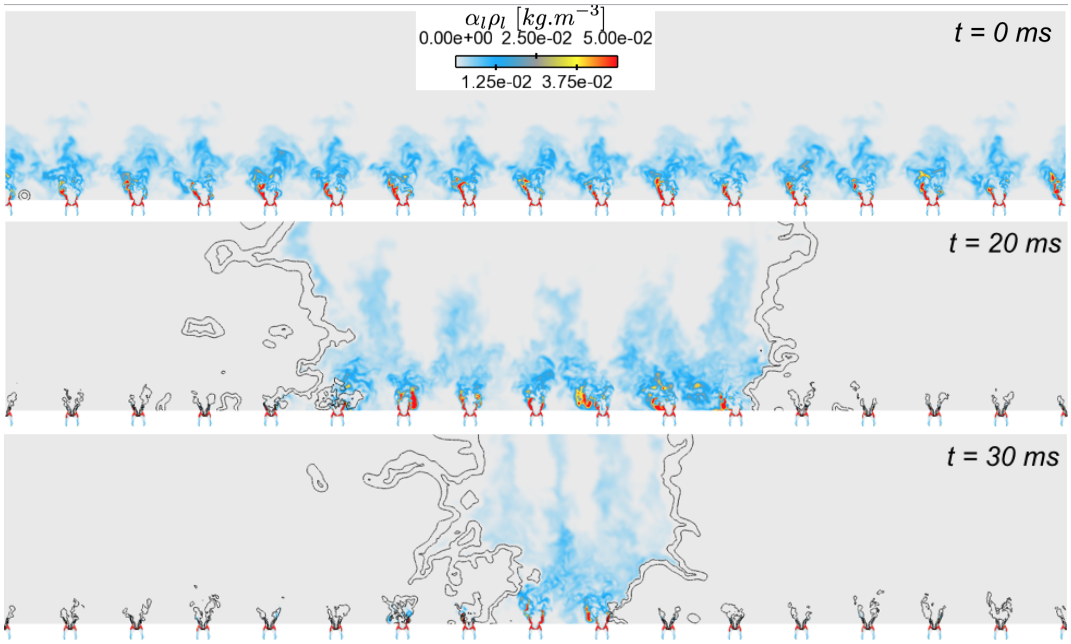

Figure 5.29: Visualisation of the liquid density $\alpha_l\rho_l$ during the flame propagation in case $\Phi = 0.89$ on a cylinder of radius $r^{cut} = 175$ mm, crossing the injectors' centerlines, unfolded on a plane surface. Data is presented for $t = 0$ ms (top), $t = 20$ ms (middle) and $t = 30$ ms (bottom). Two iso-lines of the progress variable $\widetilde{c} = 0.1$ and $\widetilde{c} = 0.9$ (in black) highlight the position of the flame fronts.

The fact that the two-phase flame can be analysed as a premixed flame front allows for defining flame surfaces as done for the premixed configuration. The analysis of the associated quantities that are $\{\Xi_\Delta\}_{res}$ and Ξ_{res} is similar except that the subgrid flame wrinkling is seen to decrease from 2.2 to 1.6 during phase (III) of these two-phase cases. While the profiles for cases $\Phi = 0.8$ and $\Phi = 0.89$ are very similar (not shown here), the behaviour of case $\Phi = 1.0$ steps aside from the others for both $\{\Xi_\Delta\}$ and Ξ_{res} which could be the manifestation of the larger error obtained for this richer simulation.

The evolution of the flame surface-average of the flame gaseous equivalence ratio $\{\Phi\}_{res}$ is shown in Fig. 5.31. Several observations can be made from it. First of all, even though the amount

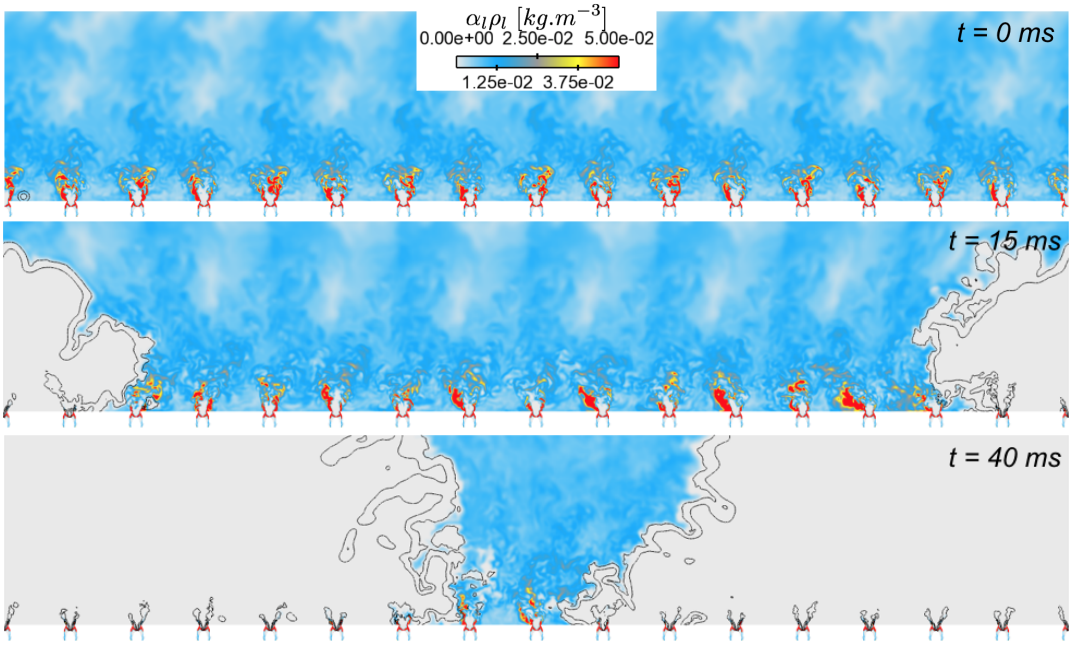

Figure 5.30: Visualisation of the liquid density $\alpha_l\rho_l$ during the flame propagation in case $\Phi = 1.0$ on a cylinder of radius $r^{cut} = 175$ mm, crossing the injectors' centerlines, unfolded on a plane surface. Data is presented for $t = 0$ ms (top), $t = 15$ ms (middle) and $t = 40$ ms (bottom). Two iso-lines of the progress variable $\widetilde{c} = 0.1$ and $\widetilde{c} = 0.9$ (in black) highlight the position of the flame fronts.

of flame surface and its shape vary a lot during the light-round, $\{\Phi\}_{res}$ remains quite constant throughout the whole ignition sequence. The other striking feature is the mean value of $\{\Phi\}_{res}$ for each case, which is systematically almost 10% greater than the global injected equivalence ratio. On average, the flame therefore evolves in a mixture that is richer than was expected from the injected equivalence ratio. This is bound to have an impact on local quantities such as the consumption speed. The misprediction for case $\Phi = 1.0$ could be due to an erroneous behaviour for globally rich two-phase flame, highlighting the limitation of the retained modelling approach.

After analysis, the presence of richer mixtures at the flame fronts for all cases is due to the interaction of the flow induced by the flame in fresh gases and the liquid sprays. This effect can be noticed in Figs. 5.29 and 5.30 but is clarified in Fig. 5.32. The azimuthal flow strongly perturbs the liquid phase distribution: the sprays generated by the un-ignited injectors are inclined away from the flame. Additionally, some pockets of droplets are created and pushed away from the flame fronts, forming patterns similar to those found in the case of jets in cross-flows. Hence, during the light-round sequence, the droplets are pushed and trapped in the outer recirculation zones between the injectors. Strong modifications are observed up to three injectors ahead of the flame fronts. This accumulation of droplet and resulting gaseous fuel results in the higher equivalence ratio observed at the flame fronts for all light-round cases with liquid fuel injection.

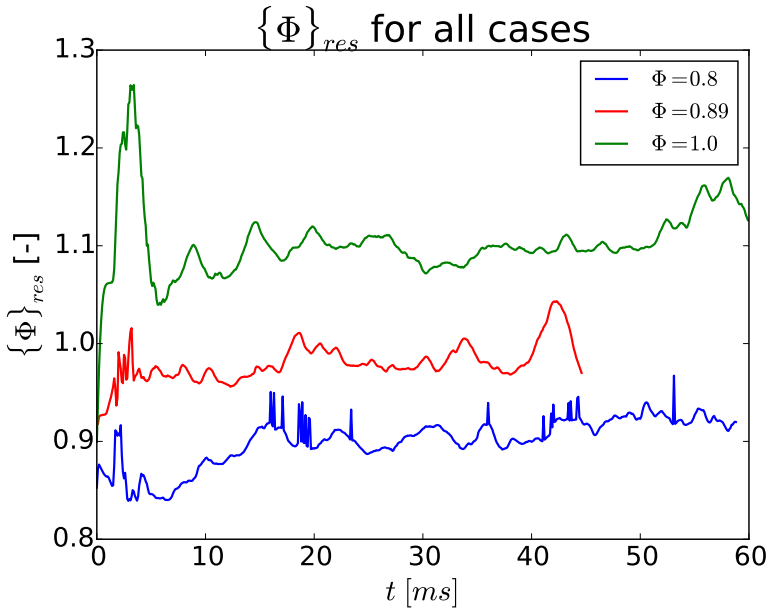

Figure 5.31: Evolution of the equivalence ratio averaged on the resolved flame front $\{\Phi\}_{res}$ for cases $\Phi = 0.8$ in blue, $\Phi = 0.89$ in red and $\Phi = 1.0$ in green during the light-round sequence.

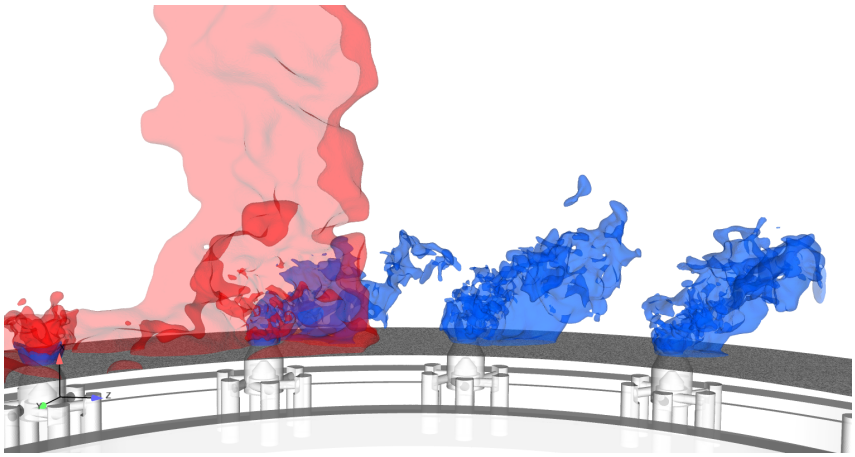

Figure 5.32: Visualisation of the effect of the flame fronts on the liquid sprays at $t = 25$ ms from case $\Phi = 0.8$, evidenced by blue iso-surfaces of the liquid mass density $\alpha_l \rho_l = 0.01$ kg.m^{-3}. The flame front is represented by an iso-surface of the progress variable and moves from left to right.

5.4.4 Flow dynamic at the combustor exit plane and refinement of phases definition

References: [T3]

Careful analysis of the ignition process invites to refine phase (III) into three subphases:

- **Phase (III)a**: after the end of phase (II) with the arch-like flame reaching the top of the combustion chamber, burnt gases are suddenly expelled outside of the combustor and the two flame fronts that are initially inclined straighten up.
- **Phase (III)b**: the separate flame fronts propagate and ignite successively the burners in a regular manner, outlining a sort of *pure* light-round phase that is not perturbed by its initialization nor by its termination.
- **Phase (III)c**: the inclination of flame fronts drops strongly, outlining a strong interaction of both flame front before the merging due to the reduced size of the region of fresh gases.

This splitting of phase (III) allows for distinguishing different effects at the beginning and end of this phase. This is particularly marked in the flow dynamic at the combustor exit plane which is here illustrated with the premixed gaseous case #2. The outlet mass flow rates of fresh gases $\dot{m}_u^{out}$, burnt gases $\dot{m}_b^{out}$ and sum of both $\dot{m}^{out} = \dot{m}_u^{out} + \dot{m}_b^{out}$ are shown in Fig. 5.33(a). During the first instants in phases (I) and (II), only fresh gases exit the chamber and $\dot{m}^{out} = \dot{m}_u^{out}$. A peak in $\dot{m}_u^{out}$ is seen at the transition between phases (II) et (III)a. Then, during phase (III)a $\dot{m}_b^{out}$ suddenly grows from its null value and $\dot{m}_u^{out}$ drops significantly. During phase (III)b, $\dot{m}_u^{out}$ oscillates around a constant value while the mass flow rate of burnt gases grows linearly. Then, the fronts interaction in phase (III)c make $\dot{m}_u^{out}$ drop whereas $\dot{m}_b^{out}$ continues its linear growth. All flow rates decrease upon the flame fronts merging in phase (IV) before reaching their steady-state values with $\dot{m}^{out} = \dot{m}_b^{out}$. The marked passage between the newly introduced phases is also observed in the outlet cross-section-averaged velocity in the fresh (u_u) and burnt (u_b) gases streams. These profiles are shown in Fig. 5.33(b) which removes from the flow rates the effect of the variable cross-section area of burnt/unburnt gases at the outlet.

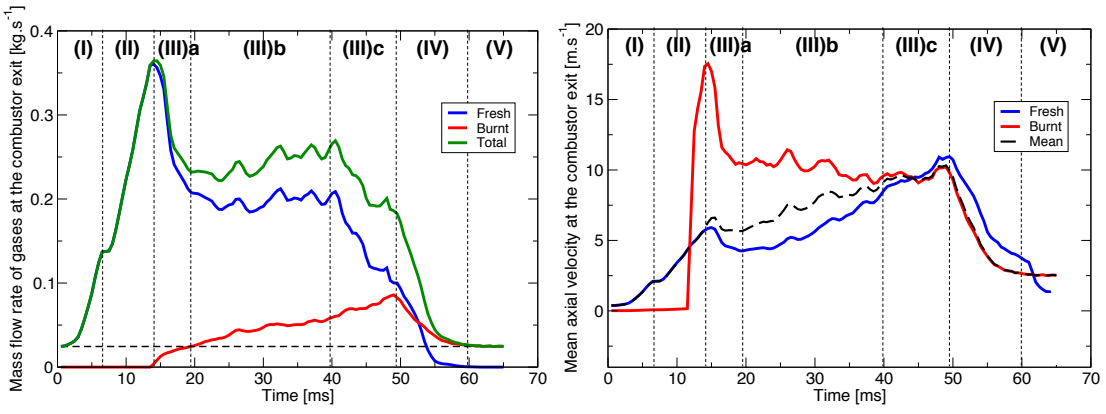

(a) (b)

Figure 5.33: (a) Temporal evolution of outlet mass flow rates: fresh gases $\dot{m}_u^{out}$ (blue), burnt gases $\dot{m}_b^{out}$ (red), total $\dot{m}^{out}$ (green). (b) Temporal evolution of outlet cross-section-averaged velocities: fresh gases (blue), burnt gases (red), total mean (dashed, black).

5.5 Mechanisms controlling the flame propagation: a chicken and egg question

The large induced flow that promotes the flame propagation is the result of the conversion of fresh gases into burnt gases with a lower density. One can seek an explanation of the flame velocity during light-round by modelling it as a mean turbulent flame brush with its absolute, displacement and consumption speeds. Closing the relationships between these different quantities requires to write macroscopic balances of mass, species and momentum in the chamber. This is the topic of the first next subsection. On the other hand, another possible scenario is the specific role of the flame leading point investigated in Sec. 5.5.2. Determining which mechanism is responsible for the flame propagation is difficult as both phenomena coexist: the turbulent flame is always accompanied by a leading-point for each flame front and the propagating leading point is attached to a flame that spans on the entire chamber height. No answer has been found yet for this chicken and egg question. This section briefly presents results from the analysis of both scenarios.

5.5.1 Global point of view through macroscopic balances

References: [T3, T5]

The absolute flame speed S_a^T The turbulent flame fronts are modelled as two vertical planes (see Fig. 5.23(a)) whose absolute velocity is assimilated to the searched quantity: the absolute turbulent flame speed S_a^T during phase (III). In this geometrical model, the volume variation of burnt gases is then linked to S_a^T as $\dfrac{dV_b}{dt} = S_a^T A_0$. The obtained flame velocity is shown in Fig. 5.34. During phase (III)b where the geometrical model is the most relevant, the fairly constant flame speed is retrieved. In the other phases (III)a, (III)c and (IV), the absolute speed decreases with marked transitions between the different phases.

Derivation of a model for S_a^T Manipulation of macroscopic balance of mass of burnt gases and transport theorems allows for expressing the absolute flame speed as a function of the global consumption speed and yields the following expression:

$$S_a^T = \frac{\rho_u}{\rho_b} \{\Xi_\Delta\}_{res} \Xi_{res} S_l^0 - \frac{\dot{m}_b^{out}}{\rho_b A_0}. \tag{5.7}$$

This equation illustrates some classical behaviours. In stationary flames, $S_a^T = 0$ and one retrieves that the mass flow rate of burnt gases is related to the flame consumption speed: $\dot{m}_b^{out} = \rho_u A_{tot} S_l^0 = \rho_u S_c^T A_0$. In fully confined flames or when the burnt gases have not reached the outlet yet, $\dot{m}_b^{out} = 0$ and $S_a^T = \dfrac{\rho_u}{\rho_b} S_c^T$. The absolute flame speed is then the consumption speed multiplied by the ratio of unburnt and burnt gases densities. This expression is well known is canonical configuration such as spherical flames or 1D flames in one-sided confined ducts.

Equation 5.7 contains several terms. All of them must be determined or known to close the model. We have chosen not to model the total wrinkling factor $\{\Xi_\Delta\}_{res}\Xi_{res}$ and will use the LES data directly for this quantity. The remaining unknown to determine is the mass flow rate $\dot{m}_b^{out}$. A global mass balance on the combustor yields

$$\dot{m}^{out} = \dot{m}^{in} + (\rho_u - \rho_b) A_0 S_a^T = \dot{m}_b^{out} + \dot{m}_u^{out},$$

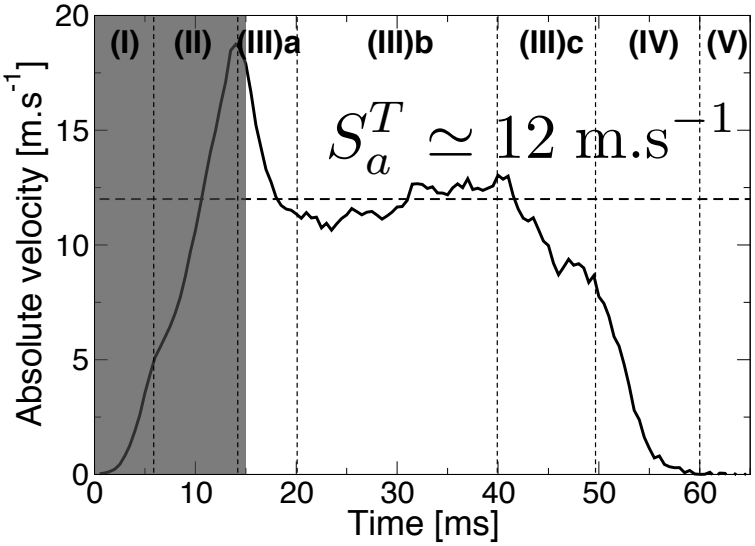

Figure 5.34: Temporal evolution of the turbulent flame speed S_a^T for the premixed case #2. The grey area corresponds to phases (I) and (II) where the two-plane model does not hold. The horizontal dashed line indicates the mean turbulent flame speed observed experimentally: $S_a^T \simeq 12$ m.s^{-1}. The vertical dashed lines mark the different light-round phases.

with $\dot{m}_b^{out} = \rho_b u_b A_b^{out}$ and $\dot{m}_u^{out} = \rho_u u_u A_u^{out}$. This does not allow for closing the problem yet but one sees how critical is the characterization the flow dynamics at the outlet cross-section. Indeed, the behaviour of the flame in phase (III) is the one of a semi-confined expanding flame ruled by Eq. 5.7. Outlet cross-section areas A_b^{out} and A_u^{out} can be linked to S_a^T by kinematic relationships and only one additional equation is needed to close the set of equations obtained below

$$\begin{cases} S_a^T = \Xi_{res}\frac{\rho_u}{\rho_b}\{\Xi_\Delta\}_{res}S_l^0 - \frac{\dot{m}_b^{out}}{\rho_b A_0} \\ \dot{m}^{out} = \dot{m}^{in} + (\rho_u - \rho_b)\, S_a^T A_0 \\ \dot{m}^{out} = \dot{m}_u^{out} + \dot{m}_b^{out} = \rho_u u_u A_u^{out} + \rho_b u_b A_b^{out} \\ \frac{dA_b^{out}}{dt} = 2\Delta R S_a^T \\ A_u^{out} = \Delta R\,(2\pi R_m) - A_b^{out} \end{cases} . \tag{5.8}$$

An additional relationship is then found through a macroscopic balance of momentum in the combustor. Its closed form yields an ordinary differential equation (ODE) written as

$$\begin{aligned} &\alpha_{t_u}\,(\rho_u - \rho_b)\,A_0 h\frac{dS_a^T}{dt} + (\alpha_{t_b} - \alpha_{t_u})\left[\rho_b\frac{du_b}{dt}A_b^{out}h + \rho_b A_0 S_a^T u_b\right] \\ &\qquad = \alpha_i\left[\dot{m}^{in}u^{in}\right] - \left[\alpha_{o_u}\dot{m}_u^{out}u_u + \alpha_{o_b}\dot{m}_b^{out}u_b\right] - \Delta p A^{out}. \end{aligned} \tag{5.9}$$

The α terms are form factors that accounts for inhomogeneous profiles at the inlet and outlet. Their average value during the light-round is retained. The pressure term $\Delta p = p^{out} - p^{bot}$, difference between the outlet mean pressure and the pressure at the chamber bottom plane, is the last piece of the puzzle. Neglecting it yields incorrect results. Figure 5.35(a) shows the prediction of S_a^T by combining Eqs. 5.8 and 5.9 altogether while taking the pressure term as a polynomial fit from the LES data. The result is very satisfactory and shows the consistency of the derived equations.

The identification of a counterflow in the different zones in Sec. 5.4.2, and notably in the fresh gases, enables to derive the pressure term from the counterflow strain rate which can be related

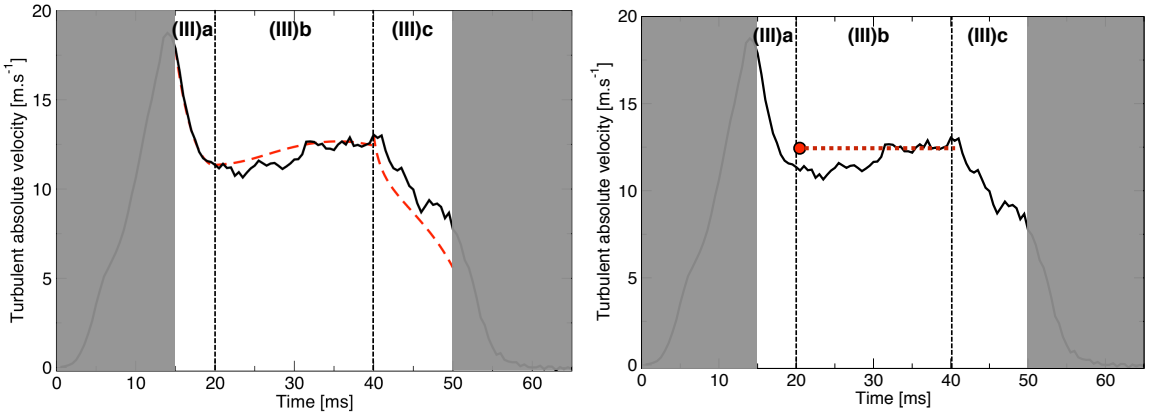

Figure 5.35: Predicted absolute turbulent flame speed S_a^T from the LES pressure fitted with a polynomial (a) and the modelled pressure term (b). The red circle in (b) indicates the predicted value from the closed system of algebraic equation.

with a good fidelity to the inlet and outlet mean velocities. The full of equations is now closed but unfortunately yields to some instabilities in the solving of the ODE. Further analysis of the ODE terms with LES data reveals that the unsteady term can be neglected in phase (III)b. The obtained set of algebraic equations can then predict a value for phase (III)b without any prior knowledge of an initial value. The final result is shown in Fig. 5.35(b). Given the retained macroscopic level of modelling, the predictive quality is deemed satisfactory.

Further validation A sensitivity study of the different terms in the equations is conducted. It gives a sensitivity coefficient of -0.55 for the pressure term and 0.32 for the combustion model in particular. Hence, the model predicts that a 10% error in the combustion model leads to a 3% final error on the flame propagation speed. The model predictions are also confronted to other experimental data. Figure 5.36 shows the prediction of light-round duration as a function of the mass flow rate, here denoted by the bulk velocity U_{bulk} in the injector, for the premixed MICCA configuration. LES results for cases #2 and #3 are represented as well. One limitation in the exercise is the prescribed total wrinkling factor from case #2 for all cases in the low-order model. Nonetheless the model predicts accurately the acceleration of the flame with U_{bulk}. The level of agreement is fair. The largest discrepancy of 7 ms is obtained for case #3.

The derived model must not be considered as fully predictive but should provide insights in the effects of parametric changes. While a first interpretation of the decrease of the light-round with the total mass flow rate could be the enhanced turbulence and flame consumption speed [21], such information is not prescribed to the model that yet delivers a correct prediction of the trend. This outlines that the first-order believed effect might not be the correct one. The evidenced coupling of the different equations makes the anticipation of flame speed tedious. The coarse description of the different submodels allows for easily estimating the effects of combustor geometry, fuel modification, ...

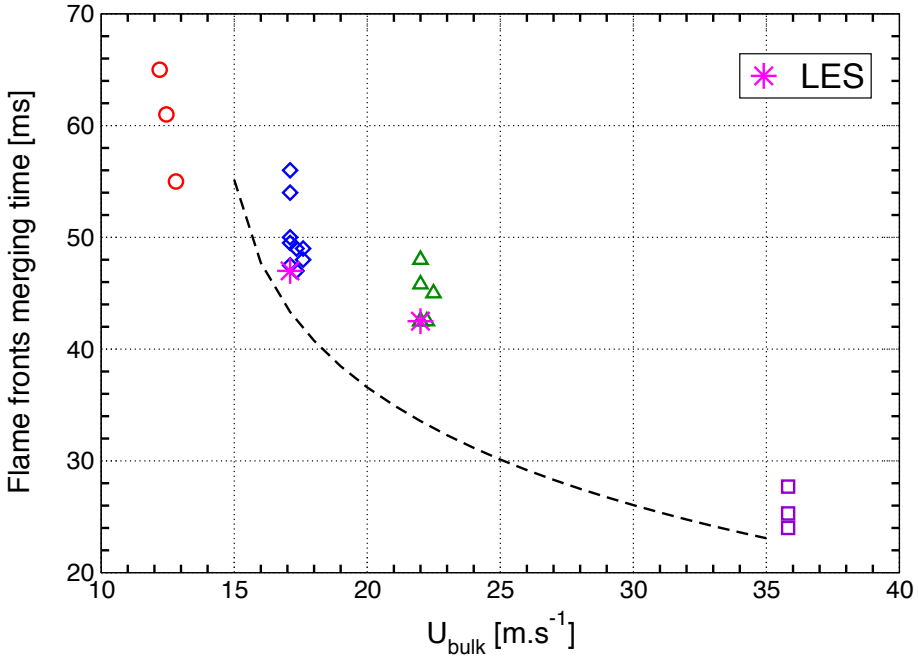

Figure 5.36: Light-round duration as a function of the injector bulk velocity U_{bulk}. Symbols correspond to experimental data: circles (case #1), diamonds (case #2), triangles (case#3), squares (new case with the courtesy of D. Durox and K. Prieur). LES results are denoted by star symbols. The dashed line represents the results of the low-order model.

5.5.2 Behaviour of the leading point

References: [A3], [T3, T5]

For each half chamber, the leading point (LP) is defined as the most forward point in the azimuthal direction on an iso-surface of the progress variable. In the following, the LP is then taken on the $\widetilde{c} = 0.9$ iso-surface. This choice does not impact the post-processing results and the conclusions presented hereafter.

Leading-point trajectory Figure 5.37 displays the trajectory of the LP for both halves of the chamber and for premixed and two-phase cases. The same behaviour is observed for all conditions. On the H- side (left side), the leading point is systematically located close to the inner wall of the chamber, which indicates that a preferential path exists in this area, probably due to the presence of the swirling flow generated by each injector. In the right half H+ however, the trajectories are more complex. For the first quarter-chamber, the preferential path seems to be located along the inner wall of the chamber. In the second quarter-chamber, the LP is not pinned to the inner wall anymore, and within one sector, moves to the middle of the chamber and evolves thereafter close to the radius of the injector axes. The shorter path is no longer followed, suggesting that the identical clockwise orientation of the injectors plays an important role in the radial position of the leading point, and therefore in the flame propagation path. The similarity of the path followed by the leading points in these different cases could therefore be a consequence of the geometry of the chamber and the orientation of the swirling flows. The shape of the flame fronts is strongly influenced by the local flow field, and there can be some local competition between several flame elements, which explains the discontinuities observed on the trajectories when one element overtakes another. This is also seen in the axial position

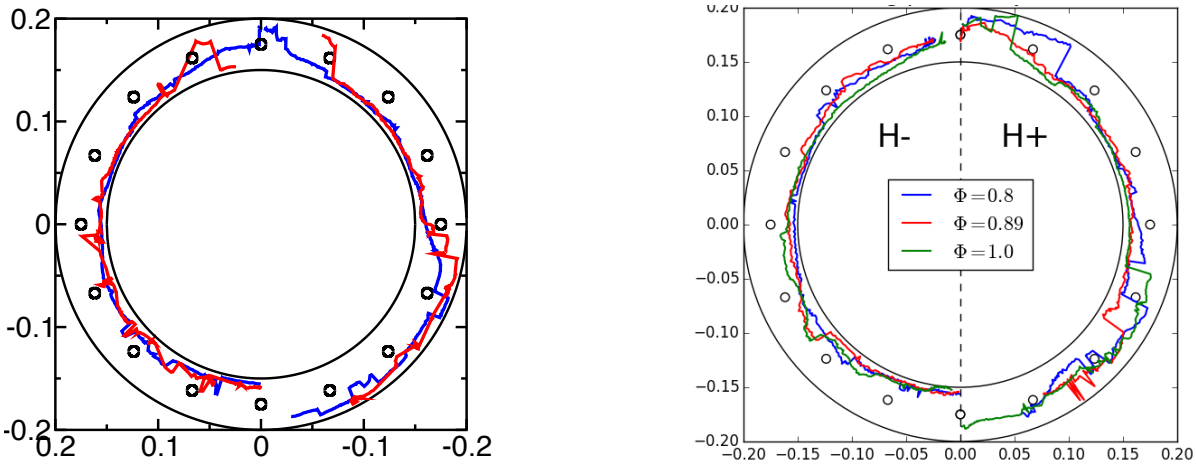

(a) (b)

Figure 5.37: Leading points trajectories projected on the chamber backplane for the premixed case #2 (left, blue line) and the three cases with liquid fuel injection (right: blue for $\Phi = 0.8$, red for $\Phi = 0.89$ and green for $\Phi = 1.0$). The red line in (a) is the trajectory of the upper flame trailing edge not discussed here.

i.e. the height of the LP for both halves of the chamber (not shown here). At the beginning of the azimuthal propagation, corresponding to phase (II), the LP is lifted up due to the arch-like flame. After the separation into two distinct fronts, the distance of the LP with respect to the chamber backplane is rapidly brought back below $\sim 40mm$, *i.e.* the first 25% of the chamber height.

Leading-point in two-phase flow cases The impact of azimutal flow on the liquid sprays also modifies the gaseous conditions seen by the leading point in the two-phase flow cases. This analysis can be found in [A3].

Leading-point as a waverider The flow velocity at the leading-point position is in fact very close to the leading-point velocity itself. This denotes a small contribution of the flame displacement speed associated to the reactive front in the total absolute flame speed investigated here locally. This high velocity at the LP is due to its location in the induced flow generated by the volumetric expansion of burnt gases as shown in Fig. 5.38 for premixed and two-phase cases. One hypothetical scenario would then be that the leading point, being located in regions of higher velocities, entrains the whole flame fronts during the light-round which, in return, generate the flow that supports the leading-point. This is the *waverider* LP scenario. In fact, the explanation could be even more localised around the leading-point as better seen in Fig. 5.38(e): the azimutal velocity in the vicinity of the LP is remarkably twice higher than everywhere else in the fresh gases. This yields a higher absolute tangential velocity of the leading point and strengthen the idea of the leading point being advected by its surrounding flow, thus greatly increasing its speed.

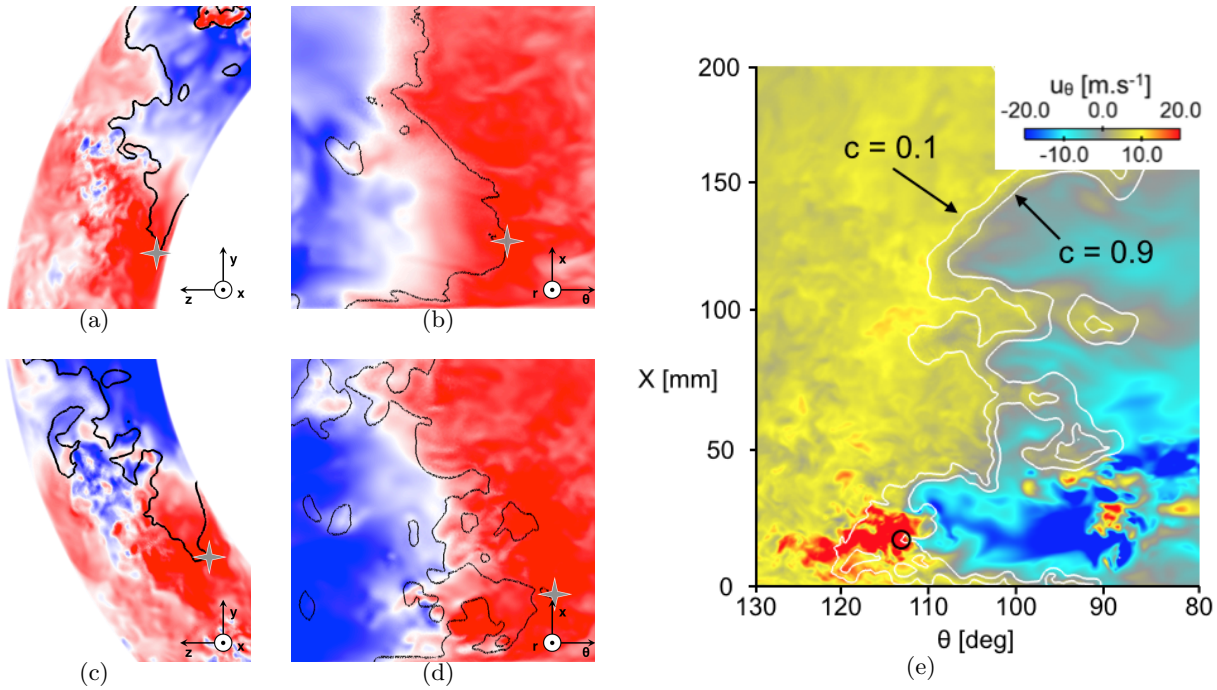

Figure 5.38: Zoom on the flame front in the leading point area for premixed case #2 (a, b, c, d) and two-phase case $\Phi = 0.80$ (e). Premixed case #2: the velocity azimutal field (blue: -10 m.s^{-1}, red: +10 m.s^{-1}) is projected on the plane corresponding to the LP (denoted by a star symbol) height for instants $t = 20$ ms (a) and $t = 30$ ms (c) and on the cylindrical cut cutting through the LP position at instants $t = 20$ ms (b) and $t = 30$ ms (d). Two-phase case: cylindrical cut through the LP (denoted by black circle) position at $t = 25.0$ ms; the flame is evidenced by white iso-lines of the progress variable $c = 0.1$ and $c = 0.9$; the flame travels here from left to right.

Chapter 6

Heat transfer and multiphysics simulations

The prediction of wall heat fluxes and temperature is of great importance in combustion systems given their impact on the material structure and because of the effects of cooled burnt gases on the flame stabilization and dynamics. In order to achieve such predictive simulations, conjugate heat transfer in the combustor walls must be taken into account. The resulting combination of three numerical solvers (reactive LES, Monte Carlo radiation solver, wall heat transfer) yields a promising multiphysics methodology for high-fidelity simulations. A first application of such multiphysics computations to a premixed swirled flame combustor has remarkably achieved to predict wall temperature fields within 2% of the 2D experimental map (**Highlight #4** in Fig. 1.4, Sec. 6.2.5). Another original contribution made possible by these simulations is the study of radiative effects in turbulent boundary layers (**Highlight #3** in Fig. 1.3, Sec. 6.3.2) with an unprecedented accuracy based on direct numerical simulations and Monte Carlo resolution of the radiative transfer equation with cK gas properties. Both studies relie on previous efforts on algorithms, optimization and validation and have led to further developments such as the study of soot radiation, high-pressure combustors and wall-models for LES. All these works are presented in this chapter dedicated to heat transfer and multiphysics simulations.

Section 6.1 presents the studies on conjugate heat transfer in reactive flows, which covers the development of a new coupling algorithm and its application in coupled simulations. The additional accounting for thermal radiation and related works in reactive flows are detailed in Sec. 6.2. Finally, research activities on analysis and modelling of convective heat transfer and coupled effects with radiation in turbulent boundary layers are given in Sec. 6.3.

Full list of **References**:

- Papers: [A2, A4, A6, A7, A10, A11, A15, A16, A17]
- Book chapters: [C4, C5]
- Theses: [T1, T2, T4, T6, T7, T8, T9]
- 23 conferences

6.1 Conjugate heat transfer in reactive flows

6.1.1 Context

The previous chapter considers simulations of relight conditions with hot walls. Without prior knowledge of the wall temperature, this condition has been coarsely modelled with adiabatic wall conditions. In reality, wall heat losses modify the burnt gases temperature and can influence the velocity field, the flame stabilization or the pollutant emission. Additionally, when the flame is near the wall, a complex flame-wall interaction can occur [187, 85, 105, 97]. Prescribing measured wall temperatures or predicting them in the MICCA chamber would have then allowed a more realistic representation.

In order to compute the wall temperature, one must solve the computational fluid dynamics problem along with the heat conduction within the solid parts. This becomes a *conjugate heat transfer* (CHT) study. In such coupled multiphysics simulations, a partitioned approach is often retained where different numerical solvers are considered to treat the different physical phenomena: one for CFD and one for wall heat transfer. With the increasing maturity of LES or DNS methods, several works [129, 225] have been carried out to characterise unsteady conjugate heat transfer with these high-fidelity approaches. Several CHT applications to turbine blades have been reported [50, 51] as well as in combustion cases [107, 13, 128]. The later studies have focused on predicting the mean thermal state of combustors' walls which is usually the first concern due to the presence of hot temperature gases. However, retaining an approach such as LES-CHT should also allow for capturing unsteady details of wall heat transfer. A key parameter is the thermal activity ratio defined as the ratio of the fluid thermal effusivity and the solid one. When the thermal activity ratio is larger than unity, the temperature fluctuations in the flow are significantly impressed on the solid wall, yielding a strong thermal unsteadiness of the solid material. In usual combustion applications, the thermal activity is small except for very high-pressure applications such as rocket engines where the impact of unsteady CHT has recently been outlined [148, 135].

In other combustion systems, unsteady aspects of wall heat transfer variations have been believed to be negligible. However, combustion dynamics of turbulent flames can yield fluctuations in the local gaseous temperature of several hundred Kelvins or even a couple of thousands Kelvins. Despite the small thermal activity factor, the absolute level of wall temperature variations is not necessarily negligible. This has recently been confirmed in [218, 247] with high-speed thermographic phosphor thermometry which shows that a stable turbulent flame can induce wall temperature fluctuations of a couple of dozens Kelvins while the wall temperature can vary up to 100 K in the case of an unstable flame. It is indeed recognised that combustion instabilities, which make the flame strongly unsteady with large variations in pressure and velocity, can cause several issues [142] that either rapidly damage the system or result in premature component wear: enhanced heat transfer and thermal stresses to combustor walls, oscillatory mechanical loads that result in low- or high-cycle fatigue of system components, and flame blow-off or flashback. In these phenomena, the combination of LES with CHT is a promising approach to address one of the fatigue contributions that is high-cycle fatigue due to unsteady heat loads.

6.1.2 Hybrid-Cell Neumann-Dirichlet coupling method

References: [A7], [T2]

Coupling methods In unsteady conjugate heat transfer, the solid and fluid solvers advance in time separately between coupling steps. The flow solver time step is denoted by Δt_f while the one for the solid solver is denoted by Δt_s. With synchronized solvers, the flow and solid solver time steps fulfil the following constraint: $\Delta t_{cpl} = N_s \Delta t_s = N_f \Delta t_f$ where N_s and N_f are the number of iterations before exchanging data at the shared interface, and Δt_{cpl} is the coupling period. While Δt_f is fixed internally by the flow solver, the number of solid solver iterations is typically set to one, $N_s = 1$, as it usually relies on an implicit time integration. The choice of the coupling period Δt_{cpl} becomes then tightly related to how often the flow solver is coupled with N_f and to the computational overhead of the coupled simulation.

During the thesis of Chaï Koren, a new coupling algorithm for unsteady CHT studies with LES have been derived to overcome some shortcomings of the standard Neumann-Dirichlet coupling between a flow solver coupled with a heat conduction solver. Indeed, most coupling algorithms for unsteady conjugate heat transfer are based on algorithms initially derived for steady conjugate heat transfer problems where domain decomposition methods for elliptic PDEs provide the framework to iteratively converge towards the steady solution on the whole domain.

The Neumann-Dirichlet coupling whose stability has been studied in [79] ensures the temperature continuity and heat flux conservation through the boundary at the discrete coupling steps: one solver is given a fixed temperature at the interface (Dirichlet condition) while the other one uses a Neumann condition with a given value of the wall heat flux. The interface boundary condition in each case is sent by the other code. For typical gas-solid CHT applications with $\rho_f c_{p_f} \Delta x_f < \rho_s c_s \Delta x_s$, Giles [79] showed that the Dirichlet boundary condition must be set to the flow solver while the wall heat transfer solver must use the Neumann boundary condition. Improvements of the stability and convergence for steady problems have been proposed [57, 56] since. Recent studies have based their coupling methodology on such a Neumann-Dirichlet coupling or one of its variant [107, 96, 95, 196].

However, as pointed out initially, the obtained set of algebraic relations originally derived for steady elliptic PDES does not inform on its adequacy or accuracy for unsteady problems, possibly making this family of methods suboptimal for other classes of problems. In particular, the coupling period parameter Δt_{cpl} is either arbitrarily chosen or, at best, the adequacy of the chosen value is verified in a posteriori tests [50, 51, 96]. The issue is then to determine this coupling period.

A new coupling approach with a self-adaptive coupling period The Hybrid-cell Neumann-Dirichlet (HCND) coupling relies on a layer of hybrid cells at the boundary between the fluid and solid domains. As described in Fig. 6.1(a), each hybrid cell is composed of solid and fluid mesh cells on each side of the interface. Writing a heat balance equation for the hybrid cell gives an ordinary differential equation (ODE) for the boundary temperature T_{bnd}:

$$\frac{dT_{bnd}}{dt} = -\frac{\Phi_{f,bnd} + \Phi_{s,bnd}}{V_f \rho_f c_{pf} + V_s \rho_s c_s}, \tag{6.1}$$

where $\Phi_{s,bnd}$ and $\Phi_{f,bnd}$ are the flux integrated over all internal faces of the hybrid cell in the solid domain and in the fluid, respectively. For each hybrid cell around an interfacial face, fluxes are

prescribed from both domain to the ODE solver and, after a time integration of Eq. 6.1 for the duration Δt_{cpl}, the updated boundary temperature is applied as Dirichlet boundary conditions in both solvers as depicted in Fig. 6.1(b). In practice, the ODE solver is embedded in each solid and flow solver so that they only exchange their respective heat fluxes with each other, yielding a computational coupling cost identical to a standard Neumann-Dirichlet coupling. It was shown that the obtained algorithm is neither a Dirichlet-Dirichlet coupling nor a Neumann-Neumann coupling but is in fact very close to a Neumann-Dirichlet coupling in terms of numerical behaviour.

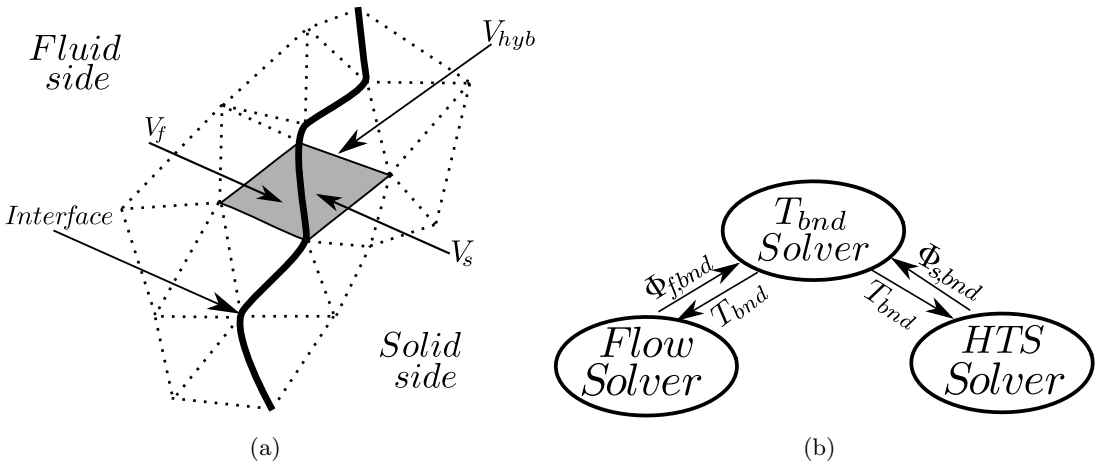

(a) (b)

Figure 6.1: (a) Fluid and solid domains used for a coupled simulation. Dashed triangles represent the cells (actual mesh cells for volume-centred formalism or dual mesh cells for vertex-centred formalism). Both grey triangles denote the fluid and solid cells of volume V_f and V_s respectively, which define the hybrid cell of volume V_{hyb} around the interface. (b) Scheme of coupling procedure: the flow solver and the solid heat transfer solver (HTS) exchange boundary fluxes, $\Phi_{s,bnd}$ and $\Phi_{f,bnd}$, and temperature, T_{bnd}, with the ODE boundary solver which determines T_{bnd}.

The HCND method was validated with the Method of Manufactured Solutions. A forward Euler resolution of Eq. 6.1 yields a first-order accuracy but was instead replaced by another 1^{st}-order method that is strictly conservative. The method stability for Δt_{cpl} was expressed in terms of a hybrid Fourier number associated to the hybrid cell and shows a restricted stability region consistent with the choice of explicit time integration. Indeed, for the target applications involving coupled DNS/LES, we do not wish to consider an iterative and implicit approach that would require to repeat the same DNS/LES step several times.

The main interest of the method is its ODE formulation which enables self-adaptation of the coupling time step from the control of numerical error [90]. The step size control algorithm is a control loop shown in Fig. 6.2(a): After the boundary temperature is integrated, a test is carried out to compare the numerical integration error ε_n to the prescribed tolerance η. If the numerical error is low enough, the time step Δt is approved and the next step is then computed. On the other hand, if the error is too large, the time step is rejected and the integration is repeated with a smaller step Δt_{opt}. For the next step, the initial guess of the step size is chosen as equal to the previously accepted one.

The error is estimated by comparing the computed boundary temperature value with the one from a 2^{nd}-order Adams-Bashforth formula which uses previous stored values of the ODE right-hand side. The new time step Δt_{opt} is determined by a control algorithm which can be a I,

PI or PID controller that adapts the time step to reach the desired error. Figure 6.2(b) shows the resulting appreciable adaptation of the coupling period in a 1D CHT case with a pulsating boundary condition in the flow domain.

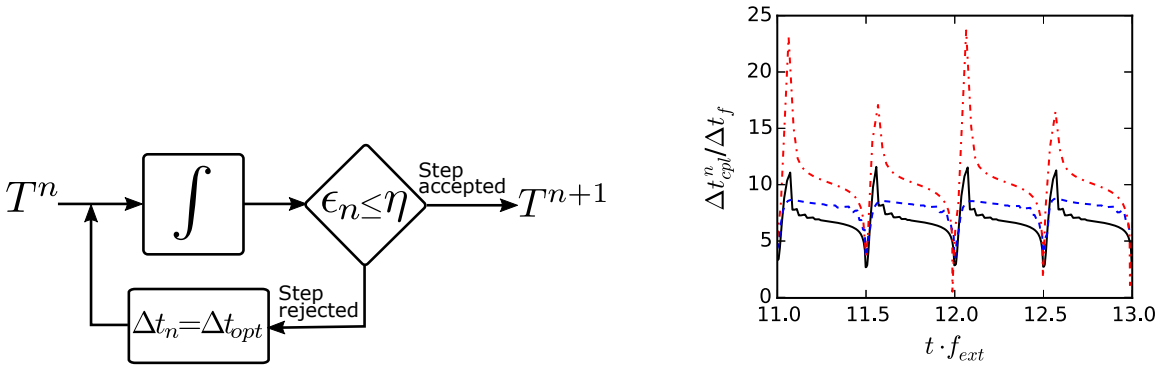

(a) (b)

Figure 6.2: (a) Generic control loop to advance the boundary temperature T^n to its value T^{n+1} with a numerical integration error ϵ_n below a given tolerance η by adapting the integration time step Δt_n. (b) Unsteady test case: evolution of the accepted coupling time step scaled by the fluid solver's time step for different controllers: I (red dashed-dotted line), PI (blue dashed line) and PID (black plain line). Case conditions: $\eta = 1\%$ and $f_{ext} = 100$ Hz.

Finally, in order to afford coupled LES/DNS, the rejection feature was disabled and we have shown that a carefully deigned PID controller was able to remain robust and efficient. With the only parameter being a prescribed tolerance to control the numerical accuracy of the coupling method, the HCNC method makes multiphysics LES benefit from the removal of an arbitrary setting that is the coupling period and enables on-the-fly control of the numerical accuracy.

6.1.3 The accelerated HCND method

References: [A2], [D7], [T2]

A need for artificial acceleration An issue to deal with in unsteady simulations of CHT problems is the slow conduction process such that the transient heating or cooling of a solid part to its permanent state requires to simulate a physical time which is not affordable with LES. This is alleviated by artificially accelerating the physical transient to reach sooner the permanent regime. Several techniques have been proposed in the literature to carry out such an acceleration [50, 13, 96, 95, 57, 107]. A first example is the coupling of an unsteady flow solver with a steady solid heat transfer solver [57]. By doing so, the mean fields are obtained at a low computational cost but this approach is limited to steady-state computations and cannot grant access to the temperature and heat flux fluctuations in the wall. A second approach is the desynchronization method [50, 13, 107] which can be used with fully unsteady coupled simulations. In this method, codes are no longer synchronized in terms of physical time: while the flow solver simulates a physical time of Δt_{cpl} the solid heat transfer solver simulates a physical time of $\alpha \Delta t_{cpl}$l where $\alpha \approx 100 - 500$. This methodology provides an efficient and robust mean to compute the mean temperature and wall heat flux fields on the interface boundary. However, by modifying the frequencies perceived by the solid, such a technique amplifies the level of heat loads fluctuations.

Superposition principle to accelerate the HCND method Being based on synchronized solid and flow domain, the HCND method is not compatible with the desynchronization technique. Another acceleration technique has therefore been developed for HCND which does not perturb the statistics (mean and rms) in permanent regimes. The acceleration method is similar to [96, 95]: the temperature field inside the walls is described as the superposition of a steady and a transient component: $T_s = \widehat{T}_s + T'_s$. Each component is then solved using the adequate heat transfer equation:

$$0 = \nabla.(\lambda_s \nabla \widehat{T}_s), \tag{6.2}$$

$$\rho_s c_{p,s} \frac{\partial T'_s}{\partial t} = \nabla.(\lambda_s \nabla T'_s). \tag{6.3}$$

The instantaneous wall heat flux on the fluid side, $\Phi_{f,bnd}$, is also split into two components: A mean wall heat flux $\widehat{\Phi}_{f,bnd}$ and a fluctuating heat flux $\Phi'_{f,bnd}$ such that

$$\Phi'_{f,bnd} = \Phi_{f,bnd} - \widehat{\Phi}_{f,bnd}. \tag{6.4}$$

Solving Eq. 6.2 is accomplished by using the mean wall heat flux $\widehat{\Phi}_{f,bnd}$ as a boundary condition on the shared interface, and yields the solid mean temperature field of $\widehat{T}_s$ including the interface mean temperature $\widehat{T}_{bnd}$. In the unsteady fluid solver, the estimated mean wall heat flux at a time τ is computed by time averaging the instantaneous wall heat flux:

$$\widehat{\Phi}_{f,bnd}(\tau) = \frac{1}{\tau} \int_0^\tau \Phi_{f,bnd}(t) dt. \tag{6.5}$$

As the cumulating duration τ in this integral increases, the computed quantity $\widehat{\Phi}_{f,bnd}(\tau)$ converges to the steady mean flux $\overline{\Phi}_{f,bnd}$. The unsteady fluctuating solid temperature equation, Eq. 6.3, is coupled to a fluctuating variant of the boundary temperature equation, Eq. 6.1,

$$\frac{dT'_{bnd}}{dt} = -\frac{\Phi'_{f,bnd} + \Phi'_{s,bnd}}{V_f \rho_f c_{pf} + V_s \rho_s c_{ps}}. \tag{6.6}$$

following the usual HCND coupling method, which still self-adapts the coupling time step given a prescribed tolerance. Finally, the instantaneous boundary temperature, used as a boundary condition by the flow solver, is obtained by summing both parts:

$$T_{bnd} = \widehat{T}_{bnd} + T'_{bnd}. \tag{6.7}$$

In [96, 95], the considered mean/fluctuation splitting is carried out on all considered Fourier modes. The fundamental mode, *i.e.* the steady state, is solved with a steady heat transfer equation solver while the unsteady heat conduction is solved for other spectral modes in the frequency-domain. With the introduced splitting, keeping a time-domain resolution to describe all types of fluctuations enables to account for a single unsteady equation which is solved numerically with a controlled accuracy provided by the HCND method. As in [96, 95], the acceleration to a permanent regime by disregarding the slow solid conduction process results from providing the mean heat flux $\widehat{\Phi}_{f,bnd}$, which converges within several flow time scales, directly as a boundary condition to the steady conduction problem in Eq. 6.2.

Validation The method is tested in a 1D CHT case with a pulsating boundary condition on the non-coupled side of the flow domain. The mean component of the boundary temperature is plotted in Fig. 6.3(a). The reference solution shows that the transient heating determined

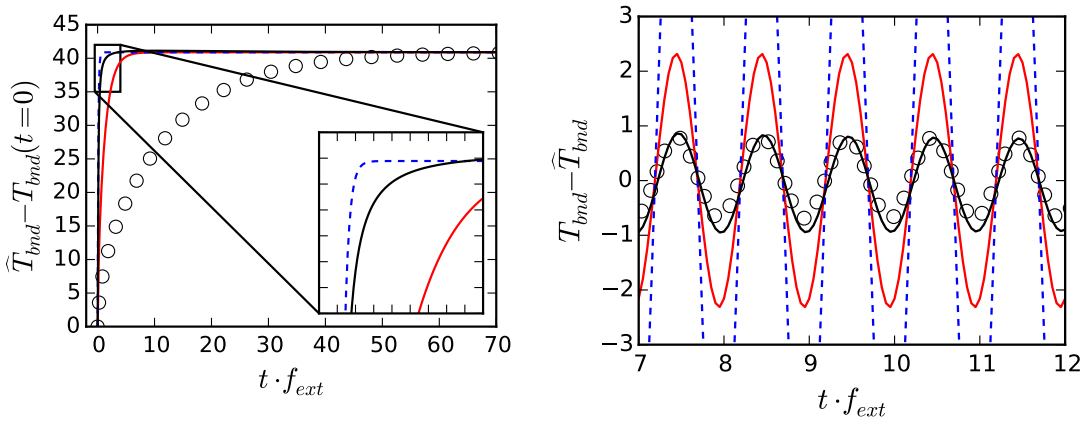

(a) (b)

Figure 6.3: Temporal evolution of the mean (a) and unsteady (b) components of the boundary temperature. Circles: Non-accelerated reference case. Red solid line: Neumann-Dirichlet coupling approach with a desynchronization factor $\alpha = 10$. Blue dashed line: Neumann-Dirichlet coupling approach with a desynchronization factor $\alpha = 100$. Black solid line: The HCND coupling approach with the derived acceleration method based on the superposition of mean and fluctuating states. Case conditions: $f_{ext} = 100$ Hz and prescribed tolerance $\eta = 5\%$ for the HCND approach.

by the solid time scale corresponds approximatively to fifty periods of the chosen value of excitation frequency f_{ext}. Desynchronizing the solid physical time from the one seen in the fluid enables to reach the steady plateau much faster. The accelerated HCND method also enables to quickly reach the steady value of the boundary temperature, much sooner than in the reference solution. Figure 6.3(b) shows the unsteady part of the interface temperature. According to the reference solution, the imposed fluctuations yield an amplitude of approximatively 1 Kelvin at the interface. A known weakness of the desynchronization method is the erroneous response amplitude which is seen. On the other hand, the proposed superposition approach of the mean and unsteady parts provides an excellent agreement after an initial transient time.

6.1.4 Prediction of wall temperature induced by a wall-impinging flame

References: [D7], [T2]

The accelerated Hybrid-Cell Neumann-Dirichlet coupling method is applied to a three-dimensional conjugate heat transfer problem of a wall-impinging flame. The studied experimental setup [211] is a laminar jet flame impinging a solid disc which is cooled on its other side. Given the moderate Reynolds number, the flow is quite stable with a marginal unsteadiness. The main objective of this study is a first prediction of the steady wall temperature with the enhanced HCND method when implemented in massively parallel codes as the ones used for LES.

Simulations are carried out with the low Mach-number solver YALES2. Combustion of methane is described by the Coffee mechanism [175] that involves 14 species and 38 reactions. Given the moderate Reynolds number of the jet, the flow is resolved enough so that no LES model is needed. Nonetheless, capturing the flame thickness on the mesh remains too expansive. The TFLES model [23, 38] is then considered.

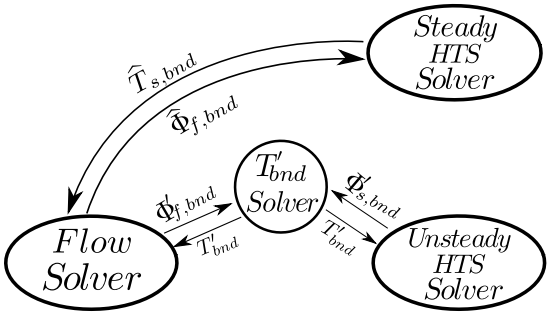

Figure 6.4: Scheme of the HCND method for coupled unsteady conjugate heat transfer when using acceleration of the physical transient heating or cooling.

The accelerated HCND method requires solving a steady and an unsteady heat equation. This is done here with two heat transfer solvers that are instances of the YALES2 framework which are represented in Fig. 6.4. In studies following the work of C. Koren, both equations are solved with a single heat transfer solver instance. On the disk cooled side, the temperature is imposed on the experimentally measured profile, i.e., between 330K in the center and 340K at the disc's extremity. The mesh of the solid domain made of quartz consists of approximately 8 million tetrahedral 0.25-mm-wide cells. The solid cells are conforming with the fluid cells at the interface. Constant quartz properties taken at $T = 400$ K, the intermediate temperature between the cooled side and the flame side, are considered.

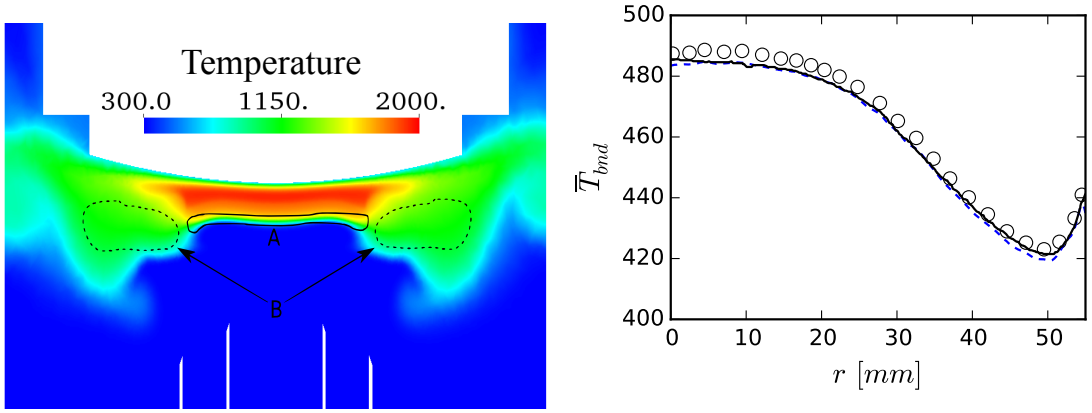

(a) (b)

Figure 6.5: (a) Field cut of the gas mean temperature. A: Reaction zone. B: Dilution zones where the hot gases encounter the coflow of N_2. (b) Comparison between experimental and numerical data for the mean boundary temperature as a function of the distance from the center of the disc. Circles: Experimental data [211]. Black plain line: accelerated HCND. Blue dashed line: Neumann-Dirichlet coupling approach with a desynchronization factor $\alpha = 1000$.

A field cut of the obtained mean temperature is shown in Fig. 6.5(a). The computed temperature field agrees with the measured flow temperature, in particular in the wall vicinity which ensures a correct prediction of the wall convective flux. The resulting prediction of the disk temperature is shown as radial profiles plotted in Fig. 6.5(b). The agreement with the experimental profile is very good. Both the accelerated HCND and desynchronized Neumann-Dirichlet methods retrieve the correct inhomogeneous profile due to the flame and nitrogen-coflow impingement. This validates the correct implementation of the HCND method in a state-of-the-art numerical

solver that is YALES2 along with the coupling library OpenPalm further described in the next section.

6.1.5 Application to a confined turbulent premixed flame

References: [A2], [T2]

Numerical setup A multiphysics simulation is applied to a confined premixed swirling flame [86, 87] whose stabilization has been shown to be sensitive to the wall conditions as in other similar flames [170, 221, 194, 50]. On the combustion modelling side, this requires to describe the effect of non-adiabaticity due to heat losses on the flame structure and its stabilization [119, 227, 152, 153]. The flame has previously been simulated successfully by Mercier et al. [153] with a non-coupled and stand-alone LES based on a non-adiabatic F-TACLES (Filtered Tabulated Chemistry for LES) model. The wall temperature profiles were then specified from the experimental ones that were measured by Laser Induced Phosphorescence. The main objective of this study is to predict this wall temperature field in order to retrieve the combustor characteristics in terms of flame stabilization and wall heat losses without any prior knowledge from the experimental data.

The numerical setup used to describe the reactive turbulent flow (mesh, models, code YALES2) is identical to the one of Mercier et al. [153]. Conjugate heat transfer is described by solving for heat conduction in the quartz viewing windows of the combustor with the accelerated Hybrid-Cell Neumann-Dirichlet coupling method. All exchanged data between solvers are communicated with the coupling library OpenPALM [22] which is developed for massively parallel coupled simulations. Flexibility in the coupling settings and efficiency are gained thanks to OpenPALM which provides generic coupling subroutines, and handles the efficient and scalable dispatching of the sent information to the correct recipient. On the one hand, the LES mesh is made 49 million elements and the YALES2 LES solver is assigned with 960 cpu cores. On the other hand, the solid domain comprises 41 million elements and the wall heat transfer solver uses 95 cpu cores. The external side of the combustor walls is specified as a mixed boundary condition with a profile for the free-convection heat transfer coefficient and the accounting for non-linear radiative exchange between the combustor wall and the surrounding ambient temperature. The coupling period is not known *a priori* and the figure 6.6 shows the predicted value for Δt_{cpl} by the HCND method during the coupled simulation.

Results Laser Induced Phosphorescence (LIP) measurements of temperature are compared to the computed field in Fig. 6.7. The results of the CHT numerical study provides a good agreement with the experimental values with a maximal local error of approximatively 10%. The similar shape of iso-lines shows that the simulated reactive flow provided by the numerical and modelling approach described in [153] is well described with its characteristics: recirculation zones and swirling motion. The level of agreement is then very satisfactory and accounting for the neglected thermal radiation should narrow the gap between experimental and numerical fields. The coupling with simulation of radiative energy transfer is the topic of the next section.

The detailed unsteady multiphysics simulation enables to study the temporal variations in temperature and heat fluxes at the walls. The access to this unsteady thermal load on the combustor walls is necessary to assess the thermal fatigue in the future as highlighted previously.

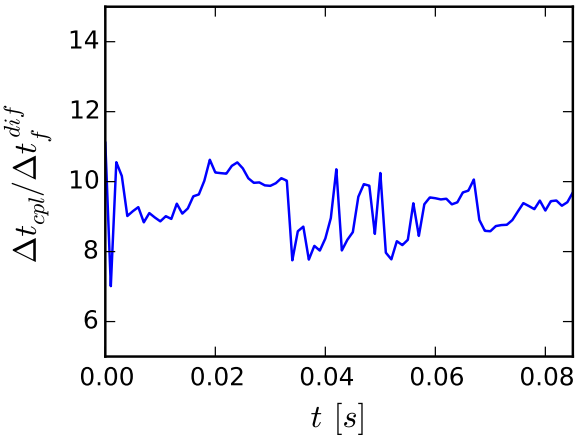

Figure 6.6: Temporal evolution of the self-adaptive coupling time step scaled by the flow solver diffusive time step, for flow-wall coupling (CASE-FW), with time origin taken at the begining of the run. Error tolerance is set to $\eta = 5\%$ for the HCND control algorithm.

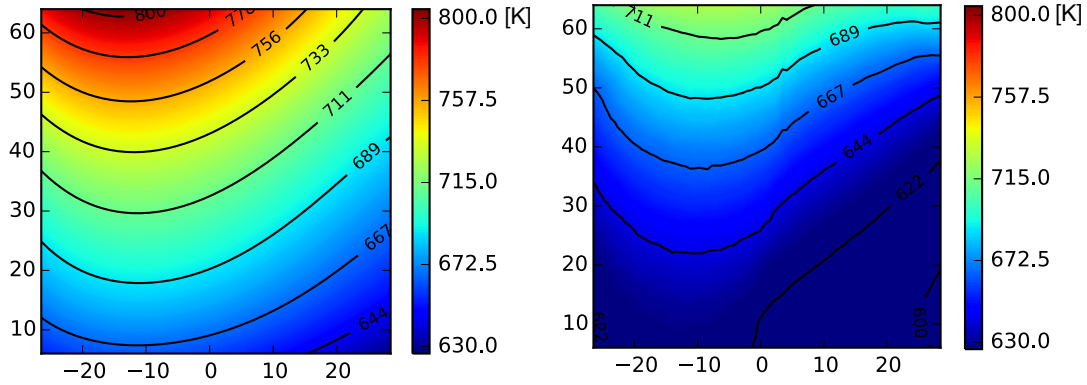

Figure 6.7: Wall temperature (in Kelvin) over the measurements zone (lengths in mm). (a): experimentally measured temperature values [153]. (b): numerically computed wall temperature.

Figure 6.8 shows root-mean-square fields in the experimentally studied window for CASE-FW which is the present coupled CHT simulation, and for CASE-FWR which additionally account for radiation. In CASE-FW, the fluctuations in wall temperature and wall conductive flux present a similar pattern, highlighting the correlation between both quantities as also deduced from Eq. 6.6. The level of relative variation in the considered zone is approximatively 20% for the wall conductive flux and a little less than 1% for the wall temperature.

In CASE-FWR, the observed maximum value of wall temperature RMS is reduced but the field is more homogeneous, yielding a similar average level of relative variations ($\approx 1\%$). Similarly, with a roughly similar level of variations ($\approx 20\%$), the RMS in wall conductive flux is larger in CASE-FWR because of the increased steady wall conductive flux in the observed zone. Finally, the amplitude of variations in wall radiative flux is around 8%. Compared to CASE-FW, no clear correlation appears between the RMS in wall temperature and either of the wall fluxes. Unfortunately, no validation data is available for this RMS fields. Nevertheless, we believe that

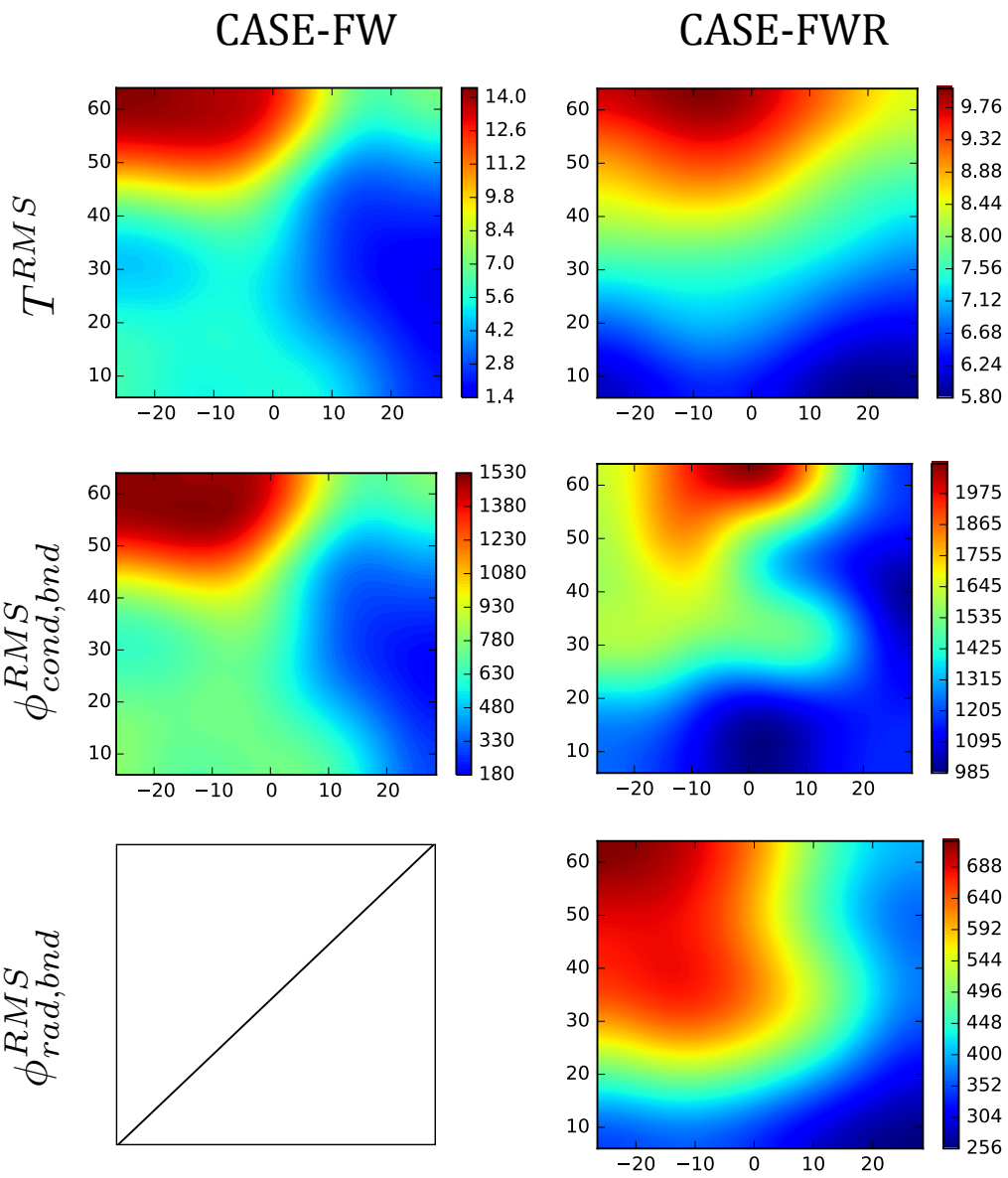

Figure 6.8: RMS of wall temperature [K] (top), wall conductive heat flux [W/m^2] (middle) and wall radiative flux [W/m^2] (bottom) for cases CASE-FW (left column) and CASE-FWR (right column).

experimental investigation similar to [218, 247] will provide such information in the near future in more and more configurations. This will challenge even more conjugate heat transfer studies with large-eddy simulations.

6.2 Thermal radiation in reactive flows

6.2.1 High-fidelity simulation of radiative heat transfer

The accurate prediction of heat flux and temperature at the combustor wall requires accounting for the coupling between the turbulent reactive flow, the heat conduction within the walls and the radiative energy transfer. The later phenomenon, radiation, has also been coupled to DNS or LES in different studies [241, 111, 81, 189, A17, 88, 13, A2]. Beside the better description of turbulence with LES, coupling LES with radiative heat transfer enables to alleviate most of the modelling issues of Turbulence-Radiation Interaction (TRI) [35, 36] which is significant in RANS simulations. Nevertheless, subgrid-scale TRI effects that are neglected in this work are not strictly negligible and sgs modelling studies can be found in [200, 215, 88].

Table 6.1: Short literature review of advances in coupled simulations of radiative heat transfer with DNS or LES. Gas radiative properties are described as: Gray Gas (GG), Global model (Glob.), narrow band CK model (CK), Line-By-Line (LBL). The type of radiation solver is also highlighted: Discrete-Ordinates Method (DOM), Monte Carlo (MC).

Year	Description	GG	Glob.	CK	LBL
2005	Wu et al. [241]: MC; DNS of a statistically 1D turbulent premixed flame	x			
	Jones and Paul [111]: DOM; LES of a gas turbine combustor	x			
2008	Gonçalves dos Santos et al. [81]: 2D ray tracing; 2D LES of a premixed flame stabilised behind a flame holder			x	
2012	Poitou et al. [189]: DOM; 3D LES of a premixed flame stabilised behind a flame holder		x		
2013	Zhang et al. [A17]: MC; DNS of a turbulent channel flow			x	
	Gupta et al. [88]: MC; LES of a turbulent jet flame				x
2016	Berger et al. [13]: DOM; LES of a helicopter combustion chamber		x		
2018	Koren et al. [A2]: MC; LES of laboratory-scale combustor with a premixed turbulent flame			x	

Table 6.1 shows the evolution of coupled numerical studies. Gas radiative properties initially described with a notoriously erroneous gray gas assumption are nowadays mainly modelled with global models (SLW-WSGG [48], FSK [157] and other full-spectrum variants) in practical applications while relying on Discrete-Ordinates Methods (DOM) to solve the radiative transfer equation. Advances in computational power and in Monte Carlo (MC) algorithms and solvers have allowed to achieve state-of-the-art results with such reference methods. Besides, very accurate gases properties can be accounted for with MC methods such as narrow band models (SNB, CK[82]) or even reference Line-By-Line (LBL) spectra. A review of infrared radiative properties of CO_2 and H_2O and models can be found in [220]. Note that CO_2 and H_2O are the main contributors to radiative heat transfer in most engineering applications. The short historical synthesis in Tab. 6.1 shows the firm trend towards involving more and more accurate solvers and gas radiative properties, and with the applications to more and more complex systems.

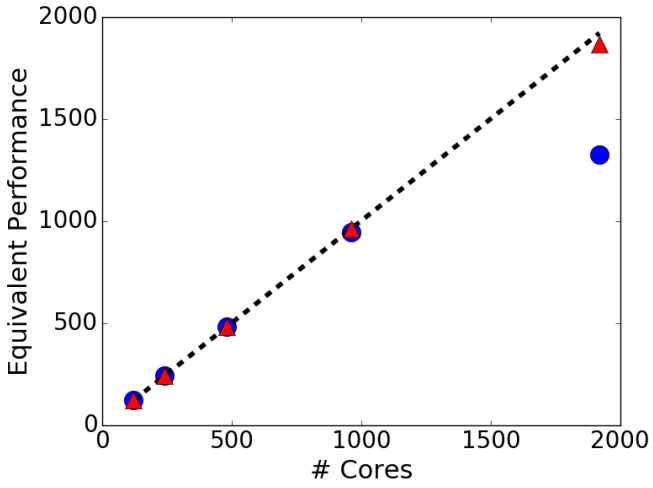

Figure 6.9: Scalability plot for a case of 8 millions cells on a cluster equipped with Intel E5-2690 processors. Blue circles: test performed with 200 rays; red triangles: test performed with 1000 rays; dashed line: ideal curve.

6.2.2 The Monte Carlo Rainier solver

References: [D10], [T1, T4, T6, T8]

The Rainier code developed by Olivier Gicquel solves the radiative transfer equation on unstructured 3D meshes with a reciprocal Monte-Carlo method, either ERM [223] or OERM [250]. The emision-based reciprocity principle of these methods allows the calculation of the radiative power at each node with a local control of the desired accuracy. Furthermore, the treatment of each mesh point independently from the others insures a high degree of scalability of the code as shown in Fig. 6.9. With a sufficient workload, the code scales almost ideally: 2000 cpu cores yield a computational result 2000 times faster. The error control is carried out with absolute and relative accuracy thresholds on the quantities of interest: radiative power, wall radiative fluxes, directional probes.

The radiative properties of CO_2 and H_2O species are modelled through a cK model based on updated parameters of Rivière and Soufiani [199]. For H_2O, 44 spectral bands, with widths varying from 50 cm^{-1} to 400 cm^{-1} are considered between 150 cm^{-1} and 9200 cm^{-1}. CO_2 absorbs radiation in only 17 of these bands. The cK database is made of 7-points Gauss quadrature per band for each gaseous component, leading to 1022 pseudo-spectral points, since 49 quadrature points are used in the 17 overlapping bands.

As illustration of the fields computed in Rainier, figure 6.10 shows the radiative power fields computed in the combustor studied in Sec. 6.1.5. The radiative power field is determined from the temperature (also shown in the figure) and the burnt gases composition fields of an instantaneous LES solution. The local radiative power is written as $P^{rad} = P_a^{rad} - P_e^{rad}$, the difference between the absorbed (P_a^{rad}) and emitted (P_e^{rad}) radiative powers. Most of the domain emits energy through radiative heat transfer (negative radiative power). The regions where energy absorption dominates (positive radiative power) are the coldest gas pockets mainly located near the walls. The middle subfigure only shows the emitted radiative power ($-P_e^{rad}$ is plotted) which is showed to be larger in magnitude than the real one (bottom figure) that accounts for the actual reabsorption. This difference outlines that an optically thin assumption that would neglect absorption phenomena for all the spectrum wavelength is wrong, even for

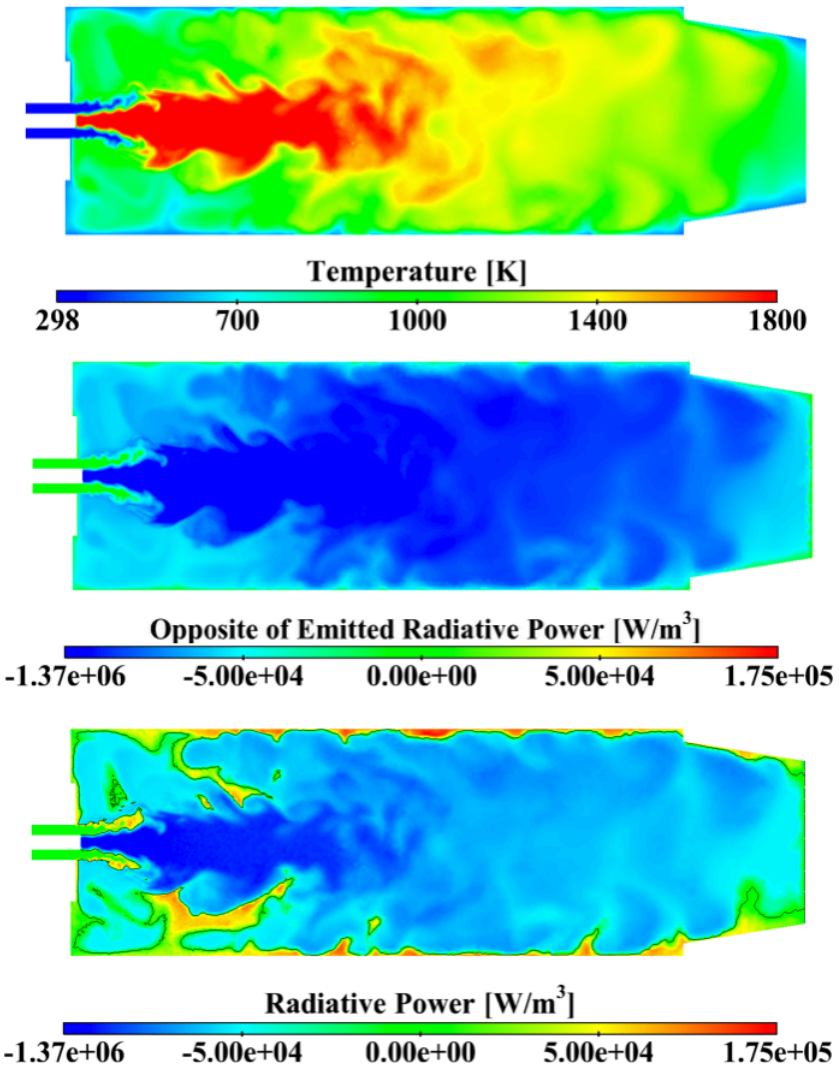

Figure 6.10: Computation of radiative fields for the combustor studied in Sec. 6.1.5. Top: Instantaneous temperature field on the center plane. Middle: Radiative power $-P_e^{rad}$ (emission only). Bottom: Radiative power $P^{rad} = P_a^{rad} - P_e^{rad}$ with emission and absorption accounted for.

the considered atmospheric combustor of a moderate size. In the combustion community, this optically thin assumption is often wrongly used in many studies which overlook the necessary detailed resolution of the radiative transfer equation.

6.2.3 Quasi Monte Carlo method

References: [D10], [T4, T6, T8]

Thanks to their statistical estimation of the radiative power and associated error control, Monte Carlo methods provide reference results. Moreover, the accounting for spectral gas radiative properties or complex geometries is straightforward. This makes this family of methods a promising candidate for coupled high-fidelity simulations. However, the drawback of all these methods is their slow convergence, making them very much computationally intensive. Several variance reduction techniques [47, 140] such as importance sampling [46, 114, 63, 250] strongly accelerates the convergence by favouring more meaningful photon rays in the computed quantity of interest. An additional improvement is the use of an alternative sampling mechanism for numerical integration usually referred to as *Quasi-Monte Carlo* integration [140]. This method has barely been studied for the numerical resolution of thermal radiation, we have used it to demonstrate its undeniable efficiency to solve 3D participating media problem such as the ones met in combustors. Besides, Quasi-Monte Carlo simulations can be combined with any variance reduction technique.

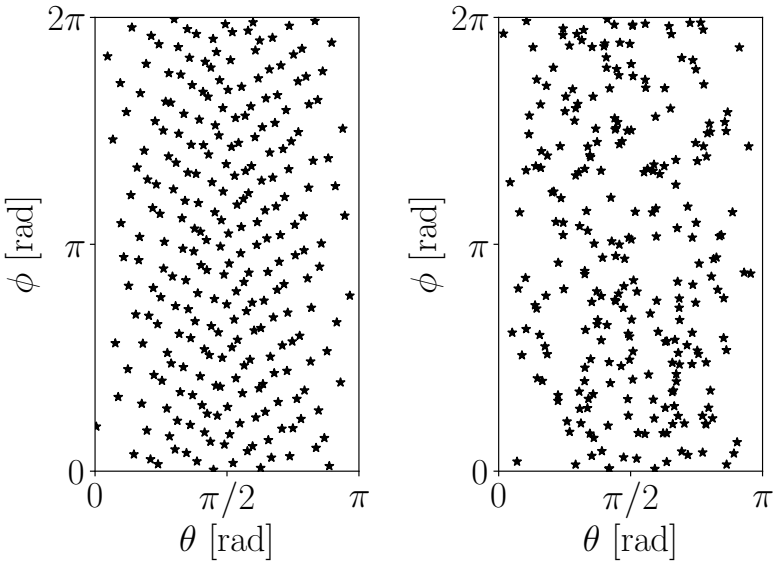

Figure 6.11: Comparison of the sampling of polar (θ) and azimuthal angle (ψ) following the probability density function $\frac{1}{4\pi}\sin(\theta)d\theta d\psi$ using a Sobol sequence (left) and a classic purely random sequence (right).

In Quasi Monte Carlo, the pure random sampling generator is replaced by a quasi-random (also called low-discrepancy) deterministic sampling. The samples' greater uniformity achieved by low-discrepancy sequences is shown in Fig. 6.11. This results in the enhancing the convergence rate of the integration method. In our work, a Sobol sequence is used following the construction from [19]. In order to keep an estimation of the integration error and the associated dynamic error control, the method is combined with a randomization technique, yielding a *Randomized Quasi-Monte Carlo* [140]: for a total of N samples, n packages are considered; within each of this package, a low-discrepancy sequence of N/n points is used; the n sequences of the packages are randomized using an I-binomial scrambling [224]. This Randomized Quasi-Monte Carlo approach allows for benefitting from the faster convergence rate of Quasi-Monte Carlo within each package and to have an estimation of the error using the variance between the packages,

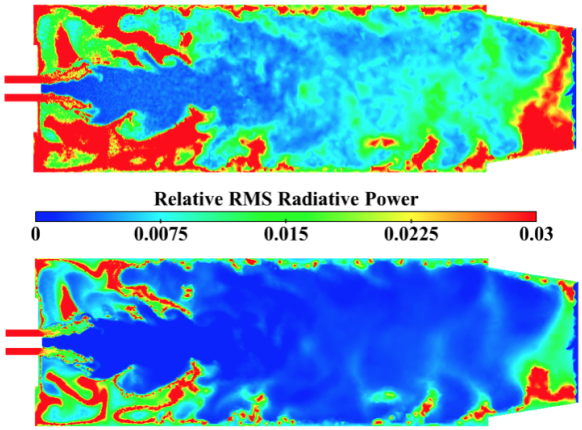

Figure 6.12: Instantaneous field of standard deviation of radiative power obtained with Monte Carlo OERM (top) and Quasi-Monte Carlo OERM (bottom) at imposed number of rays.

as it is done classically for the Monte Carlo method. Figure 6.12 shows the error of the OERM method combined with either regular Monte Carlo sampling or Quasi-Monte Carlo. The Quasi Monte Carlo error is significantly lower. Hence, practical computation with local control of the convergence of the radiative power exhibits almost a threefold speedup with Quasi Monte Carlo. This significant improvement in computational efficiency makes such a method ideal for expansive coupled simulations.

6.2.4 Prediction of radiative heat transfer from a turbulent sooted jet flame

References: [D5], [T6]

Accounting for soot in thermal radiation Taking into account the contribution of soot particles in the radiative heat transfer from sooted turbulent flames requires the modelling of these particles evolution and of the complex coupling that exists between soot, turbulence and thermal radiation. Several RANS studies have been carried out while few LES works have addressed this challenge. Table 6.2 gathers a couple of these studies to highlight the different soot radiation and formation models that have been considered. They also differ in their description of gas radiative properties, which is not detailed here. With the exception of Mehta et al. [151], all studies solving the radiative transfer equation rely on empirical or semi-empirical models for the soot formation. This introduces strong uncertainties in the prediction of soot particles emission, which penalises the validation of such computations. Additionally, the radiative properties of soot aggregates is complex: the complex refraction index of soot material is uncertain, radiation scattering is a new phenomenon that appears in presence of particles and the detailed morphology of soot fractal aggregates also impact significantly the soot particles extinction coefficient [248, 173]. Table 6.2 shows that all studies have so far retained soot radiative properties from Rayleigh theory valid for small spherical particles.

These different limitations and associated challenges make the characterization and understanding of soot formation and radiation a very active area of research. Soot radiative properties are not only involved in heat transfer but also appear as key quantities in quantitative measurement of soot with optical diagnostics.

Table 6.2: Short literature review of coupled simulation with luminous radiation. The soot radiation model and the type of radiation solver are given in the third column. The fourth column indicates the type of soot formation model

Approach	Reference	Soot radiation model	Soot formation model
RANS	Tesse et al., 2004 [222]	Rayleigh + MC	Empirical
	Wang et al., 2005 [236]	Rayleigh + S_n	Empirical
	Mehta et al., 2010 [151]	Rayleigh + MC	Method of moments
	Consalvi and Nmira, 2016 [44]	Rayleigh + FVM	Semi-Empirical
LES	Mueller and Pitsch, 2012 [162]	Optically thin assumption	Method of moments
	Gupta et al., 2013 [88]	Rayleigh + MC	Empirical
	Lecocq et al., 2014 [137]	Rayleigh + DOM	Semi-Empirical

Numerical setup The large-eddy simulation of a sooted jet flame presented in Sec. 4.3.3 has been coupled to the Rainier solver to additionally describe radiative heat transfer from burnt gases and the predicted soot particles. The coupled simulation benefits from the developed Quasi Monte Carlo method.

For the radiation of soot particles, 93 spectral bands have been introduced between 150 and 29 000 cm^{-1}, of which 44 are common to the gas. Radiation scattering by soot particles is neglected in the present simulation. The complex index of refraction of soot particles is taken as equal to $m = n - ik = 1.57 - 0.56i$ [213]. Then, the soot absorption coefficient κ_ν^{soot} is modelled using the RDG-FA theory for soot aggregates' radiative properties. However, without describing scattering, it is equivalent to the one obtained from Rayleigh's theory [156]:

$$\kappa_\nu^{soot} = C_0 f_V \nu \text{ with } C_0 = \frac{36\pi nk}{(n^2 - k^2 + 2)^2 + 4n^2k^2} \tag{6.8}$$

Both codes AVBP and RAINIER are coupled with the Open-palm library and use the same mesh. The radiative power field is updated based on the temperature, X_{CO_2}, X_{H_2O} and soot volume fractions fields provided by the LES solver every 70 iterations of the flow solver in order to preserve a relative error lower than 3% on the computed radiative power. In the following, gaseous predictions with the coupled simulation are compared with experiments and two other computations: one considering neither radiation nor soot particles formation and the computation from Sec. 4.3.3 that considered an optically thin radiation model for both both gaseous and solid phases. The cost for the simulation of the adiabatic case without considering soot sectional model is 150 000 cpu hours for a 250-ms averaging time of statistics. With the same cores and for the same physical time, the cost of the uncoupled and coupled simulations, both considering soot sectional modelling, are 600 000 and 1 200 000 cpu hours, respectively.

The coupled simulation gathers: a state-of-the-art LES describing soot formation with a sectional model, a Monte Carlo resolution of radiative transfer, accurate gas radiative properties and a spectral description of soot properties through Rayleigh theory. While uncertainties remain in the soot formation and radiation model, the present study achieves a significant progress.

Results Figure 6.13(a) presents the evolution of predicted axial temperature profiles for the three simulation cases: adiabatic hypothesis (ADIAB), optically thin (OPT) and coupled Monte-Carlo (MC). While for the first part of the flame, the temperature profiles are quite similar,

the downstream temperature decrease is largely impacted by the hypothesis done for thermal radiation. The lowest decrease rate is obtained for the computation without radiation whereas the highest decrease rate is obtained for the computation with the optically thin radiation model. The coupled simulation, which accounts for reabsorption, presents lower radiation heat losses and therefore, an intermediate temperature decrease rate.

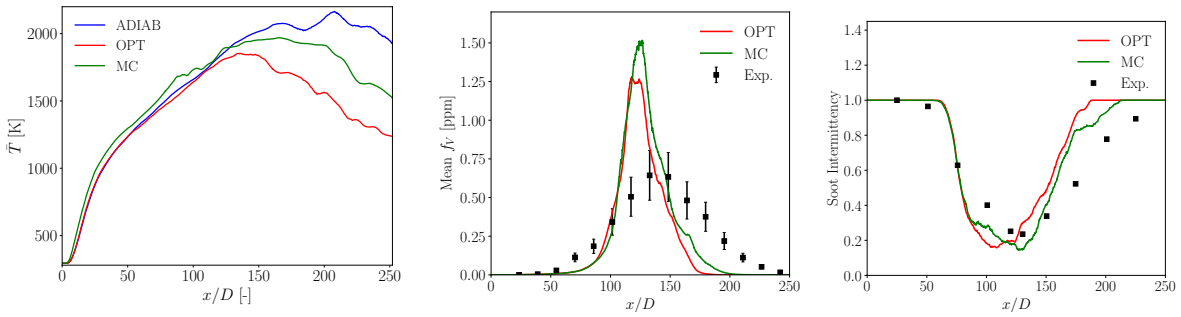

(a) Axial numerical temperature profile

(b) Soot volume fraction axial profile

(c) Soot intermittency axial profile

Figure 6.13: (a) Temperature axial profile for the different studied cases: ADIAB (blue), OPT (red) and MC (green) solid lines. (b,c) Impact of radiation modelling on soot volume fraction (b) and intermittency (c) predictions. Experimental measurements from [104] are presented in black squares.

Figure 6.13(b) presents a comparison of axial soot volume fraction profiles with experiments for two different simulations. Figure 6.13(c) compares the axial profiles of soot intermittency for both computations. First, for both quantities and for both computations, a good agreement between predictions and experimental data is observed. It can be noticed that soot depletion due to oxidation is predicted too soon compared with experiments. Secondly, detailed radiation modelling impacts slightly these results compared to results obtained with optically thin radiation model: Soot oxidation is predicted slightly later than in the optically thin radiation computation case. Achieving significantly better soot predictions is then not related here with radiation modelling as it impacts the flow mostly downstream the soot oxidation. The remaining error is therefore rather due to the uncertainties that remain in soot modelling.

Figure 6.14 compares the axial and radial profiles of radiant intensities computed by directional probes in Rainier with experimental measurements. The gaseous contribution from CO_2 and H_2O species is distinguished from the total contribution when taking into account both gaseous and solid phases. It can be observed that for the results with the total contribution, a good agreement with the experiments is observed. Comparing these results with the ones obtained for only the gaseous contribution, one can see that soot particles are an important contributor of the axial directive intensity for this flame. The discrepancies with the experimental results are mainly due to the differences observed in soot predictions (see Sec. 4.3.3). Indeed, for the heights where soot volume fraction profiles are well predicted ($x/D = 135$ and $x/D = 175$), good predictions in radial profiles of radiative intensities are also obtained. The predictions are globally in a reasonable agreement with experimental measurements.

Analysis The soot formation being localised in a finite volume, the major contributor in radiative power can be either the gas or the soot phase depending on the position. In order to investigate the role of gaseous participating species and soot particles in the total volume integrated radiative power, four separate computations have been carried out for one representative

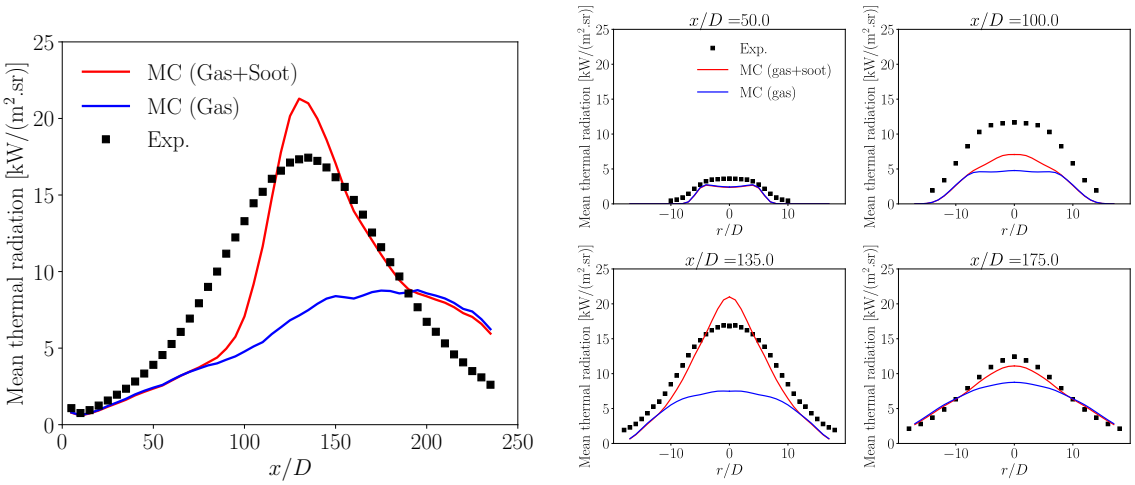

(a) Axial profile (b) Radial profiles

Figure 6.14: Comparison between experimental radiative intensity profiles from [104] and numerical predictions with the Monte-Carlo approach. The contributions of only gaseous phase is plotted in blue, whereas total contributions are plotted in red.

instantaneous field: one considering only gas emission and gas absorption (computation GEGA), one considering only gas emission and soot absorption (computation GESA), one considering only soot emission and gas absorption (computation SEGA) and one considering only soot emission and soot absorption (computation SESA). Several observations could be done from these computations:

- Approximatively 56% of the emitted power from the gaseous phase is reabsorbed by the gaseous phase,
- Less than 0.5% of the emitted power from the gaseous phase is reabsorbed by the soot phase,
- Approximatively 10% of the emitted power from the soot phase is reabsorbed by the soot phase,
- Less than 2% of the emitted power from the soot phase is reabsorbed by the gaseous phase,
- Even if for regions of high soot volume fraction soot particles are the major contributors of radiative transfer, soot particles only account for 21% of the total volume integrated radiative power.

Reabsorption phenomena are then more important for the gaseous phase. Reabsorption only slightly modifies soot total contribution to radiative power. Moreover, very small interactions are observed between soot particles and gaseous species in terms of radiative transfer: soot only slightly absorbs gaseous emission, and gas absorbs little of soot emission. The corresponding spectral volume-integrated emission and absorption of the different cases are presented in Fig. 6.15. Two cK bands from CO_2 are the major contributors of gaseous emissions (from 2000 to 2500 cm^{-1}). For these bands, important gas absorption is also observed. For soot particles, soot absorption coefficient presents a continuous wide band spectrum and lower reabsorption for soot particles is observed. Finally, gaseous reabsorption from soot emission is negligible and is only observed for the two bands mostly responsible for gaseous emissions.

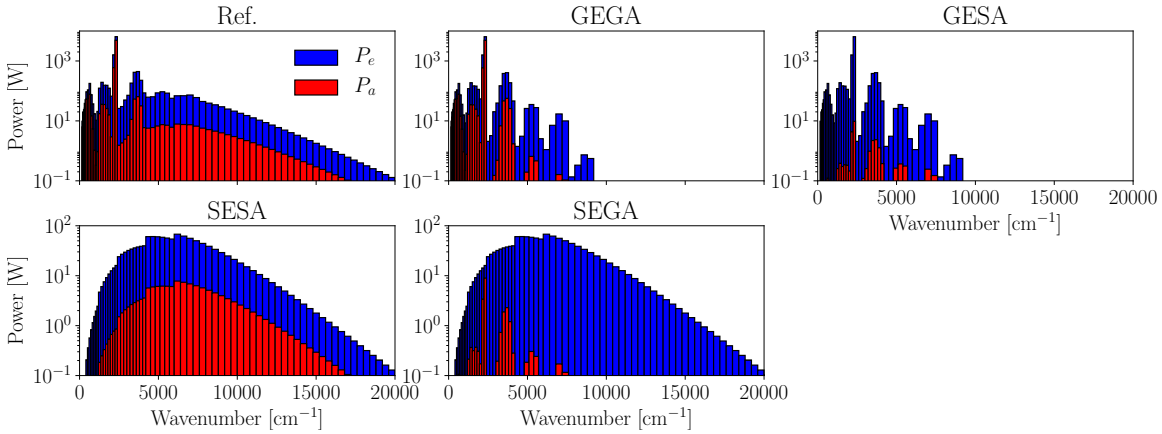

Figure 6.15: Spectral emitted and absorbed volume-integrated powers for an LES instantaneous solution. Results are shown for the reference case (Ref.) taking into account gas and soot particles emission and absorption and the four other studied cases: GEGA, GESA, SEGA and SESA.

The nature of radiative transfer in terms of optical thickness was identified for both solid and gaseous phases with spectra of transmissivity: For several gas bands, in particular the ones contributing to the radiative power, the optically thin medium assumption is not valid and reabsorption must be considered. Concerning soot particles, the optically thin medium is not valid at high wavenumbers for regions with high values of soot volume fraction.

Finally, the effects of turbulence-radiation interaction (TRI) on the average radiative power have been studied from the resolved LES fields: TRI effects increase slightly the radiative power contribution from gas while it decreases significantly the one from soot particles. This effect of soot dynamic is due to the intermittent behaviour of soot formation and the associated intense level of fluctuations previously outlined in Sec. 4.3.3. This negative soot contribution to TRI has also been observed in recent RANS studies [44, 43].

6.2.5 Role of radiation in a confined turbulent premixed flame

References: [A2], [T2]

The conjugate heat transfer study from Sec. 6.1.5 is here enriched with the description of radiative energy transfer. Figure 6.10 previously demonstrated that an optically thin approximation would lead wrong results. Since the considered lean premixed flame is not sooty, radiative emission and absorption from burnt gases is only taken into account. In order to make the simulation affordable, the Monte Carlo Rainier solver works on a coarser mesh (8 million elements) than the LES solver. For this fully coupled simulation (LES+MC+CHT) that did not benefit at that time from the Quasi-Monte-Carlo method, the cpu cores repartition is as follows: 256 for the reactive LES solver YALES2, 48 for the wall heat transfer solver from YALES2 and 991 for Rainier. The coupled case with radiation (denoted as CASE-FWR) is therefore 8.5 times more expansive than the coupled case without radiation (denoted as CASE-FW).

The difference of mean gaseous temperature for cases CASE-FW and CASE- FWR is shown for the center longitudinal plane in Fig. 6.16. The temperature maximum remains the same because the sudden temperature increase through the flame front is only marginally impacted by radiation. In the rest of the chamber, the radiative energy transfer homogenises the temperature

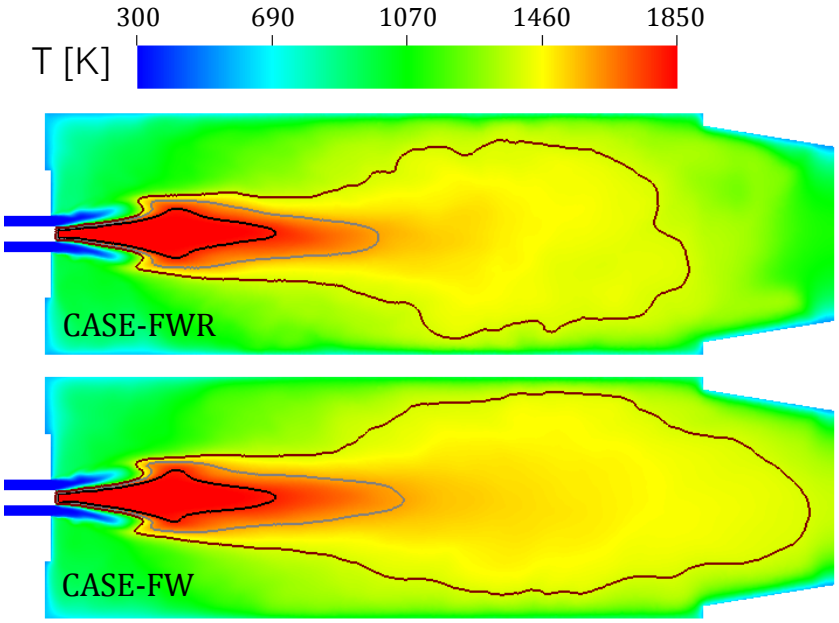

Figure 6.16: Mean temperature on center plane for CASE-FWR (top) and CASE-FW (bottom). Iso-lines are given for T=1800 K (black solid line), T=1600 K (gray solid line) and T=1400 K (brown solid line).

differences. Downstream the flame, hot burnt gases are seen to be cooler when radiation is taken into account. This is outlined by the noticeable difference for the $T = 1400$ K iso-line. On the other hand, the cold burnt gases at the bottom of the chamber are in fact hotter for CASE-FWR because of the radiation absorbed by the walls which yields a higher wall temperature as seen hereafter.

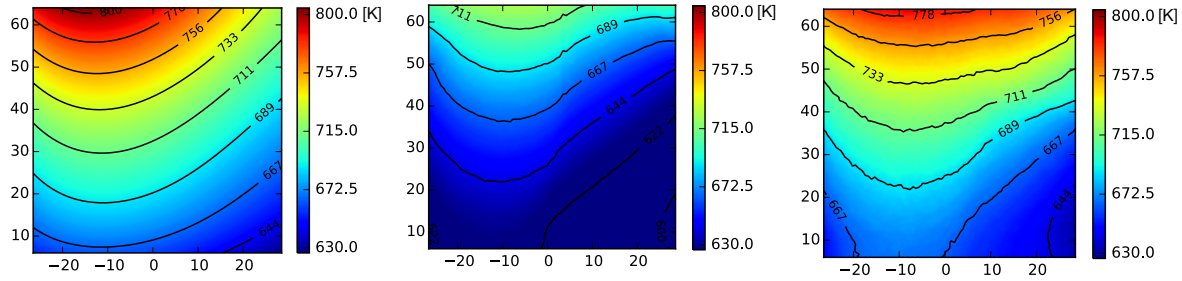

Figure 6.17: Wall temperature (in Kelvin) over the measurements zone (lengths in mm). (a): experimentally measured temperature values [153]. (b): computed wall temperature in CASE-FW without radiation. (c): computed wall temperature in CASE-FWR with radiation.

The predicted wall temperature fields in the measured region of the combustor wall are in Fig. 6.17. The first two figures are the one from Sec. 6.1.5 with the 10%-accurate field from CASE-FW. When radiation from burnt gases and quartz walls is taken into account, CASE-FWR (right subfigure) shows numerical predictions which are noticeably improved with a maximal local error of about 3% and an average error of 2%. The previous underestimation of the wall temperature is then due to the neglected radiative effects. However, further analysis reveals that

the picture is not as simple. Indeed, in CASE-FWR, the contribution of the wall radiative flux in the total wall heat flux is larger than 50%!

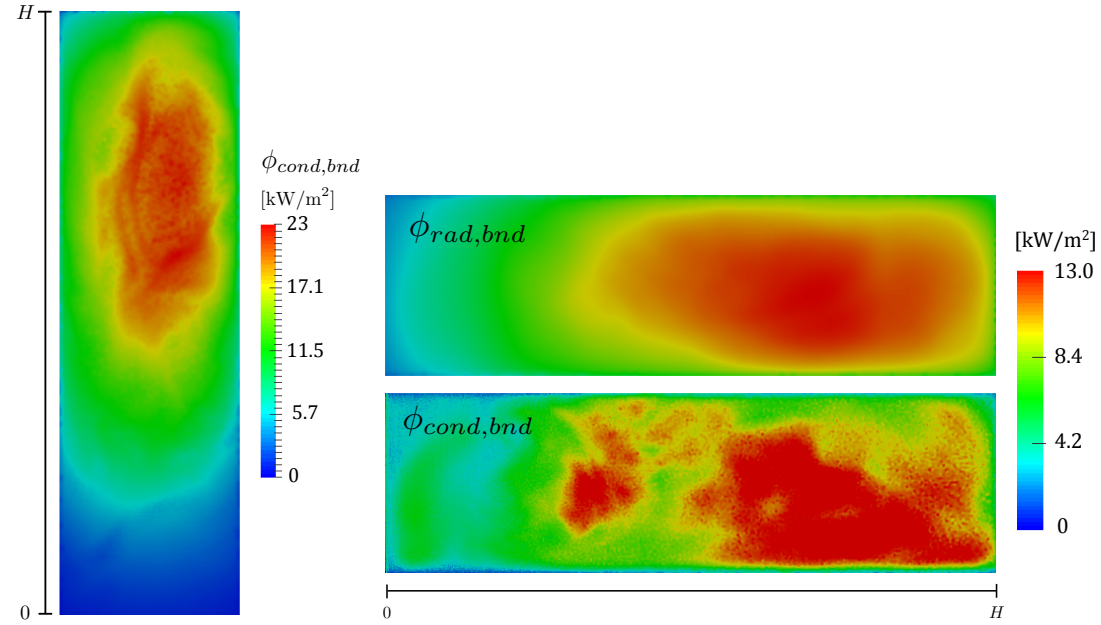

(a) CASE-FW wall conductive flux

(b) CASE-FWR wall heat fluxes

Figure 6.18: (a) Wall conductive heat flux for CASE-FW. (b) Wall radiative (top) and conductive (bottom) heat flux for CASE-FWR.

Figure 6.18 shows the wall heat fluxes for both cases along the full height of the quart window. In CASE-FW, only one flux is present: $\phi_{cond,bnd}$, the boundary conductive flux due to convective heat transfer from the hot gases to the wall. The total wall heat flux in CASE-FWR is the sum of two contribution: $\phi_{cond,bnd}$ and the wall radiative flux $\phi_{cond,rad}$. As seen in Fig. 6.18(b), both contributions in the fully coupled simulatio CASE-FWR have the same order of magnitude. Surprisingly, the wall conductive flux in CASE-FWR is quite reduced compared to CASE-FW. Let us explain this. Thermal radiation is an additional energy transfer mechanism that attenuate temperature differences between gas cells and also between the gas temperature and the wall temperature. Hence, when radiation is included, it is expected that the walls become hotter (see Fig. 6.17) while the burnt gases become cooler (see Fig. 6.16). After the thermal transient, the reduced temperature difference between the burnt gases and the walls induces a reduced wall conductive flux: $\phi_{cond,bnd}$ is indeed roughly halved when considering radiation. In CASE-FWR, the reduced wall conductive flux is finally compensated by an additional contribution from the wall radiative flux. This feed-back loop of radiative transfer on the wall conductive flux explains why the total wall fluxes in the CASE-FWR is simply not the conductive flux from the CASE-FW with an additional contribution due to the radiation.

What remains unexplained is the fact that the compensation from this feed-back loop lead roughly to the same wall temperature although the nature of the wall fluxes in the CASE-FWR is so different. This is because, in the studied configuration, the CASE-FW wall conductive heat flux, which is overestimated compared to reality, surprisingly accounts approximatively for the total wall heat flux (radiative and conductive) in case FWR.

6.2.6 Multiphysics simulation of the FIRST combustor

References: [A4], [T6]

Configuration and numerical setup In this section, results of a coupled simulation combining large-eddy simulation, conjugate heat transfer and thermal radiation is carried out on the combustor FIRST studied in DLR [74] which features a pressurised sooting ethylene/air flame. This configuration is of great interest in the combustion community as it is a first-of-its-kind setup where soot modelling can be challenged for turbulent swirled flames in pressurised conditions. The configuration shown in Fig. 6.19(a) is one of the target flame of the International Sooting Flame (ISF) workshop. Nowadays, this laboratory-scale setup is the closest to the ones met in realistic gas turbines. Several numerical studies have investigated this setup [69, 52, 127, 240] without much attention paid to the combustor heat transfer mechanisms. The nominal operating point studied in this work is characterised by a 3-bar pressure and an equivalence ratio at the injectors level of $\Phi = 1.2$. A secondary air stream is injected through four ducts located at a height of 80 mm downstream the main injectors leading to a global equivalence ratio of $\Phi_{global} = 0.86$.

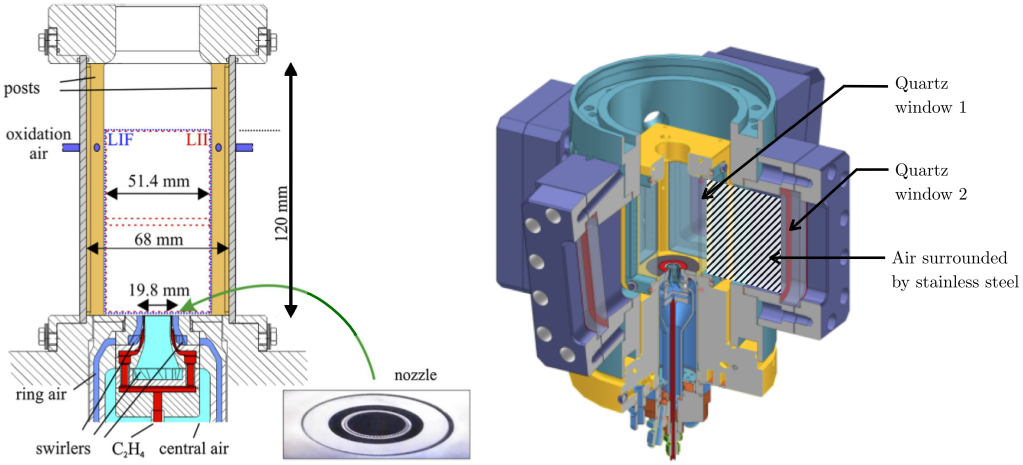

(a) (b)

Figure 6.19: (a) Burner and combustor of the FIRST test rig in DLR. (b) Design of burner, combustion chamber and optical module of pressure housing.

In order to provide an external boundary condition for the computation of heat conduction within the combustor walls, a dedicated study was necessary to model the complex external environment of the combustor. Figure 6.19(b) shows that the optical access into the combustion chamber is provided through four separate quartz windows, collectively labelled as quartz windows 1. Cooling of the quartz windows 1 is established through multiple transverse laminar air jets on the outer face, i.e. outside of the combustion chamber. The combustion chamber is finally surrounded by the stainless steel pressure housing equipped with four other quartz windows (denoted quartz windows 2) for optical access to the combustion chamber. The modelling study of this complex environment has carefully assessed the assumptions and their sensitivity. In particular, a specific care is addressed here to the semi-transparent nature of the quartz viewing windows. For the first time in radiative heat transfer simulations of combustors, the transparent or opaque nature of such windows with wavenumber will be here considered (see Fig. 6.20(a)). Given the number of laboratory-scale combustor equipped with such viewing windows, the

Table 6.3: Relative computational cost of different simulations of the DLR test rig.

Simulation	Relative cost
Adiabatic LES (FPV)	1
Non-adiabatic LES (RFPV)	1.1
Non-adiabatic LES + Soot	4
Non-adiabatic LES + Soot + CHT	4.5
Non-adiabatic LES + Soot + CHT + MC	9

number of coupled studies dealing with the impact of semitransparent windows is expecting to grow rapidly.

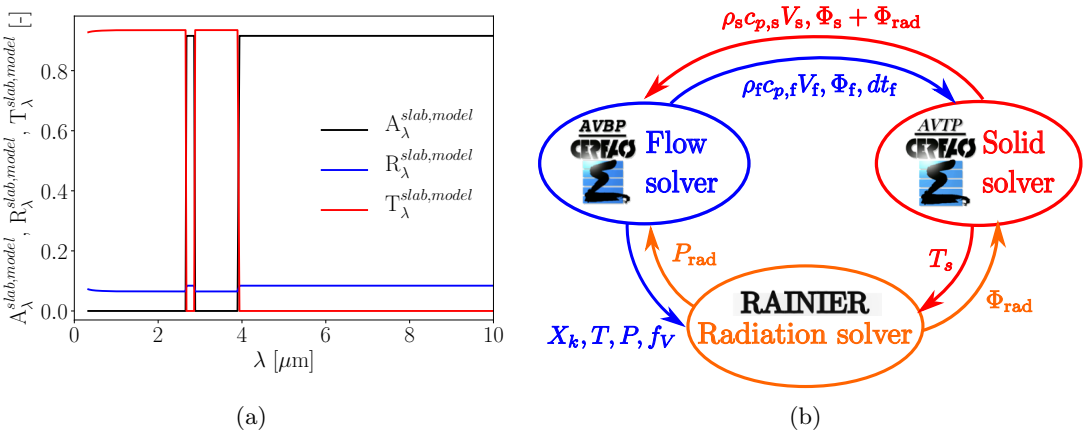

(a) (b)

Figure 6.20: (a) Transparent and non-transparent spectral band model for a 3-mm thickness Corning HPFS 7980 quartz. (b) Communication scheme between the three solvers.

The large-eddy simulation of the turbulent reactive and sooting flow follows the same modelling setup (RFPV + section model) as in Secs. 4.3.3 and 6.2.4 with the solver AVBP. The accelerated HCND coupling method is used with the wall heat transfer solver AVTP. Finally, similarly to the simulated sooted jet flame in Sec. 6.2.4, the Quasi-Monte-Carlo method from the Rainier solver is here used with ERM to solve radiative transfer between burnt gases, soot particles and the combustor windows considered semi-transparent. The communication scheme between the three solvers is shown in Fig. 6.20(b). The solver meshes are composed of 45 million, 16 million and 13 million elements for AVBP, AVTP and Rainier, respectively. Table 6.3 represents the computational cost of the different simulations that have been performed. The adiabatic case based on the FPV flamelet model and without the section model transport equation is taken as the reference for the reported computational cost. The final coupled simulation is almost ten times more expansive than the adiabatic case. However, compared to the already expansive soot sectional model, the cost to add detailed radiation is only twofold. Note that without the Quasi-Monte-Carlo acceleration, the cost would have been doubled.

Results The gaseous temperature field computed by the fully coupled simulation is shown in Fig. 6.21(a). It is the result of several captured phenomena:

- Combustion yields to the sharp raise of temperature from the fresh gases temperature. In cases without radiation (adiabatic or CHT alone), the flame stabilises in the injector

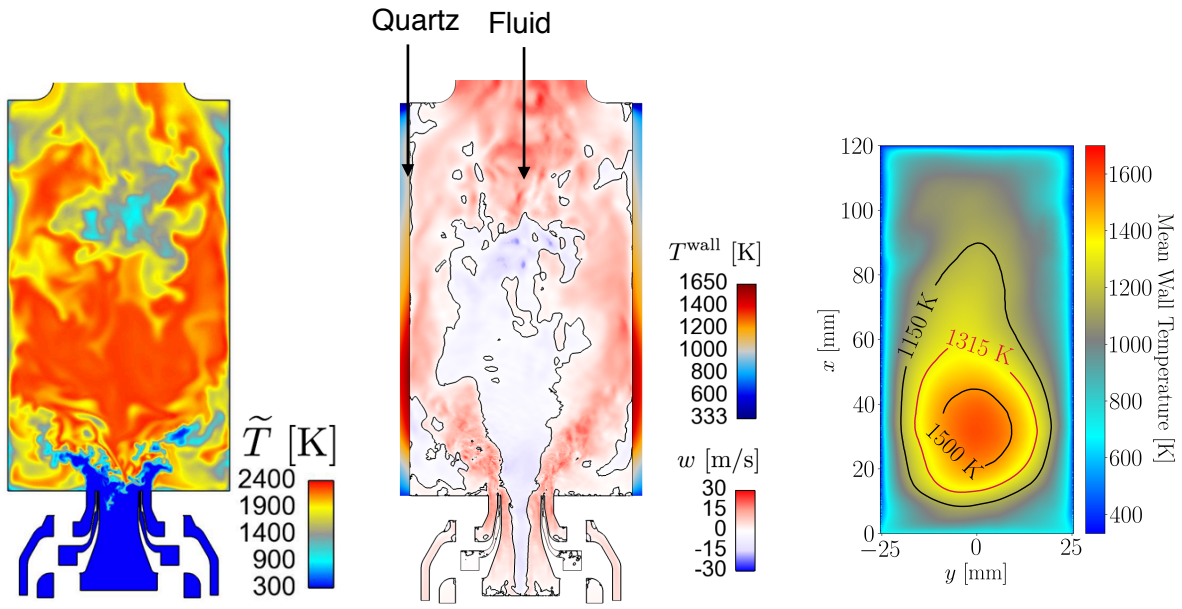

(a) (b) (c)

Figure 6.21: (a) Temperature field inside the combustor predicted by the fully coupled simulation (CHT+MC). (b) Flow field and wall temperature on the same longitudinal cut. (c) Corresponding combustor wall temperature (inner side) .

whereas, when radiation is taken into account, the flame is stabilised in the combustion chamber as seen in the experiment.

- Downstream cold gases from secondary air inlets in the FIRST combustor are entrained in the inner recirculation zone (IRZ). Thus, a mixing between these cold air gases and the hot burnt gases from combustion is observed and a lower temperature in the IRZ is obtained.
- The pockets of burnt gases near the walls are cooled down by the predicted wall heat losses. This is particularly visible in the outer recirculating zone (ORZ). The cooled burnt gases then mix with the other regions.
- Radiation emission and reabsorption generate an additional source term which can be either positive or negative as seen in Fig. 6.22 (right). A negative radiative power is computed in the hotter pockets of burnt gases while the cooler ones near the wall or in he IRZ reabsorbs radiation, yielding a positive radiative power. In this pressurised combustor, the medium is relatively optically thick and makes an optically thin approximation totally erroneous as seen in Fig. 6.22.

Figure 6.21(b) shows that the flow in the combustor makes the hot gases impinge on the windows. This generates high convective fluxes on the walls with a maximum occurring at approximatively one-third of the chamber height. The corresponding computed wall temperature is seen in Fig. 6.21(c). The low temperature at the bottom side (650 K) of the window is prescribed from the estimated temperature on the combustor flange in the experiment. The four copper posts located at the chamber corners and that surround each window are accounted for in the wall heat transfer simulation. They are cooled at 333 K and yields the low temperature seen on the sides of Fig. 6.21(c). These boundary conditions explain the obtained bi-dimensionality of the wall temperature field with a maximum temperature located where the wall convective flux is maximum. The maximum temperature is well above the quartz annealing temperature and

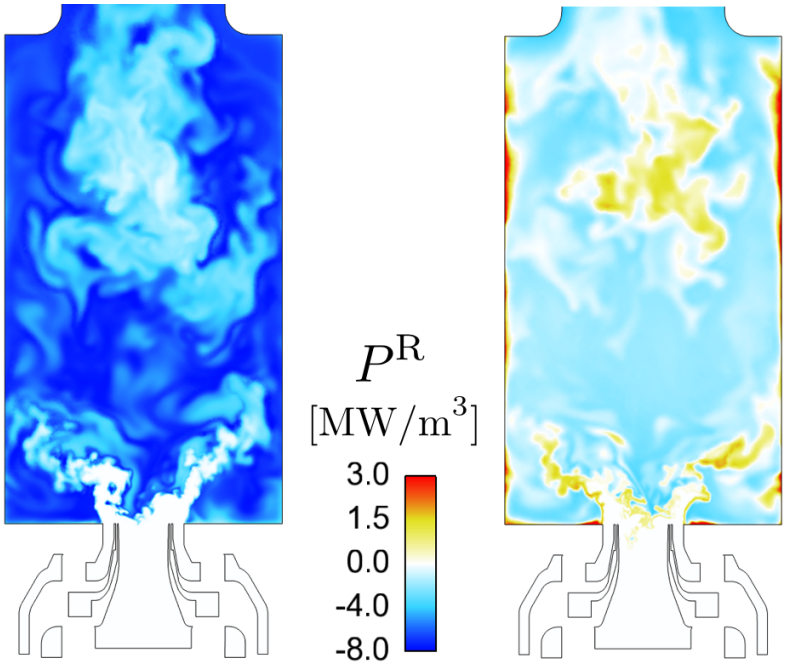

Figure 6.22: Comparison between radiative powers instantaneous fields for an optically thin approximation (left) and the Monte-Carlo computation (right).

explains the damages seen on the windows in the experiments. This outlines the great interest of such coupled simulation to estimate heat loads.

Figure 6.23 presents a comparison of wall temperature prediction and experimental LIP measurements [163] of the inner and outer faces of the combustion chamber windows. A good general agreement can be observed for both CHT cases with or without radiation. In the case with radiation, the wall convective fluxes are four to ten times larger than the magnitude of wall radiative flux. Nonetheless, it can be observed that radiative effects tend to decrease the highest temperature leading to a very good prediction of quartz temperature in the first part of the quartz (until $x = 40$ mm). For highest heights, an under-prediction of quartz temperature is observed by approximatively 100 K. Given the complexity of the described flow, this misprediction could be due to different sources of error: the simulated flow in LES, the derived external heat transfer model, the radiative transfers, the retained wall laws for the turbulent boundary layers. The next section will investigate another class of wall-models to better describe wall convective flux. In particular, the possible coupling effects with radiation in turbulent boundary layers will be investigated. It can be noticed indeed in Fig. 6.22 (right) that a sudden change in the radiative power takes place very near the wall, which is unlikely to be correctly resolved on the retained mesh. This takes place for the heights where the misprediction was observed.

The effects of heat losses on soot emission is presented in Fig. 6.24 for different simulation cases: an adiabatic simulation (ADIABATIC), an uncoupled LES with 2D wall temperature fields prescribed from the 1D experimental profile and with an optically thin approximation (ISOT + OPT radiation), the coupled simulation without radiation (CHT + no radiation) and the fully coupled simulation (CHT + MC). For all cases, soot production position is well retrieved compared with experimental data. Soot magnitude is underestimated with a factor varying from 2 to 5 depending on the modelling of radiative and wall heat losses. Soot magnitude is therefore dependent on heat losses modelling: the highest soot magnitude level is obtained for

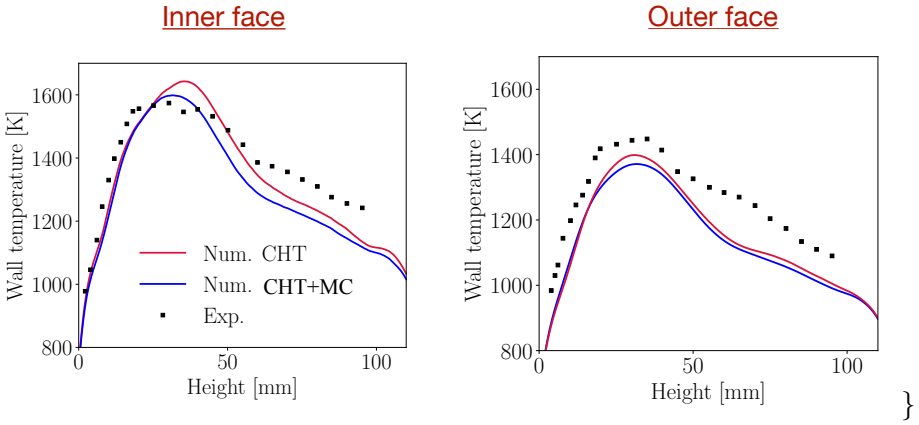

Figure 6.23: Comparison between wall temperature predictions and experimental LIP measurements [163].

the adiabatic case which neglects all heat losses, and the level then decreases with the increase of heat losses. It is important to outline that the adiabatic case giving the best agreement with experimental data is due to cancelling errors between the soot model and the wrong description of heat transfer. The modified amount of soot particles in the fully coupled simulation demonstrate the need to describe accurately the different heat transfer mechanisms to quantitatively predict the soot volume fraction.

Additional analyses have been conducted on the radiative transfer in the chamber and the balance of different fluxes in the fluid domain and the combustor walls. In particular, the simulation predicts that approximatively half of the internal radiation is leaving the combustion chamber through the described transparent bands of the quartz windows. Finally, although soot radiation was taken into account, they marginally participate here to radiative heat transfers. This is due to the small level of soot particles in the FIRST combustor ($f_v \approx 30$ ppb) compared to aeroengines where luminous radiation from soot particles is known to contribute significantly [139, 138]. Validation of radiative heat transfer from soot in realistic configurations will then require further experimental studies.

6.3 Convective heat transfer: coupled effects with radiation

In the atmospheric combustor studied in Sec. 6.2.5, the Reynolds number based on the chamber cross-section was low enough to allow a wall-resolved LES (WRLES). However, in high Reynolds number flows, large-eddy simulations cannot afford resolving the large eddies in turbulent boundary layers. That is why, the LES of the pressurised combustor in the previous section (Sec. 6.2.6) has relied on wall laws to model the turbulent boundary layers and predict the associated wall convective flux. However, such standard wall laws have a restricted domain of applications (constant properties, equilibrium boundary layer: no unsteadiness, no pressure gradient) and are often applied outside of the boundary inner layer where they are not valid. In this section, specific studies on the analysis and modelling of convective heat transfer are presented. TBLE wall models are presented in Sec. 6.3.1 with their application to high-speed flows. Then, section 6.3.2 enquires about the possible effect of radiation in turbulent boundary layers. These effects are analysed in coupled direct numerical simulations (DNS) of channel flows. They are finally accounted for in wall-modelled LES (WMLES) with a newly derived

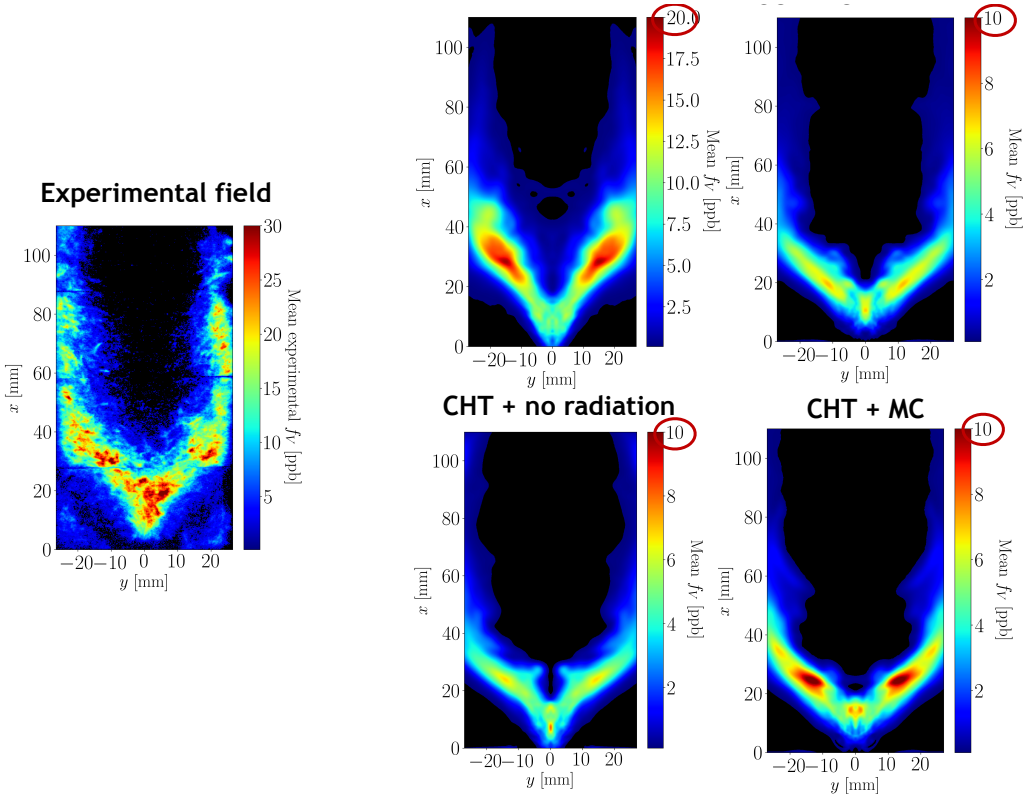

Figure 6.24: Comparison between soot volume fraction measurements [74] and numerical predictions for different cases.

wall-model.

6.3.1 Wall-modelled large-eddy simulations of high-speed flows

References: [A11], [C5, C4]

The pressure profile in the HyShot II scramjet studied in Sec. 4.2.6 can be shown to be equally sensitive to the heat release, wall heat losses and wall friction from a Rayleigh-Fanno analysis. The conclusion is that near-wall processes are of paramount importance in this scramjet flow, and thus they must be accurately predicted by the LES. The friction Reynolds number Re_τ of the boundary layers in the HyShot II isolator and combustor varies from 1500 to 4000; with reasonable resolution of the viscous length scale this implies that a grid of order 10^{11} points would be needed with wall-resolved LES. This is unfeasible and the presented computation results have relied on a wall-model instead.

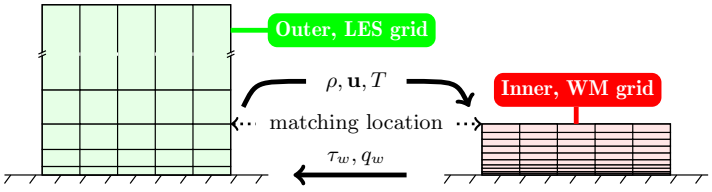

Figure 6.25: Wall-model schematic diagram.

A recent review of wall-modelled large-eddy simulations can be found in [20]. The wall-model used here is taken from the work of Kawai and Larsson [115]. For the lowest 10% of the boundary layer (based on δ_{99}), the flow is described by thin boundary layer equations (TBLE) while the LES resolves the rest of the boundary layer and the combustor. The chosen equilibrium TBLE wall-model is defined by the two ordinary differential equations (ODEs):

$$\frac{d}{dn}\left[(\mu+\mu_t)\frac{dU_{||}}{dn}\right] = 0, \tag{6.9}$$

$$\frac{d}{dn}\left[(\mu+\mu_t)U_{||}\frac{dU_{||}}{dn} + c_p\left(\frac{\mu}{\mathrm{Pr}}+\frac{\mu_t}{\mathrm{Pr}_t}\right)\frac{dT}{dn}\right] = 0, \tag{6.10}$$

where n is a local wall-normal coordinate; $U_{||}$ is the velocity magnitude locally parallel to the wall; and μ, c_p, Pr and T are the viscosity, specific heat at constant pressure, Prandtl number and temperature, respectively. Turbulent transfer is modelled with the eddy viscosity μ_t used in the wall-model taken from a mixing-length hypothesis and a constant turbulent Prandtl number Pr_t. The boundary value problem for both ODES is then solved at each face where the wall-model is applied. Boundary conditions are the no-slip and temperature conditions at the wall and off-the-wall LES data as shown in Fig. 6.25. Once solved, the model returns the wall shear stress and heat flux. The predicted wall heat flux in the HyShot II scramjet is shown in Fig. 6.26. The computed wall heat flux agrees quite well with the measurements, though less well for the upper wall. The present wall-model implemented in CharlesX was also used for the simulation of shock/turbulent boundary-layer interaction in a duct [C4].

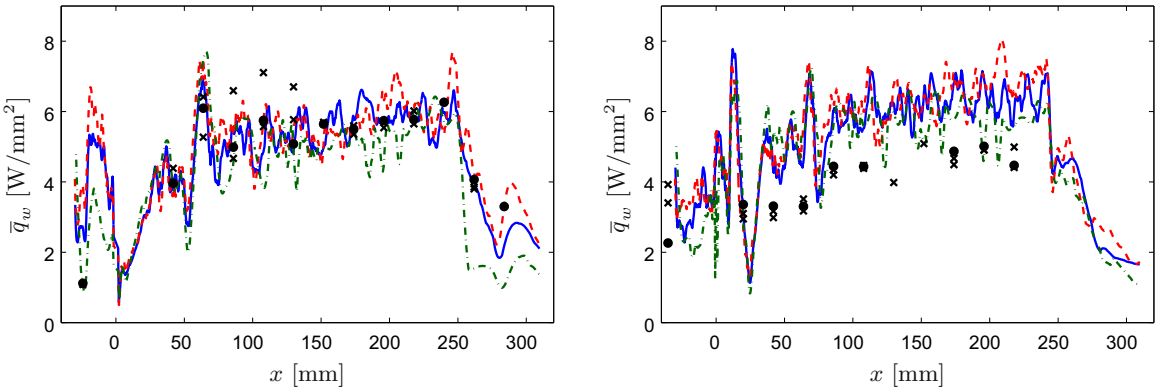

Figure 6.26: Mean wall heat flux along a line through the injector in HyShot II from LES (lines) for run #810 with ER=0.35. Compared with experiments [93, 92] for the same run #810 (circles) as well as runs #804 and #809 (ERs=0.34 and 0.33; both marked with crosses) to show the run-to-run variation. LES on fine mesh (100M cells, dashed), medium mesh (43M cells, solid) and coarse mesh (14M cells, dash-dotted). Left column: Lower wall. Right column: Upper wall.

The validated TBLE wall-model allows for accounting for variable properties (ρ, c_p, μ, λ) as often met in boundary layers in combustors with a large variation in temperature and it remains accurate as long as non-equilibrium effects, if any, remain outside of the inner layer and are captured by the LES directly. In the next section, radiation is shown to modify the classical universal law-of-the-wall throughout the boundary layer. These effects are first analysed before being finally taken into account in LES with an improved TBLE wall-model derived in Sec. 6.3.3.

6.3.2 Coupled radiative effects in turbulent boundary layers

References: [A10, A15, A17], [T1]

Previous studies on the impact of radiation in a channel flow configuration [217, 216, 89, 3, 75] do not expose a general trend or understanding of the influence of radiation in turbulent boundary layers. Several direct numerical simulations of channel flows with YALES2 have then been coupled with the Monte Carlo solver Rainier to thoroughly analyse these effects in multiple cases.

Control of channel flow bulk Reynolds number It is however beforehand necessary to develop a numerical algorithm to properly control the channel flow simulations. Such simulations are periodic in longitudinal and spanwise directions and require to specify a homogeneous source term that replaces the mean pressure gradient to drive the flow at the chosen mass flow rate *i.e* the bulk Reynolds number Re_b in the computed channel flow. The latter key quantity is defined as $\mathrm{Re}_b = \frac{\rho_b u_b \delta}{\mu_b}$ where ρ_b, u_b and μ_b are the bulk density, velocity and dynamic viscosity. The channel half-width is denoted by δ. Usually, the source term, which will be balanced by the integrated wall shear stress, is unknown, especially for the envisioned coupled simulation. One must then adapt the source term to obtain the target Reynolds number. Similarly, in an isothermal walls case, a source term is prescribed in the energy equation to drive the flow to a desired bulk temperature.

To determine these source terms, a control algorithm was developed to replace the unsatisfactory previous method. The derived method appears as PI controllers with a thorough setting of the coefficients so that the dynamics of the quantities of interest is exactly controlled. This allows for setting the desired target values for the bulk Reynolds number and bulk temperature by temporally adapting the prescribed homogeneous source terms. The controlling method is validated in several cases and is shown to be robust and efficient. Figure 6.27 presents DNS results with the simultaneous control of the bulk Reynolds number and temperature to new target values. These quantities closely follow the prescribed temporal evolution (symbols) for any response time τ. On the other hand, the wall shear stress τ_w and wall flux q_w, denoted by the friction Reynolds number $\mathrm{Re}_\tau = \dfrac{\rho_w u_\tau \delta}{\mu_w}$ and Nusselt number, follow their own dynamics determined by the channel flow response time estimated as δ / u_τ^{ref}. The friction velocity is defined as $u_\tau = (\tau_w/\rho_w)^{1/2}$. The reference value u_τ^{ref} is estimated from classical correlations.

Numerical setup and case definition The low Mach number Navier-Stokes equations are solved with the YALES2 code. The channel is filled with a homogeneous composition: the molar fractions of CO_2, H_2O and N_2 are 0.116, 0.155 and 0.729, respectively. The two parallel walls are set with different temperatures, which allows for studying two boundary layers at once. For the case detailed here, the cold wall temperature is $T_{w,c} = 950$ K and the hot wall temperature is $T_{w,h} = 1150$ K. The system is studied at a pressure $p = 40$ atm. The channel flow control strategy enables to study the case without radiation (C1) and the case with radiation (C1R1) for the same bulk Reynolds number $\mathrm{Re}_b = 5850$. Other cases $\mathrm{C}_n\mathrm{R}_m$ have been studied for the effects of pressure, Reynolds number, wall temperature difference and wall emissivity. They are defined through Tabs. 6.4 and 6.5. The radiative transfer equation is solved by the Monte Carlo Rainier solver with the OERM method [250]. A visualization of the instantaneous flow fields was shown in Fig. 1.3.

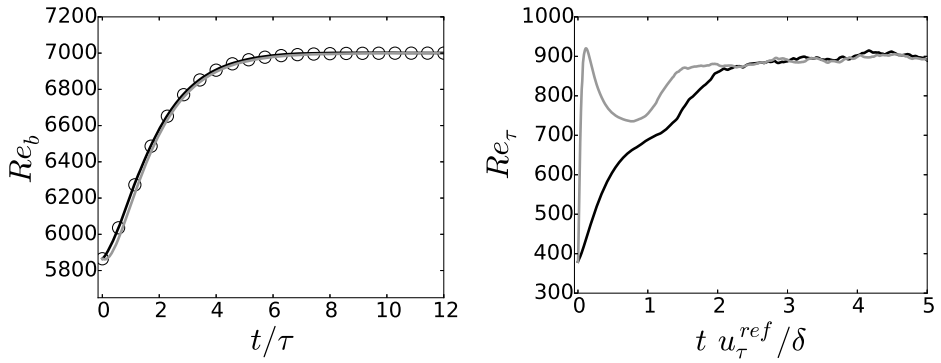

(a) Flow control with varying T_b at the same time.

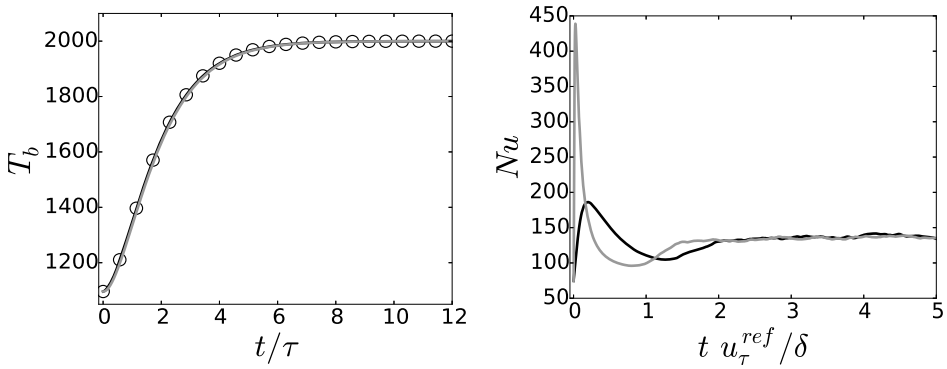

(b) Temperature control with varying Re_b at the same time.

Figure 6.27: Temporal evolution of bulk and friction Reynolds number (a) and bulk temperature (in Kelvin) and Nusselt number (b). Circles: theoretical solution; Black plain: $\tau = 0.33\delta/u_\tau^{ref}$; Gray plain line: $\tau = 0.033\delta/u_\tau^{ref}$.

Finally, the effects of radiation are due to different coupled phenomena, in particular gas–gas (GG) and gas–wall (GW) interactions. The effects of gas–gas and gas–wall interactions have then been separated by considering cases C1R1_GG and C1R1_GW where only gas–gas (respectively gas–wall) radiative interactions are computed.

Results: a new temperature law-of-the-wall The profiles of the mean temperature $\overline{T}$ associated with the cases C1 and C1R1 are compared in Fig. 6.28(a). The corresponding $\overline{T}^+$ profiles, for both the cold and the hot sides, are plotted in Fig. 6.28(b). The wall-units scaling of the mean temperature profile is given as

$$\overline{T}^+ = \frac{|T - T_w|}{T_\tau},$$

where T_w is the considered wall temperature and $T_\tau = \left|q_w^{cd}\right| / (\overline{\rho_w}\,\overline{c_{p_w}} u_\tau)$ is the friction temperature. In the case C1, without radiation, the distribution of $\overline{T}$ is practically antisymmetric and the $\overline{T}^+$ profiles are identical for the two sides. As the agreement with the DNS by KIM et al. [122] confirms, the $\overline{T}^+$ profiles of case C1 follow the universal law-of-the-wall.

When only gas-wall radiation is considered, in the C1R1_GW case, the temperature gradient is smaller in the vicinity of a wall than in C1 case: The associated wall conductive fluxes presented

Table 6.4: Channel flow parameters.

	$\mathrm{Re_b}$	Re_{D_h}	$T_{w,c}$ [K]	$T_{w,h}$ [K]	p [atm]
C1	5850	23400	950	1150	40.0
C2	5850	23400	950	1150	1.0
C3	5850	23400	950	2050	40.0
C4	11750	47000	950	1150	40.0

Table 6.5: Wall emissivities in radiative conditions R1, R2, R3 and R4.

	R1	R2	R3	R4
ϵ_1 (cold wall)	0.8	0.3	0.1	0.1
ϵ_2 (hot wall)	0.8	0.3	0.1	1.0

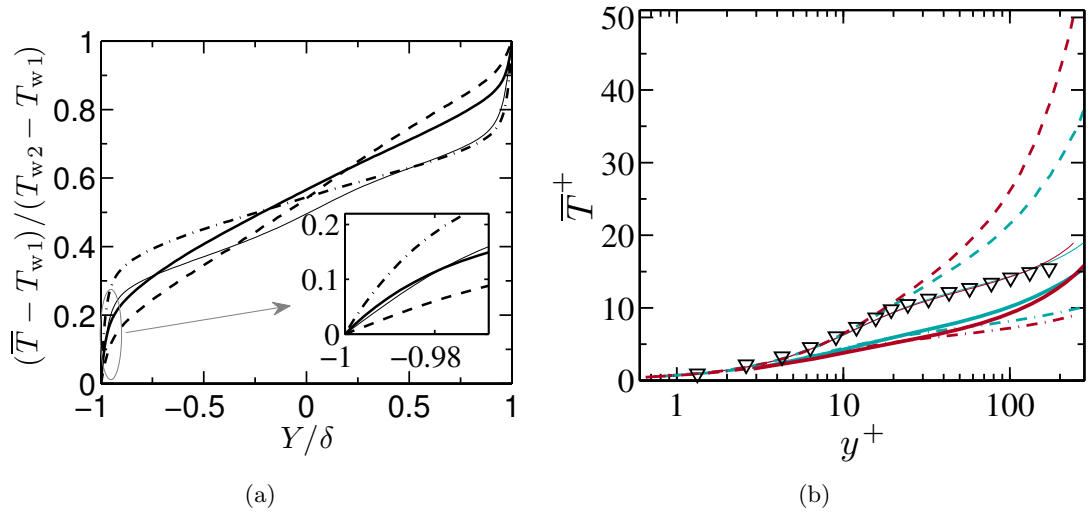

(a) (b)

Figure 6.28: Mean temperature profiles in global coordinates (a) and in wall units (b). Symbols (▽): DNS results (Pr= 0.71) [122]. Thin plain line (—): C1. Thick dashed line (– –): C1R1_GW. Thick dashed-dotted line (– · –): C1R1_GG. Thick plain line (——): C1R1. In (b), blue lines (——): old side; red lines (——): hot side.

in Table 6.6 are two to three times smaller than in C1 case. Indeed, the wall tends to impose its temperature to the fluid. Consequently, the temperature variation is higher in the core of the flow than in case C1. The conductive flux variations are more important at the hot side than at the cold one, as gas-wall radiative interactions strongly increase with the temperature.

On the other hand, in the case C1R1_GG, the gas-gas radiative transfer is a supplementary transfer that homogenises the temperature field within the gas by comparison with the case C1, without radiation, as shown in Figs. 6.28 (a) and (b). Consequently the temperature gradients and the conductive fluxes strongly increase at the two walls, as shown in Table 6.6.

Table 6.6: Wall fluxes (in W/m^2) $\overline{q_w^{\mathrm{cd}}}$ and $\overline{q_w^{\mathrm{R}^*}}$ for different cases at cold and hot walls. The relative variation of $\overline{q_w^{\mathrm{cd}}}$ compared to the case without radiation is put between parentheses. Flux values are rounded, typical errors are within 2-3 %.

	$Re_{\tau,c}$ (cold)	$Re_{\tau,h}$ (hot)	$\overline{q_{w,c}^{\mathrm{cd}}}$ (cold)	$\overline{q_{w,h}^{\mathrm{cd}}}$ (hot)	$\overline{q_{w,c}^{\mathrm{R}^*}}$ (cold)	$\overline{q_{w,h}^{\mathrm{R}^*}}$ (hot)
C1	386.6	305.7	-875	-875	–	–
C1R1	390.8	303.3	-1230 (+40.6%)	-960 (+9.7%)	-6970	-7240
C1R1_GW	394.7	304.4	-460 (-47.4%)	-270 (-69.1%)	–	–
C1R1_GG	389.5	306.1	-1930 (+120.6%)	-1750 (+100.0%)	–	–

When all the radiative effects are accounted for, in the case C1R1, the gas-gas and gas-wall interactions, that have opposite effects, are coupled. As shown in Fig. 6.29, in the vicinity of the wall, the amplitude of the radiative power associated with gas-gas interaction is much larger than the one associated with gas-wall interactions. Consequently, in the present conditions, the wall temperature gradients and the conductive fluxes increase, as in the gas-gas case, at the two walls by comparison with the case C1 without radiation, as shown in Tab. 6.6 and Fig. 6.28(a).

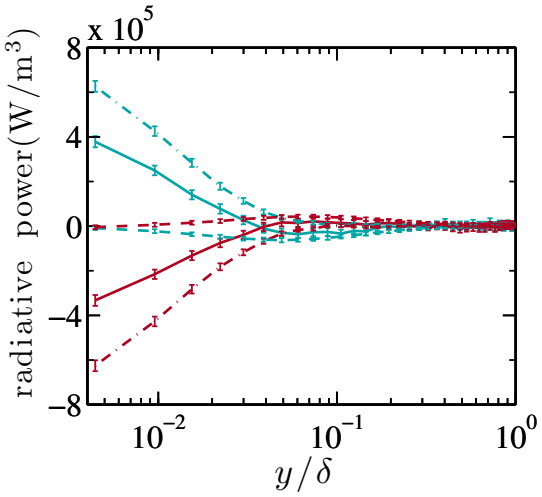

Figure 6.29: Comparison of mean radiative power of C1R1, C1R1_GG and C1R1_GW Plain line: C1R1; Dashed line: C1R1_GW; Dashed-dooted line: C1R1_GG; Blue lines (—): cold side; Red lines (—): hot side. Error bars represent the Monte-Carlo standard deviation.

Several parameter variations have been taken into account in additional coupled direct numerical simulations. Their effects are summarised below:

- At atmospheric pressure (case C2R1), the smaller optical thickness allows interaction phenomena between the two walls. The previous analysis still stands but the effects related to gas–gas and gas–wall interactions are smaller than at high-pressure.
- The wall emissivity (cases C2R1, C2R2, C2R3, C2R4) modifies the balance of antagonist gas–gas and gas–wall effects: when the wall emissivity decreases, gas–gas effects become more and more important and the temperature profile becomes more uniform in the flow center part while the temperature gradient near the wall increases.
- A hotter wall (case C3R1) increases the temperature in the channel which individually magnify the gas–gas and gas–wall radiative interactions. The final effect is the result of the balance between the opposite effects of these contributions. For all investigated cases, gas-gas effects generally win.
- Increasing the Reynolds number (case C4R1) has two effects. First, the enhanced turbulent heat transfer relatively weakens the radiation effects and the profile $\overline{T}(y^+)$ relaxes to the curve corresponding to the universal law-of-the-wall. Secondly, the change in Reynolds number modifies the nature of the radiative energy transfer: magnitude of the gas–gas contribution decreases for the larger Reynolds number case while the magnitude of the gas–wall contribution increases. This draws the profile $\overline{T}(y^+)$ upwards. Among these two effects, the second one was dominating for the studied configuration.

In all cases, an important result is that radiation modifies the standard law-of-the-wall and no logarithmic-law can be clearly identified. Besides, each case yields a different profile: no universal profile exits anymore. This modified behaviour is also seen in the modified value of the wall conductive heat flux. The effect of radiation is then much more complex than the addition of a supplemental wall radiative flux.

Further analysis: impact on temperature fluctuations In coupled simulations, the root-mean-square of enthalpy or temperature fluctuations is significantly damped compared to the corresponding cases without radiation. The explanation is found the balance equation of enthalpy variance. The different terms scaled in wall-units are shown in Fig. 6.30. On the one hand, in case C1, production and molecular dissipation terms are dominant and decrease away from the wall as expected in such standard conditions. On the other hand, in case C1R1, a third dominant term appears in the balance of enthalpy variance: the enthalpy–radiative-power correlation $\overline{h'' P'_{rad}}$. Since this term appears as a negative contribution to the budget, it is referred to as radiative dissipation. Hence, equilibrium between production and molecular dissipation away from the buffer layer for $y^+ > 30$ is replaced by a balance of production with molecular and radiative dissipations in the case with radiation. In the case studied, this equilibrium takes place sooner for $y^+ > 20$ and molecular dissipation remains weaker than radiative dissipation for $y^+ > 50$ approximatively. The budget equation of the turbulent heat flux also impacted by radiation exhibits a new term as well that perturbs significantly the usual balance.

In turbulent boundary layer without radiation, the profiles of different terms in the budget of enthalpy rms computed in different flow conditions overlap on each other if they are properly scaled in wall-units or with semi-local scaling [37, 99, 176] to account for variable property effects. When considering different cases with radiation, this universal overlapping breaks down and each profile is different from the others. A new radiation-based scaling has been derived instead and has significantly improved the profiles similarity. This new scaling has been finally used to write a model for the turbulent Prandtl number that is also significantly affected in coupled simulations. The results of the model shown in Fig. 6.31 present a very good agreement with the coupled DNS data.

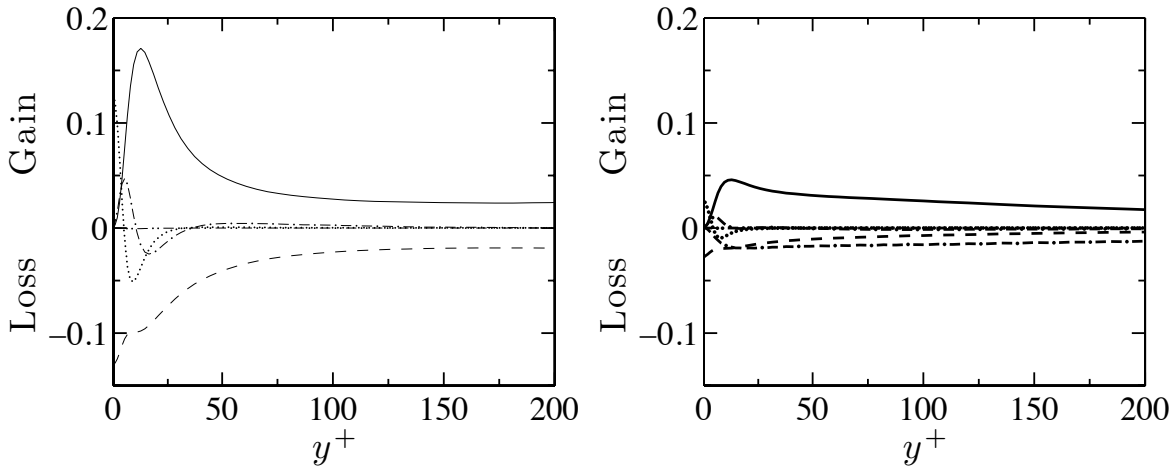

Figure 6.30: Budget of enthalpy variance (cold side only) in cases C1 (a) and C1R1 (b): Production (plain line); Molecular dissipation (dashed line); Radiative dissipation (dashed-dashed-dotted line); Turbulent diffusion (dashed-dotted line); Molecular diffusion (dotted line); Density-enthalpy correlation term (dashed-dotted-dotted line).

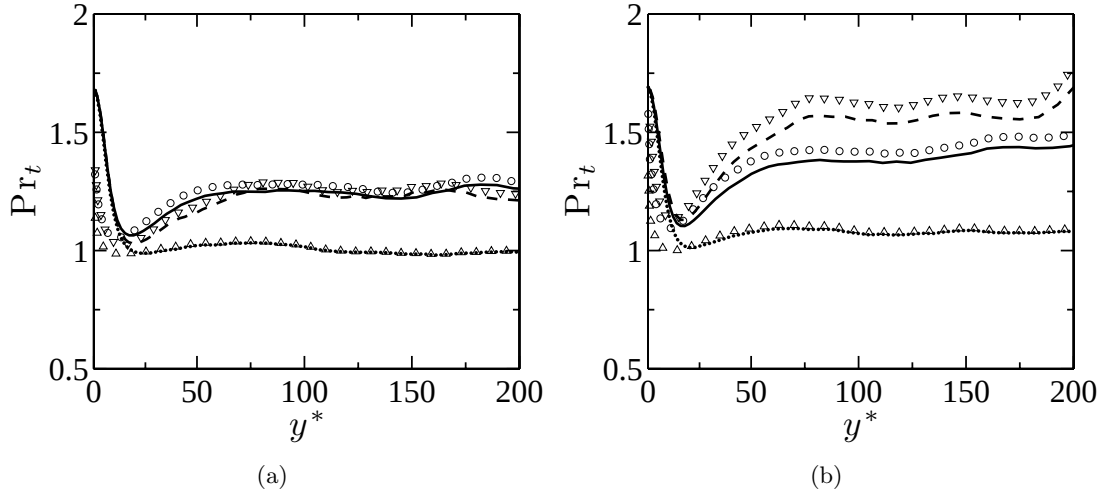

Figure 6.31: Profiles of modelled turbulent Prandtl number on the cold side (a) and hot side (b) compared to DNS results in cases C1R1 (DNS: Circles; Model: Plain line) , C3R1 (DNS: Down-pointing triangles; Model: Dashed line) and C4R1 (DNS: Up-pointing triangles; Model: Dotted line).

6.3.3 Development of a new wall-model and criteria accounting for radiation effects

References: [A6, A16], [T1]

Derivation of a wall model accounting for radiation effects A wall-model is developed in order to account for the studied effects of radiation in turbulent boundary layers. In low-Mach flows, the wall-model equations for a thin equilibrium boundary layer with the additional radiative power source term P^R are

$$\frac{d}{dn}\left[(\mu+\mu_t)\frac{dU_{||}}{dn}\right] = 0, \tag{6.11}$$

$$\frac{d}{dn}\left[c_p\left(\frac{\mu}{\mathrm{Pr}}+\frac{\mu_t}{\mathrm{Pr}_t}\right)\frac{dT}{dn}\right]+P^R = 0. \tag{6.12}$$

The obtained TBLE wall-model is iteratively solved until convergence and resolution of the coupled set of equations: the ODEs for velocity and temperature are solved with the wall model boundary conditions and the 1D radiative power field P^R_{1D}; the field P^R_{1D} is computed with a semi-analytical method from the 1D temperature field T_{1D} and prescribed spectral incoming intensities $\overline{I^-_\nu}$ in predefined solid angles. The latter quantities are computed from the Monte Carlo solver coupled to the LES and describe the anisotropy of radiation. The connections between the LES, the Monte Carlo solver and the wall-model are given in the scheme in Fig. 6.32.

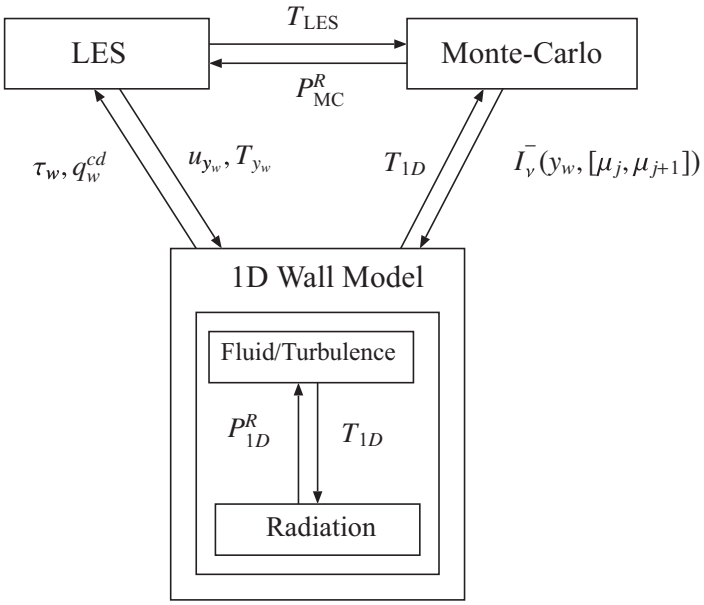

Figure 6.32: Scheme of coupling between LES, the Monte-Carlo method and the 1D wall models located at each point of the walls. T_{1D} and P^R_{1D} are the inner layer temperature and radiative power fields on the embedded grids.

An *a priori* study was carried out to carefully select the different submodels and parameters of the wall-model (formulation of the eddy viscosity, variable turbulent Prandtl number formula, number of solid angles to describe anisotropy) by providing exact DNS inputs and comparing the predicted scaled profiles $T^+(y^+)$. Figure 6.33 shows that the final version of the wall model accurately predicts the temperature field for the two near wall regions of the three considered

coupled DNS cases. Note that the results of wall models that do not account for radiative power source term strongly deviate from the DNS corresponding results, which indicates that in these three cases, radiation strongly modifies the mean temperature field within the inner layer.

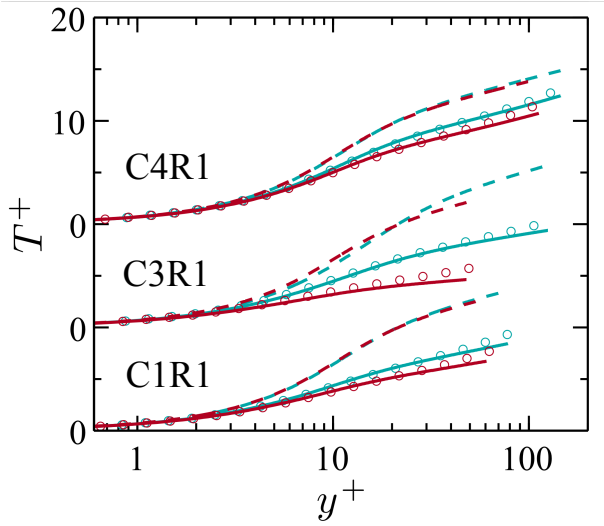

Figure 6.33: Mean temperature profile in wall units of cases C1R1, C3R1 and C4R1 from [A17] on the cold side (blue colour) and hot side (red colour). Circles: coupled DNS data. Dashed line: wall model without radiative power source term. Plain line: wall model with radiative power source term.

Validation of wall-modelled LES For all these cases, the LES grid consists of $36 \times 36 \times 36$ points. The derived wall-model is implemented in the YALES2 code and is used in coupled simulations between the LES solver YALES2 and the Monte Carlo solver Rainier. Figure 6.34 presents the corresponding results. The new wall-model is compared to a *standard* TBLE wall-model where the radiative source term is not accounted for. Note that the combination of such a standard TBLE wall-model with coupled LES simulations based on Monte-Carlo simulation is already a state-of-the-art simulation. However, this combination is not able to retrieve the correct mean temperature profile and wall conductive flux. On the other hand, the wall-modelled LES based on the new model yields an excellent agreement.

Results for other cases are shown in Tab. 6.7 along with additional results from coupled LES without any wall model.

Criteria for a quick estimation of radiation effects The new wall-model is proven to be accurate but one can wonder when it is necessary to account for radiative effects in boundary inner layers. A costless indicator has then been built to know whether a specific wall model must be used. Two indicators have been defined. $\widetilde{\mathcal{I}}$ quantifies the importance of averaged wall radiative flux compared to the conductive one. $\widetilde{\mathcal{I}} > 1$ indicates that the radiative flux is larger. This simple indicator can be used to determine when a coupled LES simulation is even necessary. The indicator $\widetilde{\mathcal{J}}$ quantifies the departure of the mean temperature profile from the universal law-of-the-wall due to radiation effects: $\widetilde{\mathcal{J}} = 0.1$ means that the coupled scaled temperature profile $T^+(y^+)$ is 10% below the universal wall law. These indicators are computed from 1D non-coupled RANS simulations of channel flows and the computation of radiative power on the

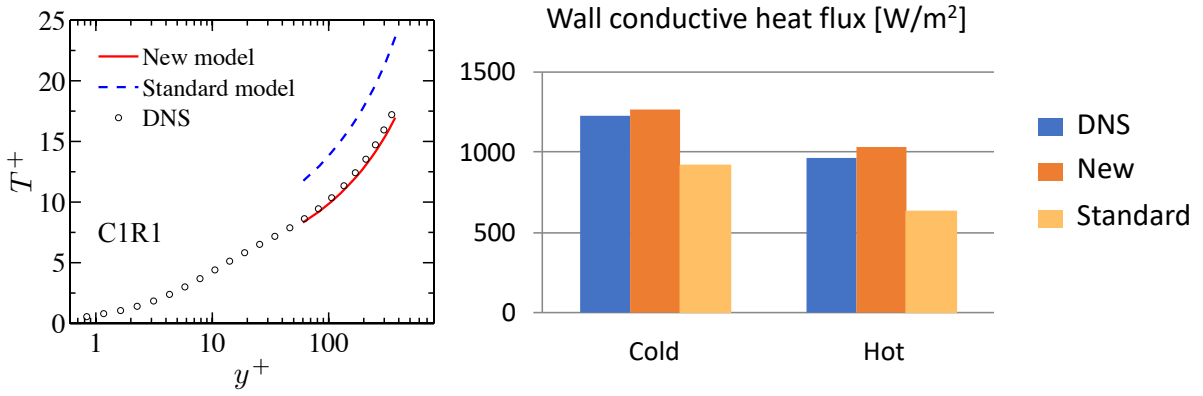

Figure 6.34: Comparison of wall-modelled LES results for the new model and a standard one: mean temperature in wall units (left) and value of the wall conductive flux (right).

Table 6.7: Comparison of mean wall conductive heat flux q_w^{cd} [W.m^{-2}] between wall-modelled LES (new, standard and no wall model) and DNS results.

	side	DNS	new model	standard model	no model
C1R1	cold	1230	1270	918	443
	hot	960	1030	631	363
C3R1	cold	16260	16041	10985	6583
	hot	8720	8911	3738	3303
C4R1	cold	1650	1666	1288	660
	hot	1290	1358	925	569
C2R2	cold	1220	1180	1105	677
	hot	1100	1055	955	622
C2R1	cold	1070	1040	1018	773
	hot	930	926	821	750

corresponding mean temperature field. Further details on the definition of $\widetilde{\mathcal{I}}$ and $\widetilde{\mathcal{J}}$ and their validation compared to DNS data can be found in [A6].

The low cost of these indicators allow for exploring fully the parameter space which is not affordable with coupled DNS. Several 2D maps of both indicators have been drawn by varying the system geometrical size, Reynolds number, wall emissivity and pressure. All results generalise the trends already identified and explained in DNS cases. For example, the criterion $\widetilde{\mathcal{I}}$ values are plotted as a function of the channel hydraulic diameter D_h and the Reynolds number Re_{D_h} in Figure 6.35(a). The criterion threshold value where one must consider a radiation computation is arbitrarily chosen equal to 0.2 to simplify the discussion. It corresponds to a radiative flux equal to 20% of the conductive flux. As expected in such a high-pressure case, the region where a radiation simulation is needed covers the main part of the domain (grey zone in the figure where $\widetilde{\mathcal{I}} \geq 0.2$). On the one hand, for a given Reynolds number, the importance of wall radiative flux increases with the channel hydraulic diameter of the channel, due to an increased optical thickness. On the other hand, the weight of wall radiative flux becomes less important at higher Reynolds number as the wall conductive flux increases with Reynolds number.

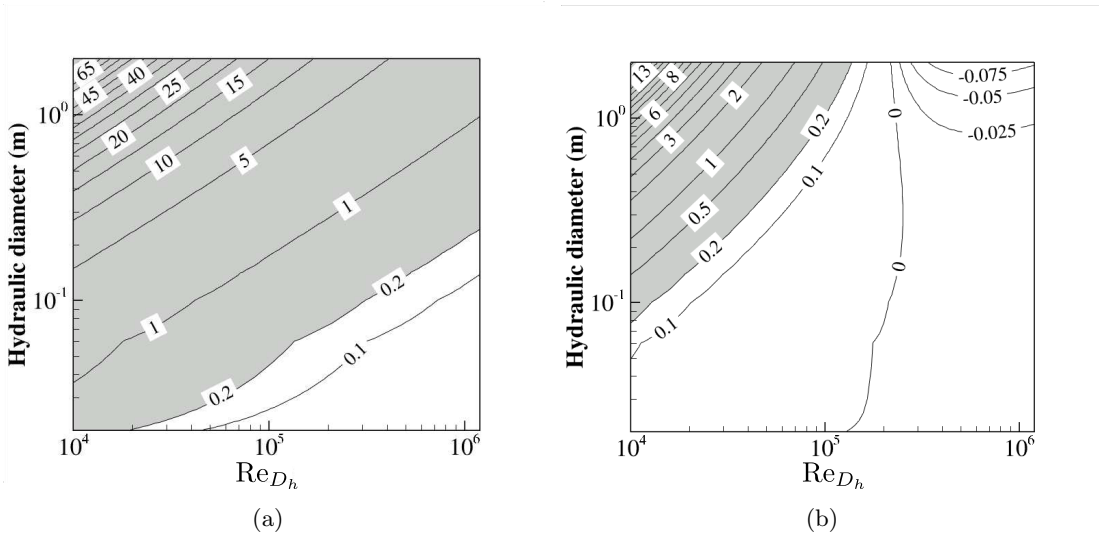

Figure 6.35: Contour plots of the $\widetilde{\mathcal{I}}$ (a) and $\widetilde{\mathcal{J}}$ (b) indicators as functions of the Reynolds number Re_{D_h} and the channel hydraulic diameter D_h. The pressure is set to 40 atm and the walls emissivity to 0.8.

The criterion $\widetilde{\mathcal{J}}$ values are plotted as a function of Re_{D_h} and D_h in the same conditions in Fig. 6.35(b). A criterion threshold value of 0.2 similarly characterises non-negligible radiation effects on the law-of-the-wall $\overline{T}^+(y^+)$: a specific coupled wall model has then to be accounted for. The grey region, such that $\widetilde{\mathcal{J}} \geq 0.2$, is smaller than the grey one associated with $\widetilde{\mathcal{I}}$: In some region, although the wall radiative flux is important, the radiation effect is not strong enough to influence $\overline{T}^+$ profiles near the wall.

The magnitude of the $\widetilde{\mathcal{J}}$-indicator value increases with D_h as the optical thickness becomes larger. The dependency of $\widetilde{\mathcal{J}}$ with the Reynolds number is more complex. Two aspects have been enlightened previously regarding the influence of the Reynolds number Re_{D_h} on the wall-scaled temperature. First, while Re_{D_h} increases, the weight of turbulent convective heat transfer increases: radiation effect is then relatively less important. Consequently, the $\overline{T}^+$ profile gets closer to the classical law-of-the-wall, and the absolute value of $\widetilde{\mathcal{J}}$ decreases. On the other hand, the weight of gas-gas radiation is reduced while the gas-wall radiation effect is enhanced. Moreover, gas-gas radiation decreases the $\overline{T}^+$ value and yields a positive $\widetilde{\mathcal{J}}$ value whereas gas-wall radiation has an opposite effect. Therefore, as Reynolds number increases, the value of the $\widetilde{\mathcal{J}}$ criterion is expected to decrease and to even become negative when gas-wall radiation dominates over gas-gas radiation. The latter effect ($\widetilde{\mathcal{J}} < 0$), that has been anticipated from DNS studies but could not be observed due to the computational limitations associated with high Reynolds numbers, is clearly shown in the top-right corner of Fig. 6.35(b). For smaller Reynolds number values, gas-gas radiation is dominant and a positive value of $\widetilde{\mathcal{J}}$ is obtained. Both of the two aforementioned aspects tend to decrease the criterion value when Reynolds number increases.

Part III

Perspectives

Chapter 7

Synthesis of research activities

My research activities cover the study of turbulent reactive flows and coupled heat transfers. From an initial expertise in combustion modelling, I have enriched my activities with two original themes. The first is application-driven thanks to the maturity of combustion models. It studies the ignition in annular combustion chambers with numerical simulations. The second was initiated from the acknowledgement that wall temperatures in large-eddy simulations of combustors were unknown, which penalizes their validation. The requirement of accurate prediction of heat transfer in our computations has led the development of multiphysics high-fidelity simulations of coupled heat transfer, notably radiative transfers. Since 2011, these activities are being conducted through the co-supervision of several Ph.D. students ($\sim$ 5 graduated, 7 in progress) and the participation to several national and European projects. All these studies could not have been achieved without access to supercomputers: the CentraleSupélec mésocentre and the clusters from GENCI and PRACE. The development, validation and analysis of massively parallel simulations rely a lot on continuous investment in public supercomputing facilities.

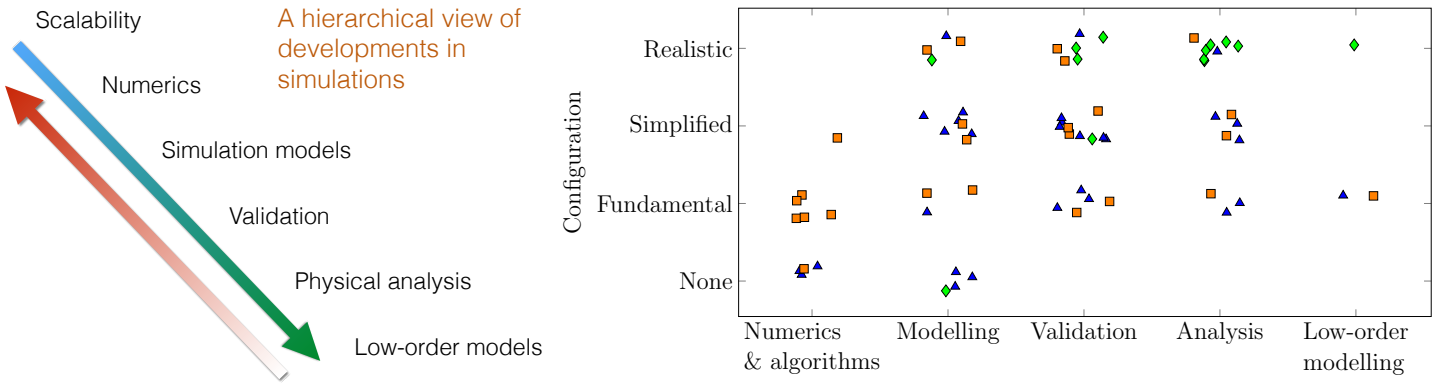

Figure 7.1: (a) Scheme of developments in numerical simulations. (b) Synthesis of different contributions ordered by type of research activity and configuration. Chapters are denoted by the different symbols: blue triangles for Chapter 4, green diamonds for Chapter 5 and orange squares for Chapter 6

The results of studies in the first research theme on modelling and simulations of turbulent reactive flows were presented in Chapter 4. The works were mainly focused on model development and their validation, which are two important steps in research developments with large-scale

simulations. Other steps are shown in Fig 7.1(a). The decreasing arrow indicates the goal-driven direction of these developments, the ultimate objective being the analysis and macroscopic understanding of a given phenomenon with a costless low-order model. The uprising arrow outlines the upstream flow of developments: one must first have an efficient numerical solver before implementing and validating models with it. Without access to high-scalability LES codes such as AVBP and YALES2, the presented results could not have been achieved. Hopefully with the scalability and numerics kindly handled by CERFACS and CORIA, we have been able to focus on other features. Chapter 4 has demonstrated the growing maturity of combustion models. This has led to the two new research themes in Chapters 5 and 6 and also additional contributions in terms of numerics, analysis and low-order modelling throughout this manuscript. A synthesis of the different contributions is given in Fig. 7.1(b). They are ordered by types of configuration and contribution.

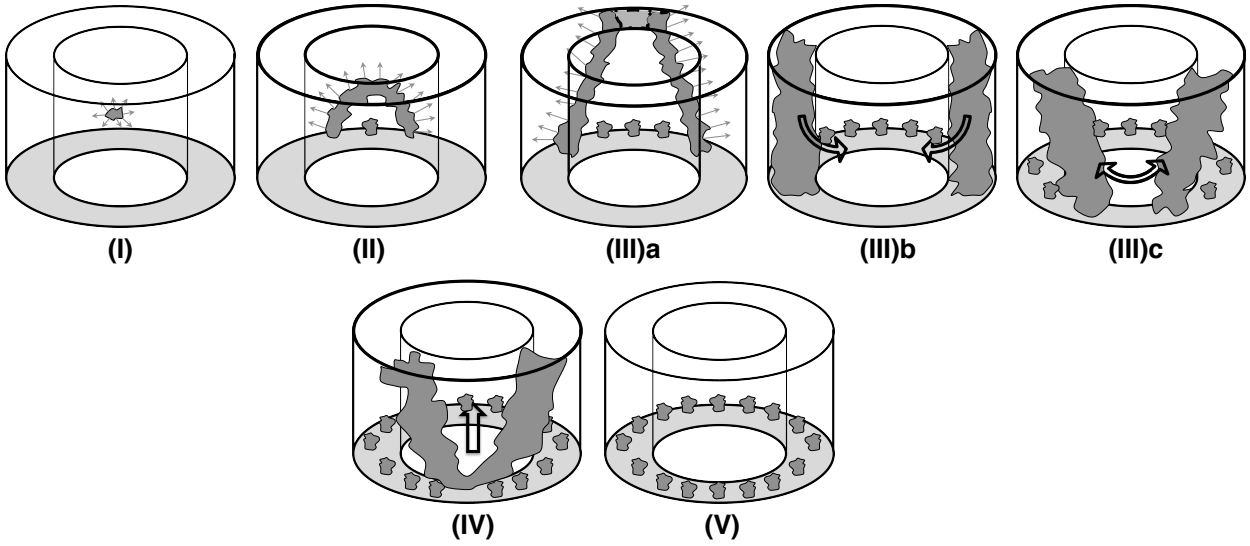

Figure 7.2: Scheme of ignition in annular combustors with multiple burners.

With the use of mature combustion models, the light-round in the MICCA combustion chamber was studied under gaseous premixed conditions and with liquid fuel in Chapter 5. With the exception of the richer condition with liquid fuel, very good agreement was obtained between numerical simulations and experiments. The flame development during the ignition of such annular combustors is quite particular. The analysis of the flame topology and the flows inside the fresh and burnt gases has led to define different phases during the light-round of MICCA. They are represented in Fig. 7.2. This definition refines the initial 3-phase splitting proposed by Lefebvre and Ballal [138] (see Fig. 7.3(a)). On the other hand, for the ignition of a single-burner, Eyssartier et al. [61] have distinguished 6 phases (see Fig. 7.3(b)). All these definitions are synthesised in Fig. 7.4.

The impact of the induced flow due to the burnt gases volumetric expansion was also outlined in Chapter 5: it propels the flame fronts to a much higher velocity than the consumption speed; it presents particular features in annular combustors with the presence of counterflows in the regions of fresh and burnt gases; in two-phase flows, it creates a complex coupling with the flame propagation through the generation of rich fresh gases in the wake of the swirlers behaving like jets in crossflows. Finally, the leading point behaviour was highlighted as a possible driving mechanism for the flame propagation while another macroscopic point of view enabled to derive a low-order model for the flame absolute flame speed.

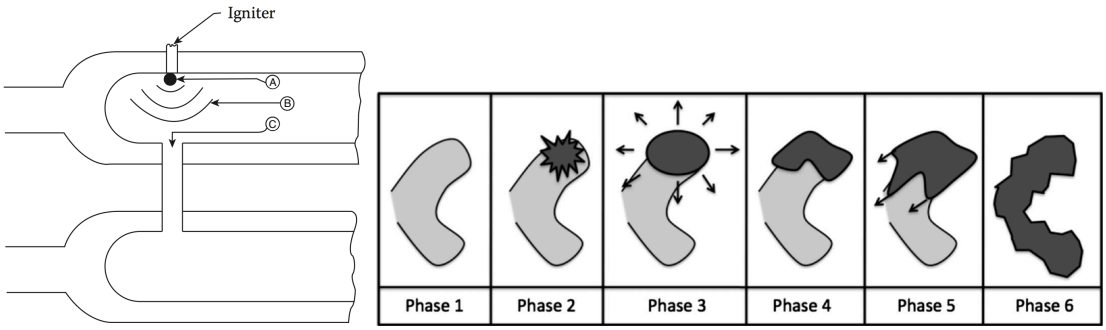

(a) Lefebvre and Ballal [138] (b) Eyssartier et al. [61]

Figure 7.3: (a) Scheme of ignition in aeroengines. (b) Scheme of ignition of a single burner.

Developments around heat transfer (a new coupling algorithm for unsteady conjugate heat transfer, the Quasi Monte Carlo method to solve radiation) and the associated multiphysics simulations were detailed in Chapter 6. The growing complexity of the target applications (see Fig. 7.5) demonstrate the increasing maturity of the conducted simulations. The retained methodology combines reactive large-eddy simulations with conjugate heat transfer and a Monte Carlo solver to describe thermal radiation. The expansive fidelity of such simulations was awarded with accurate predictions of wall temperature while outlining the coupling effects of radiation.

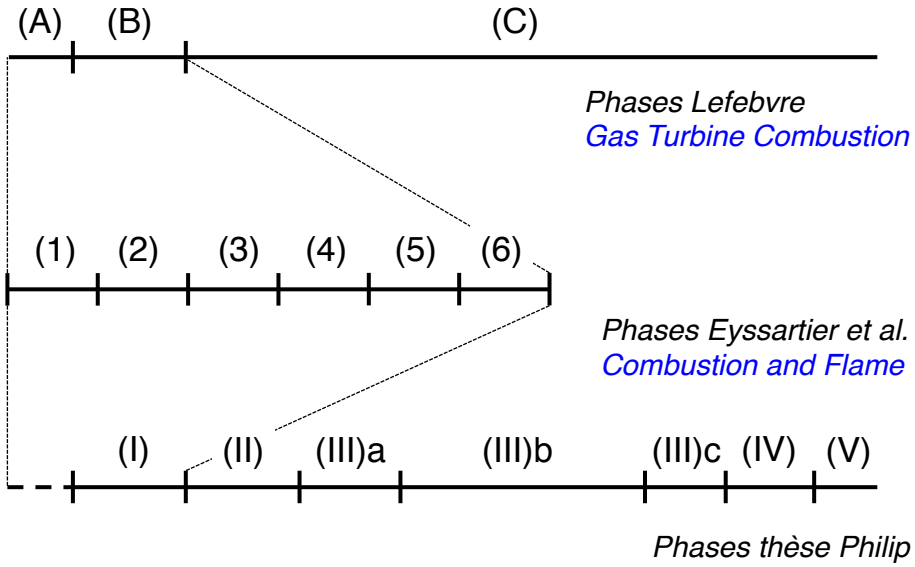

Figure 7.4: Synoptic splitting of ignition in annular combustion chamber from the energy deposit to steady state.

Such coupled effects have been separately studied in turbulent boundary layers. They revealed that the classical mean temperature profile can be strongly impacted by radiation effects (see Fig. 7.6(a)) and that new mechanisms perturb the natural equilibrium of temperature fluctuations and turbulent transport in boundary layers (see Fig. 7.6(b)). A wall-model for LES has then been developed and validated to account for the modified law-of-the-wall and costless criteria have finally been derived to determine when such a wall-model is necessary.

With the developments of the two new research themes from the first one (see Fig. 7.7(a)), the necessity to have more interconnections (black arrows in the figure) between the different research

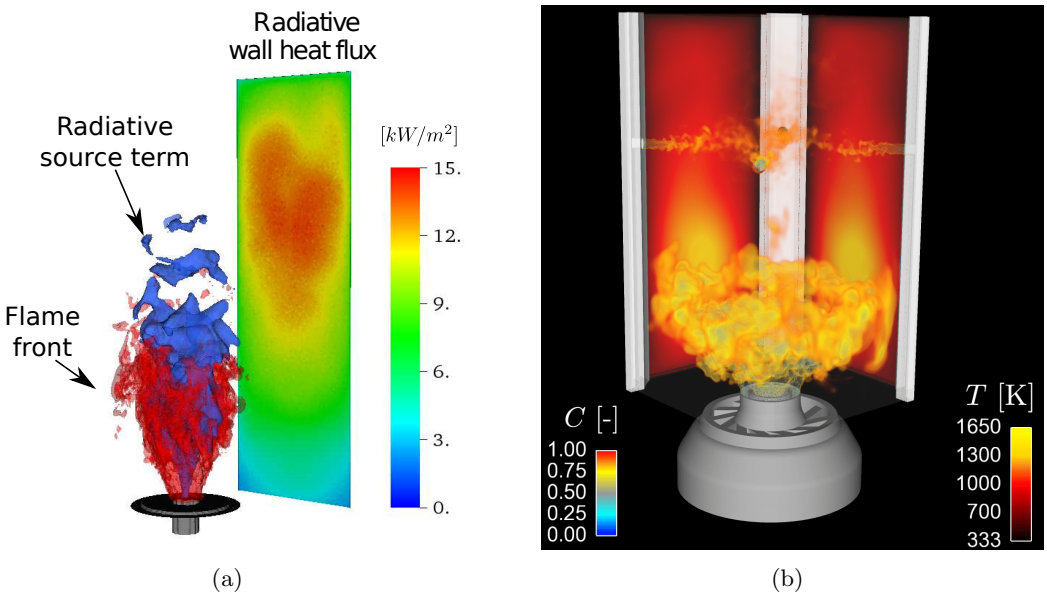

(a) (b)

Figure 7.5: Coupled simulations of different combustion chambers: (a) atmospheric combustor from [86] featuring a premixed flame (b) DLR FIRST combustor [74] (normalized progress variable volume-rendering and wall temperature field) with a pressurised sooted flame.

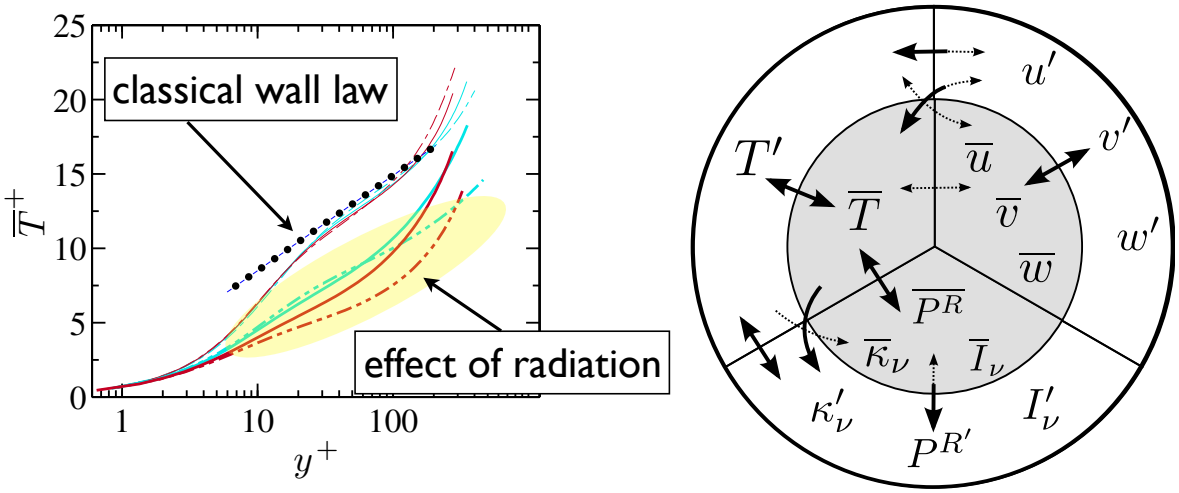

(a) (b)

Figure 7.6: (a) Modification of the temperature law-of-the-wall duo to radiation effects. (b) Scheme of coupling effects in turbulent channel flow with radiation. The fields of velocity (u, v, w), temperature (T) and radiative power (P^R) are split into mean and fluctuating components. Other quantities are considered for the radiation field: The spectral intensity (I_ν) and absorption coefficient (κ_ν). Main effects are represented by thick plain arrows while thin dotted arrows indicate negligible or null effects.

activities is made stronger and stronger. The accurate prediction of wall temperature now allows for going back and (i) developing and validating combustion models aiming at describing effects of heat transfer on turbulent flames, (ii) and analysing these effects in flames strongly involved with heat transfer challenges such as in oxycombustion. The limitations of light-round

simulations for the richer two-phase conditions invite to consider a more accurate representation of the two-phase flow and to improve the understanding of two-phase combustion. Furthermore, the sensitivity of MICCA ignition to the wall temperature that was observed experimentally highlights the critical role of wall heat losses. In particular, prescribing realistic boundary conditions for the wall temperature in PREHEATED cases will rely on predicting such steady-state temperature field from coupled simulations. All these connections invite to consider the three research themes as more entangled as shown in Fig. 7.7(b). All these perspectives are considered in future and on-going studies which are described in the next Chapter.

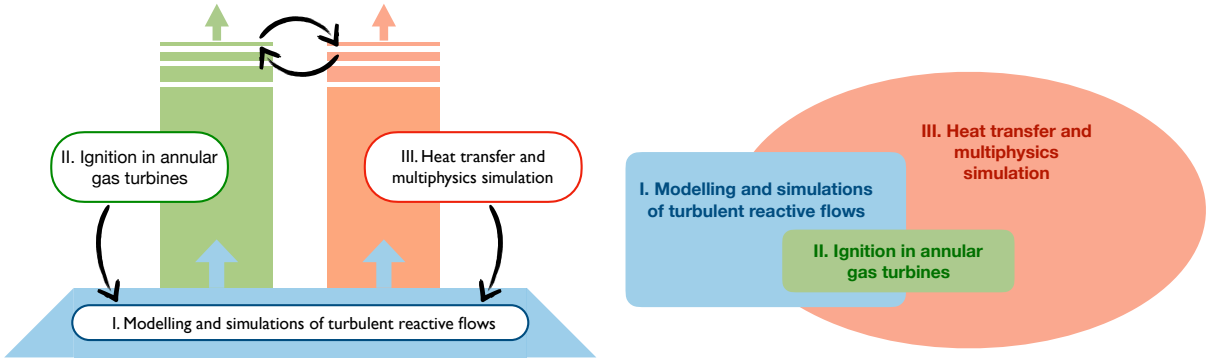

(a) (b)

Figure 7.7: Historical development of research themes (left) and connexions between my research activities: black arrows in (a) and scheme in (b).

Chapter 8

Research perspectives

My current and future research studies in numerical simulations rely on unique experimental setups in the EM2C laboratory: the MICCA annular chamber developed by Daniel Durox and Sébastien Candel and the OxyTeC test rig designed for the investigation of pressurised oxyflames by Clément Mirat and Thierry Schuller. I continue to pursue several activities to extend the present works and open new perspectives. Beforehand, a substantive work has been undertaken for several years to develop in-house codes (a flexible flamelet library, numerical methods for uncertainty quantification) in order to anticipate these future developments.

8.1 Preparing future developments with established new library codes

In addition to new developments in existing solvers such as AVBP, YALES2 or Rainier, several entirely new libraries have been coded since 2011. They have enabled to accelerate the initial stage of PhD theses based on programming, to easily compute 1D flames for combustion analysis and modelling and to implement and use uncertainty quantification numerical methods. Several future developments mentioned in Sec. 8.2 rely on these newly established codes.

CommComb: Common Tools for Combustion Codes
65 000 lines of code
CommComb first provides an in-house equivalent of the C++ STL library for modern Fortran codes. The addition of high-level interface to I/O (keywords input file, XML, HDF5) allows for manipulating such files with a minimum level of code. Similarly, a set of objects and functions was developed for handling multi-dimensional flamelet tables. All these functionalities along with numerical methods (Linear systems, Newton solvers, ODE solvers, Cubature) are used in several codes developed in EM2C. CommComb is the foundation core of the Agath, Rainier and UnliQ codes. Most of the developed modules rely on oriented object programming, which strengthens modularity, reusability and unit testing.

Agath: Gas Thermodynamics, Kinetics, Transport, 0D/1D flame simulations
55 000 lines of code
CommComb and Agath have been developed since 2012 with the initial acknowledgment that uncertainty quantification (UQ) studies based on heritage codes such as CHEMKIN are not

only impractical but penalize the computation and programming efficiency, and ultimately the scientific advances. Since UQ studies involve manipulating several instances of the same system (chemical mechanisms, homogeneous reactor solutions or 1D flamelets), both library rely on the object-oriented paradigm. Beyond the initial design guidelines for UQ, this entirely new flamelet library focuses on flexibility towards the developer and user side to carry out computations of simple flame configurations with different modeling approaches seamlessly. For example, the thermodynamics can be described with constant properties, NASA polynomials, AVBP thermodynamics or tabulated chemistry. The different Agath solvers rely on similar flexibility for the kinetics and transport description. A non-exhaustive list of available solvers is: homogeneous reactors, detonation, steady and unsteady counterflow flames in spatial or mixture fraction space, premixed flames, spherical flames. During the NextFlame ANR project, two-phase flames were also enabled with multi-class and multi-fluid descriptions of polydisperse sprays.

UnliQ : UQ toolbox
105 000 lines of code
A set of algorithms and methods related to uncertainty quantification studies [140, 136] has been implemented during the thesis of Nicolas Dumont. The object-oriented Agath library enables easily manipulating different mechanism objects with modified uncertain parameters. Several probabilistic sampling methods are available: Classic Monte-Carlo, Latin Hypercube Sampling, Quasi Monte-Carlo with low-discrepancy sampling and their randomization. The latter is preferred for its higher convergence rate with a Sobol sequence built following [108] and randomized with full or linearized scrambling [174]. When the number of uncertain parameters is below 4-5, Monte-Carlo methods are outperformed by deterministic cubature formula. Several techniques are available in UnliQ: plain or sparse grids based on Gauss-Legendre, Clenshaw-Curtis or Féjer quadrature rule. An adaptive sparse grip method following the Smolyak algorithm is also implemented. Pre- and post-treatment analyses are based on several mathematical expansions and key quantities that are computed in the toolbox: Random Sampling-High Dimensional Representation and its corresponding Sobol indices [214], Polynomial Chaos Expansion [244, 136]. Computation of Karhunen-Loève expansion KLE (equivalent of POD or PCA for stochastic processes) is also available following the Nyström method [17].

8.2 Ongoing and future developments

Several works will continue to develop and validate models for turbulent reactive flows associated the first research theme. This research theme will in fact diffuse into the other ones to support the corresponding developments. Ongoing studies and perspectives for the recently developed research axes are given below. Two new sets of activities on oxycombustion and uncertainty quantification are then presented.

8.2.1 Ignition in gas turbines

Given the critical process that is ignition in aeroengines and the remaining associated unknowns, there will still be numerous studies to analyse, simulate and model the different phases of ignition in a gas turbine. The study of light-round in the MICCA chamber allows for the investigation of the last stage of this process which remains the most uncharted. Following the works of Maxime Philip and Théa Lancien, several studies are planned to improve the understanding and prediction of ignition in full-scale engines.

Many phenomena impact the ignition process: the wall temperature, the liquid fuel injection, the type of fuel or the droplet polydispersion. It is then primordial to understand these effects. In order to model them accurately, the numerical simulation faces multiple modelling challenges: chemical models, turbulent combustion models, description of the dispersed liquid phase, two-phase combustion models, prediction of heat losses and their effects on the flame. The development and validation of new models usually take place in simplified single-burner configurations that can be associated with multiple diagnostics rather than large-scale and complex configurations like MICCA which are not suitable to assess the modelling of fundamental mechanisms. Nonetheless, several modelling advances have proven themselves and are nowadays mature enough to consider them in light-round simulations. Quantifying the impact of more advanced modelling approaches in a system such as MICCA will be of great interest. The planned studies are:

- The impact of combustion modelling with the use of a dynamic model for the flame wrinkling factor [235, 206, 233] is being investigated by Stefano Puggelli during his postdoctoral fellowship at EM2C.
- The impact of a polydisperse Lagrangian description of the n-heptane spray in MICCA-Spray is studied by Félix Collin-Bastiani at CERFACS under the supervision of Eleonore Riber and Bénédicte Cuenot.
- The accounting for heat losses in light-round simulations will be studied in the thesis of Karl Töpperwien. *A priori* analysis suggests that describing wall heat losses under the unsteady ignition process will require specific wall models.
- The investigation of less volatile liquid fuels such as dodecane is likely to require additional modelling efforts in two-phase combustion. In particular, the specific propagation of a flame in a mist of droplets will require a specific fundamental study that can be carried out with the two-phase flame solvers in Agath.

As midterm perspectives, tackling the different phases in ignition is most desirable to assess the global ignitability of the system. Additionally, experimental and numerical studies have so far investigated successful ignition sequences. Exploring operating conditions closer to the lean ignition limit is a necessary next step. Finally, more realistic high-altitude relight conditions with low pressure and temperature would be of high relevance but such numerical studies are not envisioned in the short term without the development of a dedicated experimental setup.

As longterm perspectives, the MICCA chamber gives the opportunity to study multiple phenomena linked to the operability conditions of an aeroengine, not just ignition. Therefore, combustion instabilities (already studied experimentally) and lean blowout are two important subjects where a combined experimental and numerical investigation will be interesting. The impact of modelling choices in such simulations of a complete system will be of great value. Several of these points will be addressed in the European project ANNULIGHT.

8.2.2 Heat transfer and multiphysics simulation

Several works will keep enriching this research theme in terms of numerical methods, models and applications:

- A first axis is the developments and improvements of numerical methods to solve radiative energy transfer. The retained approach remains the use of Monte Carlo methods for reference results of coupled simulations. The parallel study on statistical methods from the

uncertainty quantification area has enabled anticipating several and original improvements for a solver dedicated to radiation: importance sampling, Quasi Monte Carlo, ... The impact of these improvements has started in the thesis of Lorella Palluotto and will be pursued. The results obtained with such a type of solvers will nonetheless remain more expansive than with other approaches such as Discrete Ordinated Methods with a global model for gas radiative properties. It will then be interesting to further compare these approaches in collaboration with other research teams such as CERFACS or CORIA where other solvers are used to describe radiative transfer in combustion simulations. Finally, one must not forget that the present Monte Carlo simulations rely on physical models and assumptions. Line-by-line gas properties as considered in the studies by Michael Modest and co-workers and more accurate wall boundary properties will be investigated to achieve a higher fidelity of the simulations. A better description of soot radiative properties, notably with the accounting for scattering, will be studied during the thesis of Kévin Torres.

- The detailed computations can be used to analyse Turbulence-Radiation Interactions (TRI) with uncommon accuracy. The thesis of Jan Mateu Armengol thus studies such effects in direct numerical simulations of non-reacting jets of water vapor. In the meantime, the soot dynamics was shown to have a significant impact during the thesis of Pedro Rodrigues. Finally, the effects of subgrid-scale TRI which have been neglected so far will be studied. They can be in particular magnify by the use of coarser meshes in coupled simulations.

- The maturity of coupled large-eddy simulations remains low. Another axis of numerical developments will deal with the coupling procedure between the corresponding different solvers. While the matter has been studied for conjugate heat transfer with the HCND method, coupling simulations with radiation suffer from the same *ad hoc* parameters and choices. It is then necessary to make these coupling methods more reliable and robust by quantifying and controlling the associated numerical errors. This is all the more true for simulations standing as high-fidelity computations. The effects of the coupling period and mesh coarsening in coupled simulations with radiation will then be studied it order to better control their impact.

- The efforts on better predictions of convective heat transfer will be pursued in the thesis of Matteo Gelain where TBLE wall models will be implemented in AVBP before investigating non-equilibrium effects. In the meantime, following the thesis results of Yufang Zhang, the application of such wall models augmented with radiation effects will allow better prediction of coupled heat transfer through turbulent boundary layers. Mid-term developments should also consider thermal barriers which can be implemented in such wall models. This will require a pluridisciplinary and collaborative study given the complex porous and semitransparent properties of such material.

- Multiphysics simulations enable to study several types of flames where coupled heat transfer has a great impact. This is the case for example of pressurised flames, oxyflames (developed in next section) and sooted flames (thesis of Kévin Torres). The further applications of coupled simulations and subsequent analysis will of course form a large portion of future activities. First, this will improve the validation of such simulations that are founded on an increasingly richer set of models. Secondly, such computations increase the understanding of heat transfer and their reciprocal effects in the considered combustors.

- Finally, with a better estimation of heat transfer, the impact of combustion models describing heat loss effect on the flame will be better assessed. The addressed topics are the

pollutants emission and the flame stabilisation.

8.2.3 Oxycombustion

The enrichment of oxygen in oxyflames amplifies the role of heat transfer mechanisms in the corresponding combustor either through the maximum temperature that is greatly increased or because of the large dilution with burnt gases often used to neutralise the temperature peak. In both cases, wall heat transfer and radiative heat transfer are enhanced. Thanks to the development on multiphysics simulations and successful applications, this new research theme will be further nourished with dedicated applications to oxycombustion. This activity benefits from the OxyTeC test rig in EM2C designed for the investigation of pressurised oxyflames. The combined experimental and numerical study of oxycombustion is exciting and has already begun. An atmospheric confined oxyflame studied experimentally by Paul Jourdaine [113] is being simulated during the thesis of Lorella Palluotto by combining the AVBP and Rainier solver. In 2017, I was invited by Thierry Schuller to participate to the supervision of the thesis of Arthur Degenève. This is a very pleasant experience for me to participate to the analysis of experimental data and combine numerical and experimental investigations in the same thesis. Several studies on the stabilisation, length and heat transfer of oxyflames have recently been accepted for publication or are under review.

Activities will naturally pursue then the coupled simulation of oxyflames and associated challenges. I also intend to continue the supervision of combined numerical and experimental studies on the OxyTec test rig.

8.2.4 Uncertainty quantification

Finally, I present here another new research theme dedicated to uncertainty quantification (UQ). Indeed, with the increasing physical complexity of our current developments, the number of uncertainties in so-called high-fidelity simulations strongly grows. It is then necessary to quantify these uncertainties, to associate numerical error bars with the reported results and to distinguish the contributions from each submodel. Such studies with reactive large-eddy simulations [161, 121] are seldom although they are more then relevant. The actual computational resources make such a study affordable nowadays, outlining the timeliness of the topic.

Given the low maturity of LES applications, such a UQ investigation on all described phenomena in multiphysics simulations is today unrealistic but should be seen as an ultimate goal to tend to. In order to advance on this path then and allow for a growing reliability of LES validations, it is planned, in the midterm, to study the uncertainty associated to different models separately:

- In reactive flows: uncertainties in chemical mechanisms.
- In heat transfer applications : uncertainties of soot radiative properties, wall emissivities, material properties.
- Two-phase flows: uncertainty in the droplet injection model.

These points are borne of my scientific interests in different areas (combustion modelling, multiphysics simulations, two-phase flames) that made me sensitive to the uncertainties in the achieved computations. Turbulent combustion modelling should be added as a fourth uncertainty contribution. However, the treatment of such epistemic uncertainties remains difficult and will not be investigated at the beginning.

Several efforts have been initiated on this theme already. Several UQ methods have been tested and validated during the thesis of Nicolas Dumont and yielded the UnliQ library. Nicolas Dumont also developed a new framework to define reduced order models based on flamelets that retain the uncertainty information from the detailed mechanisms they are derived from. A LASIPS project with Oliver La Maître will extend this study to global mechanisms. Developing such studies on uncertainties in chemical mechanisms is critical as detailed mechanisms are indeed affected by uncertainties [10], even for hydrogen [126]. The associated CFD simulations are then sensitive as well to the underlying uncertainty of chemical mechanisms, especially in configurations where detailed kinetics effects prevail such as in the Cabra flame (see Fig. 4.4). Furthermore, mechanisms for biofuels and emerging ones are impacted by even larger uncertainties, which makes the use of UQ methodology even more critical in computations if one wants to certify their usage in aeroengines for example. This activity will soon be strengthened with the thesis of Guilhem Lavabre who will assess the global sensitivity of large-eddy simulations of the H_2/N_2 Cabra flame with uncertainty quantification.

8.3 Synthesis

The aforementioned five research themes are of course interconnected, which is shown in Fig. 8.1 that extends the previous picture in Fig. 7.7(b). The effects of wall temperature in light-round anchors the associated activities between the combustion and heat transfer modelling challenges. Oxycombustion features even more connexion with the heat transfer axis, notably with the enhanced radiative transfer. Finally, the uncertainty quantification studies will ultimately encompass all these activities.

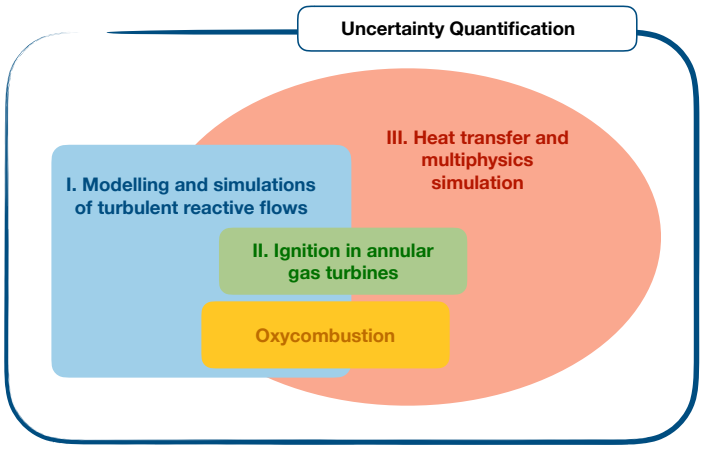

Figure 8.1: Connexions between future research activities.

The range of activities is large and exciting. It will keep me and many collaborators busy for some time!

References

[1] B. Abramzon and W. Sirignano. "Droplet vaporization model for spray combustion calculations". In: *International Journal of Heat and Mass Transfer* 32.9 (1989), pp. 1605–1618.

[2] S. Ahmed, R. Balachandran, T. Marchione, and E. Mastorakos. "Spark ignition of turbulent nonpremixed bluff-body flames". In: *Combustion and Flame* 151.1 (2007), pp. 366–385.

[3] J. Amaya, O. Cabrit, D. Poitou, B. Cuenot, and M. El Hafi. "Unsteady coupling of Navier-Stokes and radiative heat transfer solvers applied to an anisothermal multicomponent turbulent channel flow". In: *Journal of Quantitative Spectroscopy and Radiative Transfer* 111.2 (2010). Eurotherm Seminar 83 on Computational Thermal Radiation in Participating Media III, Lisbon, Portugal, APR 15-17, 2009, 295–301.

[4] ANSYS. *Ansys CFX website*. http://www.ansys.com/products/fluid-dynamics/cfx/. 2010.

[5] P. Auzillon, O. Gicquel, N. Darabiha, D. Veynante, and B. Fiorina. "A Filtered Tabulated Chemistry model for LES of stratified flames". In: *Combustion and Flame* 159.8, SI (2012), 2704–2717.

[6] AVBP, CERFACS. *http://www.cerfacs.fr/avbp7x/*.

[7] E. Bach, J. Kariuki, J. R. Dawson, E. Mastorakos, and H.-j. Bauer. "Spark ignition of single bluff-body premixed flames and annular combustors". In: *51st AIAA Aerospace Sciences Meeting including the New Horizons Forum and Aerospace Exposition*. American Institute of Aeronautics and Astronautics, 2013.

[8] D. Ballal and A. Lefebvre. "Flame propagation in heterogeneous mixtures of fuel droplets, fuel vapor and air". In: *International Symposium on Combustion* 18.1 (1981), pp. 321–328.

[9] D. Barré, L. Esclapez, M. Cordier, E. Riber, B. Cuenot, G. Staffelbach, B. Renou, A. Vandel, L. Y. Gicquel, and G. Cabot. "Flame propagation in aeronautical swirled multiburners: Experimental and numerical investigation". In: *Combustion and Flame* 161.9 (2014), pp. 2387–2405.

[10] D. Baulch, C. Bowman, C. Cobos, R. Cox, T. Just, J. Kerr, M. Pilling, D. Stocker, J. Troe, W. Tsang, R. Walker, and J. Warnatz. "Evaluated kinetic data for combustion modeling: Supplement II". In: *JOURNAL OF PHYSICAL AND CHEMICAL REFERENCE DATA* 34.3 (2005), 757–1397.

[11] M. Baum and T. Poinsot. "Effects of mean flow on premixed flame ignition". In: *Combustion Science and Technology* 106.1-3 (1995), 19–&.

[12] J. Beduneau, B. Kim, L. Zimmer, and Y. Ikeda. "Measurements of minimum ignition energy in premixed laminar methane/air flow by using laser induced spark". In: *Combustion and Flame* 132.4 (2003), 653–665.

[13] S. Berger, S. Richard, F. Duchaine, G. Staffelbach, and L. Y. M. Gicquel. "On the sensitivity of a helicopter combustor wall temperature to convective and radiative thermal loads". In: *Applied Thermal Engineering* 103 (2016), pp. 1450–1459.

[14] M. Berglund and C. Fureby. "LES of supersonic combustion in a scramjet engine model". In: *Proceedings of the Combustion Institute* 31 (2007), pp. 2497–2504.

[15] I. Bermejo-Moreno, J. Bodart, J. Larsson, B. M. Barney, J. W. Nichols, and S. Jones. "Solving the compressible Navier-Stokes equations on up to 1.97 million cores and 4.1 trillion grid points". In: *SC '13: Proceedings of the International Conference on High Performance Computing, Networking, Storage and Analysis*. 2013, pp. 1–10.

[16] I. Bermejo-Moreno, L. Campo, J. Larsson, J. Bodart, D. Helmer, and J. K. Eaton. "Confinement effects in shock wave/turbulent boundary layer interactions through wall-modelled large-eddy simulations". In: *Journal of Fluid Mechanics* 758 (2014), pp. 5–62.

[17] W. Betz, I. Papaioannou, and D. Straub. "Numerical methods for the discretization of random fields by means of the Karhunen–Loève expansion". In: *Computer Methods in Applied Mechanics and Engineering* 271 (2014), pp. 109–129.

[18] M. Boileau, G. Staffelbach, B. Cuenot, T. Poinsot, and C. Bérat. "Large eddy simulation of an ignition sequence in a gas turbine engine". In: *Combustion and Flame* 154.1–2 (2008), pp. 2–22.

[19] M. Boileau. "Large eddy simulation of two-phase ignition in aeronautical combustors". Theses. Institut National Polytechnique de Toulouse - INPT, 2007.

[20] S. T. Bose and G. I. Park. "Wall-Modeled Large-Eddy Simulation for Complex Turbulent Flows". In: *Annual Review of Fluid Mechanics* 50.1 (2018), pp. 535–561.

[21] J.-F. Bourgouin, D. Durox, T. Schuller, J. Beaunier, and S. Candel. "Ignition dynamics of an annular combustor equipped with multiple swirling injectors". In: *Combustion and Flame* 160.8 (2013), pp. 1398–1413.

[22] S. Buis, A. Piacentini, and D. Déclat. "PALM: a computational framework for assembling high-performance computing applications". In: *Concurrency and Computation: Practice and Experience* 18.2 (2006), pp. 231–245.

[23] T. D. Butler and P. J. O'Rourke. "A numerical method for two-dimensional unsteady reacting flows." In: *Proceedings of the Combustion Institute* 16 (1977), pp. 1503–1515.

[24] V. Bykov and U. Maas. "The extension of the ILDM concept to reaction-diffusion manifolds". In: *Combustion Theory and Modelling* 11.6 (2007), 839–862.

[25] R. Cabra, J. .-.-Y. Chen, R. W. Dibble, A. N. Karpetis, and R. S. Barlow. "Lifted methane-air jet flames in a vitiated coflow". In: *Combustion and Flame* 143.4 (2005), pp. 491–506.

[26] R. Cabra, T. Myhrvold, J. Y. Chen, R. W. Dibble, A. N. Karpetis, and R. S. Barlow. "Simultaneous laser raman-rayleigh-lif measurements and numerical modeling results of a lifted turbulent H2/N2 jet flame in a vitiated coflow". In: *Proceedings of the Combustion Institute* 29.2 (2002), pp. 1881–1888.

[27] S. Candel. "Combustion dynamics and control: Progress and challenges". In: *Proceedings of the Combustion Institute* 29.1 (2002), pp. 1–28.

[28] S. Candel and T. Poinsot. "Flame stretch and the balance equation for the flame area". In: *Combustion Science and Technology* 70.1-3 (1990), pp. 1–15.

[29] C. Cardin, B. Renou, G. Cabot, and A. M. Boukhalfa. "Experimental analysis of laser-induced spark ignition of lean turbulent premixed flames: New insight into ignition transition". In: *Combustion and Flame* 160.8 (2013), pp. 1414–1427.

[30] M. Castela, S. Stepanyan, B. Fiorina, A. Coussement, O. Gicquel, N. Darabiha, and C. O. Laux. "A 3-D DNS and experimental study of the effect of the recirculating flow pattern inside a reactive kernel produced by nanosecond plasma discharges in a methane-air mixture". In: *Proceedings of the Combustion Institute* 36.3 (2017), pp. 4095–4103.

[31] M. Champion, B. Deshaies, G. Joulin, and K. Kinoshita. "Spherical flame initiation - Theory versus experiments for lean propane-air mixtures". In: *Combustion and Flame* 65.3 (1986), 319–337.

[32] C. S. Chang, Y. Zhang, K. N. C. Bray, and B. Rogg. "Modelling and simulation of autoignition under simulated diesel-engine conditions". In: *Combustion Science and Technology* 114 (1996), pp. 205–219.

[33] M. Chapuis, E. Fedina, C. Fureby, K. Hannemann, S. Karl, and J. Martinez Schramm. "A computational study of the HyShot II combustor performance". In: *Proceedings of the Combustion Institute* 34 (2013), pp. 2101–2109.

[34] F. Charlette, C. Meneveau, and D. Veynante. "A power-law flame wrinkling model for LES of premixed turbulent combustion Part I: non-dynamic formulation and initial tests". In: *Combustion and Flame* 131.1-2 (2002), pp. 159–180.

[35] P. J. Coelho. "Numerical simulation of the interaction between turbulence and radiation in reactive flows". In: *Progress in Energy and Combustion Science* 33 (2007), pp. 311–383.

[36] P. J. Coelho. "Turbulence-Radiation Interaction: From Theory to Application in Numerical Simulations". In: *Journal of Heat Transfer-Transactions of the ASME* 134.3 (2012).

[37] G. Coleman, J. Kim, and R. Moser. "A numerical study of turbulent supersonic isothermal-wall channel flow". In: *Journal of Fluid Mechanics* 305 (1995), 159–183.

[38] O. Colin, F. Ducros, D. Veynante, and T. Poinsot. "A thickened flame model for large eddy simulations of turbulent premixed combustion". In: *Physics of Fluids* 12.7 (2000), pp. 1843–1863.

[39] O. Colin and M. Rudgyard. "Development of high-order Taylor-Galerkin schemes for LES". In: *Journal of Computational Physics* 162.2 (2000), pp. 338–371.

[40] O. Colin, A. Pires da Cruz, and S. Jay. "Detailed chemistry-based auto-ignition model including low temperature phenomena applied to 3-D engine calculations". In: *Proceedings of the Combustion Institute* 30.2 (2005), pp. 2649–2656.

[41] F. Collin-Bastiani, J. M. Santiago, E. Riber, G. Cabot, B. Renou, and B. Cuenot. "A joint experimental and numerical study of ignition in a spray burner". In: *Proceedings of the Combustion Institute* (2018).

[42] F. Collin-Bastiani, O. Vermorel, C. Lacour, B. Lecordier, and B. Cuenot. "DNS of spark ignition using analytically reduced chemistry including plasma". In: *Proceedings of the Combustion Institute* in press (2018).

[43] J. L. Consalvi and F. Nmira. "Absorption turbulence-radiation interactions in sooting turbulent jet flames". In: *Journal of Quantitative Spectroscopy and Radiative Transfer* 201 (2017), pp. 1–9.

[44] J. L. Consalvi and F. Nmira. "Transported scalar PDF modeling of oxygen-enriched turbulent jet diffusion flames: Soot production and radiative heat transfer". In: *Fuel* 178 (2016), pp. 37–48.

[45] A. Coussement, T. Schmitt, and B. Fiorina. “Filtered Tabulated Chemistry for non-premixed flames”. In: *Proceedings of the Combustion Institute* 35.2 (2015), pp. 1183–1190.

[46] A. de Lataillade, J. L. Dufresne, M. El Hafi, V. Eymet, and R. Fournier. “A net-exchange Monte Carlo approach to radiation in optically thick systems”. In: *Journal of Quantitative Spectroscopy and Radiative Transfer* 74.5 (2002), pp. 563–584.

[47] J. Delatorre, G. Baud, J. J. Bézian, S. Blanco, C. Caliot, J. F. Cornet, C. Coustet, J. Dauchet, M. El Hafi, V. Eymet, R. Fournier, J. Gautrais, O. Gourmel, D. Joseph, N. Meilhac, A. Pajot, M. Paulin, P. Perez, B. Piaud, M. Roger, J. Rolland, F. Veynandt, and S. Weitz. “Monte Carlo advances and concentrated solar applications”. In: *Solar Energy* 103 (2014), pp. 653–681.

[48] M. K. Denison and B. W. Webb. “A Spectral Line-Based Weighted-Sum-of-Gray-Gases Model for Arbitrary RTE Solvers”. In: *Journal of Heat Transfer* 115.4 (1993), pp. 1004–1012.

[49] P. Domingo, L. Vervisch, and D. Veynante. “Large-eddy simulation of a lifted methane jet flame in a vitiated coflow”. In: *Combustion and Flame* 152.3 (2008), pp. 415–432.

[50] F. Duchaine, A. Corpron, L. Pons, V. Moureau, F. Nicoud, and T. Poinsot. “Development and assessment of a coupled strategy for conjugate heat transfer with Large Eddy Simulation: Application to a cooled turbine blade”. In: *International Journal of Heat and Fluid Flow* 30.6 (2009), 1129–1141.

[51] F. Duchaine, N. Maheu, V. Moureau, G. Balarac, and S. Moreau. “Large-Eddy Simulation and Conjugate Heat Transfer Around a Low-Mach Turbine Blade”. In: *Journal of Turbomachinery* 136.5 (2013), pp. 051015–051015.

[52] C. Eberle, P. Gerlinger, K. P. Geigle, and M. Aigner. “Numerical Investigation of Transient Soot Evolution Processes in an Aero-Engine Model Combustor”. In: *Combustion Science and Technology* 187.12 (2015), pp. 1841–1866.

[53] J. R. Edwards, J. A. Boles, and R. A. Baurle. “Large-eddy/Reynolds-averaged Navier-Stokes simulation of a supersonic reacting wall jet”. In: *Combustion and Flame* 159 (2012), pp. 1127–1138.

[54] E. Effelsberg and N. Peters. “Scalar dissipation rates in turbulent jets and jet diffusion flames”. In: *Proceedings of the Combustion Institute* 22.1 (1989), pp. 693–700.

[55] M. Embouazza. “Etude de l’Auto-Allumage par Réduction des Schémas Cinétiques Chimiques. Application à la Combustion Homogène diesel.” PhD thesis. Ecole Centrale Paris, 2005.

[56] M. .-.-P. Errera and F. Duchaine. “Comparative study of coupling coefficients in Dirichlet–Robin procedure for fluid–structure aerothermal simulations”. In: *Journal of Computational Physics* 312 (2016), pp. 218–234.

[57] M.-P. Errera and S. Chemin. “Optimal solutions of numerical interface conditions in fluid–structure thermal analysis”. In: *Journal of Computational Physics* 245 (2013), pp. 431–455.

[58] L. Esclapez. “Numerical Study of Ignition and Inter-Sector Flame Propagation in Gas Turbine”. PhD thesis. INP Toulouse, 2015.

[59] L. Esclapez, E. Riber, and B. Cuenot. “Ignition probability of a partially premixed burner using LES”. In: *Proceedings of the Combustion Institute* 35.3 (2015), pp. 3133–3141.

[60] A. Eyssartier, G. Hannebique, D. Barré, L. Gicquel, and B. Cuenot. "Ignition predictions from non-reacting LES: application and assessment on complex configurations". In: *Comptes Rendus Mécanique* 333 (2011).

[61] A. Eyssartier, B. Cuenot, L. Y. Gicquel, and T. Poinsot. "Using LES to predict ignition sequences and ignition probability of turbulent two-phase flames". In: *Combustion and Flame* 160.7 (2013), pp. 1191–1207.

[62] A. Felden, E. Riber, and B. Cuenot. "Impact of direct integration of Analytically Reduced Chemistry in LES of a sooting swirled non-premixed combustor". In: *Combustion and Flame* 191 (2018), pp. 270–286.

[63] A. Feldick, A. Bansal, and M. Modest. "Variance Reduction Techniques For Monte Carlo Solution of Radiative Transfer in Hypersonic Flows: Hybrid P-1-Monte Carlo". In: *49th AIAA Aerospace Sciences Meeting including the New Horizons Forum and Aerospace Exposition*. 2011, p. 245.

[64] V. Fichet. "Modélisation de la combustion du gaz naturel par réseaux de réacteurs avec cinétique chimique détaillée". PhD thesis. Ecole Centrale Paris, 2008.

[65] B. Fiorina, R. Baron, O. Gicquel, D. Thevenin, S. Carpentier, and N. Darabiha. "Modelling non-adiabatic partially premixed flames using flame-prolongation of ILDM". In: *Combustion Theory and Modelling* 7 (2003), pp. 449–470.

[66] B. Fiorina, O. Gicquel, L. Vervisch, S. Carpentier, and N. Darabiha. "Premixed turbulent combustion modeling using tabulated detailed chemistry and PDF". In: *Proceedings of the Combustion Institute* 30 (2005), pp. 867–874.

[67] B. Fiorina, D. Veynante, and S. Candel. "Modeling Combustion Chemistry in Large Eddy Simulation of Turbulent Flames". In: *Flow, Turbulence and Combustion* 94.1 (2015), pp. 3–42.

[68] B. Franzelli, B. Fiorina, and N. Darabiha. "A tabulated chemistry method for spray combustion". In: *Proceedings of the Combustion Institute* 34.1 (2013), pp. 1659–1666.

[69] B. Franzelli, E. Riber, B. Cuenot, and M. Ihme. *Numerical Modeling of Soot Production in aero-engine combustors using large eddy simulations*. ASME Turbo Expo, Paper No. GT2015-43630, pp. V04BT04A049. 2015.

[70] B. Franzelli, E. Riber, M. Sanjosé, and T. Poinsot. "A two-step chemical scheme for kerosene–air premixed flames". In: *Combustion and Flame* 157.7 (2010), pp. 1364–1373.

[71] C. Fureby, M. Chapuis, E. Fedina, and S. Karl. "CFD analysis of the HyShot II scramjet combustor". In: *Proceedings of the Combustion Institute* 33 (2011), pp. 2399–2405.

[72] J. Galpin, C. Angelberger, A. Naudin, and L. Vervisch. "Large-eddy simulation of H-2-air auto-ignition using tabulated detailed chemistry". In: *Journal of Turbulence* 9.13 (2008), pp. 1–21.

[73] J. Galpin, A. Naudin, L. Vervisch, C. Angelberger, O. Colin, and P. Domingo. "Large-eddy simulation of a fuel-lean premixed turbulent swirl-burner". In: *Combustion and Flame* 155.1-2 (2008), pp. 247–266.

[74] K. P. Geigle, R. Hadef, and W. Meier. "Soot Formation and Flame Characterization of an Aero-Engine Model Combustor Burning Ethylene at Elevated Pressure". In: *Journal of Engineering for Gas Turbines and Power* 136.2 (2014), pp. 021505–021505.

[75] S. Ghosh, R. Friedrich, M. Pfitzner, C. Stemmer, B. Cuenot, and M. El Hafi. "Effects of radiative heat transfer on the structure of turbulent supersonic channel flow". In: *Journal of Fluid Mechanics* 677 (2011), 417–444.

[76] L. Y. M. Gicquel, G. Staffelbach, and T. Poinsot. "Large Eddy Simulations of gaseous flames in gas turbine combustion chambers". In: *Progress in Energy and Combustion Science* 38.6 (2012), 782–817.

[77] O. Gicquel. "Développement d'une nouvelle méthode de réduction des schémas cinétiques : Application au méthane". PhD thesis. Ecole Centrale Paris, 1999.

[78] O. Gicquel, N. Darabiha, and D. Thevenin. "Laminar premixed hydrogen/air counterflow flame simulations using flame prolongation of ILDM with differential diffusion". In: *Proceedings of the Combustion Institute* 28.Part 2 (2000), 1901–1908.

[79] M. B. Giles. "Stability analysis of numerical interface conditions in fluid-structure thermal analysis". In: *Iternational Journal for Numerical Methods in Fluids* 25.4 (1997), pp. 421–436.

[80] K. Gkagkas and R. P. Lindstedt. "Transported PDF modelling with detailed chemistry of pre- and auto-ignition in CH4/air mixtures". In: *Proceedings of the Combustion Institute* 31.1 (2007), pp. 1559–1566.

[81] R. Gonçalves dos Santos, M. Lecanu, S. Ducruix, O. Gicquel, E. Iacona, and D. Veynante. "Coupled large eddy simulations of turbulent combustion and radiative heat transfer". In: *Combustion and Flame* 152.3 (2008), pp. 387–400.

[82] R. M. Goody and Y. L. Yung. *Atmospheric radiation: theoretical basis*. Oxford university press, 1995.

[83] R. L. Gordon, S. H. Starner, A. R. Masri, and R. W. Bilger. "Further Characterisation of Lifted Hydrogen and Methane Flames issuing into a Vitiated Coflow". In: *Proceedings of the 5th Asia-Pacific Conference on Combustion*. University of Adelaide, 2005, pp. 333–336.

[84] R. L. Gordon, A. R. Masri, S. B. Pope, and G. M. Goldin. "Transport budgets in turbulent lifted flames of methane autoigniting in a vitiated co-flow". In: *Combustion and Flame* 151.3 (2007), pp. 495–511.

[85] A. Gruber, J. H. Chen, D. Valiev, and C. K. Law. "Direct numerical simulation of premixed flame boundary layer flashback in turbulent channel flow". In: *Journal of Fluid Mechanics* 709 (2012), pp. 516–542.

[86] T. F. Guiberti, D. Durox, P. Scouflaire, and T. Schuller. "Impact of heat loss and hydrogen enrichment on the shape of confined swirling flames". In: *Proceedings of the Combustion Institute* 35.2 (2015), pp. 1385–1392.

[87] T. F. Guiberti, D. Durox, L. Zimmer, and T. Schuller. "Analysis of topology transitions of swirl flames interacting with the combustor side wall". In: *Combustion and Flame* 162.11 (2015), pp. 4342–4357.

[88] A. Gupta, D. Haworth, and M. Modest. "Turbulence-radiation interactions in large-eddy simulations of luminous and nonluminous nonpremixed flames". In: *Proceedings of the Combustion Institute* 34.1 (2013), pp. 1281–1288.

[89] A. Gupta, M. F. Modest, and D. C. Haworth. "Large-Eddy Simulation of Turbulence-Radiation Interactions in a Turbulent Planar Channel Flow". In: *Journal of Heat Transfer-Transactions of the ASME* 131.6 (2009).

[90] E. Hairer and G. Wanner. *Solving Ordinary Differential Equations I*. Spinger; 2nd Edition, 2000.

[91] W. Han, V. Raman, and Z. Chen. "LES/PDF modeling of autoignition in a lifted turbulent flame: Analysis of flame sensitivity to differential diffusion and scalar mixing time-scale". In: *Combustion and Flame* 171 (2016), pp. 69–86.

[92] K. Hannemann, S. Karl, J. Martinez Schramm, and J. Steelant. "Methodology of a combined ground based testing and numerical modelling analysis of supersonic combustion flow paths". In: *Shock Waves* 20 (2010), pp. 353–366.

[93] K. Hannemann, J. Martinez Schramm, S. Karl, and J. Steelant. "Experimental investigation of different scramjet hydrogen injection systems". In: *Proc. 6th European Symposium on Aerothermodynamics for Space Vehicles*. ESA-SP-659. 2009.

[94] C. Hasse and N. Peters. "A two mixture fraction flamelet model applied to split injections in a DI Diesel engine". In: *Proceedings of the Combustion Institute* 30.2 (2005), pp. 2755–2762.

[95] L. He. "Fourier spectral modelling for multi-scale aero-thermal analysis". In: *International Journal of Computational Fluid Dynamics* 27.2 (2013), pp. 118–129.

[96] L. He and M. Oldfield. "Unsteady conjugate heat transfer modelling". In: *ASME Journal of Turbomachinery* 133.3 (2011), p. 031022.

[97] A. Heinrich, F. Ries, G. Kuenne, S. Ganter, C. Hasse, A. Sadiki, and J. Janicka. "Large Eddy Simulation with tabulated chemistry of an experimental sidewall quenching burner". In: *International Journal of Heat and Fluid Flow* 71 (2018), pp. 95–110.

[98] Z. Hong, D. F. Davidson, and R. K. Hanson. "An improved H_2/O_2 mechanism based on recent shock tube/laser absorption measurements". In: *Combustion and Flame* 158 (2011), pp. 633–644.

[99] P. Huang, G. Coleman, and P. Bradshaw. "Compressible turbulent channel flows: DNS results and modelling". In: *Journal of Fluid Mechanics* 305 (1995), 185–218.

[100] M. Ihme, C. M. Cha, and H. Pitsch. "Prediction of local extinction and re-ignition effects in non-premixed turbulent combustion using a flamelet/progress variable approach". In: *Proceedings of the Combustion Institute* 30 (2005), pp. 793–800.

[101] M. Ihme and H. Pitsch. "Modeling of radiation and nitric oxide formation in turbulent nonpremixed flames using flamelet/progress variable formulation". In: *Physics of Fluids* 20.5 (2008), p. 055110.

[102] M. Ihme and H. Pitsch. "Prediction of extinction and reignition in nonpremixed turbulent flames using a flamelet/progress variable model: 1. A priori study and presumed PDF closure". In: *Combustion and Flame* 155.1-2 (2008), pp. 70–89.

[103] M. Ihme and Y. C. See. "Prediction of autoignition in a lifted methane/air flame using an unsteady flamelet/progress variable model". In: *Combustion and Flame* 157.10 (2010), 1850–1862.

[104] ISF3. *International Sooting Flame Workshop, http://www.adelaide.edu.au/cet/isfworkshop/datasets/*. 2017.

[105] C. Jainski, M. Rißmann, B. Böhm, and A. Dreizler. "Experimental investigation of flame surface density and mean reaction rate during flame–wall interaction". In: *Proceedings of the Combustion Institute* 36.2 (2017), pp. 1827–1834.

[106] T. Jaravel, E. Riber, B. Cuenot, and G. Bulat. "Large Eddy Simulation of an industrial gas turbine combustor using reduced chemistry with accurate pollutant prediction". In: *Proceedings of the Combustion Institute* 36.3 (2017), pp. 3817–3825.

[107] S. Jaure, F. Duchaine, G. Staffelbach, and L. Gicquel. "Massively parallel conjugate heat transfer methods relying on large eddy simulation applied to an aeronautical combustor". In: *Computational Science & Discovery* 6.1 (2013), p. 015008.

[108] S. Joe and F. Y. Kuo. "Constructing Sobol sequences with better two-dimensional projections". In: *SIAM Journal on Scientific Computing* 30.5 (2008), pp. 2635–2654.

[109] W. P. Jones and R. P. Lindstedt. "Global reaction schemes for hydrocarbon combustion". In: *Combustion and Flame* 73.3 (1988), pp. 233–249.

[110] W. P. Jones and S. Navarro-Martinez. "Large eddy simulation of autoignition with a subgrid probability density function method". In: *Combustion and Flame* 150.3 (2007), pp. 170–187.

[111] W. P. Jones and M. C. Paul. "Combination of DOM with LES in a gas turbine combustor". In: *International Journal of Engineering Science* 43.5–6 (2005), pp. 379–397.

[112] W. P. Jones and A. Tyliszczak. "Large Eddy Simulation of Spark Ignition in a Gas Turbine Combustor". In: *Flow, Turbulence and Combustion* 85.3 (2010), pp. 711–734.

[113] P. Jourdaine, C. Mirat, J. Caudal, A. Lo, and T. Schuller. "A comparison between the stabilization of premixed swirling CO2-diluted methane oxy-flames and methane/air flames". In: *Fuel* 201.1 (2017), pp. 156–164.

[114] M. Juvela. "Efficient Monte Carlo methods for continuum radiative transfer". In: *Astronomy & Astrophysics* 440.2 (2005), pp. 531–546.

[115] S. Kawai and J. Larsson. "Wall-modeling in large eddy simulation: Length scales, grid resolution, and accuracy". In: *Physics of Fluids* 24.1 (2012).

[116] S. N. Laboratories, ed. *Temperature, Oxygen, and Soot-Volume-Fraction Measurements in a Turbulent C2H4-Fueled Jet Flame*. 2015.

[117] R. J. Kee, J. A. Miller, G. H. Evans, and G. Dixon-Lewis. "A computational model of the structure and extinction of strained, opposed flow, premixed methane-air flames". In: *Symposium (International) on Combustion* 22.1 (1989), pp. 1479–1494.

[118] A. P. Kelley, G. Jomaas, and C. K. Law. "Critical radius for sustained propagation of spark-ignited spherical flames". In: *Combustion and Flame* 156.5 (2009), pp. 1006–1013.

[119] A. Ketelheun, G. Kuenne, and J. Janicka. "Heat Transfer Modeling in the Context of Large Eddy Simulation of Premixed Combustion with Tabulated Chemistry". In: *Flow, Turbulence and Combustion* 91.4 (2013), pp. 867–893.

[120] Y. Khalighi, J. W. Nichols, S. K. Lele, F. Ham, and P. Moin. "Unstructured Large Eddy Simulation for Prediction of Noise Issued from Turbulent Jets in Various Configurations". In: *AIAA Paper No AIAA-2011-2886* (2011).

[121] M. Khalil, G. Lacaze, J. C. Oefelein, and H. N. Najm. "Uncertainty quantification in LES of a turbulent bluff-body stabilized flame". In: *Proceedings of the Combustion Institute* 35.2 (2015), pp. 1147–1156.

[122] J. KIM, P. MOIN, and R. MOSER. "TURBULENCE STATISTICS IN FULLY-DEVELOPED CHANNEL FLOW AT LOW REYNOLDS-NUMBER". In: *Journal of Fluid Mechanics* 177 (1987), 133–166.

[123] V. Knop, J.-B. Michel, and O. Colin. "On the use of a tabulation approach to model auto-ignition during flame propagation in SI engines". In: *Applied Energy* 88.12 (2011), pp. 4968–4979.

[124] Y. Ko, R. W. Anderson, and V. S. Arpaci. "Spark ignition of propane-air mixtures near the minimum ignition energy. Part I. An experimental study". In: *Combustion and Flame* 83 (1991), pp. 75–87.

[125] Y. Ko, V. Arpaci, and R. Anderson. "Spark-ignition of propane air mixtures near the minimum ignition energy .2. A model development". In: *Combustion and Flame* 83.1-2 (1991), 83–88.

[126] A. A. Konnov. "Remaining uncertainties in the kinetic mechanism of hydrogen combustion". In: *Combustion and Flame* 152.4 (2008), pp. 507–528.

[127] H. Koo, M. Hassanaly, V. Raman, M. E. Mueller, and K. Peter Geigle. "Large-Eddy Simulation of Soot Formation in a Model Gas Turbine Combustor". In: *Journal of Engineering for Gas Turbines and Power* 139.3 (2016), pp. 031503–031503-9.

[128] C. Kraus, L. Selle, and T. Poinsot. "Coupling heat transfer and large eddy simulation for combustion instability prediction in a swirl burner". In: *Combustion and Flame* 191 (2018), pp. 239–251.

[129] S. Kuhn, O. Braillard, B. Ničeno, and H.-M. Prasser. "Computational study of conjugate heat transfer in T-junctions". In: *Nuclear Engineering and Design* 240.6 (2010), pp. 1548–1557.

[130] V. Kurdyumov, J. Blasco, A. Sanchez, and A. Linan. "On the calculation of the minimum ignition energy". In: *Combustion and Flame* 136.3 (2004), 394–397.

[131] G. Lacaze, E. Richardson, and T. Poinsot. "Large eddy simulation of spark ignition in a turbulent methane jet". In: *Combustion and Flame* 156.10 (2009), pp. 1993–2009.

[132] S. J. Laurence, S. Karl, J. Martinez Schramm, and K. Hannemann. "Transient fluid-combustion phenomena in a model scramjet". In: *Journal of Fluid Mechanics* 722 (2013), pp. 85–120.

[133] S. J. Laurence, H. Ozawa, D. Lieber, J. Martinez Schramm, and K. Hannemann. "Investigation of unsteady/quasi-steady scramjet behavior using high-speed visualization techniques". In: AIAA Paper 2012-5913, 2012.

[134] S. Laurence, D. Lieber, J. M. Schramm, K. Hannemann, and J. Larsson. "Incipient thermal choking and stable shock-train formation in the heat-release region of a scramjet combustor. Part I: Shock-tunnel experiments". In: *Combustion and Flame* 162.4 (2015), pp. 921–931.

[135] C. Laurent, L. Esclapez, D. Maestro, G. Staffelbach, B. Cuenot, L. Selle, T. Schmitt, F. Duchaine, and T. Poinsot. "Flame–wall interaction effects on the flame root stabilization mechanisms of a doubly-transcritical LO2/LCH4 cryogenic flame". In: *Proceedings of the Combustion Institute* (2018).

[136] O. Le Maître and O. M. Knio. *Spectral methods for uncertainty quantification: with applications to computational fluid dynamics*. Springer Science & Business Media, 2010.

[137] G. Lecocq, D. Poitou, I. Hernández, F. Duchaine, E. Riber, and B. Cuenot. "A Methodology for Soot Prediction Including Thermal Radiation in Complex Industrial Burners". In: *Flow, Turbulence and Combustion* 92.4 (2014), pp. 947–970.

[138] A. Lefebvre and D. R. Ballal. *Gas Turbine Combustion*. Taylor and Francis, 2010.

[139] A. H. Lefebvre. "Flame radiation in gas turbine combustion chambers". In: *International Journal of Heat and Mass Transfer* 27.9 (1984), pp. 1493–1510.

[140] C. Lemieux. *Monte Carlo and Quasi-Monte Carlo Sampling*. Springer, 2009.

[141] C. Letty, E. Mastorakos, A. R. Masri, M. Juddoo, and W. O'Loughlin. "Structure of igniting ethanol and n-heptane spray flames with and without swirl". In: *Experimental Thermal and Fluid Science* 43 (2012). Seventh Mediterranean Combustion Symposium, pp. 47–54.

[142] T. C. Lieuwen. *Unsteady combustor physics*. Cambridge University Press, 2012.

[143] T. Lu and C. K. Law. "A directed relation graph method for mechanism reduction". In: *Proceedings of the Combustion Institute* 30.1 (2005), pp. 1333–1341.

[144] U. Maas and S. B. Pope. "Simplifying chemical kinetics: Intrinsic Low-Dimensional manifolds in composition space". In: *Combustion and Flame* 88.3-4 (1992), 239–264.

[145] E. Machover and E. Mastorakos. “Spark ignition of annular non-premixed combustors”. In: *Experimental Thermal and Fluid Science* 73 (2016), pp. 64–70.

[146] E. Machover and E. Mastorakos. “Experimental investigation on spark ignition of annular premixed combustors”. In: *Combustion and Flame* 178.Supplement C (2017), pp. 148–157.

[147] T. Marchione, S. Ahmed, and E. Mastorakos. “Ignition of turbulent swirling n-heptane spray flames using single and multiple sparks”. In: *Combustion and Flame* 156.1 (2009), pp. 166–180.

[148] R. Mari, B. Cuenot, J.-P. Rocchi, L. Selle, and F. Duchaine. “Effect of pressure on hydrogen/oxygen coupled flame–wall interaction”. In: *Combustion and Flame* 168 (2016), pp. 409–419.

[149] J. Marrero Santiago, A. Verdier, C. Brunet, A. Vandel, G. Godard, G. Cabot, A. Boukhalfa, and B. Renou. “Experimental study of aeronautical ignition in a swirled confined jet-spray burner”. In: *Journal of Engineering for Gas Turbines and Power* 140 (2017).

[150] A. R. Masri, R. Cao, S. B. Pope, and G. M. Goldin. “PDF calculations of turbulent lifted flames of H_2/N_2 fuel issuing into a vitiated co-flow.” In: *Combustion Theory and Modelling* 8 (2004), pp. 1–22.

[151] R. S. Mehta, D. C. Haworth, and M. F. Modest. “Composition PDF/photon Monte Carlo modeling of moderately sooting turbulent jet flames”. In: *Combustion and Flame* 157.5 (2010), 982–994.

[152] R. Mercier, P. Auzillon, V. Moureau, N. Darabiha, O. Gicquel, D. Veynante, and B. Fiorina. “LES Modeling of the Impact of Heat Losses and Differential Diffusion on Turbulent Stratified Flame Propagation: Application to the TU Darmstadt Stratified Flame”. In: *Flow, Turbulence and Combustion* 93.2 (2014), pp. 349–381.

[153] R. Mercier, T. F. Guiberti, A. Chatelier, D. Durox, O. Gicquel, N. Darabiha, T. Schuller, and B. Fiorina. “Experimental and numerical investigation of the influence of thermal boundary conditions on premixed swirling flame stabilization”. In: *Combustion and Flame* 171 (2016), pp. 42–58.

[154] R. Mercier, V. Moureau, D. Veynante, and B. Fiorina. “LES of turbulent combustion: On the consistency between flame and flow filter scales”. In: *Proceedings of the Combustion Institute* 35.2 (2015), pp. 1359–1366.

[155] J.-B. Michel, O. Colin, C. Angelberger, and D. Veynante. “Using the tabulated diffusion flamelet model ADF-PCM to simulate a lifted methane-air jet flame”. In: *Combustion and Flame* 156.7 (2009), pp. 1318–1331.

[156] M. F. Modest. *Radiative Heat Transfer, 3rd Edition.* Academic Press Inc., 2013.

[157] M. F. Modest and H. Zhang. “The Full-Spectrum Correlated-k Distribution for Thermal Radiation From Molecular Gas-Particulate Mixtures”. In: *Journal of Heat Transfer* 124.1 (2001), pp. 30–38.

[158] V. Moureau, P. Domingo, and L. Vervisch. “Design of a massively parallel CFD code for complex geometries”. In: *Comptes Rendus Mathematique* 339.2-3 (2011), pp. 141–148.

[159] V. Moureau, P. Domingo, and L. Vervisch. “From Large-Eddy Simulation to Direct Numerical Simulation of a lean premixed swirl flame: Filtered laminar flame-PDF modeling”. In: *Combustion and Flame* 158.7 (2011), 1340–1357.

[160] V. Moureau, G. Lartigue, Y. Sommerer, C. Angelberger, O. Colin, and T. Poinsot. “Numerical methods for unsteady compressible multi-component reacting flows on fixed and moving grids”. In: *Journal of Computational Physics* 202.2 (2005), pp. 710–736.

[161] M. E. Mueller, G. Iaccarino, and H. Pitsch. "Chemical kinetic uncertainty quantification for Large Eddy Simulation of turbulent nonpremixed combustion". In: *Proceedings of the Combustion Institute* 34.1 (2013), pp. 1299–1306.

[162] M. E. Mueller and H. Pitsch. "LES model for sooting turbulent nonpremixed flames". In: *Combustion and Flame* 159.6 (2012), pp. 2166–2180.

[163] P. Nau, Z. Yin, K. P. Geigle, and W. Meier. "Wall temperature measurements at high pressures and temperatures in sooting flames in a gas turbine model combustor". In: *Applied Physics B* 123.12 (2017), p. 279.

[164] B. Naud, R. Novella, J. Pastor, and J. F. Winklinger. "RANS modelling of a lifted H2/N2 flame using an unsteady flamelet progress variable approach with presumed PDF". In: *Combustion and Flame* 162.4 (2015), pp. 893–906.

[165] S. Navarro-Martinez and A. Kronenburg. "LES-CMC simulations of a lifted methane flame". In: *Proceedings of the Combustion Institute* 32.Part 1 (2009), 1509–1516.

[166] A. Neophytou, E. Mastorakos, and R. Cant. "DNS of spark ignition and edge flame propagation in turbulent droplet-laden mixing layers". In: *Combustion and Flame* 157.6 (2010), pp. 1071–1086.

[167] P.-D. Nguyen, L. Vervisch, V. Subramanian, and P. Domingo. "Multidimensional flamelet-generated manifolds for partially premixed combustion". In: *Combustion and Flame* 157.1 (2010), pp. 43–61.

[168] F. Nicoud and F. Ducros. "Subgrid-scale stress modelling based on the square of the velocity gradient tensor". In: *Flow, Turbulence and Combustion* 62.3 (1999), 183–200.

[169] M. Nishioka, C. K. Law, and T. Takeno. "A flame-controlling continuation method for generating S-curve responses with detailed chemistry". In: *Combustion and Flame* 104.3 (1996), pp. 328–342.

[170] K. .-.-J. Nogenmyr, H. J. Cao, C. K. Chan, and R. K. Cheng. "Effects of confinement on premixed turbulent swirling flame using large Eddy simulation". In: *Combustion Theory and Modelling* 17.6 (2013), pp. 1003–1019.

[171] A. C. Nunno and M. E. Mueller. "Manifold assumptions in modeling radiation heat losses in turbulent nonpremixed combustion". In: *Proceedings of the Combustion Institute* (2018).

[172] M. Ó Conaire, H. J. Curran, J. M. Simmie, W. J. Pitz, and C. K. Westbrook. "A comprehensive modeling study of hydrogen oxidation". In: *International Journal of Chemical Kinetics* 36.11 (2004), pp. 603–622.

[173] G. Okyay. "Impact of the morphology of soot aggregates on their radiative properties and the subsequent radiative heat transfer through sooty gaseous mixtures". Theses. Université Paris-Saclay, 2016.

[174] A. B. Owen. "Randomly permuted (t, m, s)-nets and (t, s)-sequences". In: *Monte Carlo and quasi-Monte Carlo methods in scientific computing*. Springer, 1995, pp. 299–317.

[175] T. P. P. Coffee. "Kinetic mechanisms for premixed, laminar, steady state methane/air flames". In: *Combustion and Flame* 55 (1984), pp. 161–170.

[176] A. Patel, J. W. R. Peeters, B. J. Boersma, and R. Pecnik. "Semi-local scaling and turbulence modulation in variable property turbulent channel flows". In: *Physics of Fluids* 27.9 (2015), p. 095101.

[177] S. S. Patwardhan, S. De, K. N. Lakshmisha, and B. N. Raghunandan. "CMC simulations of lifted turbulent jet flame in a vitiated coflow". In: *Proceedings of the Combustion Institute* 32.Part 2 (2009), 1705–1712.

[178] D. Paulhiac. "Modélisation de la Combustion d'un spray dans un Bruleur Aéronautique". PhD thesis. INP Toulouse, 2015.

[179] R. Pecnik, V. E. Terrapon, F. Ham, G. Iaccarino, and H. Pitsch. "Reynolds-averaged Navier-Stokes simulations of the HyShot II scramjet". In: *AIAA journal* 50.8 (2012), pp. 1717–1732.

[180] P. Pepiot-Desjardins and H. Pitsch. "An efficient error-propagation-based reduction method for large chemical kinetic mechanisms". In: *Combustion and Flame* 154.1 (2008), pp. 67–81.

[181] N. Peters. *Turbulent combustion*. Cambridge University Press, 2000.

[182] X. Petit, G. Ribert, and P. Domingo. "Framework for real-gas compressible reacting flows with tabulated thermochemistry". In: *The Journal of Supercritical Fluids* 101 (2015), pp. 1–16.

[183] C. D. Pierce and P. Moin. "Progress-variable approach for large-eddy simulation of non-premixed turbulent combustion". In: *Journal of Fluid Mechanics* 504 (2004), pp. 73–97.

[184] H. Pitsch. "Large-eddy simulation of turbulent combustion". In: *Annual Review of Fluid Mechanics* 38 (2006), 453–482.

[185] H. Pitsch. *A C++ computer program for 0-D combustion and 1-D laminar flame calculations*. Tech. rep. RWTH Aachen, 1998.

[186] T. Poinsot. "Prediction and control of combustion instabilities in real engines". In: *Proceedings of the Combustion Institute* 36.1 (2017), pp. 1–28.

[187] T. J. Poinsot, D. C. Haworth, and G. Bruneaux. "Direct simulation and modeling of flame-wall interaction for premixed turbulent combustion". In: *Combustion and Flame* 95.1 (1993), pp. 118–132.

[188] T. J. Poinsot and S. K. Lele. "Boundary-conditions for direct simulations of compressible viscous flows". In: *Journal of Computational Physics* 101.1 (1992), pp. 104–129.

[189] D. Poitou, J. Amaya, M. El Hafi, and B. Cuénot. "Analysis of the interaction between turbulent combustion and thermal radiation using unsteady coupled LES/DOM simulations". In: *Combustion and Flame* 159.4 (2012), pp. 1605–1618.

[190] S. B. Pope. *Turbulent Flows*. Cambridge University Press, 2000.

[191] K. Prieur. "Dynamique de la combustion dans un foyer annulaire multi-injecteurs diphasique". PhD thesis. Université Paris-Saclay, 2017.

[192] K. Prieur, D. Durox, J. Beaunier, T. Schuller, and S. Candel. "Ignition dynamics in an annular combustor for liquid spray and premixed gaseous injection". In: *Proceedings of the Combustion Institute* 36.3 (2017), pp. 3717–3724.

[193] K. Prieur, D. Durox, G. Vignat, T. Schuller, and S. Candel. "Flame and spray dynamics during the light-round process in an annular system equipped with multiple swirl spray injectors". In: *Proceedings of the ASME Turbo Expo* (2018).

[194] F. Proch and A. M. Kempf. "Modeling heat loss effects in the large eddy simulation of a model gas turbine combustor with premixed flamelet generated manifolds". In: *Proceedings of the Combustion Institute* 35.3 (2015), pp. 3337–3345.

[195] Z. Qin, V. V. Lissianski, H. Yang, W. C. Gardiner, S. G. Davis, and H. Wang. "Combustion chemistry of propane: A case study of detailed reaction mechanism optimization". In: *Proceedings of the Combustion Institute* 28.2 (2000), pp. 1663–1669.

[196] E. Radenac, J. Gressier, and P. Millan. "Methodology of numerical coupling for transient conjugate heat transfer". In: *Computers & Fluids* 100 (2014), pp. 95–107.

[197] M. T. Reagana, H. N. Najm, R. G. Ghanem, and O. M. Knio. "Uncertainty quantification in reacting-flow simulations through non-intrusive spectral projection". In: *Combustion and Flame* 132.3 (2003), pp. 545–555.

[198] Z. Ren, S. Pope, A. Vladimirsky, and J. Guckenheimer. "The invariant constrained equilibrium edge preimage curve method for the dimension reduction of chemical kinetics". In: *Journal of Chemical Physics* 124.11 (2006), p. 114111.

[199] P. Rivière and A. Soufiani. "Updated band model parameters for H2O, CO2, CH4 and CO radiation at high temperature". In: *International Journal of Heat and Mass Transfer* 55.13–14 (2012), pp. 3349–3358.

[200] M. Roger, P. J. Coelho, and C. B. da Silva. "The influence of the non-resolved scales of thermal radiation in large eddy simulation of turbulent flows: A fundamental study". In: *International Journal of Heat and Mass Transfer* 53.13-14 (2010), 2897–2907.

[201] V. Sabelnikov, B. Deshaies, and L. F. F. Da Silva. "Revisited flamelet model for non-premixed combustion in supersonic flows". In: *Combustion and Flame* 114 (1998), pp. 577–584.

[202] A. Saghafian. *High-fidelity simulations and modeling of compressible reacting flows*. PhD thesis. Department of Mechanical Engineering, Stanford University, 2014.

[203] A. Saghafian, V. E. Terrapon, and H. Pitsch. "An efficient flamelet-based combustion model for compressible flows". In: *Combustion and Flame* 162.3 (2015), pp. 652–667.

[204] M. Sanjosé, J. Senoner, F. Jaegle, B. Cuenot, S. Moreau, and T. Poinsot. "Fuel injection model for Euler–Euler and Euler–Lagrange large-eddy simulations of an evaporating spray inside an aeronautical combustor". In: *International Journal of Multiphase Flow* 37.5 (2011), pp. 514–529.

[205] B. G. Sarnacki, G. Esposito, R. H. Krauss, and H. K. Chelliah. "Extinction limits and associated uncertainties of nonpremixed counterflow flames of methane, ethylene, propylene and n-butane in air". In: *Combustion and Flame* 159.3 (2012), pp. 1026–1043.

[206] T. Schmitt, A. Sadiki, B. Fiorina, and D. Veynante. "Impact of dynamic wrinkling model on the prediction accuracy using the F-TACLES combustion model in swirling premixed turbulent flames". In: *Proceedings of the Combustion Institute* 34.1 (2013), pp. 1261–1268.

[207] J. Senoner, M. Sanjosé, T. Lederlin, F. Jaegle, M. García, E. Riber, B. Cuenot, L. Gicquel, H. Pitsch, and T. Poinsot. "Eulerian and Lagrangian Large-Eddy Simulations of an evaporating two-phase flow". In: *Comptes Rendus Mécanique* 337.6 (2009), p. 458.

[208] C. Shaddix, J. Zhang, R. Schefer, J. Doom, J. Oefelein, S. Kook, L. Pickett, and H. Wang. *Understanding and Predicting Soot Generation in Turbulent Non-Premixed Jet Flames*. Tech. rep. SAND2010-7178. Sandia Report, 2010.

[209] F. Shum-Kivan, J. M. Santiago, A. Verdier, E. Riber, B. Renou, G. Cabot, and B. Cuenot. "Experimental and numerical analysis of a turbulent spray flame structure". In: *Proceedings of the Combustion Institute* 36.2 (2016), pp. 2567–2575.

[210] S. Shy, C. Liu, and W. Shih. "Ignition transition in turbulent premixed combustion". In: *Combustion and Flame* 157.2 (2010), pp. 341–350.

[211] A. Singh, M. Mann, T. Kissel, J. Brübach, and A. Dreizler. "Simultaneous Measurements of Temperature and CO Concentration in Stagnation Stabilized Flames". In: *Flow, Turbulence and Combustion* 90.4 (2013), pp. 723–739.

[212] T. Sloane. “Numerical-simulation of electric spark-ignition in methane air mixtures at pressures above one atmosphere”. In: *Combustion Science and Technology* 86.1-6 (1992), 121–133.

[213] K. C. Smyth and C. R. Shaddix. “The elusive history of m = 1.57–0.56 i for the refractive index of soot”. In: *Combustion and Flame* 107.3 (1996), pp. 314–320.

[214] I. M. Sobol’. “On sensitivity estimation for nonlinear mathematical models”. In: *Matematicheskoe modelirovanie* 2.1 (1990), pp. 112–118.

[215] L. Soucasse, P. Riviere, and A. Soufiani. “Subgrid-scale model for radiative transfer in turbulent participating media”. In: *Journal of Computational Physics* 257.A (2014), 442–459.

[216] A. Soufiani, P. Mignon, and J. Taine. “Radiation-turbulence interaction in channel flows of infrared active gases”. In: *Proceedings of the Ninth International Heat Transfer Conference*. Ed. by D. Hemisphere Washington. Vol. 6. 1990, pp. 403–408.

[217] A. Soufiani and J. Taine. “Application of statistical narrow-band model to coupled radiation and convection at high temperature”. In: *International Journal of Heat and Mass Transfer* 30.3 (1987), pp. 437–447.

[218] M. Stöhr, K. Oberleithner, M. Sieber, Z. Yin, and W. Meier. “Experimental Study of Transient Mechanisms of Bistable Flame Shape Transitions in a Swirl Combustor”. In: *Journal of Engineering for Gas Turbines and Power* 140.1 (2017), pp. 011503–011503-8.

[219] V. Subramanian, P. Domingo, and L. Vervisch. “Large eddy simulation of forced ignition of an annular bluff-body burner”. In: *Combustion and Flame* 157.3 (2010), pp. 579–601.

[220] J. Taine and A. Soufiani. “Gas {IR} Radiative Properties: From Spectroscopic Data to Approximate Models”. In: *Advances in Heat Transfer*. Ed. by Y. I. C. James P. Hartnett Thomas F. Irvine and G. A. Greene. Vol. 33. Elsevier, 1999, pp. 295–414.

[221] L. Tay-Wo-Chong, M. Zellhuber, T. Komarek, H. G. Im, and W. Polifke. “Combined Influence of Strain and Heat Loss on Turbulent Premixed Flame Stabilization”. In: *Flow, Turbulence and Combustion* 97.1 (2016), pp. 263–294.

[222] L. Tesse, F. Dupoirieux, and J. Taine. “Monte Carlo modeling of radiative transfer in a turbulent sooty flame”. In: *International Journal of Heat and Mass Transfer* 47.3 (2004), 555–572.

[223] L. Tesse, F. Dupoirieux, B. Zamuner, and J. Taine. “Radiative transfer in real gases using reciprocal and forward Monte Carlo methods and a correlated-k approach”. In: *International Journal of Heat and Mass Transfer* 45.13 (2002), 2797–2814.

[224] S. Tezuka and H. Faure. “I-binomial scrambling of digital nets and sequences”. In: *Journal of complexity* 19.6 (2003), pp. 744–757.

[225] I. Tiselj, J. Oder, and L. Cizelj. “Double-sided cooling of heated slab: Conjugate heat transfer {DNS}”. In: *International Journal of Heat and Mass Transfer* 66 (2013), pp. 781–790.

[226] A. S. Tomlin, T. Turànyi, M. J. Pilling, and M. J. Pilling. “Chapter 4 Mathematical tools for the construction, investigation and reduction of combustion mechanisms”. In: *Comprehensive Chemical Kinetics*. Vol. Volume 35. Elsevier, 1997, pp. 293–437.

[227] P. Trisjono, K. Kleinheinz, H. Pitsch, and S. Kang. “Large Eddy Simulation of Stratified and Sheared Flames of a Premixed Turbulent Stratified Flame Burner Using a Flamelet Model with Heat Loss”. In: *Flow, Turbulence and Combustion* 92.1 (2014), pp. 201–235.

[228] T. Turanyi. “Reduction of large reaction-mechanisms”. In: *New Journal of Chemistry* 14.11 (1990), 795–803.

[229] J. A. van Oijen, A. Donini, R. J. M. Bastiaans, J. H. M. ten Thije Boonkkamp, and L. P. H. de Goey. "State-of-the-art in premixed combustion modeling using flamelet generated manifolds". In: *Progress in Energy and Combustion Science* 57 (2016), pp. 30–74.

[230] J. van Oijen and L. de Goey. "Modelling of premixed laminar flames using flamelet-generated manifolds". In: *Combustion Science and Technology* 161 (2000), 113–137.

[231] L. Vervisch, R. Haugel, P. Domingo, and M. Rullaud. "Three facets of turbulent combustion modelling: DNS of premixed flame, LES of lifted nonpremixed V-flame and RANS of jet-flame". In: *Journal of Turbulence* 5.4 (2004), pp. 1–36.

[232] D. Veynante and L. Vervisch. "Turbulent combustion modeling". In: *Progress in Energy and Combustion Science* 28.3 (2002), pp. 193–266.

[233] P. S. Volpiani, T. Schmitt, and D. Veynante. "A posteriori tests of a dynamic thickened flame model for large eddy simulations of turbulent premixed combustion". In: *Combustion and Flame* 174 (2016), pp. 166–178.

[234] A. P. Wandel. "Influence of scalar dissipation on flame success in turbulent sprays with spark ignition". In: *Combustion and Flame* 161.10 (2014), pp. 2579–2600.

[235] G. Wang, M. Boileau, D. Veynante, and K. Truffin. "Large eddy simulation of a growing turbulent premixed flame kernel using a dynamic flame surface density model". In: *Combustion and Flame* 159.8 (2012), pp. 2742–2754.

[236] L. Wang, M. Modest, D. Haworth, and S. Turns. "Modelling nongrey gas-phase and soot radiation in luminous turbulent nonpremixed jet flames". In: *Combustion Theory and Modelling* 9.3 (2005), pp. 479–498.

[237] Y. Wang, A. Raj, and S. H. Chung. "A PAH growth mechanism and synergistic effect on PAH formation in counterflow diffusion flames". In: *Combustion and Flame* 160.9 (2013), pp. 1667–1676.

[238] J. Warnatz, U. Mass, and R. W. Dibble. *Combustion: Physical and Chemical Fundamentals, Modeling and Simulation, Experiments, Pollutant formation.* 4th. Spinger, 2006.

[239] C. K. Westbrook and F. L. Dryer. "Simplified Reaction Mechanisms for the Oxidation of Hydrocarbon Fuels in Flames". In: *Combustion Science and Technology* 27.1-2 (1981), pp. 31–43.

[240] A. Wick, F. Priesack, and H. Pitsch. *Large-Eddy Simulation and Detailed Modeling of Soot Evolution in a Model Aero Engine Combustor.* ASME Turbo Expo, Paper No. GT2017-63293, pp. V04AT04A020. 2017.

[241] Y. Wu, D. C. Haworth, M. F. Modest, and B. Cuenot. "Direct numerical simulation of turbulence/radiation interaction in premixed combustion systems". In: *Proceedings of the Combustion Institute* 30.1 (2005), pp. 639–646.

[242] Z. J. Wu, A. R. Masri, and R. W. Bilger. "An experimental investigation of the turbulence structure of a lifted H-2/N-2 jet flame in a vitiated co-flow". In: *Flow, Turbulence and Combustion* 76.1 (2006), pp. 61–81.

[243] Z. Wu, S. H. Starner, and R. W. Bilger. "Lift-off heights of turbulent H_2/N_2 jet flames in a vitiated coflow". In: *Proceedings of the 2003 Australian Symposium on Combustion and the 8th Australian Flame Days.* Monash University, Australia, 2003.

[244] D. Xiu and G. E. Karniadakis. "The Wiener–Askey polynomial chaos for stochastic differential equations". In: *SIAM journal on scientific computing* 24.2 (2002), pp. 619–644.

[245] Y. Xuan and G. Blanquart. "Effects of aromatic chemistry-turbulence interactions on soot formation in a turbulent non-premixed flame". In: *Proceedings of the Combustion Institute* 35.2 (2015), pp. 1911–1919.

[246] YALES2, CORIA. *https://www.coria-cfd.fr/index.php/YALES2*.

[247] Z. Yin, P. Nau, and W. Meier. "Responses of combustor surface temperature to flame shape transitions in a turbulent bi-stable swirl flame". In: *Experimental Thermal and Fluid Science* 82 (2017), pp. 50–57.

[248] J. Yon, A. Bescond, and F. Liu. "On the radiative properties of soot aggregates part 1: Necking and overlapping". In: *Journal of Quantitative Spectroscopy and Radiative Transfer* 162 (2015), pp. 197–206.

[249] J. Zhang, C. R. Shaddix, and R. W. Schefer. "Design of model-friendly turbulent non-premixed jet burners for C2+ hydrocarbon fuels". In: *Review of Scientific Instruments* 82.7 (2011), p. 074101.

[250] Y. F. Zhang, O. Gicquel, and J. Taine. "Optimized Emission-based Reciprocity Monte Carlo Method to speed up computation in complex systems". In: *International Journal of Heat and Mass Transfer* 55.25–26 (2012), pp. 8172–8177.

[251] Y. Zhang, B. Rogg, and K. N. C. Bray. "2-D simulation of turbulent autoignition with transient laminar flamelet source term closure". In: *Combustion Science and Technology* 105.4-6 (1995), pp. 211–227.

Manuscrit Habilitation à Diriger des Recherches
Délivrée par l'Université Rouen Normandie

Ronan Vicquelin

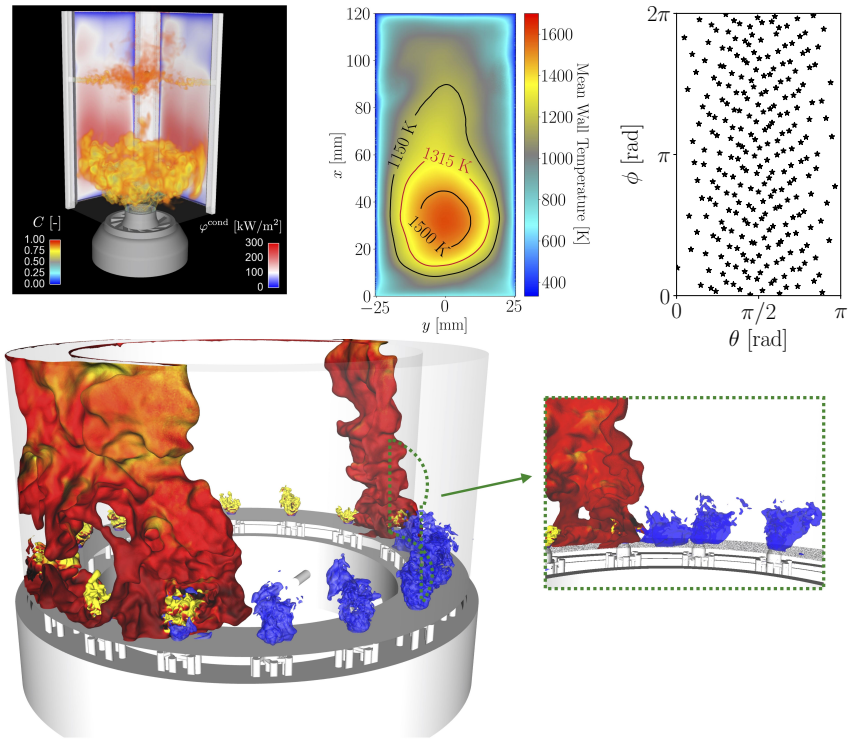

Un grand merci à l'ensemble des doctorants que j'ai co-encadrés : Yufang, Chaï, Maxime, Nicolas, Théa, Pedro, Lorella, Jan, Arthur et tous les suivants.

Unité de Recherche : Laboratoire d'Energétique Moléculaire et Macroscopique, Combustion (EM2C) du CNRS (UPR 288)